UNIVERSITY OF ROCHESTER
LABORATORY FOR LASER ENERGETICS

Volume 128
July–September 2011
DOE/NA/28302-1034

LLE Review

Quarterly Report

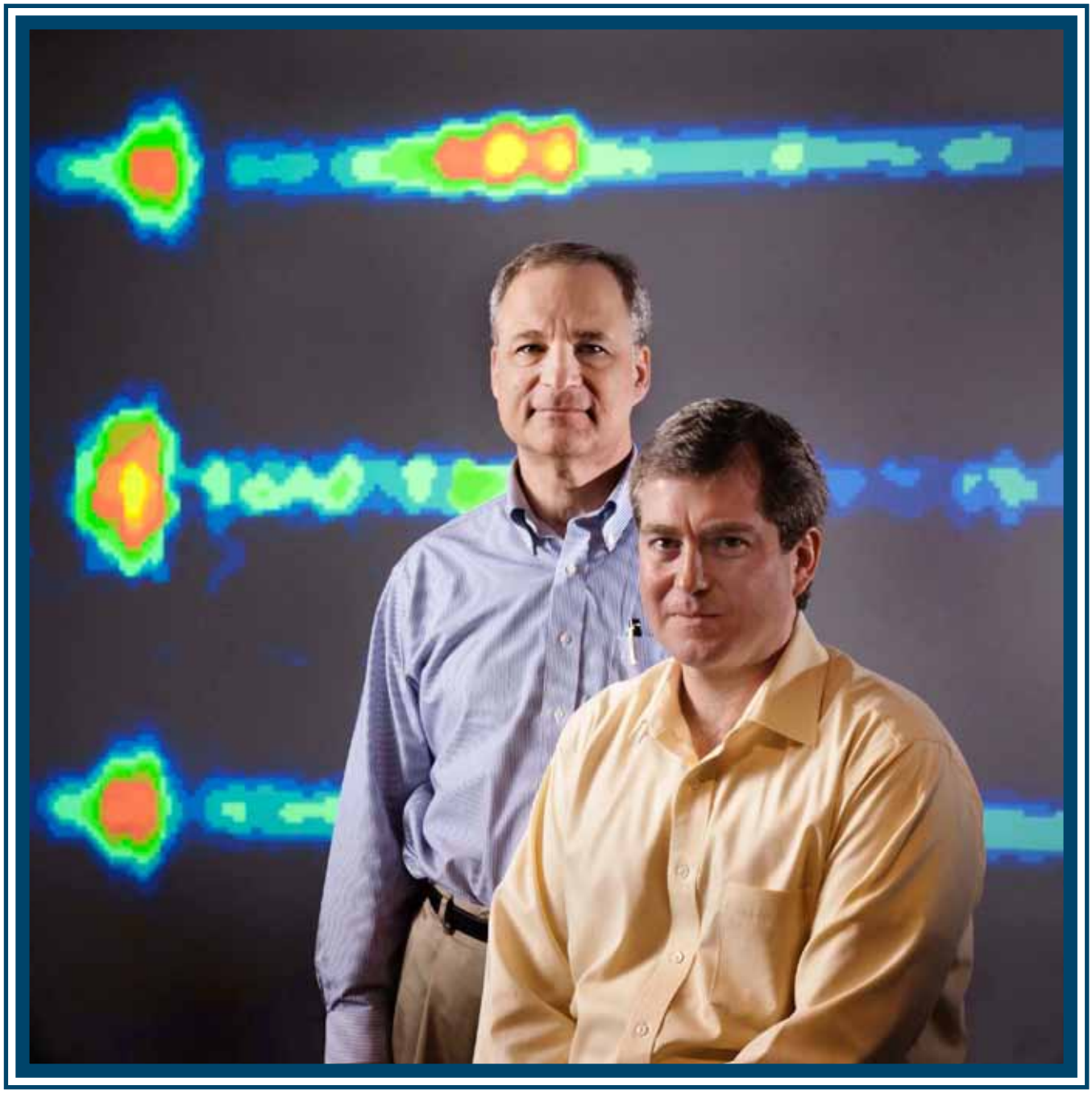

About the Cover:

The cover photo highlights Laboratory for Laser Energetics (LLE) senior scientists Dr. Sean Regan (right) and Dr. Reuben Epstein presenting results on hot-spot mix mass in ignition-scale inertial confinement fusion (ICF) targets. Studies led by these scientists have used x-ray spectroscopy to infer values of hot-spot mix mass for implosions on the National Ignition Facility (NIF). In the background are experimental 1-D spectral imaging data that provide clear evidence for Ge-doped material mixing with the assembled hot spot. These results are important for ICF because there is a requirement for ignition (that the hot-spot mix mass be less than 75 ng) set from multidimensional radiation–hydrodynamic simulations. The amount of hot-spot mix mass, estimated from the Ge K-shell line brightness using a detailed atomic physics code, was found to be comparable to the 75-ng allowance for hot-spot mix.

The image to the left shows the x-ray spectrometer "Supersnout" developed by LLE to diagnose hot-spot mix in NIF implosions. The Supersnout contains the hot-spot x-ray spectrometer (HSXRS). HSXRS is a time-integrated spectrometer that combines a slit aperture with a pentaerythritol (PET) Bragg crystal to record 1-D spectral images of an implosion core with a magnification of ~11 and a spatial resolution of ~100 μm. Absolute photometric calibration of HSXRS (9.75 to 13.1 keV) relates Ge K-shell emission-line brightness to the hot-spot mix mass.

The work described in this volume includes current research at the Laboratory for Laser Energetics, which is supported by New York State Energy Research and Development Authority, the University of Rochester, the U.S. Department of Energy Office of Inertial Confinement Fusion under Cooperative Agreement No. DE-FC52-08NA28302, and other agencies.

Printed in the United States of America
Available from
National Technical Information Services
U.S. Department of Commerce
5285 Port Royal Road
Springfield, VA 22161
www.ntis.gov

For questions or comments, contact Philip M. Nilson, Editor,
Laboratory for Laser Energetics
250 East River Road
Rochester, NY 14623-1299
(585) 275-9527
www.lle.rochester.edu

UNIVERSITY OF ROCHESTER
LABORATORY FOR LASER ENERGETICS

Volume 128
July–September 2011
DOE/NA/28302-1034

LLE Review

Quarterly Report

UR LLE

Contents

In Brief

This volume of the LLE Review, covering July–September 2011, features "Hot-Spot Mix in Ignition-Scale Inertial Confinement Fusion Targets" by S. P. Regan, R. Epstein, and T. C. Sangster (LLE); R. L. McCrory and D. D. Meyerhofer (LLE and Departments of Mechanical Engineering and Physics, University of Rochester); B. A. Hammel, L. J. Suter, J. Ralph, H. Scott, M. A. Barrios, D. K. Bradley, D. A. Callahan, C. Cerjan, G. W. Collins, S. N. Dixit, M. J. Edwards, D. R. Farley, S. Glenn, S. H. Glenzer, D. G. Hicks, N. Izumi, O. L. Landen, T. Ma, P. Springer, R. P. J. Town, S. W. Haan, A. Hamza, and N. B. Meezan (LLNL); J. D. Kilkenny (LLNL and GA); I. E. Golovkin and J. J. MacFarlane (Prism Computational Sciences, Inc.); J. L. Kline and G. A. Kyrala (LANL); R. C. Mancini (University of Reno); A. Nikroo (GA); and K. J. Peterson (SNL). In this article (p. 145), mixing of ablator material into the hot spot of ignition-scale inertial confinement fusion implosions by hydrodynamic instabilities is diagnosed with x-ray spectroscopy at the National Ignition Facility. The experimentally inferred values of hot-spot mix mass, based on the absolute spectral brightness of the emergent Ge K-shell emission, range from 2 to 400 ng. Most implosions have less than 75 ng of hot-spot mix, consistent with the requirements for ignition.

Additional highlights of research presented in this issue include the following:

- J. A. Frenje, C. K. Li, F. H. Séguin, D. T. Casey, and R. D. Petrasso (Plasma Science and Fusion Center, MIT); D. P. McNabb, P. Navratil, and S. Quaglioni (LLNL); T. C. Sangster and V. Yu Glebov (LLE); and D. D. Meyerhofer (LLE and Departments of Mechanical Engineering and Physics, University of Rochester) measure for the first time the differential cross section for the elastic neutron–triton (n–^{3}H) and neutron-deuteron (n–^{2}H) scattering at 14.1 MeV using an inertial confinement fusion (ICF) facility (p. 151). By measuring elastically scattered ^{3}H and ^{2}H ions from a deuterium–tritium gas-filled ICF capsule implosion, the differential cross section for the elastic n–^{3}H scattering was obtained. Significantly higher accuracy was achieved than in previous accelerator experiments. The results compare well with calculations that combine the resonating-group method with an *ab initio* no-core shell model, which demonstrates that recent advances in *ab initio* theory can provide an accurate description of light-ion reactions.

- J. D. Hager J. P. Knauer, S. X. Hu, and T. C. Sangster (LLE); D. D. Meyerhofer (LLE and Departments of Mechanical Engineering and Physics, University of Rochester); and V. A. Smalyuk (LLNL) have performed direct-drive, Rayleigh–Taylor (RT) growth experiments in liquid deuterium (D_2) on the OMEGA laser with planar cryogenic targets at a laser intensity of $\sim 4 \times 10^{14}$ W/cm^2 (p. 157). These are the first RT measurements in deuterium at conditions relevant to inertial confinement fusion (ICF) using a mass-preimposed initial modulation. The measured modulation optical depths are in agreement with the 2-D hydrodynamics code *DRACO* using flux-limited local thermal transport, providing an important step in the experimental validation of simulations for direct-drive ignition.

- A. V. Okishev (LLE) demonstrates a highly efficient pulsed-diode–pumped, room-temperature Yb:YAG ceramic laser with a slope efficiency of 78% and an optical-to-optical efficiency of 51% (p. 163). This is the highest slope efficiency for a room-temperature Yb:YAG ceramic laser reported to date. A regenerative amplifier with ~15-mJ output energy and fourth-order super-Gaussian beam profile based on this laser has been demonstrated.

- A summary of LLE's Summer High School Research Program (p. 166), the FY11 Laser Facility Report (p. 168), and the National Laser Users' Facility and External Users' Programs (p. 171) are presented.
- This volume concludes with R. D. Petrasso's (Plasma Science and Fusion Center, MIT) report on the Third Omega Laser Facility Users' Group Workshop (27–29 April 2011) on p. 250. LLE hosted more than 115 researchers from 25 universities and laboratories and 9 countries. The goal for the three-day workshop was to facilitate communications and exchanges among individual OMEGA users and between users and LLE; to present ongoing and proposed research; to encourage research opportunities and collaborations that could be undertaken at the Omega Laser Facility and in a complementary fashion at other facilities; to provide an opportunity for students and postdoctoral fellows to present their research at LLE in an interactive and informal atmosphere; and to provide feedback to LLE about ways to improve the facility and future experimental campaigns.

Philip M. Nilson
Editor

Hot-Spot Mix in Ignition-Scale Inertial Confinement Fusion Targets

Inertial confinement fusion (ICF) depends on the formation of a central hot spot with sufficient temperature and areal density for ignition.[1,2] Laser-driven hohlraums are used to accelerate targets via x-ray ablation[1,2] at the 192-beam, 351-nm, 1.8-MJ National Ignition Facility (NIF).[3] Shock-timing,[4,5] implosion velocity,[6] and symmetry[7,8] experiments on the NIF are underway with ignition-scale targets[5,9] to optimize the hot-spot formation. The concentric spherical layers of current NIF ignition targets consist of a plastic Ge-doped ablator surrounding a thin shell of cryogenic thermonuclear fuel (i.e., hydrogen isotopes), with fuel vapor filling the interior volume.[10] Liquid deuterium–tritium (DT) is directed inside the ablator shell using a fill tube, and a DT-ice layer is formed using the beta-layering technique.[11] As the shell converges, it compresses the fuel vapor, forming a hot spot as it decelerates. The hot spot contains ~20 μg of DT mass, which undergoes fusion reactions. As the DT-fusion alpha particles deposit their energy in the hot spot, the hot-spot temperature sharply rises, and a thermonuclear burn wave propagates out through the surrounding cold and dense DT fuel. Ignition is predicted to occur when the temperature and areal density of the hot spot reach a minimum of 5 keV and 0.3 mg/cm^2, respectively.[10]

Radiative and conductive losses from the hot spot can be increased by hydrodynamic instabilities.[10] The Richtmyer–Meshkov and Rayleigh–Taylor hydrodynamic instabilities seeded by high-mode ($50 < \ell < 200$) ablator-surface mass perturbations from intrinsic CH surface roughness, the fill tube, or microscopic dust particles are predicted to mix ablator material into the interior of the shell at the end of the acceleration phase and into the hot spot as it forms (i.e., hot-spot mix), producing Ge K-shell emission.[12] This article presents conclusive experimental evidence of hot-spot mix occurring in ignition-scale implosions, for the first time, and quantifies the amount of hot-spot mix mass. These experimental observations are important for ICF because there is a requirement for ignition, set from multidimensional radiation–hydrodynamic simulations, that the hot-spot mix mass be less than 75 ng (Ref. 10). The amount of hot-spot mix mass, estimated from the Ge K-shell line brightness using a detailed atomic physics code,[13] was found to be comparable to the 75-ng allowance for hot-spot mix. Predictions of a simple mix model[14] based on linear growth of the measured surface-mass modulations are close to the experimental results. The strategy to control the amount of hot-spot mix involves reducing the capsule-surface mass perturbations and reducing the growth factors of the hydrodynamic instability[12] of the plastic ablator through dopant and laser pulse shape choices, or changing to another ablator material (e.g., Cu-doped Be).[15]

The amount of hot-spot mix mass in ignition-scale NIF implosions was diagnosed using x-ray spectroscopy.[16] The ablator was doped with Ge to minimize preheat of the ablator closest to the DT ice caused by Au M-band emission from the hohlraum x-ray drive.[17] A schematic of an ignition target highlighting the Ge-doped ablator surrounding the cryogenic-DT layer and DT vapor is shown in Fig. 128.1(a). The K-shell line emission from the ionized Ge that has penetrated into the hot spot provides an experimental signature of hot-spot mix.[12] If the Ge remains in the cold and dense ablator, the Ge ionization will be insufficient to create K-shell line radiation; therefore, the Ge K-shell line emission provides a direct diagnosis of Ge-doped plastic mixing with the hot spot.

The Ge emission from DT and tritium–hydrogen–deuterium (THD) cryogenic targets and gas-filled plastic-shell capsules, which replace the cryogenic fuel layer with a mass-equivalent CH layer[7,8] [shown in Fig. 128.1(b)] was examined. The latter, called a symmetry capsule or symcap, is used to infer the symmetry of the hohlraum x-ray drive by measuring the spatial distribution of the x-ray emission from the hot spot around the time of peak compression under simpler noncryogenically layered conditions. Symcap targets have a D^{3}He (30:70) gas fill. Ignition targets have an equimolar mixture of D and T; however, tritium-rich layered targets with H and D were imploded to exploit the lower neutron yields for diagnostic purposes.[10] The THD implosions are hydrodynamically equivalent to the DT implosions. As seen in Fig. 128.1, the ignition target had an outside diameter of 2.2 mm and an ablator thickness of 190 μm. The radial distribution of the Ge-dopant atomic percentage

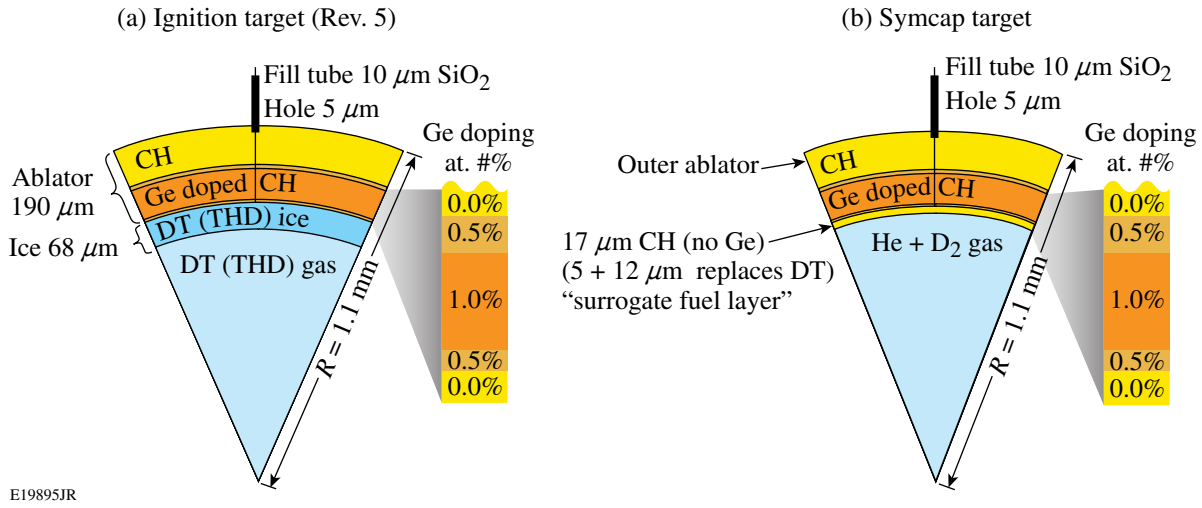

Figure 128.1
Schematic of (a) an ignition target and (b) a symcap target. The cryogenic fuel of the ignition target and the D^3He gas fill of the symcap are transported to the interior of the Ge-doped, plastic ablator using a fill tube. The radial distribution of the Ge atomic doping level in the plastic ablator is shown.

in the plastic ablator was varied to achieve a more-optimal Atwood number between the ablator and the fuel layer at peak shell velocity.[10] In an ignition target the Ge-doped plastic layer is separated from the DT fuel by an undoped plastic layer of 5-μm thickness. In the symcap target, an extra inner 12 μm of plastic of equivalent mass replaces the DT fuel layer.

Bright spots in broadband, gated x-ray implosion images for photon energies greater than 8 keV indicate that hot-spot mix may be occurring in NIF implosions.[18] These bright spots do not provide conclusive evidence, however, of ablator mixing into the hot spot nor do they allow for quantification of the mix mass since the bright spots depend on the plasma composition and conditions and on spatial variations in shell x-ray attenuation caused by regions of low shell areal density. Consequently, a hot-spot x-ray spectrometer (HSXRS) providing coverage in the 9.75- to 13.1-keV range for analysis of the Ge K-shell emission was installed on the NIF.[19] This time-integrated, one-dimensional (1-D) imaging spectrometer viewed the implosion capsule through the laser entrance hole within ~2° of the hohlraum symmetry axis. The HSXRS combines a 100-μm-wide slit aperture and a pentaerythritol (PET) Bragg crystal to record 1-D spectral images of the implosion core with a magnification of about 11, a spatial resolution in the target plane of approximately 100 μm, and a spectral resolution of 12 eV (Ref. 19). Therefore, the implosion emission is spatially discriminated from the background hohlraum plasma emission in the time-integrated 1-D spectral images. Figure 128.2 shows an x-ray spectrum measured on symcap implosion N110208 from this diagnostic (black curve), highlighting the spectral features resulting from cold Ge in the pusher (edge drop at 11 keV and fluorescent emission at 9.8 keV) and, most importantly, the emission from the highly ionized Ge in the hot-spot mix mass between 10 and 10.5 keV. He-like Ge is the highest charge state observed. This emission is the first direct evidence of ablator mix into the hot spot of ignition-scale targets. In Fig. 128.2 the x-ray continuum from the hot spot transmitted through the compressed shell is modeled (red curve) assuming the x-ray continuum and the shell optical thickness scale with photon energy ($h\nu$) as $e^{-h\nu/\mathrm{kT}}$ and $h\nu^{-3}$, respectively. I_C, M_L, and $M_\mathrm{K+L}$ are the fitting constants and $h\nu_\mathrm{K}$ is the Ge K-edge photon energy.

The Ge K-shell line emission in the 10- to 10.5-keV range from the hot-spot mix mass is highlighted in Fig. 128.3(a) for symcap implosion N110208. As shown in Fig. 128.3(b) a similar spectrum is observed for DT implosion N110620. In these plots the hot-spot x-ray continuum was subtracted and a correction for pusher absorption was applied. This photon-energy range contains a rich spectrum of line emissions from Ge He-like resonance $1s^2$–$1s2p$(1P) and intercombination $1s^2$–$1s2p$(3P) transitions as well as from Ge B-like $1s^2(2s,2p)^3$–$1s2p(2s,2p)^3$, Ge Be-like $1s^2(2s,2p)^2$–$1s2p(2s,2p)^2$, and Ge Li-like $1s^2(2s,2p)^1$–$1s2p(2s,2p)^1$ satellite lines. The spectral envelope of the He_α + satellite feature is sensitive to variations in the electron temperature (T_e) and electron density (n_e) of the mix mass.[20]

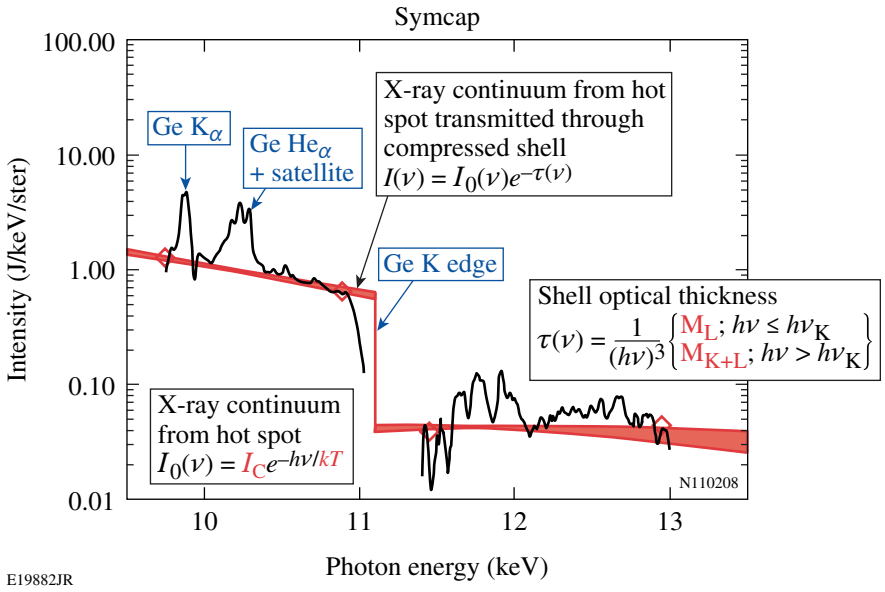

Figure 128.2
Spatially integrated and photometrically calibrated measured x-ray spectrum for symcap implosion N110208 showing Ge He$_\alpha$ + satellite and Ge K$_\alpha$ emissions and the Ge K edge (black curve). The x-ray continuum from the hot spot transmitted through the compressed shell is modeled (red curve) assuming the x-ray continuum and the shell optical thickness scale with photon energy ($h\nu$) as $e^{-h\nu/kT}$ and $h\nu^{-3}$, respectively. I_C, M_L, and M_{K+L} are the fitting constants and $h\nu_K$ is the Ge K-edge photon energy.

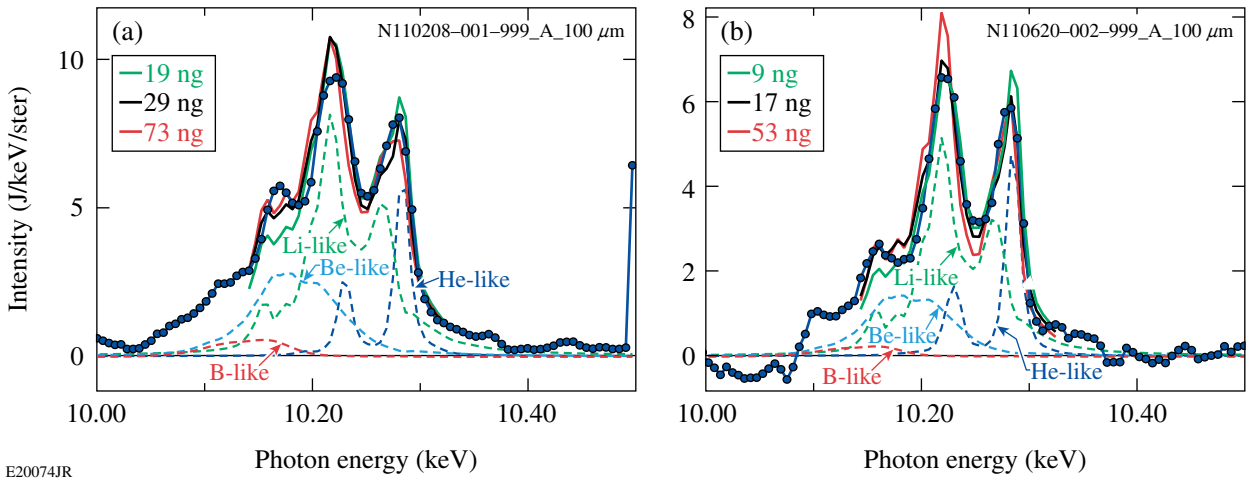

Figure 128.3
Measured Ge K-shell line emission in the 10- to 10.5-keV range from the hot-spot mix mass (blue circles) for (a) symcap implosion N110208 and (b) DT implosion N110620. Modeled spectra assuming uniform plasma conditions and based on least squares fitting are shown [best fit (black curve); 1σ spectral fits (red and green curves)]. Uniform plasma conditions determined from spectral fitting and inferred mix masses are given in Tables 128.I and 128.II. Dashed lines show contributions from He-like, Li-like, Be-like, and B-like charge states for the best fit.

The physical picture of the hot-spot mix is shown in Fig. 128.4. Most of the Ge remains in the compressed shell and absorbs x rays from the hot spot. Depending on the temperature of the shell, this absorption manifests as either Ge K$_\alpha$ emission or Ge 1s–2p absorption features.[20] The ablator material mixed into the hot spot is ionized and emits Ge K-shell x rays. The mix mass is modeled as multiple identical independent spheres of CH ablator mass doped with 1% atomic Ge, each at the same single electron density and temperature, and with areal densities of Ge-doped CH ($\rho R_{\text{CH Ge}}$) and Ge (ρR_{Ge}). A detailed atomic and radiation physics model[13] is used to estimate the amount of mix mass from the Ge K-shell line spectrum as follows: The temperature- and density-dependent emissivity model gives the total emission per Ge mass within the Ge He$_\alpha$ + satellite feature. The spectral fit includes self-absorption–coupled level kinetics, giving an estimate of the areal density of Ge in the mix-mass sphere. The Ne through H-like species are represented with detailed-configuration

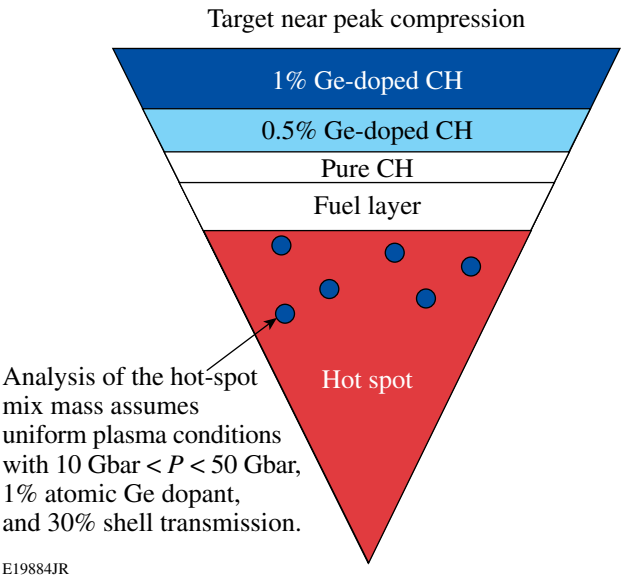

Figure 128.4
Schematic of mix mass in compressed target near peak compression.

accounting (DCA) including all single excitations through $n = 10$, all double excitations through $n = 3$, and splitting important resonance-line–emitting configurations. The Stark-broadening of the Ge line shapes was calculated using the MERL code,[21] but it is not significant for $n_e < 10^{25}$ cm^{-3}. The calculated emergent intensity distribution is sensitive to variations in n_e, T_e, and ρR_{Ge} (Ref. 20). The measured spectra are compared with modeled spectra, including instrumental broadening effects for several thousand combinations of n_e, T_e, and ρR_{Ge}, and the best match is determined based on a least squares fit. The amount of mix mass is then determined from the inferred plasma conditions (n_e, T_e, and ρR_{Ge}) and the absolute brightness of the Ge He$_\alpha$ + satellite feature. From the inferred plasma conditions, each sphere of radius R has a CH Ge mass $M_{CH\,Ge} = 4\pi R^3 \rho_{CH\,Ge}/3$, where $R = \rho R_{CH\,Ge}/\rho_{CH\,Ge}$ is calculated using the inferred areal densities and electron density of the mix mass and assuming the average ionization is 3.75. The number of spheres the total mix mass are determined by comparing the brightness per sphere to the total measured brightness of the Ge He$_\alpha$ + satellite measurement.

An analysis of the hot-spot mix mass assumes uniform plasma conditions (n_e, T_e, and ρR_{Ge}), electron pressures between 10 and 50 Gbar, 1% atomic Ge dopant, and 30% shell transmission for the Ge He$_\alpha$ + satellite feature (per 1-D hydrodynamic simulations). The estimated shell transmission represents a lower limit for the experiment, leading to an upper limit of inferred mix mass. The two-dimensional (2-D) hydrodynamic simulations show that most of the hot-spot mix mass originates from the shell layer doped with 1% atomic Ge.[12] The modeled spectra are shown in Fig. 128.3 with the black curve representing the best fit (i.e., minimum χ^2) and the red/green curves representing 1σ spectral fits. The latter define the upper and lower limits of the hot-spot mix mass. The dashed curves in Fig. 128.3 show the contributions to the spectrum from the He-like, Li-like, Be-like, and B-like charge states. Similar mix-mass observations were made on other symcap shots (as shown in Table 128.I) and on DT and THD implosions (as shown in Table 128.II). The mix-mass sphere diameter from the spectral analysis is micron scale, and the number of mix-mass spheres varies from hundreds to thousands, depending on the implosion.

The expected hot-spot mix mass for each capsule is independently estimated with a simple hot-spot mix-mass model that combines linear analysis of the perturbation growth with detailed 2-D hydrodynamic simulations following these steps:[14] (1) transform the capsule-surface perturbation measurements into Legendre-mode space; (2) multiply the decomposed initial perturbations by linear growth factors, calculated for a final perturbation at the ice–ablator interface at peak shell velocity that resulted from a small initial bump on the outside of the ablator; (3) transform back to physical space; (4) find the volume of the ablator that is inside the ice for a DT or THD implosion or the inner CH for a symcap; and (5) multiply by the density calibrated with a detailed bump simulation (~10 g/cm^3), yielding an estimate of the hot-spot mix mass.[14] The simple hot-spot mix model does not describe the detailed shape of perturbations, but it is calibrated against simulations with actual bump sizes and nonlinear perturbation growth. The hot-spot mix mass (i.e., CH doped with 1% atomic Ge) inferred from the x-ray spectroscopy is compared with the simple hot-spot mix-mass model in Fig. 128.5, and the model is close to the measured results. Most ignition-scale implosions have hot-spot mix mass below the 75-ng requirement for ignition. The experimentally inferred values of hot-spot mix mass in Fig. 128.5 represent a lower bound since the x-ray spectroscopy is only sensitive to the Ge hot-spot mix mass and inferring the CH mass requires an assumed doping level of Ge in the mix mass. Measurements of the mass remaining of ignition-scale targets are close to or slightly larger than predicted, but the implosion velocity is about 10% low.[6] Higher levels of hot-spot mix mass may occur when higher laser powers and/or thinner shells are used to increase the peak implosion velocity to reach the ignition requirement of 350 μm/ns (Ref. 10).

In the future, hot-spot mix will be examined with Cu and Ge dopants located at different radial locations in the ablator to test

Table 128.I: Fitting parameters and hot-spot mix mass inferred for symcap implosions.

Shot	Mix n_e (10^{25} cm^{-3})	Mix T_e (keV)	Mix ρR_{Ge} (mg/cm^2)	CH Ge mix mass (ng)
N101004	0.8 (+0.2, –0.5)	2.4 (+0.6, –0.3)	0.150 (–0, +0.25)	14 (–7, +30)
N110208	1.0 (+0, –0.5)	2.3 (+0.4, –0.3)	0.125 (+0.025, +0.1)	29 (–10, +44)
N110211	0.9 (+0.1, –0.4)	2.0 (+0.3, –0.2)	0.150 (–0, +0.125)	20 (–8, +24)
N110612	0.9 (+0.1, –0.5)	2.2 (+0.5, –0.5)	0.075 (+0.025, –0)	79 (–39, +300)

Table 128.II: Fitting parameters and hot-spot mix mass inferred for DT and THD implosions.

Shot	Mix n_e ($\times 10^{25}$ cm^{-3})	Mix T_e (keV)	Mix ρR_{Ge} (mg/cm^2)	CH Ge mix mass (ng)	
N100929	0.4 (+0.6, +0.1)	1.7 (+0.2, –0.2)	0.075 (+0, –0)	74 (–48, +55)	
N110121	0.3 (+0.6, +0.1)	2.1 (+0.3, –0.5)	0.075 (+0, –0)	67 (–47, +110)	
N110201	1.0 (+0, –0.4)	1.6 (+0.8, –0.5)	0.2 (–0.1, +0.15)	15 (–12, +285)	
N110212	0.5 (+0.1, +0.1)	1.6 (+0.8, –0.5)	0.075 (–0, +0.15)	20 (–17, +265)	
N110603	0.4 (+0.6, +0)	1.9 (+0.6, –0.3)	0.075 (+0.025, –0)	18 (–14, +23)	THD
N110608	0.4 (+0.6, +0)	2.0 (+0.4, –0.3)	0.075 (+0, –0)	63 (–44, +65)	DT
N110615	0.9 (+0, –0.5)	2.2 (+1.0, –0.5)	0.075 (+0, –0)	15 (–10, +56)	
N110620	0.8 (+0.2, –0.5)	2.4 (+0.6, –0.3)	0.075 (+0, –0)	17 (–8, +36)	

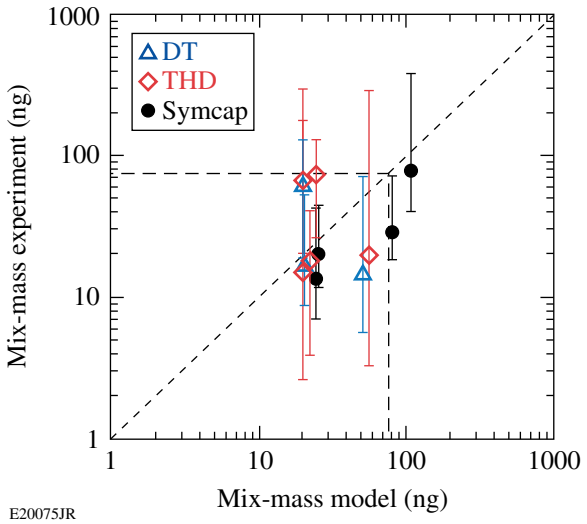

Figure 128.5
Comparison of hot-spot mix mass (i.e., CH doped with 1% atomic Ge) inferred from x-ray spectroscopy with a simple hot-spot mix-mass model that combines linear analysis of the perturbation growth with detailed 2-D hydrodynamic simulations.

assumptions of the origin of the hot-spot mix mass, and x-ray radiography of imposed surface perturbations will be studied to directly relate surface perturbations with the hot-spot mix mass inferred from the x-ray spectroscopy.[12]

Conclusive experimental evidence of the hot-spot mix predicted to occur in ignition-scale implosions as a result of the Richtmyer–Meshkov combined with Rayleigh–Taylor hydrodynamic instabilities[12] has been presented. The amount of hot-spot mix mass in NIF implosions inferred from x-ray spectroscopy is close to or below the 75-ng limit for ignition. These experimental observations are important for ICF because predictions from multidimensional hydrodynamic simulations show that hot-spot mix mass in excess of 75 ng could quench the temperature of the hot spot, reduce the thermonuclear fusion rate, and jeopardize the realization of ignition in the laboratory.[10] Further efforts to control hot-spot mix by reducing the capsule surface-mass perturbations and reducing the growth factors of the hydrodynamic instability of the plastic ablator, or by changing to another ablator material [e.g., Cu-doped Be (Ref. 16)] are ongoing.

ACKNOWLEDGMENT

The authors acknowledge the excellent operation of the National Ignition Facility and helpful suggestions from M. H. Key. This work was supported by the U.S. Department of Energy Office of Inertial Confinement Fusion under Cooperative Agreement No. DE-FC52-08NA28302, the University of Rochester, and the New York State Energy Research and Development Authority. The support of DOE does not constitute an endorsement by DOE of the views expressed in this article.

REFERENCES

1. J. D. Lindl *et al.*, Phys. Plasmas **11**, 339 (2004).
2. S. H. Glenzer *et al.*, Science **327**, 1228 (2010).
3. G. H. Miller, E. I. Moses, and C. R. Wuest, Opt. Eng. **43**, 2841 (2004).
4. T. R. Boehly, D. H. Munro, P. M. Celliers, R. E. Olson, D. G. Hicks, V. N. Goncharov, G. W. Collins, H. F. Robey, S. X. Hu, J. A. Marozas, T. C. Sangster, O. L. Landen, and D. D. Meyerhofer, Phys. Plasmas **16**, 056302 (2009).
5. O. L. Landen, J. Edwards, S. W. Haan, H. F. Robey, J. Milovich, B. K. Spears, S. V. Weber, D. S. Clark, J. D. Lindl, B. J. MacGowan, E. I. Moses, J. Atherton, P. A. Amendt, T. R. Boehly, D. K. Bradley, D. G. Braun, D. A. Callahan, P. M. Celliers, G. W. Collins, E. L. Dewald, L. Divol, J. A. Frenje, S. H. Glenzer, A. Hamza, B. A. Hammel, D. G. Hicks, N. Hoffman, N. Izumi, O. S. Jones, J. D. Kilkenny, R. K. Kirkwood, J. L. Kline, G. A. Kyrala, M. M. Marinak, N. Meezan, D. D. Meyerhofer, P. Michel, D. H. Munro, R. E. Olson, A. Nikroo, S. P. Regan, L. J. Suter, C. A. Thomas, and D. C. Wilson, Phys. Plasmas **18**, 051002 (2011).
6. D. G. Hicks, presented at The Seventh International Conference on Inertial Fusion Sciences and Applications, Bordeaux-Lac, France, 12–16 September 2011.
7. P. Michel *et al.*, Phys. Plasmas **17**, 056305 (2010).
8. G. A. Kyrala *et al.*, Phys. Plasmas **18**, 056307 (2011).
9. M. J. Edwards, J. D. Lindl, B. K. Spears, S. V. Weber, L. J. Atherton, D. L. Bleuel, D. K. Bradley, D. A. Callahan, C. J. Cerjan, D. Clark, G. W. Collins, J. E. Fair, R. J. Fortner, S. H. Glenzer, S. W. Haan, B. A. Hammel, A. V. Hamza, S. P. Hatchett, N. Izumi, B. Jacoby, O. S. Jones, J. A. Koch, B. J. Kozioziemski, O. L. Landen, R. A. Lerche, B. J. MacGowan, A. J. MacKinnon, E. R. Mapoles, M. M. Marinak, M. Moran, E. I. Moses, D. H. Munro, D. H. Schneider, S. M. Sepke, D. A. Shaughnessy, P. T. Springer, R. Tommasini, L. Bernstein, W. Stoeffl, R. Betti, T. R. Boehly, T. C. Sangster, V. Yu. Glebov, P. W. McKenty, S. P. Regan, D. H. Edgell, J. P. Knauer, C. Stoeckl, D. R. Harding, S. Batha, G. Grim, H. W. Herrmann, G. Kyrala, M. Wilke, D. C. Wilson, J. Frenje, R. Petrasso, K. Moreno, H. Huang, K. C. Chen, E. Giraldez, J. D. Kilkenny, M. Mauldin, N. Hein, M. Hoppe, A. Nikroo, and R. J. Leeper, Phys. Plasmas **18**, 051003 (2011).
10. S. W. Haan, J. D. Lindl, D. A. Callahan, D. S. Clark, J. D. Salmonson, B. A. Hammel, L. J. Atherton, R. C. Cook, M. J. Edwards, S. Glenzer, A. V. Hamza, S. P. Hatchett, M. C. Herrmann, D. E. Hinkel, D. D. Ho, H. Huang, O. S. Jones, J. Kline, G. Kyrala, O. L. Landen, B. J. MacGowan, M. M. Marinak, D. D. Meyerhofer, J. L. Milovich, K. A. Moreno, E. I. Moses, D. H. Munro, A. Nikroo, R. E. Olson, K. Peterson, S. M. Pollaine, J. E. Ralph, H. F. Robey, B. K. Spears, P. T. Springer, L. J. Suter, C. A. Thomas, R. P. Town, R. Vesey, S. V. Weber, H. L. Wilkens, and D. C Wilson, Phys. Plasmas **18**, 051001 (2011).
11. A. J. Martin, R. J. Simms, and R. B. Jacobs, J. Vac. Sci. Technol. A **6**, 1885 (1988); B. J. Kozioziemski *et al.*, Fusion Sci. Technol. **59**, 14 (2011).
12. B. A. Hammel *et al.*, High Energy Density Phys. **6**, 171 (2010); B. A. Hammel, H. A. Scott, S. P. Regan, C. Cerjan, D. S. Clark, M. J. Edwards, R. Epstein, S. H. Glenzer, S. W. Haan, N. Izumi, J. A. Koch, G. A. Kyrala, O. L. Landen, S. H. Langer, K. Peterson, V. A. Smalyuk, L. J. Suter, and D. C. Wilson, Phys. Plasmas **18**, 056310 (2011).
13. J. J. MacFarlane *et al.*, High Energy Density Phys. **3**, 181 (2007).
14. J. Ralph *et al.*, Bull. Am. Phys. Soc. **55**, 294 (2010).
15. P. A. Bradley and D. C. Wilson, Bull. Am. Phys. Soc. **41**, 1557 (1996); P. Bradley and D. C. Wilson, Phys. Plasmas **8**, 3724 (2001).
16. H. R. Griem, *Principles of Plasma Spectroscopy* (Cambridge University Press, Cambridge, England, 1997).
17. D. S. Clark *et al.*, Phys. Plasmas **17**, 052703 (2010).
18. G. A. Kyrala *et al.*, Rev. Sci. Instrum. **81**, 10E316 (2010).
19. S. P. Regan, B. A. Hammel, R. Prasad, L. J. Suter, P. Bell, M. Eckart, M. A. Barrios, D. K. Bradley, N. Izumi, J. D. Kilkenny, J. L. Kline, G. A. Kyrala, O. L. Landen, T. Ma, R. L. McCrory, D. D. Meyerhofer, T. C. Sangster, and H. Scott, "Hot-Spot X-Ray Spectrometer for the National Ignition Facility," to be submitted to Review of Scientific Instruments.
20. S. P. Regan, R. Epstein, B. A. Hammel, L. J. Suter, J. Ralph, H. Scott, M. A. Barrios, D. K. Bradley, D. A. Callahan, G. W. Collins, S. Dixit, M. J. Edwards, D. R. Farley, S. H. Glenzer, I. E. Golovkin, S. W. Haan, A. Hamza, D. G. Hicks, N. Izumi, J. D. Kilkenny, J. L. Kline, G. A. Kyrala, O. L. Landen, T. Ma, J. J. MacFarlane, A. J. MacKinnon, R. C. Mancini, F. J. Marshall, R. L. McCrory, N. B. Meezan, D. D. Meyerhofer, A. Nikroo, K. J. Peterson, T. C. Sangster, P. Springer, and R. P. J. Town, "Diagnosing Implosions at the National Ignition Facility with X-Ray Spectroscopy," to be published in the *AIP Proceedings on the 17th International Conference on Atomic Processes in Plasmas*.
21. R. C. Mancini *et al.*, Comput. Phys. Commun. **63**, 314 (1991).

Measurements of the Differential Cross Section for the Elastic n–^{3}H and n–^{2}H Scattering at 14.1 MeV by Using an Inertial Confinement Fusion Facility

The development of an accurate description of light-ion reactions is currently of great interest since it would provide valuable insights into low-energy nuclear reactions important to nuclear astrophysics. Radiative capture reactions, for example, occur in red giants at temperatures low enough that the reaction rates are too small to be directly measured in a laboratory. Extrapolation from measurements at higher energies is also suspect without a fundamental theory for computing these reactions. Fusion energy research also requires accurate cross sections for light-ion reactions to constrain models of inertial confinement fusion (ICF) experiments involving deuterium–tritium fuel. For instance, uncertainties in the differential cross section for the elastic n–^{3}H scattering need to be ~5% to reliably infer a fuel areal density (ρR) from the yield ratio between scattered neutrons and primary 14.1-MeV neutrons, called down-scatter ratio (DSR),[1] produced in an ICF implosion. The determination of the ρR from the DSR value is essential for understanding how the fuel is assembled in an implosion and for ultimately guiding the community toward the demonstration of thermonuclear ignition and net energy gain[2] at the National Ignition Facility (NIF).[3]

Since the 1950s, the differential cross section for the elastic n–^{3}H scattering at 14.1 MeV has been subject to both experimental and theoretical studies. Kootsey *et al.*[4] measured the cross section at center-of-mass (CM) angles ranging from 55° to 165°, resulting in data with statistical uncertainties of ~20% and a systematic uncertainty of 11%. Shirato *et al.*[5] and Debertin *et al.*[6] measured the cross section in the CM angular range of 100° to 175° with an uncertainty varying from ~10% to ~70%, and their results are in good agreement with each other, but up to a factor-of-2 smaller than the Kootsey data. Optical-model calculations conducted by DeVries *et al.*[7] and by Sherif and Podmore[8] reproduced the Shirato and Debertin data in this CM angular range. Additionally, Hale *et al.*[9] conducted an *R*-matrix analysis of all experimental data sets, and the result from that analysis forms the basis of the current ENDF/B-VII evaluation[10] of the differential cross section for the elastic n–^{3}H scattering that can be found in nuclear databases. Although efforts have been made to quantify this fundamental cross section, significant discrepancies exist between the different measurements and between measurements and models. However, a theoretical understanding of the n + ^{3}H scattering based on first-principles calculations is within reach.[11] For example, *ab initio* variational calculations using a hyperspherical harmonics basis expansion performed with a modern nuclear Hamiltonian consisting of an accurate nucleon–nucleon (NN) potential and a three-nucleon interaction (NNN) provide a good description of the differential cross section for elastic n + ^{3}H scattering at low energies.[12] This type of calculation is currently limited, however, to energies below the breakup threshold.

This article describes the first measurement of the differential cross section for the elastic n–^{3}H scattering at 14.1 MeV by an ICF facility. It also describes a theoretical calculation[13] of this cross section, which combines the *ab initio* no-core shell model[14] with the resonating group method[15] into a unified method (NCSM/RGM).[16] Using this theoretical approach, an accurate assessment of the n–^{3}H cross section can be made from precision data taken for the isobaric analogue p–^{3}He reaction. In these experiments, carried out on the OMEGA laser,[17] deuterium–tritium-gas–filled, thin-glass capsules were used. Each capsule, made of SiO_2, had a diameter of about 850 μm, a gas-fill pressure of about 20 atm, and a shell thickness of 3.5 μm. The fuel–gas mixture was 48.2%±0.3% deuterium, 48.8%±0.3% tritium, 2.5% hydrogen, and 0.5% helium-3 from the tritium decay. These capsules were imploded by 60 laser beams that uniformly delivered 30 kJ to the capsule in a 1-ns square pulse. Since the laser energy is quickly absorbed by the glass, the outer part of the glass shell explodes outward while the remaining part moves inward. The imploding part of the shell acts as a piston and drives a shock through the deuterium–tritium fuel that heats the ions. The glass shell continues to move inward behind the shock front, isentropically compressing the post-shock region of the fuel and additionally heating the ions to thermonuclear temperatures. Each implosion, acting as both a 14.1-MeV neutron source and a deuterium–tritium target, produced a burn-averaged ion temperature of 8.5±0.5 keV and neutron yield of about 4×10^{13}, which were measured with a neutron time-of-flight diagnostic.[18] The energy spectra of

the emitted tritons and deuterons, elastically scattered by the 14.1-MeV neutrons, were measured simultaneously using a magnet-based charged-particle spectrometer (CPS)[19] installed on the OMEGA chamber (Fig. 128.6). To cover the energy range of interest in this experiment, the detector plane of the CPS was comprised of two pieces of CR-39, which is a plastic polymer that is insensitive to γ rays and x rays produced in an implosion.[19] Different particle track characteristics in CR-39 enables the CPS to make simultaneous measurements of the scattered deuterons (d′) and tritons (t′) with energies greater than ~3.7 MeV and ~2.5 MeV, respectively (the lower-energy limits are set by the width and position of the CR-39 piece). The proton spectrum from d–d reactions was measured as well to check that the emitted charged particles were not subject to any significant energy losses in the plasma.

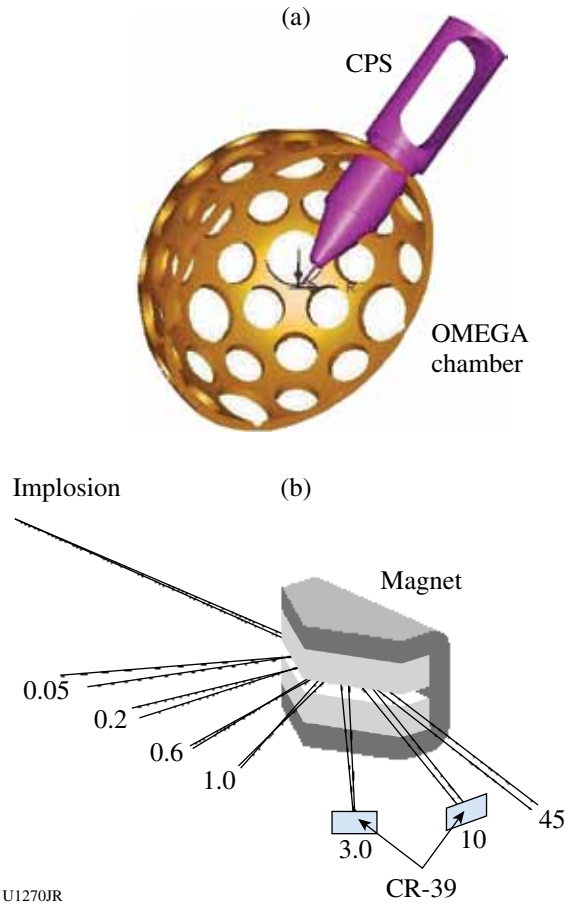

Figure 128.6
(a) The charged-particle spectrometer (CPS) on the OMEGA chamber simultaneously measures deuterons and tritons elastically scattered by 14.1-MeV neutrons and protons from d–d reactions in a deuterium–tritium-gas–filled, thin-glass capsule implosion. A bending magnet (gray) was used for momentum analysis. (b) Schematic drawing of the CPS, which uses a 2-mm-wide aperture in front of a 7.6-kG permanent magnet (Nd-Fe-B) for dispersion and high-resolution measurements of the charged particles. Two pieces of CR-39 were used to detect the dd protons and the elastically scattered deuterons and tritons. The energies are given in MeV for protons.

In Figs. 128.7(a)–128.7(c), d′ and t′ spectra measured simultaneously on three different OMEGA shots are shown. These spectra, which are background subtracted, were obtained by putting constraints on the diameter and darkness of the observed ion tracks in the CR-39 (the triton, deuteron, and background tracks have different characteristics that were used for the differentiation[19]). The remaining background that could not be rejected was characterized from regions on the CR-39, where the d′ and t′ signals cannot be detected. The error bars shown in the spectra are statistical uncertainties associated with the number of signal and background counts in each energy bin. The dd–proton spectrum measured for shot 31753 [Fig. 128.7(d)] displays an average energy that is similar to the birth energy of 3.05 MeV (temperature corrected), indicating that energy losses in the plasma are negligible. From

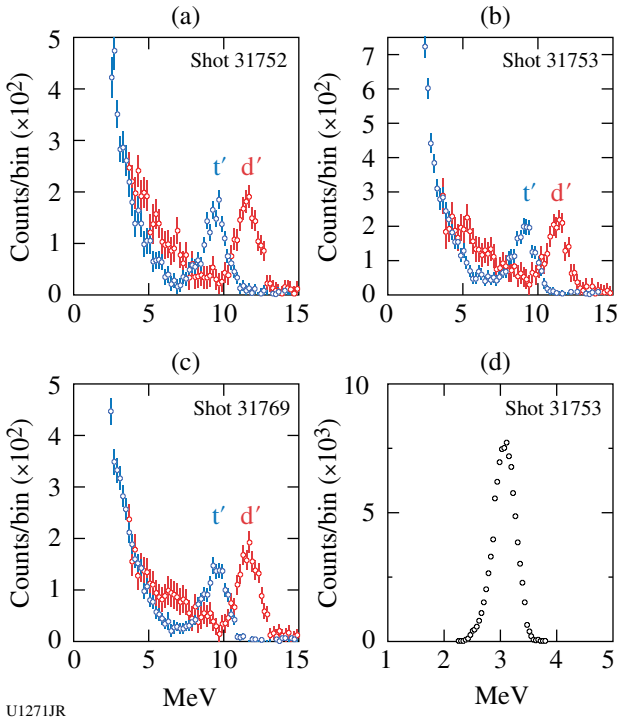

Figure 128.7
[(a)–(c)] The d′ and t′ spectra measured simultaneously on three different OMEGA shots. The broadening of these spectra is caused by the Doppler effect and CPS response. (d) The dd–proton spectrum measured for shot 31753 illustrates that the average energy is similar to the birth energy of 3.05 MeV (temperature corrected).

the measured d′ and t′ spectra, the differential cross section for the elastic n–^{3}H and n–^{2}H scattering was determined by deconvolving the CPS response[20] and the Doppler-broadened 14.1-MeV neutron spectrum.[21] While determining the n–^{2}H cross section, the effect of the deuterons from the t(n,2n)d reaction was considered and accounted for. Here, it was assumed that the cross section for this reaction was 6±4 mb, which covers the reported value in Ref. 22, or about 3%±2% of the total deuteron spectrum in the range 3.7 to 7.3 MeV. Additionally, since the plasma had a burn-averaged ion temperature of 8.5 keV, a density of ~1 g/cm^3, and a total areal density of ~2 to 3 mg/cm^2, energy-loss effects were insignificant and therefore not considered. From an energy-loss point of view, these plasma conditions correspond to a cold target with an areal density less than 0.3 mg/cm^2.

Figures 128.8(a) and 128.8(b) show the differential cross section for the elastic n–^{2}H and n–^{3}H scattering measured in this work. These cross sections, compared to the other data sets, are averages of the three measurements shown in Figs. 128.7(a)–128.7(c). The n–^{2}H cross section determined for each shot was normalized to a Faddeev calculation that is accurate to about 1%, and that normalization factor, modified by the deuterium–tritium fuel ratio, was subsequently applied to the measured n–^{3}H cross section for the same shot (the Faddeev calculation was obtained with the NNLO NN plus NNN chiral force of Ref. 23). As illustrated by Fig. 128.8(a), the angular variation of the measured n–^{2}H elastic cross section is in good agreement with the Faddeev-calculated cross section, indicating that the background subtraction, characterization of the response function, and the effect of the Doppler broadening are accurate, and that the deconvolution process provides high-fidelity data. The uncertainties shown for the n–^{3}H cross section [shown in Fig. 128.8(b) and Table 128.III] are based on the statistical uncertainty and the uncertainty associated with the normalization factor. Since the total n–^{2}H elastic cross section and the deuterium–tritium-fuel ratio in these experiments have an uncertainty of 1.0% and 0.9%, respectively, the uncertainty in the normalization factor is estimated to be 1.4%. This results in a total uncertainty ranging from 4% to 7% in the CM-angle range of 60° to 80°, which is the most important range for diagnosing ICF implosions over which the n–^{3}H cross section dominates the other ICF-relevant cross sections. This uncertainty should be contrasted to the total uncertainty larger than 20% for the Kootsey data, which is the only other data set in this angular range. Considering the uncertainties involved, the experimentally determined n–^{3}H cross section compares well with the current ENDF/B-VII evaluated cross section, which is based on Hale's *R*-matrix analysis of accurate p–^{3}He data in a wide range of energies. The fit parameters obtained in that analysis were then adjusted to account for the Coulomb effects, as explained in Ref. 9, and subsequently applied to the n–^{3}H reaction. The results from the *R*-matrix analysis are shown by the red dashed curve in Fig. 128.8(b). Another theoretical approach, described in detail in Ref. 16, was recently developed to evaluate the cross sections of light-ion reactions. This

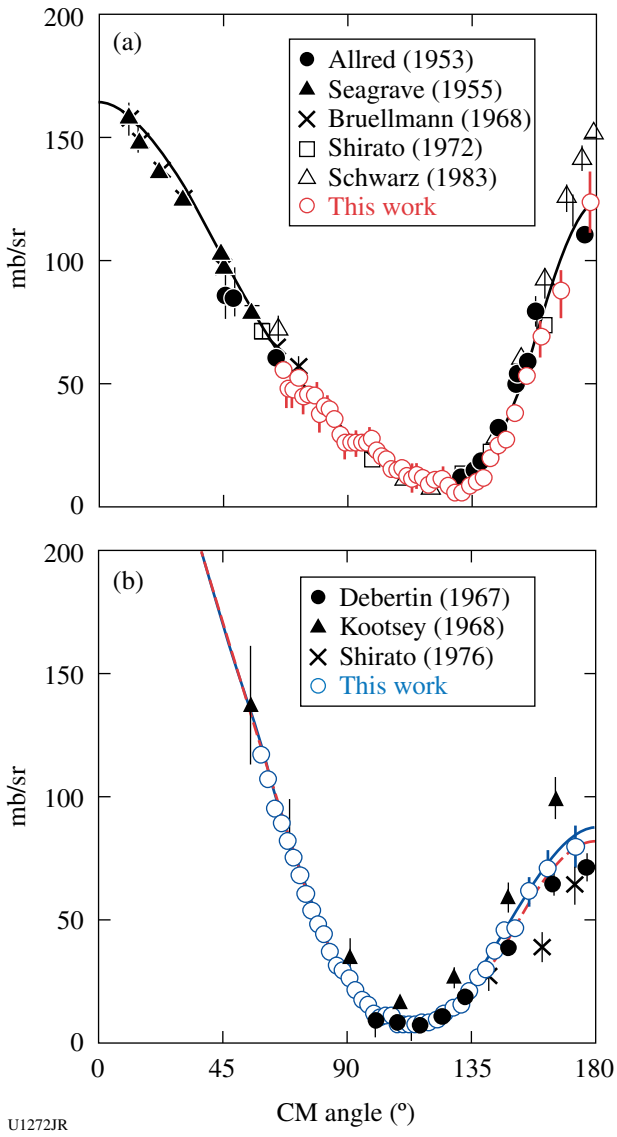

Figure 128.8
(a) Measured differential cross section for the elastic n–^{2}H scattering, which has been normalized to a Faddeev calculation. (b) Measured and calculated differential cross section for the elastic n–^{3}H scattering. The experimental data have been normalized with the deuterium–tritium fuel-ratio–modified normalization factor derived in (a). The blue solid curve represents an *ab initio* NCSM/RGM calculation; the red dashed curve represents an *R*-matrix–calculated n–^{3}H cross section

Table 128.III: Measured and calculated differential cross section for the elastic n–^{3}H scattering as a function of CM angle at 14.1 MeV. The NCSM/RGM calculation, which is corrected at forward angles as explained in the text, is considered to be accurate to about 5%.

CM angle (°)	Measured (mb/sr)	Error (mb/sr)	NCSM/RGM (mb/sr)
58.6	116.7	4.4	119.3
61.2	106.6	3.3	109.9
63.7	94.7	3.5	101.1
66.1	88.8	3.6	93.1
68.3	81.6	3.7	85.6
70.5	75.0	3.9	78.7
72.6	67.8	3.7	72.1
74.7	60.3	3.6	65.9
76.8	53.4	3.5	59.9
79.0	48.1	3.2	54.1
81.2	44.0	3.2	48.5
83.4	37.1	3.3	43.2
85.7	31.5	3.1	38.2
87.9	29.4	2.8	33.4
90.3	26.3	2.9	29.1
92.6	21.7	2.9	25.1
94.8	17.5	2.7	21.6
97.1	15.7	2.5	18.5
99.3	11.9	2.4	15.9
101.5	10.2	2.5	13.7
103.6	11.3	3.3	11.8
105.7	11.2	2.2	10.4
107.8	7.4	1.9	9.2
110.0	7.8	1.9	8.4
112.2	7.6	1.8	8.0
114.4	7.5	1.6	7.9
116.8	8.5	1.3	8.1
119.4	8.5	1.3	8.9
122.0	9.6	1.3	10.2
124.8	12.0	1.2	12.1
127.7	14.4	1.4	14.6
130.7	15.5	1.3	17.7
133.7	21.2	1.4	21.5
136.8	26.5	1.7	25.8
139.8	29.9	1.8	30.5
142.9	37.2	2.2	35.9
146.3	45.6	2.7	42.1
150.2	46.5	3.4	49.4
155.2	61.4	4.7	59.1
162.2	70.5	6.0	71.6
172.3	79.4	7.7	84.3

NCSM/RGM approach, unlike earlier *ab initio* approaches, allows one to calculate various nucleon–nucleus scattering processes for systems with A > 4, i.e., both on *s*- and *p*-shell nuclei.[13,16] The present NCSM/RGM calculations for the n–^{3}H and p–^{3}He systems use a similarity-renormalization-group–evolved chiral N^{3}LO NN interaction that includes Coulomb and other isospin breaking terms.[24] A less-than-15% inaccuracy in these calculations at forward angles is introduced by limiting the model space to channel states with the three-nucleon system in its ground state. To quantify and correct for this inaccuracy, high-precision p–^{3}He data[25] are compared to the corresponding NCSM/RGM results, and the obtained correction function is applied to the n–^{3}H calculation. The result of this procedure, which is accurate to ~5%, is illustrated by the blue solid curve in Fig. 128.8(b), which is also in good agreement with our experimental data, but differs from the *R*-matrix analysis by several percent in the backward-scattering angles of the outgoing neutron. Considering the estimated uncertainty of ~5% for the NCSM/RGM calculation, this discrepancy is, however, insignificant. Additional details of the n–^{3}H and p–^{3}He NCSM/RGM calculations are found in Ref. 13.

In summary, we report on the first measurements of the differential cross section for the elastic n–^{3}H and n–^{2}H scattering at 14.1 MeV by an ICF facility. The resulting n–^{3}H data are of higher quality than achieved in previous accelerator experiments reported in the literature and accurate enough to reliably determine the fuel ρR from the yield ratio between scattered neutrons and primary 14.1-MeV neutrons produced in an ICF implosion. The experimental results obtained at CM angles ranging from 59° to 172° are in good agreement with a theory that is based on isospin-corrected *ab initio* calculations of the isobaric analogue p + ^{3}He reaction. Both measured and calculated cross sections compare well with current ENDF/B-VII-evaluated cross section, which is based on Hale's *R*-matrix analysis. A total n–^{3}H elastic cross section of 941±47 mb was calculated using the NCSM/RGM method.

ACKNOWLEDGMENT

The authors would like to thank Prof. Dr. Evgeny Epelbaum for providing Faddeev calculations of n–^{2}H scattering at 14.1 MeV, which provided the basis for normalizing these experimental results. The work described here was supported in part by U.S. DOE (Grant No. DE-FG03-03SF22691), LLE (No. 412160-001G), LLNL (No. B504974), and General Atomics under DOE (DE-AC52-06NA27279).

REFERENCES

1. J. A. Frenje, D. T. Casey, C. K. Li, F. H. Séguin, R. D. Petrasso, V. Yu. Glebov, P. B. Radha, T. C. Sangster, D. D. Meyerhofer, S. P. Hatchett, S. W. Haan, C. J. Cerjan, O. L. Landen, K. A. Fletcher, and R. J. Leeper, Phys. Plasmas **17**, 056311 (2010).
2. B. K. Spears *et al.*, "Prediction of Ignition Implosion Performance Using Measurements of Low-Deuterium Surrogates," to be published in Physics of Plasmas.
3. G. H. Miller, E. I. Moses, and C. R. Wuest, Nucl. Fusion **44**, S228 (2004).
4. J. M. Kootsey, Nucl. Phys. **A113**, 65 (1968).
5. S. Shirato *et al.*, Nucl. Phys. **A267**, 157 (1976).
6. K. Debertin, E. Roessle, and J. U. Schott, http://www.nndc.bnl.gov/exfor/servlet/X4sGetSubent?reqx=3489&subID=21507002&plus=1, Brookhaven National Laboratory, Upton, NY (1967).
7. R. M. Devries, J. L. Perrenoud, and I. Slaus, Nucl. Phys. **A188**, 449 (1972).
8. H. S. Sherif and B. S. Podmore, in *Few Particle Problems in Nuclear Interaction*, edited by I. Slaus *et al.* (North-Holland, Amsterdam, 1972), pp. 691–694.
9. G. M. Hale *et al.*, Phys. Rev. C **42**, 438 (1990).
10. M. B. Chadwick *et al.*, Nuclear Data Sheets **107**, 2931 (2006).
11. R. Lazauskas *et al.*, Phys. Rev. C **71**, 034004 (2005).
12. M. Viviani *et al.*, Few-Body Syst. **45**, 119 (2009).
13. P. Navrátil, S. Quaglioni, and R. Roth, J. Phys., Conf. Ser. **312**, 082002 (2011); P. Navrátil *et al.*, Lawrence Livermore National Laboratory, Livermore, CA, Report LLNL-TR-423504 (2010).
14. P. Navrátil, J. P. Vary, and B. R. Barrett, Phys. Rev. Lett. **84**, 5728 (2000); P. Navrátil, J. P. Vary, and B. R. Barrett, Phys. Rev. C **62**, 054311 (2000).
15. K. Wildermuth and Y. Tang, *A Unified Theory of the Nucleus,* Clustering Phenomena in Nuclei (Vieweg, Braunschweig, Germany, 1977).
16. S. Quaglioni and P. Navrátil, Phys. Rev. Lett. **101**, 092501 (2008); S. Quaglioni and P. Navrátil, Phys. Rev. C **79**, 044606 (2009).
17. T. R. Boehly, D. L. Brown, R. S. Craxton, R. L. Keck, J. P. Knauer, J. H. Kelly, T. J. Kessler, S. A. Kumpan, S. J. Loucks, S. A. Letzring, F. J. Marshall, R. L. McCrory, S. F. B. Morse, W. Seka, J. M. Soures, and C. P. Verdon, Opt. Commun. **133**, 495 (1997).
18. V. Yu. Glebov, C. Stoeckl, T. C. Sangster, S. Roberts, G. J. Schmid, R. A. Lerche, and M. J. Moran, Rev. Sci. Instrum. **75**, 3559 (2004).

19. F. H. Séguin, J. A. Frenje, C. K. Li, D. G. Hicks, S. Kurebayashi, J. R. Rygg, B.-E. Schwartz, R. D. Petrasso, S. Roberts, J. M. Soures, D. D. Meyerhofer, T. C. Sangster, J. P. Knauer, C. Sorce, V. Yu. Glebov, C. Stoeckl, T. W. Phillips, R. J. Leeper, K. Fletcher, and S. Padalino, Rev. Sci. Instrum. **74**, 975 (2003).

20. The CPS response is described by a 300- and 1,000-keV rectangular distribution at 5 and 10 MeV, respectively. For a 8.5-keV plasma, the Doppler-broadened DT-neutron spectrum is described by a Gaussian distribution with a width of 520 keV (FWHM; see Ref. 21).

21. H. Brysk, Plasma Phys. **15**, 611 (1973).

22. I. J. Thompson, Comput. Phys. Rep. **7**, 167 (1988).

23. E. Epelbaum *et al.*, Phys. Rev. C **66**, 064001 (2002).

24. S. K. Bogner, R. J. Furnstahl, and R. J. Perry, Phys. Rev. C **75**, 061001(R) (2007); D. R. Entem and R. Machleidt, Phys. Rev. C **68**, 041001(R) (2003).

25. R. L. Hutson *et al.*, Physical Review C **4**, 17 (1971).

Study of Rayleigh–Taylor Growth in Directly Driven Cryogenic-Deuterium Targets

Introduction

In inertial confinement fusion (ICF),[1,2] a spherical capsule is uniformly irradiated to compress a target containing a deuterium–tritium (DT) ice shell, creating the hot-spot temperature and fuel-density conditions required to achieve ignition and significant thermonuclear energy gain. The growth of areal-density (ρR) perturbations resulting from Rayleigh–Taylor[3,4] (RT) instability can compromise the target's integrity, quenching the hot-spot formation prior to achieving thermonuclear ignition.[1,2,5–23] In the linear regime, modulations grow exponentially with a growth rate given by[24]

$$\gamma = \alpha\sqrt{kg/\left(1+kL_{\mathrm{m}}\right)} - \beta k V_{\mathrm{a}}, \tag{1}$$

where α and β are constants, k is the wave number of the modulation, g is the acceleration of the target, L_{m} is the density scale length at the ablation front, and V_{a} is the ablation velocity. Prior to target acceleration, during shock transit, the ablative Richtmyer–Meshkov (RM) instability causes areal-density modulations to oscillate with an oscillation frequency of[25,26]

$$\omega = k\sqrt{V_{\mathrm{b}} \cdot V_{\mathrm{a}}}, \tag{2}$$

where V_{b} is the blowoff velocity. Direct-drive–ignition designs[27] use a thick cryogenic (cryo)-DT shell encased by a thin (~4-μm) CH ablator to maximize the amount of fusion fuel contained in the compressed target at peak burn of the implosion.[28] As the thin CH layer is ablated, the implosion hydrodynamics become ablative in DT. Targets with DT ablators are predicted to be more robust to the RT instability than mass-equivalent CH ablators.[24] Reduced density in DT ablators compared to CH increases the ablation velocity, reducing the growth rate while also allowing for thicker ablators without compromising target acceleration and implosion velocity. The ablative stabilization constant β [Eq. (1)] is ~1.7 for CH and ~2.6 for DT, providing increased hydrodynamic stability for DT ablators.[24] The growth rate of the RT instability has been measured experimentally under a variety of target and drive conditions for room-temperature materials, such as CH, showing good agreement with theoretical predictions and hydrodynamic simulations at drive intensities up to ~5×10^{14} W/cm^2 (Refs. 2,10,12,29,30). Areal-density modulations can be seeded by target defects created during manufacturing and/or nonuniformities in the target driver (laser imprinting). Significant mitigation of laser imprinting is achieved by the use of distributed phase plates (DPP's)[31] and smoothing by spectral dispersion (SSD).[32] To design a target that is robust to RT instability and will achieve thermonuclear ignition, it is essential to understand the evolution of ρR modulations in cryo DT. This article presents the first experiments that verify hydrodynamic simulations of RT growth in cryo D_2 (hydrodynamically equivalent to DT) at conditions relevant to achieving direct-drive thermonuclear ignition with a mass preimposed initial condition. Previous experiments have been performed using intensity-imprinted initial modulations, although they could not be simulated because of software limitations.[33] The following sections describe the experimental design; present the experimental configuration and the experimental results; compare results with simulations; and present conclusions.

Experimental Design

Laser-driven RT experiments are typically performed in planar geometry using face-on x-ray radiography.[12,12,29,30] A target with a known seed modulation (either preimposed or laser imprinted) is irradiated while a high-Z x-ray backlighter foil is used to image the modulation evolution. Figure 128.9 shows the basic face-on radiography configuration used in most direct-drive planar RT experiments. The drive target is irradiated with overlapping drive beams while x rays from a high-Z backlighter traverse the target and are measured on an x-ray framing camera with an imaging pinhole array.[34] X-ray radiography relies on the attenuation of backlighter x rays (typically greater than 1 keV because of the spectral response of the framing camera) by the drive target such that variations in the target's areal density will be measured as variations in the optical depth of the radiograph. Measuring ρR modulation evolution in cryo D_2 presents two significant challenges to the typical face-on x-ray radiography scheme: D_2 has little x-ray attenuation at energies greater than 1 keV and a cryo-D_2 layer must be contained by a solid ambient material, typically plas-

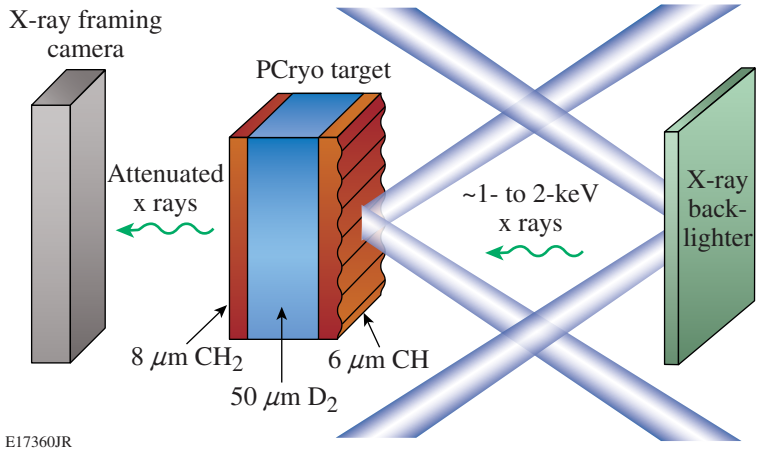

Figure 128.9
Experimental configuration for face-on x-ray radiography. A planar cryogenic (PCryo) target with a sinusoidal seed areal-density modulation is driven by 12 OMEGA drive beams while a backlighter emits 1.3-keV x rays, which are imaged with a time-gated x-ray framing camera. The planar cryogenic drive target consists of a 50-μm, liquid-D_2 layer sandwiched between a 6-μm-thick front CH window and an 8-μm-thick rear CH_2 window. The entire assembly is held in a 2-μm-sq Cu washer with a 1.5-mm inner diameter (not pictured) and is cryogenically cooled to ~20 K. The front CH window is seeded with a 60-μm-wavelength sinusoidal modulation with an initial amplitude of 0.25 μm, which will imprint into the D_2 layer as the window is ablated by the drive beams.

tic (CH). Lower-energy x rays required to directly radiograph the cryo D_2 would suffer from severe attenuation in the CH layer and increased background from the soft x rays produced by the CH plasma. Instead, the modulation evolution in D_2 is measured indirectly using modulation feedthrough[35] into the rear window of a planar cryo-D_2 target. A schematic of the planar cryo-D_2 target can be seen in Fig. 128.9. The target consists of a 50-μm-thick D_2 "sandwich" held in place by a 6-μm-thick front CH window and an 8-μm-thick rear CH_2 window mounted in a 2-mm-sq copper washer with an inner diameter of 1.5 mm. The front CH window is seeded with a 60-μm-wavelength sinusoidal modulation with an initial amplitude of 0.25 μm, and the entire assembly is mounted to a cryo finger that cools the target to ~20 K so a liquid-D_2 layer exists between the two plastic windows. As the target is driven, the front CH window is ablated away and the modulation evolution at the ablation front is governed by the ablative growth in D_2. These D_2 modulations feed through to the rear CH_2 window of the target with the relationship

$$a_{CH_2}(k,t) = a_{D_2}(k,t)e^{-k\cdot d(t)}, \qquad (3)$$

where α_{D_2} is the modulation amplitude at the D_2 ablation front, α_{CH_2} is the modulation amplitude at the rear CH_2 window, k is the modulation wave number, and $d(t)$ is the distance between the D_2 ablation front and the rear CH_2 window of the target. Equation (3) indicates that the modulation amplitude at the D_2 ablation front will always be greater than in the CH_2 window. *DRACO*[36] simulations indicate that the modulations in D_2 correlate well with the observed modulation on the rear CH_2 window. The modulation amplitude at the ablation surface in D_2 feeds through to the back D_2 surface and is governed by the same feedthrough relation as defined in Eq. (3). Figure 128.10 shows the simulated modulation amplitude evolution at the

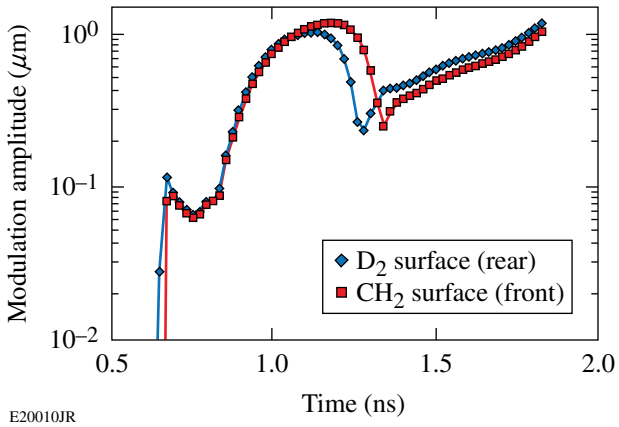

Figure 128.10
Simulated rear-surface modulation for a 50-μm-thick liquid-D_2 target with a 6-μm-thick modulated front CH window and an 8-μm-thick rear CH_2 window driven by a 2-ns square pulse. The plot shows the modulation amplitude at the back D_2 surface (blue diamonds) and the modulation in the rear CH_2 window of the target (red squares), indicating that the CH_2 window modulation evolution is dominated by feedthrough from the D_2 ablation front.

back D_2 surface (blue diamonds) as well as the modulation in the rear CH_2 window (red squares) from *DRACO* for a target with a 50-μm-thick D_2 layer held in place by a 6-μm-thick front CH window and an 8-μm-thick rear CH_2 window with an initial front-surface modulation with an amplitude of 0.25 μm at a wavelength of 60 μm being driven by a 2-ns square pulse with an intensity of 4×10^{14} W/cm^2, showing good correlation between the D_2 and CH_2 layers.

Experimental Configuration

The target shown in Fig. 128.9 was irradiated by 12 overlapping UV beams from OMEGA with a spot diameter of ~750 μm using a 2-ns square pulse at a peak intensity of 4×10^{14} W/cm^2. The spatial profiles of the beams were smoothed

using SSD[32] and DPP's.[31] A uranium backlighter located 9 mm from the drive target was irradiated by ten UV beams with a spot diameter of 1 mm, creating x-ray radiographs on a time-gated x-ray framing camera[34] filtered with 1 μm of Al with an additional 3-μm-Al blast shield located 4.5 mm from the drive target to prevent preheating of the target by soft x rays. This configuration yielded a peak x-ray energy of ~1.3 keV to radiograph the front and rear plastic windows of the target. The framing camera captured eight radiographs with a temporal resolution of ~80 ps and a spatial resolution of ~10 μm. Data were extracted from five radiographs from 0.8 to 1.6 ns.

A Weiner filter was constructed to extract the signal from the noise from each individual image.[37] The true signal was reconstructed only from data with spatial frequencies near 16.6 mm^{-1}, corresponding to the 60-μm-wavelength seed modulation. For each image, the noise was approximated by the lineout perpendicular to the seed modulation. The noise for all of the images was compared to ensure that the noise spectrum was not changing significantly during the target drive, which would indicate true broadband modulation growth and not noise. Figure 128.11 shows a filtered 300-μm-sq radiograph taken at 1.25 ns into the drive.

The two-dimensional (2-D) hydrodynamics code *DRACO*[36] simulated the modulation evolution using flux-limited local electron transport, where the heat flux is taken as the smaller of the *Spitzer–Härm heat flux*[38] and the *flux-limited free-streaming heat flux*,[39] with a standard flux limiter of $f = 0.06$. The simulation used *SESAME* 5263 (Ref. 40) for the equation of state (EOS) of the cryogenic-D_2 layer. Figure 128.12 shows the temperature and pressure profiles of the D_2 shock front from *DRACO*. The simulated shocked D_2 density reaches 3 to 4× the initial liquid-D_2 density (0.171 g/cc) with pressures ranging from 15 to 25 Mbar and temperatures from 20 to 30 eV during the shock transit into the D_2 liquid. Multiple shocks and rarefactions traverse the target prior to the onset of target acceleration caused by the multiple interfaces. At 0.8 ns, the D_2 layer achieves its peak pressure of 65 Mbar at a temperature of 50 eV because of the rarefaction wave heating from the rear CH_2 window. For these conditions, *SESAME* 5263 is in good agreement with the first principles EOS (FPEOS) for D_2 calculated by S. X. Hu *et al.*[41]

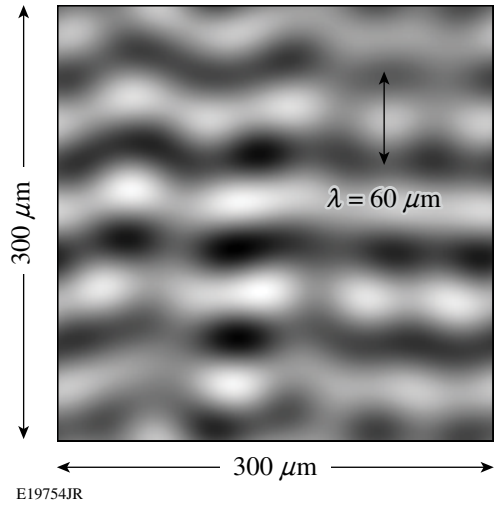

Figure 128.11
A Weiner-filtered, 300-μm-sq face-on radiograph for the planar-cryogenic-D_2 target in Fig. 128.9 driven by 12 drive beams with a 2-ns square pulse with a peak overlapped intensity of 4×10^{14} W/cm^2 taken at 1.25 ns. The 60-μm wavelength appears as horizontal fringes in the image.

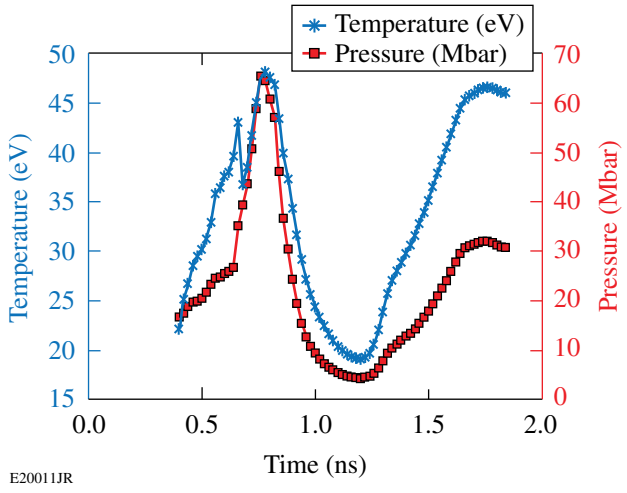

Figure 128.12
Simulated temperature (blue stars) and pressure (red squares) profiles of the D_2 shock front of the planar cryogenic target from *DRACO*. The shocked D_2 density reaches 3 to 4× the initial liquid-D_2 density (0.171 g/cc) with pressures ranging from 15 to 25 Mbar and temperatures from 20 to 30 eV during the shock transit into the D_2 liquid. At 0.8 ns, the D_2 layer achieves its peak pressure of 65 Mbar at a temperature of 50 eV as a result of the rarefaction wave heating from the rear CH_2 window.

Experimental Results

Figure 128.13 shows the measured modulation optical depth of the planar cryogenic target in Fig. 128.9 seeded with a 60-μm-wavelength preimposed mass modulation with an initial amplitude of 0.25 μm. The target was driven by a 2-ns square pulse with an intensity of 4×10^{14} W/cm^2 [Fig. 128.13(a)]. The measured modulation amplitude(blue diamonds) are overplotted with the prediction from the 2-D hydrodynamics simulation *DRACO* (red line) showing relatively good agreement [Fig. 128.13(b)]. The measurement and simulation include contributions from both the front and rear plastic windows of

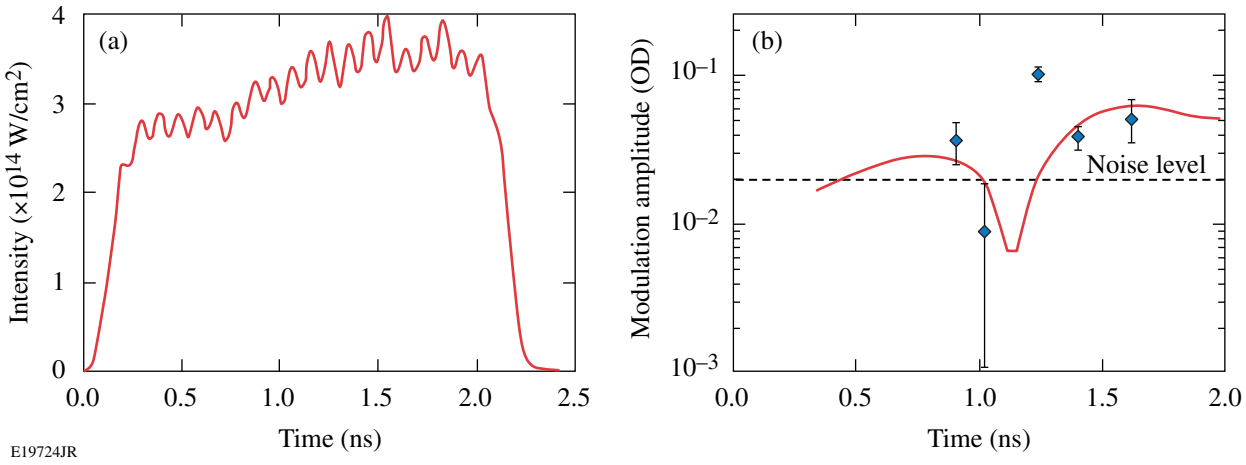

Figure 128.13
(a) The planar cryogenic target in Fig. 128.9 is driven by 12 overlapping drive beams with a 2-ns square pulse at a peak intensity of 4×10^{14} W/cm^2. (b) The measured modulation amplitude is plotted (blue diamonds) as well as the prediction by *DRACO* using flux-limited thermal transport (red line) showing relatively good agreement.

the target up to ~1.2 ns, when the front window is ablated. The target acceleration begins at ~1.4 ns, so the modulation signal up to this time is dominated by the oscillating ablative RM instability,[25] observed as the large oscillating feature in the simulation. This characteristic of the ablative RM instability has been experimentally observed by U. Aglitskiy *et al.*[42,43] and O. Gotchev *et al.*[44,45] in pure-CH targets. After ~1.2 ns, simulation and measurements are dominated by the feedthrough modulations in the rear 8-μm CH_2 window, which are related to the modulation at the D_2 ablation front by Eq. (3).

Discussion

The experiment demonstrates that *DRACO* closely reproduces the experiment using flux-limited local electron transport at an intensity of 4×10^{14} W/cm^2. The large discrepancy between the experiment and simulation at the data point at 1.25 ns is likely the result of a difference between the experimental and simulated mass-ablation rates. Early in the drive ($t \ll 1.2$ ns), both the experimental and simulated optical depths include contributions from the front and rear plastic windows, while later in the drive ($t \gg 1.2$ ns) the front window is completely ablated, leaving only the rear window as the optical-depth contributor. In these regions, a small difference in ablation velocity between experiment and simulation could exist without disagreement in measured and simulated optical depths as a result of the slow growth observed in the target. Measurements taken as the front window is being completely ablated away ($t \sim 1.2$ ns) would show a larger discrepancy. In this case, if the simulated ablation velocity is greater than the experimental ablation velocity, the measurement at 1.25 ns would include contributions from both the front and rear windows, while the simulation includes only the rear window, contributing to the difference between experiment and simulation for that data point. In the other temporal regions, the simulation reproduces the behavior of the modulation evolution in this complex target, indicating that the measured hydrodynamic stability characteristics of D_2 are close to those predicted through theory and simulation.

Signal levels can be increased by designing an experiment with a longer pulse duration, causing the modulation to grow to larger amplitudes or decreasing the distance between the D_2 ablation front and the rear CH_2 window of the target, while still keeping a thick-enough D_2 layer such that the hydrodynamics of D_2 are relevant to the measurement. Noise is dominated by x-ray photon statistics as a result of condensation on the windows of the target, resulting in large-scale features with low x-ray transmissions. This effect was significantly reduced by the use of a target shroud and selective image analysis, although it remains the dominate noise contributor.

An alternative radiography approach to that presented here is the use of charged particles or low-energy x rays to directly measure the modulation evolution at the D_2 ablation front as well as the front and rear plastic windows. Targets designed for this approach would use thinner plastic windows that would directly measure the modulation evolution in the D_2 layer, allowing for higher-confidence comparisons between experiment and simulation.

Conclusion

A direct-drive, RT experiment with a planar cryogenic-D_2 target was performed at the Omega Laser Facility. These are the first RT measurements in D_2 at conditions relevant to ICF using a mass-preimposed initial modulation. A planar cryogenic target was seeded with a 60-μm-wavelength mass modulation and driven with a 2-ns square pulse with a peak intensity of 4×10^{14} W/cm^2 and radiographed using 1.3-keV x rays from a uranium backlighter. Experimental measurements showed reasonable agreement with the 2-D hydrodynamics code *DRACO*.

ACKNOWLEDGMENT

This work was supported by the U.S. DOE Office of Inertial Confinement Fusion under Cooperative Agreement No. DE-FC52-08NA28302, the University of Rochester, and the New York State Energy Research and Development Authority. The support of DOE does not constitute an endorsement by DOE of the views expressed in this article.

REFERENCES

1. S. Atzeni and J. Meyer-ter-Vehn, *The Physics of Inertial Fusion: Beam Plasma Interaction, Hydrodynamics, Hot Dense Matter*, International Series of Monographs on Physics (Clarendon Press, Oxford, 2004).
2. J. D. Lindl, *Inertial Confinement Fusion: The Quest for Ignition and Energy Gain Using Indirect Drive* (Springer-Verlag, New York, 1998).
3. Lord Rayleigh, Proc. London Math Soc. **XIV**, 170 (1883).
4. G. Taylor, Proc. R. Soc. London Ser. A **201**, 192 (1950).
5. S. E. Bodner, Phys. Rev. Lett. **33**, 761 (1974).
6. B. A. Remington *et al.*, Phys. Rev. Lett. **73**, 545 (1994).
7. S. G. Glendinning, S. N. Dixit, B. A. Hammel, D. H. Kalantar, M. H. Key, J. D. Kilkenny, J. P. Knauer, D. M. Pennington, B. A. Remington, R. J. Wallace, and S. V. Weber, Phys. Rev. Lett. **78**, 3318 (1997).
8. J. Grun *et al.*, Phys. Rev. Lett. **58**, 2672 (1987).
9. K. Shigemori *et al.*, Phys. Rev. Lett. **78**, 250 (1997).
10. H. Azechi *et al.*, Phys. Plasmas **4**, 4079 (1997).
11. C. J. Pawley *et al.*, Phys. Plasmas **6**, 565 (1999).
12. J. P. Knauer, R. Betti, D. K. Bradley, T. R. Boehly, T. J. B. Collins, V. N. Goncharov, P. W. McKenty, D. D. Meyerhofer, V. A. Smalyuk, C. P. Verdon, S. G. Glendinning, D. H. Kalantar, and R. G. Watt, Phys. Plasmas **7**, 338 (2000).
13. H. Azechi *et al.*, Phys. Rev. Lett. **98**, 045002 (2007).
14. V. A. Smalyuk, T. R. Boehly, D. K. Bradley, V. N. Goncharov, J. A. Delettrez, J. P. Knauer, D. D. Meyerhofer, D. Oron, and D. Shvarts, Phys. Rev. Lett. **81**, 5342 (1998).
15. M. M. Marinak *et al.*, Phys. Plasmas **5**, 1125 (1998).
16. V. A. Smalyuk, O. Sadot, J. A. Delettrez, D. D. Meyerhofer, S. P. Regan, and T. C. Sangster, Phys. Rev. Lett. **95**, 215001 (2005).
17. V. A. Smalyuk, O. Sadot, R. Betti, V. N. Goncharov, J. A. Delettrez, D. D. Meyerhofer, S. P. Regan, T. C. Sangster, and D. Shvarts, Phys. Plasmas **13**, 056312 (2006).
18. W. W. Hsing *et al.*, Phys. Plasmas **4**, 1832 (1997).
19. D. L. Tubbs, C. W. Barnes, J. B. Beck, N. M. Hoffman, J. A. Oertel, R. G. Watt, T. Boehly, D. Bradley, P. Jaanimagi, and J. Knauer, Phys. Plasmas **6**, 2095 (1999).
20. C. Cherfils *et al.*, Phys. Rev. Lett. **83**, 5507 (1999).
21. S. G. Glendinning *et al.*, Phys. Plasmas **7**, 2033 (2000).
22. V. A. Smalyuk, V. N. Goncharov, J. A. Delettrez, F. J. Marshall, D. D. Meyerhofer, S. P. Regan, and B. Yaakobi, Phys. Rev. Lett. **87**, 155002 (2001).
23. V. A. Smalyuk, S. B. Dumanis, F. J. Marshall, J. A. Delettrez, D. D. Meyerhofer, S. P. Regan, T. C. Sangster, B. Yaakobi, and J. A. Koch, Phys. Plasmas **10**, 830 (2003).
24. R. Betti, V. N. Goncharov, R. L. McCrory, and C. P. Verdon, Phys. Plasmas **5**, 1446 (1998).
25. V. N. Goncharov, Phys. Rev. Lett. **82**, 2091 (1999).
26. J. G. Wouchuk and K. Nishihara, Phys. Plasmas **3**, 3761 (1996).
27. P. W. McKenty, V. N. Goncharov, R. P. J. Town, S. Skupsky, R. Betti, and R. L. McCrory, Phys. Plasmas **8**, 2315 (2001).
28. C. P. Verdon, Bull. Am. Phys. Soc. **38**, 2010 (1993).
29. B. A. Remington *et al.*, Phys. Plasmas **22**, 241 (1995).
30. S. G. Glendinning, Bull. Am. Phys. Soc. **36**, 2375 (1991).
31. Y. Lin, T. J. Kessler, and G. N. Lawrence, Opt. Lett. **20**, 764 (1995).
32. S. Skupsky, R. W. Short, T. Kessler, R. S. Craxton, S. Letzring, and J. M. Soures, J. Appl. Phys. **66**, 3456 (1989).
33. V. Smalyuk, T. Boehly, and J. Knauer, Laboratory for Laser Energetics, private communication (2005).
34. D. G. Stearns *et al.*, Rev. Sci. Instrum. **57**, 2455 (1986).
35. R. Betti, V. Lobatchev, and R. L. McCrory, Phys. Rev. Lett. **81**, 5560 (1998).
36. P. B. Radha, T. J. B. Collins, J. A. Delettrez, Y. Elbaz, R. Epstein, V. Yu. Glebov, V. N. Goncharov, R. L. Keck, J. P. Knauer, J. A. Marozas, F. J. Marshall, R. L. McCrory, P. W. McKenty, D. D. Meyerhofer, S. P. Regan, T. C. Sangster, W. Seka, D. Shvarts, S. Skupsky, Y. Srebro, and C. Stoeckl, Phys. Plasmas **12**, 056307 (2005).
37. V. A. Smalyuk, T. R. Boehly, D. K. Bradley, J. P. Knauer, and D. D. Meyerhofer, Rev. Sci. Instrum. **70**, 647 (1999).

38. L. Spitzer, Jr. and R. Härm, Phys. Rev. **89**, 977 (1953).

39. R. C. Malone, R. L. McCrory, and R. L. Morse, Phys. Rev. Lett. **34**, 721 (1975).

40. S. P. Lyon and J. D. Johnson, Los Alamos National Laboratory, Los Alamos, NM, Report LA-UR-92-3407, NTIS Order No. DE85014241 (1992).

41. S. X. Hu, B. Militzer, V. N. Goncharov, and S. Skupsky, Phys. Rev. Lett. **104**, 235003 (2010).

42. Y. Aglitskiy *et al.*, Phys. Rev. Lett. **87**, 265001 (2001).

43. Y. Aglitskiy *et al.*, Phys. Plasmas **9**, 2264 (2002).

44. O. Gotchev, "Experiments on Dynamic Overpressure Stabilization of the Ablative Richtmyer–Meshkov Instability in ICF Targets," Ph.D. thesis, University of Rochester, 2004.

45. V. N. Goncharov, O. V. Gotchev, R. L. McCrory, P. W. McKenty, D. D. Meyerhofer, T. C. Sangster, S. Skupsky, and C. Cherfils-Clérouin, J. Phys. IV France **133**, 123 (2006).

Highly Efficient Room-Temperature Yb:YAG Ceramic Laser and Regenerative Amplifier

Room-temperature, Yb-doped YAG ceramics are attractive materials for high-efficiency broadband lasers and scalable amplifiers.[1–5] Their properties make them an excellent choice for high-energy, broadband, diode-pumped lasers and amplifiers.[6] They have a reasonably large emission cross section (2×10^{-20} cm^2), a long upper-level lifetime (>1 ms), a high saturation fluence, a small quantum defect (8.6%), and broadband absorption (18 nm) and emission (>100 nm) spectra. Their hardness and fracture toughness are higher than for YAG crystals, high doping levels are possible (up to 20%), and active elements with large apertures (tens of centimeters) are available. In addition, they function as a quasi-three-level system at room temperature and a four-level system at liquid-nitrogen temperature, and they are polarization insensitive, enabling one to easily configure multipass amplifiers using polarization switching schemes.

A room-temperature diode-pumped Yb:YAG ceramic pulsed laser has been developed that produces 120 mJ at 1030 nm in free-running mode with a high optical efficiency (laser output power divided by diode pump power) of 51%. The laser (Fig. 128.14) has a folded, ~280-cm linear resonator that is close to semiconcentric. The mode diameter in the active element is tuned by moving the 3-m concave end mirror along the resonator axis. Initially, the mode diameter was set to 550 μm at the $1/e^2$ level. The $8 \times 8 \times 10$-mm, 7% Yb-doped YAG ceramic active element[7] is wedged and AR coated for the pump and laser wavelengths. A 940-nm, 250-W–rated, fiber-coupled pump diode (Jenoptik JOLD-250-CPXF-2P2) (Ref. 8) is used in pulsed mode with a 1-ms pulse width at a 5-Hz repetition rate. The pump radiation is 1:1 re-imaged from a 0.4-mm fiber core into the active element. Approximately 235 mJ of pump-pulse energy is absorbed in the active element at the maximum 140-A diode-driver current.

A single-pass, small-signal gain of 160 has been measured at the maximum driver current. The laser output energy was maximized by optimizing the output-coupler reflectivity, using a set of flat mirrors with reflectivities from 10% to 90% with 10% steps. The optimum reflectivity has been found to be 50%, resulting in output energy in excess of 102 mJ.

Further optimization was accomplished by fine tuning the mode size inside the active element to achieve the highest-possible energy. A mode-diameter increase from 550 μm to 665 μm (when the pump-to-mode-diameter ratio is 0.6) led to an output-energy increase from 102 mJ to 120 mJ, corresponding to an optical-to-optical efficiency of 51%. The output energy of the laser as a function of absorbed pump energy is shown in

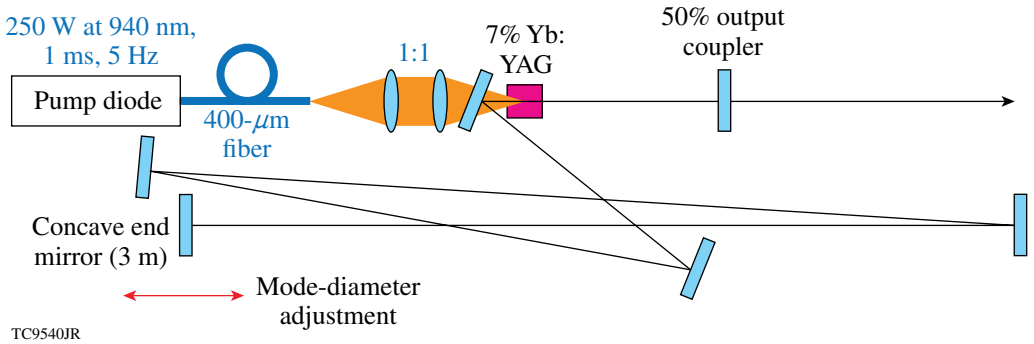

Figure 128.14
Block diagram of the Yb:YAG ceramic laser.

Fig. 128.15(a). Taking into account that contemporary pump laser diodes can provide an electrical-to-optical efficiency of up to 80%, a Yb:YAG ceramic laser can potentially achieve a wall-plug efficiency of >40%. The fine tuning of the mode diameter made it possible to achieve a slope efficiency of 78%, which is slightly higher than has been previously achieved in a room-temperature Yb:YAG ceramic laser.[1,2] Figure 128.15(b) shows a good-quality output-beam profile with lineouts through the center that are approximately Gaussian.

The active element has also been demonstrated in a regenerative amplifier (regen) used to amplify 8-ns FWHM (full-width-at-half-maximum) square pulses (Fig. 128.16). Here optical damage was avoided by increasing the mode and pump-beam diameters. The pump fiber was re-imaged into the active element with a 50% expansion, producing a 600-μm pump spot. The regen mode diameter was optimized for maximum output energy with a pump–to–mode-diameter ratio of 0.62. The output energy was limited to 5 mJ because of intracavity polarizer

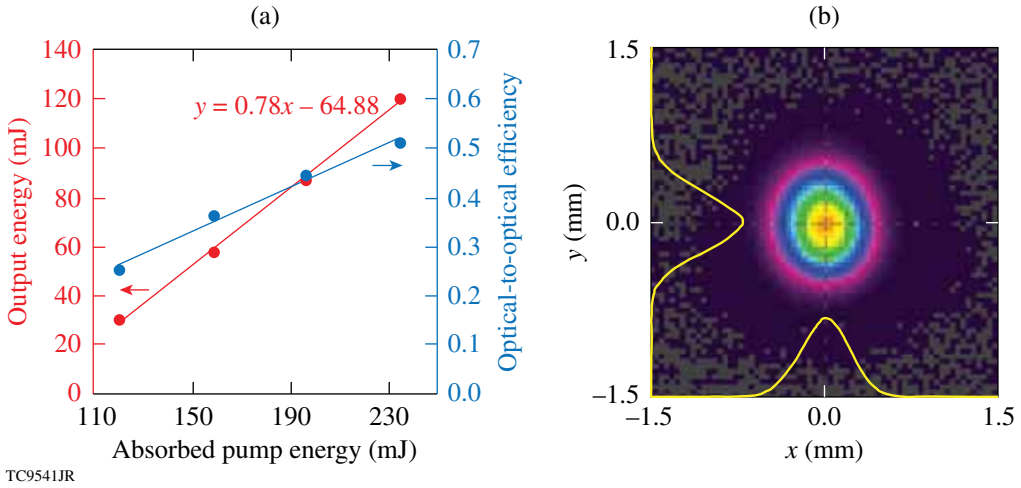

Figure 128.15
(a) Output energy and optical efficiency as functions of absorbed pump energy for the optimized Yb:YAG laser. (b) Near-field image of the laser output at maximum energy with one-dimensional (1-D) lineouts overlaid.

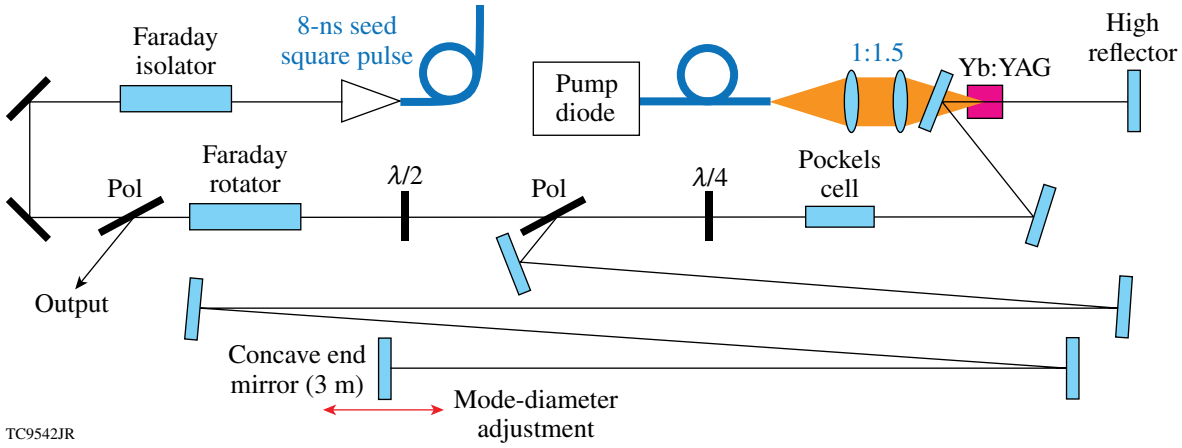

Figure 128.16
Yb:YAG ceramic regenerative amplifier. Pol: polarizer; λ/2: half-wave plate; λ/4: quarter-wave plate.

damage. The pump current was 80 A at this point, with the 140-A maximum current available indicating that more energy can be achieved from the regen with increased pump-volume diameter. The output-beam profile was of similar quality to that of the free-running laser and was close to TEM_{00}.

The pump-volume diameter was further increased to 670 μm with the mode diameter increased in proportion. Output energy of 14.5 mJ was produced at the 140-A maximum pump current [Fig. 128.17(a)]. The output energy variations decreased to ~0.2% rms as the output energy was increased, as a result of the increase of the gain/loss ratio.[9] The number of round trips in the regen at this point is 4, with the regen functioning more as a multipass amplifier, where the beam profile is defined not by the resonator but by the radial-gain variations in the Yb:YAG.

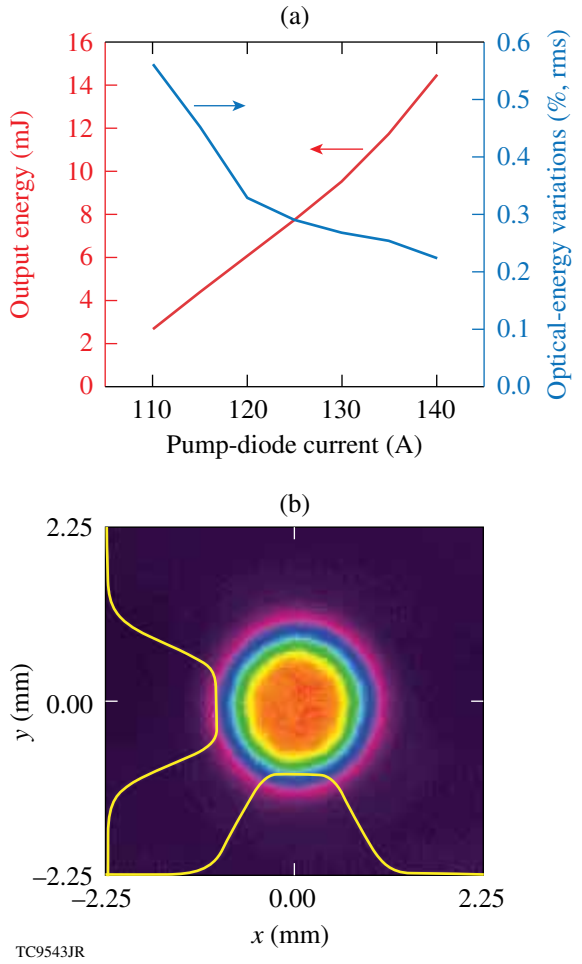

Figure 128.17
(a) Output energy and energy variations of the regen pumped with a 670-μm pump spot. (b) Near-field image of the output beam at maximum energy with 1-D lineouts overlaid.

The output profile was a fourth-order super-Gaussian, resulting from heavy gain saturation along the beam axis [Fig. 128.17(b)].

The broad bandwidth of the Yb:YAG makes this regen suitable for the amplification of stretched broadband pulses in chirped-pulse–amplification laser systems and also for systems that require bandwidth for SSD (smoothing by spectral dispersion).[10]

In conclusion, a room-temperature, diode-pumped pulsed Yb:YAG free-running laser with 78% slope efficiency has been demonstrated. It has been shown that fine tuning of the mode diameter to the diameter of the pumped volume is important to achieve maximum laser efficiency with a Gaussian-like beam profile. A regenerative Yb:YAG amplifier with maximum output energy of 14.5 mJ and a super-Gaussian beam profile has been built and tested.

ACKNOWLEDGMENT

This work was supported by the U.S. Department of Energy Office of Inertial Confinement Fusion under Cooperative Agreement No. DE-FC52-08NA28302, the University of Rochester, and the New York State Energy Research and Development Authority. The support of DOE does not constitute and endorsement by DOE of the views expressed in this article.

REFERENCES

1. S. Nakamura *et al.*, Opt. Commun. **281**, 4411 (2008).
2. B. Zhou *et al.*, Opt. Lett. **35**, 288 (2010).
3. A. Pirri *et al.*, Opt. Express **18**, 17,262 (2010).
4. S. T. Fredrich-Thornton *et al.*, in *Advanced Solid-State Photonics*, OSA Technical Digest Series (CD) (Optical Society of America, Washington, DC, 2008), Paper WB13.
5. S. Pearce *et al.*, Opt. Commun. **282**, 2199 (2009).
6. P. Lacovara *et al.*, Opt. Lett. **16**, 1089 (1991).
7. Baikowski International Corporation, Charlotte, NC, 28216-2385.
8. JENOPTIK Laser GmbH, 07745 Jena, Germany.
9. A. V. Okishev and J. D. Zuegel, Appl. Opt. **43**, 6180 (2004).
10. S. Skupsky, R. W. Short, T. Kessler, R. S. Craxton, S. Letzring, and J. M. Soures, J. Appl. Phys. **66**, 3456 (1989).

LLE's Summer High School Research Program

During the summer of 2011, 16 students from Rochester-area high schools participated in the Laboratory for Laser Energetics' Summer High School Research Program. The goal of this program is to excite a group of high school students about careers in the areas of science and technology by exposing them to research in a state-of-the-art environment. Too often, students are exposed to "research" only through classroom laboratories, which have prescribed procedures and predictable results. In LLE's summer program, the students experience many of the trials, tribulations, and rewards of scientific research. By participating in research in a real environment, the students often become more excited about careers in science and technology. In addition, LLE gains from the contributions of the many highly talented students who are attracted to the program.

The students spent most of their time working on their individual research projects with members of LLE's technical staff. The projects were related to current research activities at LLE and covered a broad range of areas of interest including experimental systems and diagnostic development, computational modeling of implosion physics, chemistry, materials science, laser system development and diagnostics, and database development (see Table 128.IV).

The students attended weekly seminars on technical topics associated with LLE's research. Topics this year included laser physics, fusion, holography, nonlinear optics, atomic force microscopy, glass and glass fracture, and electronic paper. The students also received safety training, learned how to give scientific presentations, and were introduced to LLE's resources, especially the computational facilities.

The program culminated on 24 August with the "High School Student Summer Research Symposium," at which the students presented the results of their research to an audience including parents, teachers, and LLE staff. The students' written reports will be made available on the LLE Website and bound into a permanent record of their work that can be cited in scientific publications.

Two hundred and eighty-one high school students have now participated in the program since it began in 1989. This year's students were selected from over 50 applicants.

At the symposium LLE presented its 15th annual William D. Ryan Inspirational Teacher Award to Mrs. Deborah Reynolds, a chemistry teacher at Brighton High School. This award is presented to a teacher who motivated one of the participants in LLE's Summer High School Research Program to study science, mathematics, or technology and includes a $1000 cash prize. Teachers are nominated by alumni of the summer program. Mrs. Reynolds was nominated by Andrew Chun and Connie Jiang, participants in the 2010 program. Andrew described Mrs. Reynolds as "one of the few teachers who can take AP-level material and make it extremely easy for everyone in the class to understand…She makes learning fun and entertaining…She inspires her class through her kindness and unique ability to reach each of her individual students, in a special way that few teachers can, to want to learn more about science." For Connie, Mrs. Reynolds was "a truly inspirational teacher" who was "so outstanding because she was so thorough." Connie added, "She was kind, patient, organized and thorough, and taught me more about chemistry than I had ever thought to ask or know." Mrs. Reynolds was also enthusiastically recommended by Dr. Nancy Hackett, Brighton High School Principal, who attended the symposium. She said of Mrs. Reynolds, "She takes the students to the next level and she is passionate about chemistry. She always tries to improve herself professionally to keep her teaching at the cutting edge."

Table 128.IV: High School Students and Projects—Summer 2011.

Name	High School	Supervisor	Project Title
Brandon Avila	Allendale Columbia	R. W. Kidder	Optimizing LLE Information Operations Through Natural Language Processing
Andrew Boyce	McQuaid	W. T. Shmayda	Water-Stimulated Tritium Release from Metals
Matthew DeCross	Pittsford Sutherland	L. D. Lund	Automation of Vibration Measurement and Characterization of Cryogenic Deuterium–Tritium Target Motion
Avery Gnolek	Webster Thomas	K. L. Marshall	Photoaligned Liquid Crystal Wave Plate
Dana Gretton	Honeoye Falls Lima	R. G. Peck, E. Druszkiewicz	Design of a New Master-Timing Generator
Sean Hamlin	Fairport	R. Epstein	X-Ray Fluorescence as an Imploded-Shell Diagnostic
Felix Jin	Brighton	G. Fiksel	Characterization of Magnetic Coils for the Magneto-inertial Fusion Energy Delivery System
Jefferson Lee	Canandaigua Academy	W. T. Shmayda	Modeling Tritium Removal from Metal Surfaces
Kevin Mizes	Pittsford Sutherland	R. Boni, D. H. Froula, S. Ivancic	Two Techniques for Array Generation with Applications in Grid-Imaging Refractometry
Patricia Olson	Brighton	R. S. Craxton	Optimization of Beam Configurations for Shock-Ignition Experiments on the NIF and OMEGA
Sean Reid	Fairport	M. Burke, R. Boni, S. D. Jacobs	Surface Grinding and Polishing to Remove Etch-Induced Noise Pitting in CR-39 Samples
Madeline Rutan	Penfield	K. L. Marshall	Abrasion-Resistant Antireflection Sol-Gel Coatings
Michael Statt	School of the Arts	K. L. Marshall, C. Dorrer	Generation of Radially Polarized Beams Using Optically Patterned Liquid Crystals
Troy Thomas	Webster Thomas	B. E. Kruschwitz	Optical Time-Domain Reflectometry for the Transport Spatial Filter on the OMEGA Extended Performance Laser
Harrison Xiao	Pittsford Sutherland	P. A. Jaanimagi	Dynamic Defocusing in Streak Tubes
Andrew Zhao	Webster Thomas	R. Boni, D. H. Froula, S. Ivancic	Image Processing and Analysis of 4ω Grid-Image Refractometry Data

FY11 Laser Facility Report

During FY11, the Omega Laser Facility conducted 1348 target shots on OMEGA and 457 target shots on OMEGA EP for a total of 1805 target shots (see Tables 128.V and 128.VI). OMEGA averaged 10.3 target shots per operating day with availability and experimental effectiveness averages for FY11 were 93.3% and 96.1%, respectively.

OMEGA EP was operated extensively in FY11 for a variety of internal and external users. Of the 457 target shots, 401 were shot in the OMEGA EP target chamber and 56 were joint shots in the OMEGA target chamber. OMEGA EP averaged 5.5 target shots per operating day with availability and experimental effectiveness averages for FY11 of 85.6% and 95.2%, respectively.

Table 128.V: Omega Facility target shot summary for FY11.

Laboratory	Planned Number of Target Shots	Actual Number of Target Shots	NIC	Shots in Support of NIC	Non-NIC
LLE	335	389	0	375	14
LLNL	260	301	131	0	170
NLUF	155	203	0	0	203
LANL	170	195	45	0	150
LBS	155	170	0	0	170
CEA	40	50	0	0	50
AWE	20	23	0	0	23
U. Mich	20	17	0	0	17
Total	1155	1348	176	375	797

Table 128.VI: Omega EP Facility target shot summary for FY11.

Laboratory	Planned Number of Target Shots	Actual Number of Target Shots	NIC	Shots in Support of NIC	Non-NIC
LLE	174	192	0	192	0
LLNL	65	79	10	5	64
AWE	10	21	0	0	21
NLUF	60	57	0	0	57
LBS	65	74	0	0	74
LANL	25	28	0	0	28
CEA	5	6	0	0	6
Total	404	457	10	197	250

OMEGA EP Improved Energy Capabilities

Short-pulse (IR) and long-pulse (UV) energy on target has been increased. The UV energy was increased after the acquisition of improved optics. Lithographic-quality fused-silica substrates were finished using LLNL-developed protocols, LLNL-supported production controls, and the latest LLNL post-processing techniques for enhanced damage threshold (Acid Mitigation Process II). The extended UV energy operational envelope was made available after completion of a damage-testing laser shot campaign with the previous optics. UV energy on target was increased from 2.3 kJ per beam to 6.6 kJ at 10 ns, exceeding the 6.5-kJ system-design goal. Short-pulse IR energy was increased following the installation of improved damage-threshold gratings in the grating-compressor vessel. Additionally, a comprehensive short-pulse small-beam damage-testing program was conducted on multilayer dielectric coatings. The combination of new gratings and coating performance analysis resulted in an increase to the IR energy operational envelope for the short-pulse laser beams. IR energy on target for beamline 2 at 10 ps was increased from 1.0 kJ to 1.6 kJ, 60% of the 2.6 kJ design goal. Up-to-date limits to the energy on target are now summarized and available to all users through the Operations Website.

OMEGA EP 100-ps UV Temporal Pulse Shapes

At the request of users, the shortest UV pulse durations have been extended from the previous limit of 1 ns to 100 ps. Users are now able to request pulse shapes between 100 ps and 10 ns. The 100-ps pulse shapes have been utilized to produce short-duration x-ray pulses useful for a variety of target-physics campaigns, including backlighter platform development for the NIF. With this new functionality, the temporal co-timing of all four beamlines has been calibrated to <50 ps.

OMEGA EP Short-Pulse Focal-Spot Improvement Using a Static Wavefront Corrector

Static wavefront correction has been developed for OMEGA EP to correct high-order residual wavefront that is beyond the spatial resolution of the existing adaptive optics. A small-aperture phase corrector, manufactured by QED Technologies, using the magnetorheological finishing (MRF) process, has been added to the injection system to precompensate for repeatable high-order wavefront errors that arise in the beamlines. Following successful proof-of-principle demonstrations, these optics were implemented on both of the OMEGA EP short-pulse beamlines, providing an ~2× reduction in focal-spot extent at the output of the beamline during active wavefront correction. On amplified shots, target-plane focal-spots have met the specification of 80% of the energy in less than a 20-μm radius ($R_{80} < 20\ \mu$m). The ~25% improvement is realized on the first shots, although thermal distortion of the amplifier disks has led to focal-spot degradation after multiple shots have been taken on a day. Future revisions of the phase-corrector design will partially compensate for this effect. See Fig. 128.18 for representative focal-spot results. This work follows on the successful implementation of advanced phase-retrieval techniques developed in FY10 that allow for accurate characterization of the focal spot.

OMEGA EP Infrared Alignment Table and Beamline Injection Table Enhancement

The daily operation of the OMEGA EP laser has been improved with enhancements to the OMEGA EP infrared alignment table (IRAT). This work improved the imaging accuracy from the laser source apodizer plane to the beamline input image plane. This improvement reduces modulation on critical optics in the OMEGA EP Laser System. Additional diagnostics were added to improve the injection energy measurements and centering of beams. All of these improvements have increased system operability and are primary contributors to an increase in shots per day from FY10 to FY11.

Improved OMEGA UV On-Target Predictions

Target implosions have been shown to slowly degrade the UV transmission, primarily on the final debris shield, causing a decrease in on-target energy relative to the diagnostic prediction. During FY11, the study of UV transmission has resulted in a better understanding of the loss mechanisms. The study found that the losses are dependent on target type, target composition, target quantity, number of beams used for each shot, and beam location in the tank. The results of this study and daily measurements of transmission on representative UV optics have been incorporated into a new on-target energy prediction that is reported to the principal investigator. The system average loss is predicted within ±1% accuracy, and the rms error is <2%.

Experimental Diagnostics

Diagnostic capabilities continue to evolve with the commissioning of 24 new diagnostic instruments on OMEGA and 9 new diagnostic instruments on OMEGA EP. These include a new spherical crystal x-ray imager, upgraded hard x-ray diode arrays, B-dot magnetic field probes, an electron spectrometer,

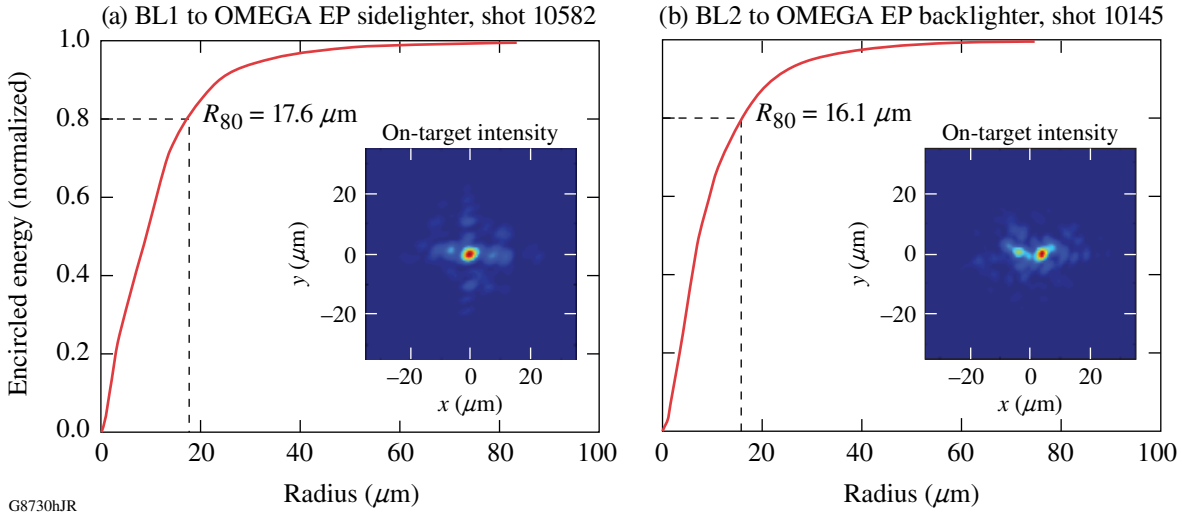

Figure 128.18
(a) Beam 1 (BL1) and (b) Beam 2 (BL2) focal-spot images from target shots with the static wavefront correctors installed.

and a new test platform for CVD-diamond neutron detectors. Many of these new instruments were developed by or in cooperation with other laboratories (including LLNL, LANL, CEA, Oxford University, Osaka University, and SNL).

Improvements to the online information systems available to our scientific users include availability of specification sheets and operating procedures for diagnostic instruments, as well as target chamber port assignment tables. Other facility improvements include commissioning of an additional image plate scanner and electromagnetic interference hardening of the target positioners on both OMEGA and OMEGA EP.

A number of safety improvements were implemented in the experimental area. These include the commissioning of filtered air flow hoods for servicing equipment that contains or is contaminated with beryllium, higher-resolution beryllium monitoring capability; and review and certification of heavy equipment lift procedures. Additionally, tracking beryllium survey data and radioactive material inventory has improved visibility to the operators and other stakeholders.

National Laser Users' Facility and External Users' Programs

Under the facility governance plan implemented in FY08 to formalize the scheduling of the Omega Laser Facility as an NNSA User Facility, Omega Facility shots are allocated by campaign. The majority (65%) of the FY11 target shots were allocated to the National Ignition Campaign (NIC) conducted by integrated teams from the national laboratories and LLE and to the high-energy-density campaigns conducted by teams led by scientists from the national laboratories.

In FY11, 27.6% of the facility shots were allocated to basic science experiments. Half of these were dedicated to university basic science under the National Laser Users' Facility (NLUF) Program, and the remaining shots were allotted to the Laboratory Basic Science (LBS) Program, comprising peer-reviewed basic science experiments conducted by the national laboratories and by LLE including the Fusion Science Center (FSC).

The Omega Facility is also being used for several campaigns by teams from the Commissariat à l'énergie atomique (CEA) of France, the Atomic Weapons Establishment (AWE) of the United Kingdom, and the Center for Radiative Shock Hydrodynamics (CRASH) of the University of Michigan.

The facility users during this year included 11 collaborative teams participating in the NLUF Program; 15 teams led by LLNL and LLE scientists participating in the LBS Program; many collaborative teams from the national laboratories and LLE conducting experiments for the NIC; investigators from LLNL and LANL conducting experiments for high-energy-density-physics programs; scientists and engineers from CEA and AWE, and scientists and students from CRASH.

In this section, we briefly review all the external user activity on OMEGA during FY11.

FY11 NLUF Program

FY11 was the first of a two-year period of performance for the NLUF projects approved for the FY11–FY12 funding and OMEGA shots. Eleven NLUF projects (see Table 128.VII) were allotted Omega Facility shot time and conducted a total of 255 target shots at the facility. This work is summarized in this section.

Study of Fast-Electron Transport into Imploded High-Density Plasmas Using Cu-Doped CD-Shell Targets

Principal Investigators: F. N. Beg (University of California, San Diego) and M. S. Wei (General Atomics)
Co-investigators: R. B. Stephens (GA); H. Sawada (UCSD); W. Theobald, C. Stoeckl, J. A. Delettrez, and R. Betti (LLE); C. D. Chen, M. H. Key, P. K. Patel, and H. McLean (LLNL); and T. Yabuuchi and H. Habara (ILE)
Lead Graduate Student: L. C. Jarrott (UCSD)

Understanding fast-electron generation in the cone and their subsequent transport into hot, dense plasma is crucial to the success of the cone-guided fast-ignition scheme. The goal of the University of California, San Diego, NLUF project is to investigate the coupling efficiency and spatial distribution of fast-electron energy deposition in imploded CD shells attached to Au cone targets. To achieve this, a Cu dopant (at ~1% atomic number density of CD) is added to the CD shell (3/4 of the inner part of the shell), which allows for the characterization of fast-electron transport via fast-electron–induced, 8-keV Cu K-shell fluorescence radiation. The experiment consists of two parts: (1) characterization of background 8-keV x-ray emission generated from the compression (by the 20-kJ OMEGA beams) of a CD shell with and without Cu dopant and (2) characterization of fast-electron–produced Cu fluorescence emission from the compressed Cu-doped CD with an additional-kJ, 10-ps, high-intensity OMEGA EP beam timed and injected into the compressed core through the Au cone tip. The primary diagnostics were a narrowband spherical crystal imager (SCI) to image 8-keV x-ray emission and a zinc Von Hamos (ZVH) x-ray spectrometer tuned for Cu K-shell and ionic-line–emission yield measurement. Several other diagnostics including broadband x-ray imaging diagnostics such as pinhole cameras and Kirkpatrick–Baez (KB) microscopes, neutron time-of-flight detectors, and magnetic electron spectrometers (one multichannel spectrometer along the OMEGA EP beam axis and one single-channel spectrometer at the side) were employed.

Table 128.VII: Approved FY11 and FY12 NLUF proposals.

Principal Investigator	Institution	Project Title
F. N. Beg	University of California, Berkeley	Systematic Study of Fast-Electron Transport in Imploded Plasmas
R. P. Drake	University of Michigan	Experimental Astrophysics on the OMEGA Laser
T. Duffy	Princeton University	Ramp Compression for Studying Equations of State, Phase Transitions, and Kinetics on OMEGA
R. Falcone	University of California, Berkeley	Detailed *In-Situ* Diagnostics of High-*Z* Shocks
P. Hartigan	Rice University	Clumpy Environments and Interacting Shock Waves: Realistic Laboratory Analogs of Astrophysical Flows
R. Jeanloz	University of California, Berkeley	Recreating Planetary Core Conditions on OMEGA
K. Krushelnick	University of Michigan	Intense Laser Interactions with Low-Density Plasma Using OMEGA EP
R. Mancini	University of Nevada, Reno	Investigation of Hydrodynamic Stability and Shock Dynamics in OMEGA Direct-Drive Implosions Using Spectrally Resolved Imaging
R. D. Petrasso	Massachusetts Institute of Technology	Charged-Particle Probing of Inertial Confinement Fusion Implosions and High-Energy-Density Plasmas
A. Spitkovsky	Princeton University	Collisionless Shocks in Laboratory High-Energy-Density Plasmas
R. Stephens	General Atomics	Investigation of Laser to Electron Energy Coupling Dependence on Laser Pulse Duration and Material Composition

Figure 128.19 shows pictures of the cone-in-shell target and experimental layout including ten-inch manipulator (TIM) and port locations for various diagnostics. In this experiment, 54 of the 60 OMEGA beams with low-adiabat pulse shape [LA24170P with smoothing by spectral dispersion (SSD) off] were used (18 to 20 kJ) to compress the shell, while the remaining six beams were used to destroy the target cone 5 ns after the short-pulse laser was fired in the cone. The 10-ps OMEGA EP backlight beam BL2 was used with a 3.65-ns delay at 10 ps, tight focus at the inner cone tip, and a minimum prepulse. The target consisted of a plastic (CD) shell with an outer diameter of 870 μm and a cone with an angle of 34° with 40-μm offset distance between the outer cone tip and the shell center. The CD shell consisted of a 10-μm pure-CD outer layer as the ablator and a 27-μm inner layer doped with Cu at 1% atomic number density of CD. The thickness of the cone tip was 15 μm, while the cone wall thickness was 10 μm.

In this experiment, the SCI was fielded for the first time on OMEGA. Figure 128.20 compares 8-keV x-ray emission recorded with the SCI in three different shots: (a) background x-ray emission from an OMEGA-only imploded cone-in-CD-shell target (without Cu dopant), (b) bremsstrahlung and fluorescence emission from an imploded cone-in-CD-shell target with Cu dopant, (c) bremsstrahlung and fluorescence emission from a joint shot of both OMEGA and OMEGA EP with OMEGA EP being fired at 300 J, and (d) enhanced contrast view of the image in (c). The Cu fluorescence emission in the OMEGA-only implosion shots with Cu-doped CD shells is due to the driver-beam–produced superthermal (tens of keV) electrons. The 8-keV x-ray image from the joint shot [as seen in Figs. 128.20(c) and 128.20(d)] shows emission from imploded plasmas just outside the cone tip area with features that were not observed in the OMEGA-only shots, which presumably is due to short-pulse, OMEGA EP beam–produced fast electrons. A detailed analysis of the data, taking into account opacity corrections, is underway. Cu K-shell and ionic line emission (not shown here) measured by the ZVH spectrometer showed extremely strong Cu He_α line emission. Radiation–hydrodynamic modeling of the implosion suggested that this is caused by the direct heating by the implosion driver beams of the Cu-doped CD layer after completely ablating off the first 10-μm non-doped CD layer. A slightly thicker ablator will be used in the improved targets for future experiments.

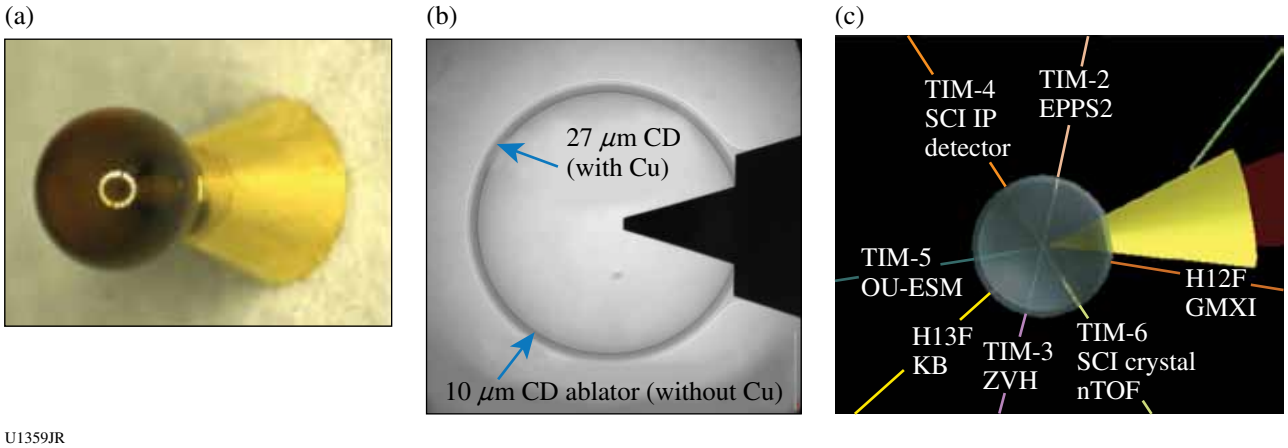

Figure 128.19
(a) A Au cone-in-(Cu-doped) CD-shell target; (b) contact x-ray radiograph image of the target; and (c) experiment and diagnostics layout.

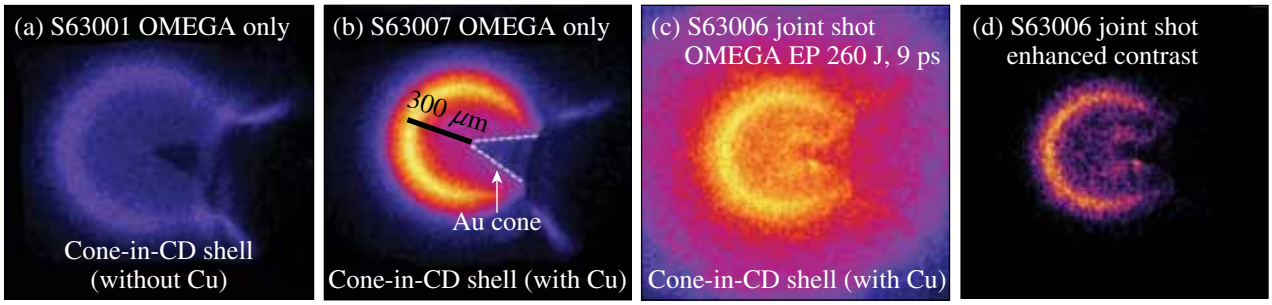

Figure 128.20
SCI-recorded, 8-keV x-ray images from (a) an OMEGA-only compression shot with cone-in-CD-shell target without Cu doping; (b) an OMEGA-only compression shot with cone-in-CD-shell target with Cu doping; (c) a joint shot with OMEGA EP beam energy of 260 J at 9 ps. Images shown in (a), (b), and (c) have the same spatial and color scales. (d) Image of (c) with enhanced contrast. Additional visible features indicate that fast electrons produced x rays outside the cone.

In summary, the NLUF fast-electron–transport experiment with a cone-in-shell (with Cu doping) target has been successfully performed on OMEGA with a comprehensive suite of x-ray, particle, and neutron diagnostics including the newly implemented monochromatic x-ray imager (SCI) and multichannel electron spectrometer. The platform for complex electron-transport physics experiments has been established and will be pursued for greater than kilojoule short-pulse–laser energies.

Experimental Astrophysics on the OMEGA Laser
Principal Investigator: R. P. Drake (University of Michigan)
Co-investigators: B. Loupias and E. Falize (CEA); D. H. Froula, T. R. Boehly, and J. P. Knauer (LLE); J. Holloway, K. Powell, and C. C. Kuranz (University of Michigan); T. Plewa (Florida State University); and B. A. Remington, S. Ross. H.-S. Park, and S. H. Glenzer (LLNL)

The OMEGA laser makes it feasible to conduct experiments relevant to astrophysical phenomena because of the very high energy-density conditions it can create. This project explores the contribution of radiative shock waves to the evolving dynamics of binary star-accretion disk systems in which they reside. Radiative shock waves produce shocked matter so hot that it radiates away most of its thermal energy. This radiation causes variable structures to develop depending on the optical properties of the material on either side of the shock. To control these properties and understand the shock-front emission, we devised an experiment that accelerates a plasma flow into vacuum and then develops a radiative shock when the flow is impeded. We study the shock structure using x-ray radiography and its radiative flux with μDMX, an x-ray diode spectrometer.

The experiments on the 60-beam OMEGA laser employ a laser configuration of 10 UV beams with a 1-ns square pulse. The laser beams are smoothed using the SSD technique and SG4 distributed phase plates. They are focused on a 10-μm plastic ablator whose opposite face is coated with 5 μm of Sn. The beams deposit a total energy of ~4.5 kJ, giving an average irradiance of $\sim 1.2 \times 10^{15}$ W/cm^2. This generates a laser ablation pressure of ~75 Mbar that initially drives a shock through the plastic and Sn, which is mounted on one side of an evacuated acrylic tube. After this ablative shock breaks out of the Sn into vacuum, the Sn plasma expands, cools, and accelerates down the target cylinder at an average velocity of ~150 km/s. About 4 mm from the laser-drive surface, the Sn ejecta impact a 100-μm-thick, cold Al foil. In response, a reverse shock develops in the flow and a forward shock is driven into the Al end wall. The traditional "upstream" velocity in the shocked system is defined by the Sn flow, which is fast enough that radiative effects play a significant role in the dynamics of the reverse shock. An additional five OMEGA laser beams irradiate a zinc foil on a backlit pinhole target for 1 ns, creating the x rays that image the reverse shock onto film and image plates. To investigate the effects of different flow velocities and oblique collisions, targets were also shot that had varied plastic-Sn thicknesses and tilted Al foils. Figure 128.21 shows an image from a single target, taken ~29 ns after the drive laser pulse was turned off and a few nanoseconds after the collision. It has a 6-μm-thick plastic ablator coated with 4 μm of Sn and an Al wall ~13° off of normal to the tube axis.

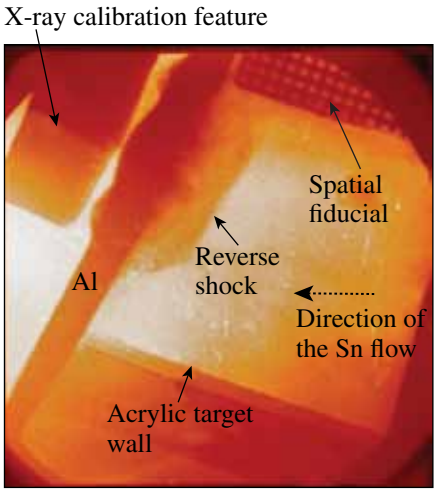

Figure 128.21
X-ray radiograph of a radiative reverse shock in Sn plasma. One can see the radiating shock, an acrylic tube wall, the spatial fiducial, and the x-ray calibration feature used in the experiment. The reverse shock, which forms in the incoming Sn flow, is to the right of the Al wall, where the laser drive is 4 mm away. As the unshocked Sn moves from right to left, it is not dense enough to resolve, while the reverse shock absorbs the diagnostic x rays, revealing its structure.

Development of a Platform for Laser-Ramp Compression of Planetary Materials on OMEGA

Principal Investigator: T. S. Duffy (Princeton University)
Co-investigators: J. Wang (Princeton University); R. F. Smith, F. Coppari, J. H. Eggert, P. M. Celliers, D. Braun, and G. W. Collins (LLNL); and T. R. Boehly (LLE)

The goal of this project is to develop techniques for quasi-isentropic ramp compression of planetary materials. This work has important applications for understanding the structure and dynamics of the interiors of planets both within and outside our solar system. Ramp compression achieves high compression at relatively modest temperatures and can be used to extract quasi-isentropic equation-of-state data and study solid–solid phase transitions. Iron (Fe) and magnesium oxide (MgO) are geologically important materials each representative of one of the two major interior regions (core and mantle) of terrestrial planets. An experimental platform for ramp loading of Fe and MgO has been established and tested in experiments on OMEGA. Target packages consisted of stepped samples and a diamond ablator attached to a Au halfraum [Fig. 128.22(a)]. Each target had four steps that were approximately 5 to 7 μm thick. Composite laser pulses are used to drive a ramp-compression wave into the sample. Detection of the ramp wave's arrival and its velocity at the free surface of each step was made using a velocity interferometer system for any reflector (VISAR). For MgO, we also carried out x-ray–diffraction experiments using the PXRDIP (powder x-ray diffraction image plate) target. The target design consisted of a 5- to 10-μm-thick powder MgO sample sandwiched between a diamond ablator and window attached to a Ta pinhole [Fig. 128.22(b)]. Initial experimental results showed that we could successfully compress samples to above 4 Mbar and obtain x-ray–diffraction images of the compressed sample. By enhancing the sample diffraction signal and further reducing background in future experiments, we expect to obtain structural information on this material. Figure 128.23 shows examples of the input pulse, VISAR signal, and wave profiles obtained for a typical MgO ramp-compression experiment. Through the use of Lagrangian analysis on the measured wave profiles, stress-density states in MgO have been determined to pressures of 260 GPa. Figure 128.24 compares the ramp-compression curve to previous diamond-anvil-cell and shock-compression data. At high pressures, the compression curve softens and is similar to the extrapolated 300-K

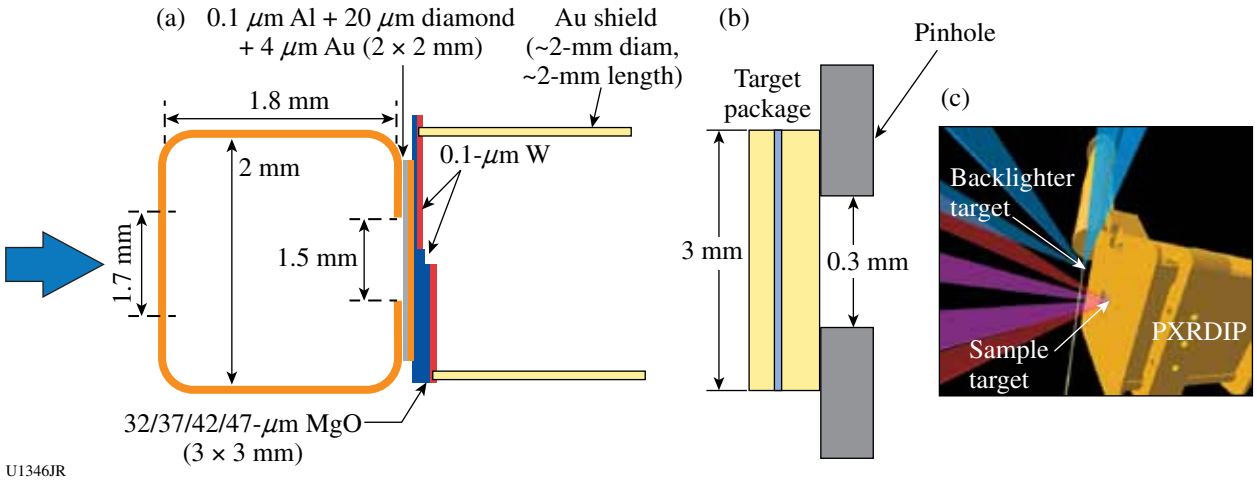

Figure 128.22
(a) Target package for the stepped MgO sample; (b) PXRDIP setup and target package for the powder MgO sample.

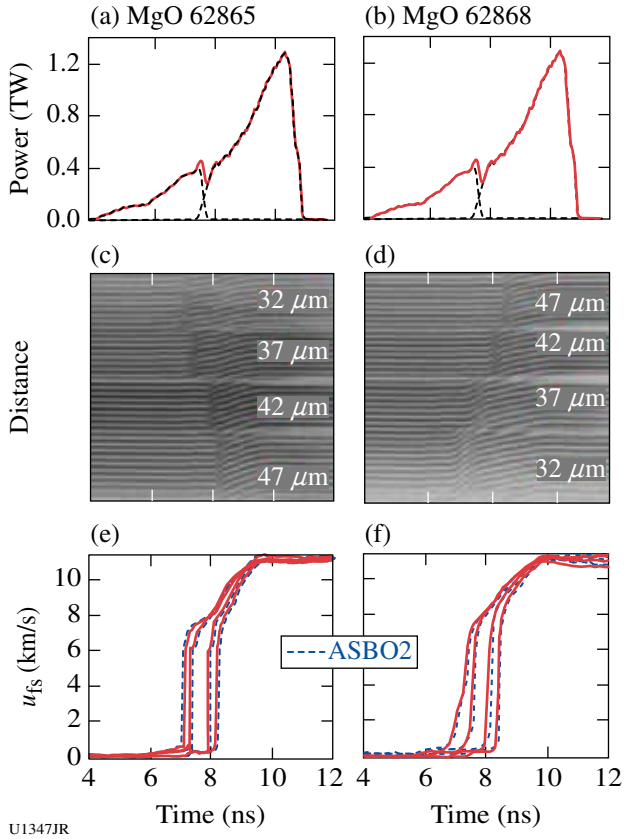

Figure 128.23
[(a),(b)] Laser pulse for two representative MgO shots (62865 and 62868). The dashed lines show the individual pulses and the solid line is the composition pulse shape. [(c),(d)] Line VISAR streak camera images from a ramp-compressed multistepped MgO target corresponding to (a) and (b), respectively. [(e),(f)] Extracted free-surface velocity profiles from (c) and (d) for both active shock breakouts (ASBO1 and ASBO2).

quasi-hydrostatic isotherm. Further experiments will focus on extending MgO ramp compression and x-ray diffraction to higher pressures and reducing experimental uncertainties. Further theoretical work will be devoted to the development of new analytical tools for analyzing ramp-compression data for materials undergoing time-dependent compression including treating the initial shock and phase transformation.

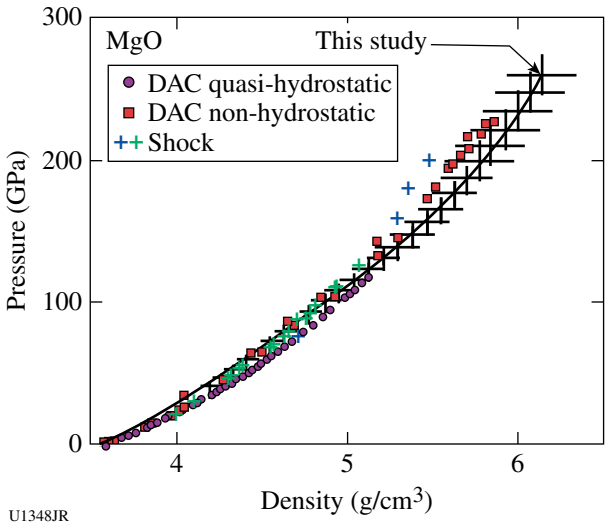

Figure 128.24
Comparison of stress versus density of MgO from the quasi-isentropic compression experiment (62868) to previous studies including diamond anvil cell (DAC) and shock data. The black curve with error bars is the quasi-isentrope from a representative MgO experiment.

Probing the Ion–Ion Structure Factor (S_{ii}) of Shocked Al Using 18-keV Angularly Resolved XRTS

Principal Investigator: R. Falcone (LBL)
Co-investigators: T. Ma, A. Pak, H. J. Lee, T. Doeppner, C. Fortmann, L. Fletcher, O. L. Landen, and S. H. Glenzer (LLNL)

The goal of the HiZShk-11A experiment is to test dense-matter models on shocked Al using a Mo He_α (18-keV) backlighter to perform x-ray Thomson scattering on the 60-beam OMEGA laser. Simulations have shown significant differences in the static ion–ion (S_{ii}) structure feature of aluminum, depending on the theoretical model used, so these predicted differences were experimentally evaluated by measuring the scattering spectrum of shocked Al at a number of different scattering **k** vectors.

The 125-μm Al targets were shock compressed to >3× solid density using nine beams with a total energy of 4.5 kJ in a stacked 1-ns configuration (Fig. 128.25). SG4 distributed phase plates were used to achieve a smooth 800-μm focal spot, yielding a total drive intensity of 3×10^{14} W/cm^2 on the sample. Sixteen beams were incident on a thin Mo foil to generate Mo He_α x rays at 17.9 keV used to probe the compressed targets.

Initial analysis is very promising: the S_{tot} (Rayleigh + background fluctuations + Compton signals) shows an increasing relative intensity as we approach lower **k** (smaller scattering angle). Work continues to extract the S_{ii} structure factor from the data.

PlanetCore 11A, 11B

Principal Investigator: R. Jeanloz
(University of California, Berkeley)
Co-investigators: J. H. Eggert, D. G. Hicks, P. M. Celliers, and G. W. Collins (LLNL); and T. R. Boehly (LLE)

Two half-day campaigns were carried out in FY11 under the Planetary Core NLUF Project: one in December 2010 (11A) and a second in March 2011 (11B). Both series focused on exploring the phase diagram of mixtures of 80% H_2 and 20% He. The primary goal of these studies was to look for evidence of He phase separation under hot, pressurized conditions. There are recent predictions of this effect,[1,2] and its existence has ramifications for understanding the interior structure of the planet Saturn. Our previous studies had focused on He/H_2 in a 50:50 ratio, using samples with initial pressures ranging from 1 kbar to 40 kbar that were then shock compressed to pressures ranging from 40 to 200 GPa. The measurements done with the ASBO/VISAR and streak optical pyrometer (SOP)

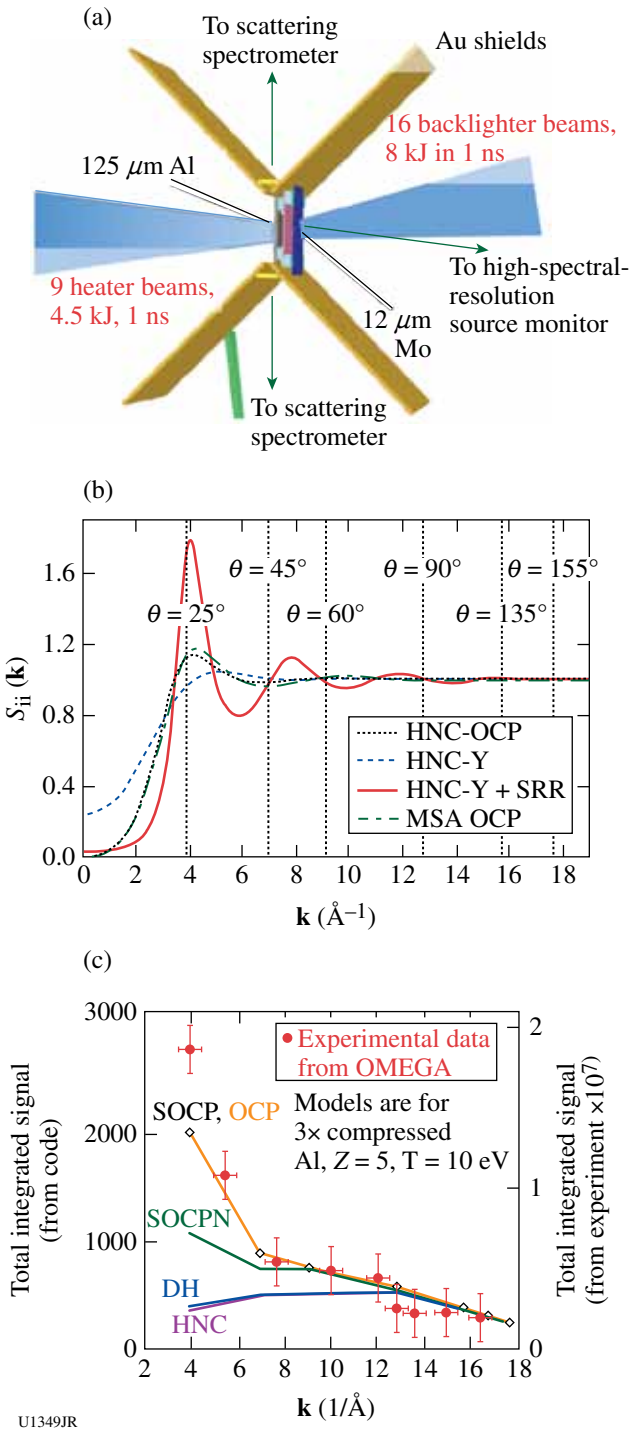

Figure 128.25
(a) The experimental setup for HiZShk-11A. (b) The S_{ii} of shocked Al oscillates as a function of scattering vector **k** for several models, where the most interesting region to probe S_{ii} and validate models is around **k** = 4 Å^{-1}. (c) Preliminary data analysis shows the total integrated signal of scattering data at varying **k** follows the trends predicted by the screened-one-component plasma (SOCP) or one-component plasma (OCP) models.

diagnostics determined the pressure, density, internal energy, shock-front reflectivity, and shock-front temperature along each Hugoniot (Fig. 128.26). The results from those studies showed no evidence of phase separation over the full range of densities and temperatures that were explored, and it turns out that this is consistent with the recent predictions. Recent calculations suggested, however, that phase-separating states in the 80%:20% mixtures could be accessed experimentally under the pressure and temperature conditions that are achieved on OMEGA. Preliminary evaluation of the results from these latest campaigns may provide the first experimental evidence of phase separation in hot, pressurized H_2/He mixtures. Relative to the 50%:50% mixture case, the 80%:20% samples precompressed to near 40 kbar and shocked to the 100- to 200-GPa range showed a clear reduction of the shock temperatures. Such a temperature reduction is expected to arise as a consequence of the entropy of mixing in these samples: the phase separation (demixing) is expected to lead to a reduction in specific entropy and a corresponding reduction in shock temperatures. A third full-day campaign to extend and confirm these results was planned for August 2011 but had to be postponed into FY12 because of equipment problems. In addition to the mixture experiments, we performed two shots with targets filled with H_2 and constructed with LiF anvils. A multipulse drive was used to test a multishock compression scheme for achieving cool, high-density states in the samples. The results from these experiments look promising but are too preliminary to reach conclusions about the technique. Further experiments with the multishock technique are planned for the future campaigns.

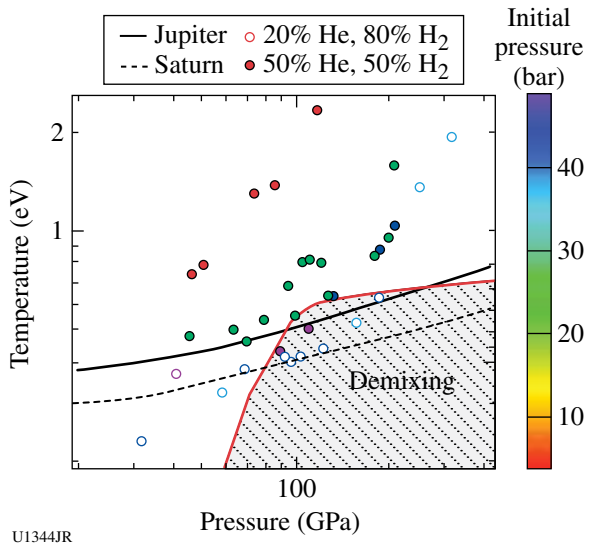

Figure 128.26
Phase diagram of precompressed shock states achieved on OMEGA for 50% H_2:50% He mixtures (filled circles) and 80% H_2:20% He (open circles). Symbol colors are associated with the sample initial pressure indicated by the color bar at left. The predicted demixing region for the 80% H_2:20% He mixture is shown by the shaded zone with a red boundary. Black curves indicate the planetary isentropes for Jupiter (solid) and Saturn (dashed). The Hugoniot temperatures for the 80% H_2:20% He case are reduced compared to the 50% H_2:50% He mixture at similar pressures, suggesting that the 80% H_2:20% He mixture may be undergoing phase separation under these conditions.

Investigation of Hydrodynamic Stability and Shock Dynamics in OMEGA Direct-Drive Implosions Using Spectrally Resolved Imaging

Principal Investigator: R. C. Mancini
(University of Nevada, Reno)
Co-investigators: R. Tommasini (LLNL);
and S. P. Regan, B. Yaakobi, V. Yu. Glebov,
W. Theobald, and J. A. Delettrez (LLE)

Arrays of spectrally resolved images recorded with the multimonochromatic x-ray imager (MMI) instrument open up new opportunities for observation and diagnosis of high-energy-density plasmas with an unprecedented level of detail. The MMI instrument records the spectrally, spatially, and time-resolved x-ray signal from a tracer element added to the plasma by combining pinhole-array imaging with the dispersion of a Bragg multilayer mirror, and the time-resolution provided by a framing camera detector. In this project, we apply spectrally resolved imaging to investigate the hydrodynamic stability and shock dynamics of low-adiabat direct-drive implosions on OMEGA. In low-adiabat implosions, a nearly isentropic compression is launched by a shaped laser pulse drive that starts from a low intensity, gradually leading to a high intensity. By minimizing preheat, higher compressions are achieved in low-adiabat implosions compared to high-adiabat implosions, therefore making fundamental studies on the stability of low-adiabat implosions relevant to high-energy-density plasma hydrodynamics and inertial confinement fusion. Furthermore, benchmarking and testing of hydrodynamic codes with data from well-characterized low-adiabat implosions are important since these codes are also used to model and design low-adiabat cryogenic implosions and advanced ignition concepts.

Figure 128.27 shows an array of about 100 gated, spectrally resolved images of the implosion core recorded with an MMI instrument in OMEGA shot 60933. This experiment was driven by a low-adiabat ($\alpha \sim 2$) laser pulse with approximately 21 kJ of UV laser energy on target. The target was a plastic shell of 27-μm wall thickness, filled with 20 atm of deuterium. It also had a 0.5-μm-thick plastic tracer layer doped with Ti at the 6% (atomic) level placed on the inner surface of the plastic shell.

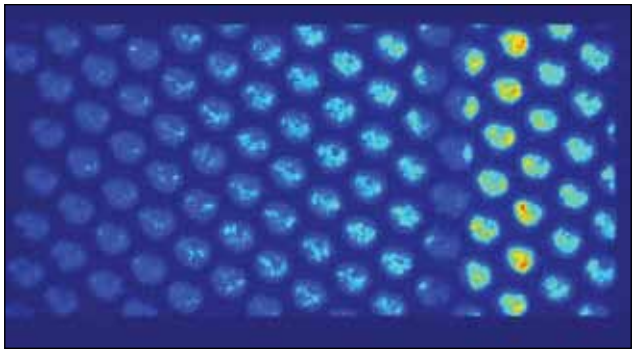

U1423JR

Figure128.27
An array of gated, spectrally resolved images recorded in OMEGA shot 60933. The horizontal axis is a photon-energy axis spanning the spectral range from 3500 eV to 5000 eV. Therefore, each image is characteristic of a slightly different photon-energy range.

The MMI instrument recorded the x-ray signal of this spectroscopic tracer. We note that while the vertical and horizontal axes of the image data in Fig. 128.27 are spatial-resolution axes, the horizontal axis is also a spectral-resolution axis. Therefore, each one of the images shown in Fig. 128.27 is characteristic of a slightly different photon-energy range.[3] The bright features observed in the image data correspond to the titanium He_α and Ly_α line emissions at 4750 eV and 4979 eV, respectively. The low-intensity or dark features observed to the left (i.e., low-energy side) of these features are due to absorption in n = 1 to 2 line transitions in L-shell titanium ions.

Processing the array of spectrally resolved images yields broad- and narrowband images as well as spatially integrated and spatially resolved line spectra. In particular, the latter provides critical information for a quantitative analysis of the spatial structure and details of the implosion core plasma.[3] In this connection, Fig. 128.28 illustrates an image mask employed to extract a spatially resolved spectrum from the data shown in Fig. 128.27. A broadband image defines the shape and spatial extension of the projection of the implosion core on the image plane, and a region within it defines the domain of integration that characterizes the spatially resolved spectrum (see Fig. 128.28). In object space, this domain corresponds to the volume defined by the intersection of the implosion core with a cylindrical shell of cross section given by the region within the image. By applying this mask to the spectrally resolved images in Fig. 128.27, an array of spectrally resolved image regions can be obtained; this array is displayed in Fig. 128.29. Finally, by integrating one photon energy at a time, the intensity distribution of the spatially resolved spectrum can be obtained; this result is displayed in Fig. 128.30.

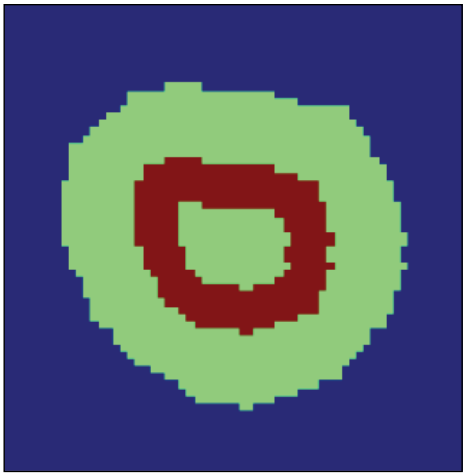

U1350JR

Figure 128.28
Illustration of an image mask employed to extract a spatially resolved spectrum. The green area represents a broadband image obtained from the data shown in Fig. 128.27; the red area is the domain of integration associated with the spatially resolved spectrum.

U1351JR

Figure 128.29
An array of spectrally resolved image regions based on the data of Fig. 128.27 and the mask displayed in Fig. 128.28.

The spatially resolved spectrum shown in Fig. 128.30 displays simultaneously line emission and absorption over a range of titanium ions from F- to H-like charge states. This suggests that the titanium tracer, initially located only on the inner surface of the shell, has spread in space and can later be found in low-temperature as well as high-temperature regions of the implosion core; i.e., close to the periphery as well as the central regions of the core. Quantitative analysis of narrowband images and spatially resolved spectra at the collapse of the implosion using a detailed atomic and radiation physics model for titanium yields information about the distribution of tracer and mixing in the implosion core, which, in turn, depend on the hydrodynamic stability of the implosion. Alternatively, measurements at earlier times permit one to investigate the tracer's state and spatial distribution at the time when the shock breaks into the core.

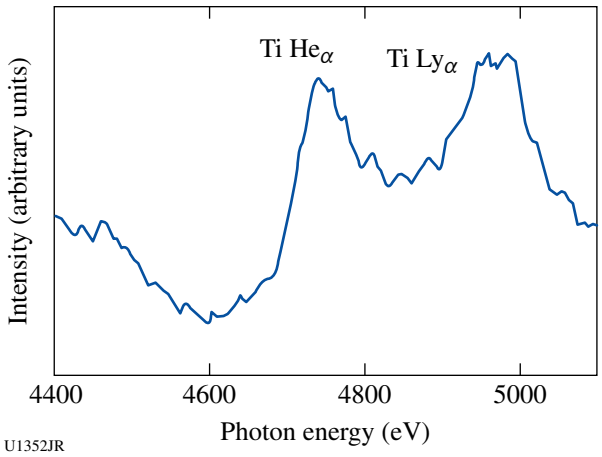

Figure 128.30
Spatially resolved spectrum based on the mask displayed in Fig. 128.28 and the array of image regions shown in Fig. 128.29. The titanium He$_\alpha$ and Ly$_\alpha$ line emissions correspond to the bright features observed in the data displayed in Fig. 128.27. The low-intensity darker features to the left of these bright features in Fig. 128.27 correspond to the absorption part of the spectrum.

Proton Radiography of Direct- and Indirect-Drive ICF and HEDP Plasmas and the First Basic Nuclear Physics Measurements in an ICF Plasma

Principal Investigators: R. D. Petrasso and C. K. Li (Massachusetts Institute of Technology)
Co-investigators: F. H. Séguin and J. A. Frenje (MIT); T. C. Sangster, V. Yu. Glebov, and D. D. Meyerhofer (LLE); and D. P. McNabb (LLNL)

MIT's NLUF work in FY11 included a wide range of experiments applying MIT-developed proton radiography methods to the study of high-energy-density physics (HEDP) and inertial confinement fusion (ICF) plasmas; it also included a completely new and groundbreaking class of experiments utilizing MIT- and LLE-developed spectrometry methods to study basic nuclear physics at an ICF facility. Our NLUF experiments also provided unique research opportunities in HEDP for eight MIT graduate students, who will use resultant data in major parts of their theses, and for several undergraduates.

During the present and previous NLUF programs, we have used the MIT-developed method of monoenergetic, charged-particle radiography[4] in new types of studies of electromagnetic fields and plasmas in HEDP and in ICF physics. These projects, undertaken at the Omega Laser Facility,[5,6] were performed because of their importance to the future of ICF, HEDP, and the physics of fields generated by laser–plasma interactions. Topics studied include the imaging, identification, and measurement of electric and magnetic fields in laser-generated plasmas; reconnection of MG magnetic fields in high-β plasmas; self-generated electromagnetic fields in ICF implosions; the dynamics of ICF capsule implosions; electromagnetic fields in laser-driven hohlraums; and the development of a proton backlighter using short-pulse beams from OMEGA EP. The work has already resulted in nine publications in Science[7,8] and Physical Review Letters,[9–15] in addition to many other papers, invited talks, and contributed talks at conferences, including three papers submitted this year.[16–18] The work has successfully addressed basic physics issues and issues directly relevant to the future success of ignition experiments at the NIF.

As described in Ref. 19 and illustrated in Figs. 128.31 and 128.32, we performed the first basic nuclear physics experiment in the context of an ICF facility, measuring the differential cross section for elastic neutron–triton (n–^{3}H) and neutron–deuteron (n–^{2}H) scattering at 14.1 MeV on OMEGA using the MIT-developed, magnet-based charged-particle spectrometer CPS-2 (Ref. 20). In these experiments, which were carried out by simultaneously measuring elastically scattered ^{3}H and ^{2}H ions from a DT (deuterium–tritium)-gas–filled inertial confinement fusion capsule implosion, the differential cross section for the elastic n–^{3}H scattering was obtained with significantly higher

Figure 128.31
The CPS-2 charged-particle spectrometer during installation on the OMEGA target chamber. The cone-shaped end contains the entry aperture, while the cylindrical section contains a 7.6-kG magnet and CR-39 nuclear track detectors. In the experiment described here, CPS-2 was used to simultaneously measure energy spectra of deuterons and tritons elastically scattered by 14.1-MeV neutrons, and protons from d–d reactions in a DT (deuterium–tritium)-gas–filled thin-glass capsule implosion.

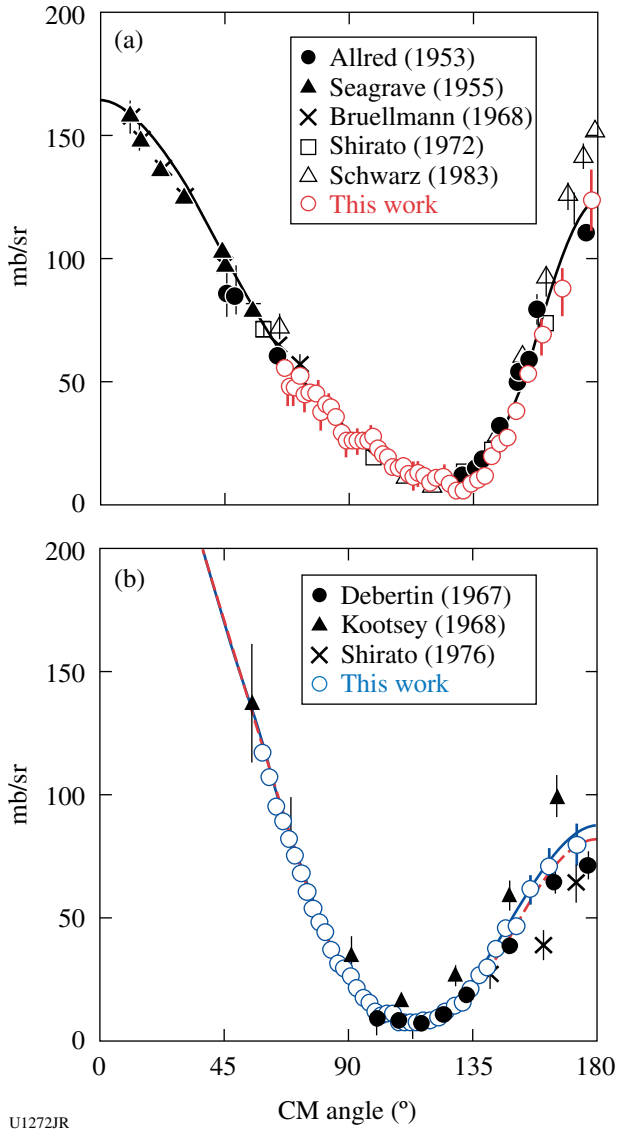

Figure 128.32
(From Ref. 19) (a) Measured differential cross section for the elastic n-^{2}H scattering, which has been normalized to a Faddeev calculation. (b) Measured and calculated differential cross section for the elastic n-^{3}H scattering. The experimental data have been normalized with the deuterium–tritium fuel-ratio–modified normalization factor derived in (a). The blue solid curve represents an *ab initio* NCSM/RGM calculation and the red dashed curve represents an *R*-matrix calculated n-^{3}H cross section.

accuracy than achieved in previous accelerator experiments. The results compare well with calculations that combine the resonating group method with an *ab initio* no-core shell model, which demonstrate that recent advances in *ab initio* theory can provide an accurate description of light-ion reactions. This work is ushering in a new and exciting field of research—Plasma Nuclear Science—blending the separate disciplines of plasma and nuclear physics.

Collisionless Shocks in Laboratory High-Energy-Density Plasmas

Principal Investigator: A. Spitkovsky (Princeton)
Co-investigators: L. Gargaté (Princeton); H.-S. Park, B. A. Remington, S. M. Pollaine, and D. Ryutov (LLNL); J. P. Knauer, G. Fiksel, and R. Betti (LLE); K. Sakawa, T. Ide, T. Kato, Y. Kurimatsu, T. Morita, and H. Takabe (Osaka University); G. Gregori and T. Bell (Oxford); F. Miniati (ETH Sci-Tech University); M. Koenig and A. Ravasio (Ecole Polytechnique); and E. Liang (Rice University)

This NLUF program studies the creation of collisionless shocks in counter-propagating laser-produced plasmas. Collisionless shocks are of great importance in astrophysical and space plasmas and occur when the mean free path to Coulomb collisions is large compared to the size of the shock transition.[21–30] The shock is then mediated by the collective plasma effects from the interaction between plasma particles and the self-generated electromagnetic fields. Collisionless plasma conditions can now be created on the OMEGA and OMEGA EP lasers, where the laser-driven plasmas propagate at speeds of ~1000 km/s and densities of ~10^{18} to 10^{19} cm^{-3}. The experiments in this program collide two streams of high-speed plasma and study the formation of shocks as a function of an externally applied magnetic field that is generated by a set of Helmholtz coils at the interaction region. The theoretical expectation is that at low external fields, the shock is mediated by the filamentation (Weibel) instability, while at higher fields, magnetic reflection of ions will form the shock. These regimes are representative of the conditions encountered in a range of astrophysical environments, including supernova remnant shocks and solar wind shocks. These experiments on OMEGA and OMEGA EP test these shock-formation mechanisms and address the open questions of astrophysical collisionless shock physics, such as the presence of particle acceleration and the mechanisms of magnetic-field amplification in shocks.

In FY11 we completed an extensive set of particle-in-cell and radiation–hydrodynamics simulations to converge on the design of the experiment. We determined the minimal interaction length necessary to achieve filamentation-mediated shocks and predicted the field strengths needed to transition the shock into the magnetized regime. In close collaboration with LLE (G. Fiksel's group), a set of Helmholtz coils capable of generating 1-T magnetic fields was designed and fabricated. Also, proton radiography and Thomson-scattering diagnostics were fielded and tested in related experiments by Principal Investigator H.-S. Park (AstroPlasmas-11A, EPColPlasmas-11B, ColPlasmas-11C, EPColPlasmas-11D). These efforts

culminated in a joint-shot day on 3 August. In this experiment, we used OMEGA to initiate two ablated plasma flows from CH foils. The OMEGA EP laser was used to provide a short pulse for proton radiography of the interaction region. Helmholtz coils were triggered to provide an external magnetic field in the experiment. Thomson scattering was used to monitor plasma conditions (see Fig. 128.33). This was one of the most-complicated experimental setups at LLE, and we are extremely pleased that the experiment worked without major problems and thankful to the facility for the extensive preparatory work required of the staff. We performed eight shots, with four OMEGA-only shots and four joint shots. On the experimental side we learned that the basic experimental setup is sound, and both the magneto-inertial fusion energy delivery system (MIFEDS) and Thomson-scattering diagnostics can survive the electromagnetic pulse (EMP) monitor from the short-pulse laser. On the science side, we studied the difference in the radiography signal between one and two beams and obtained the first evidence for filamentation in the crossing beams (Fig. 128.34). These proton radiography data demonstrate the development of magnetic fields expected from the Weibel instability, suggesting that the collisionless shock mediation mechanism is possible even in the weak magnetic fields. The experiment also produced data with MIFEDS fields, and the differences in the Thomson-scattering data and radiography are currently being analyzed. We developed a suite of post-processing diagnostics for the particle-in-cell (PIC) simulation code that allows us to calculate Thomson and radiography signals based on the full distribution function from the simulations. Preliminary analysis of the data and PIC simulations indicates that the next experiment in this program in FY12 will require stronger magnetic fields. The design work on increasing the MIFEDS fields is currently underway.

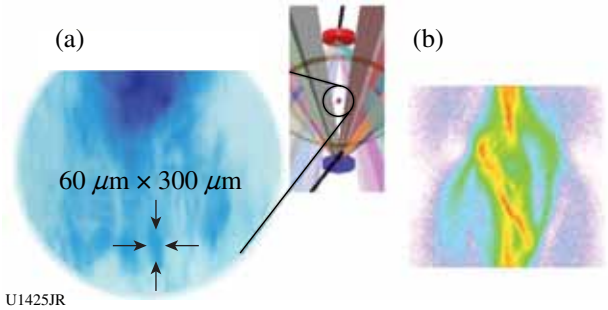

Figure 128.34
(a) Thomson parabola (TPIE) data showing high-energy protons up to nearly 70 MeV from OMEGA EP using 1 ps and ~400 J of laser energy; color indicates ion density, highest (red) to lowest (blue). (b) TPIE data showing carbon species up to 30 MeV in energy using 10 ps and 1000 J of laser energy; color scale indicates density (in arbitrary units), highest (dark blue) to lowest (white).

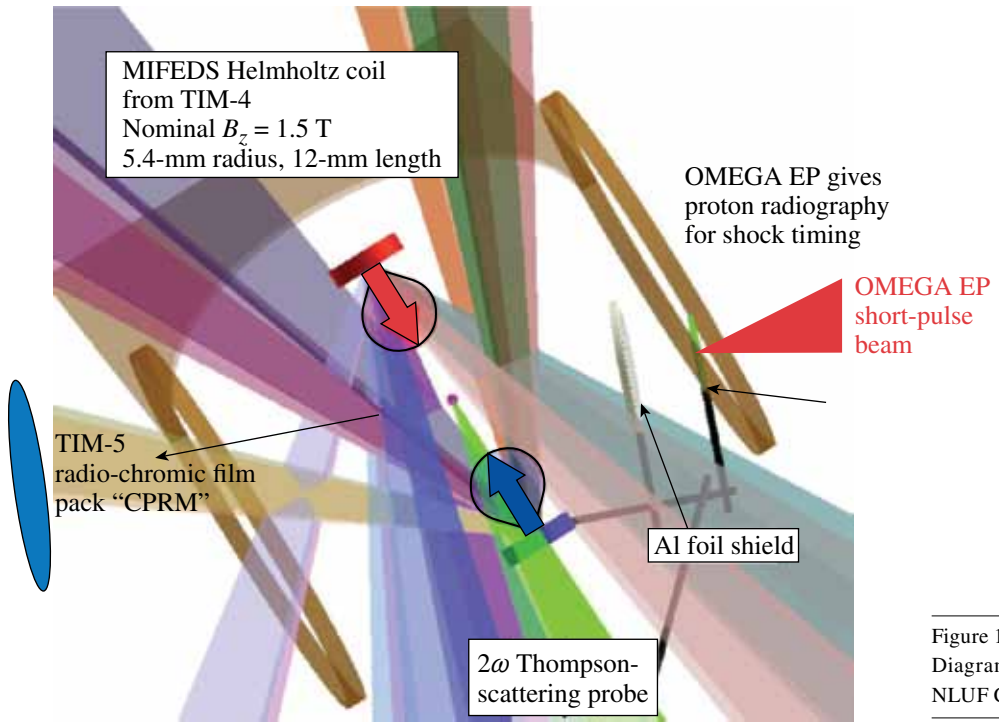

Figure 128.33
Diagram of the experimental setup for NLUF ClessShk-11A.

Dependence of Laser-Energy Coupling on Target Material and Laser Pulse Length

Principal Investigators: M. S. Wei and R. B. Stephens (General Atomics)

Co-investigators: F. N. Beg and H. Sawada (UCSD); C. D. Chen, H. McLean, and P. K. Patel (LLNL); and W. Theobald and C. Stoeckl (LLE)

Lead graduate student: A. Sorokovikova (UCSD)

Efficient conversion of laser energy to hot electrons and their subsequent energy transport to the compressed fuel are extremely important for the success of fast ignition to reduce the energy required for ignition. Energy coupling is controlled by the nature of the plasma (i.e., density profile, ionization, etc.) at the laser–plasma interface and the dynamic response of the transport material, which evolve with time, and therefore are dependent on the laser pulse length. Previous experiments[31] performed on the Titan laser (0.7-ps pulse length, 150 J) at LLNL showed that 10-μm, high-Z material in the multilayer planar solid target suppresses fast-electron angular spread and reduces the forward-going fast-electron flux. The goal of the General Atomics NLUF project is to further investigate target material effects on fast-electron transport and extend such a study to 10-ps time scale at high intensity using the OMEGA EP laser. The project consists of two steps: (1) characterization of fast-electron generation and transport through different transport materials at 1 ps with 300-J energy to compare with the Titan experiments; and (2) extend such a study to 10 ps with 1.5-kJ energy. In FY11, we performed experiments on OMEGA EP using the high-intensity, short-pulse backlighter beam (BL2) with the multilayer planar-foil targets.

Figure 128.35 shows the schematics of the target and experimental setup at the Omega Laser Facility. High-intensity, short-pulse OMEGA EP backlighter beams (300 J at 1 ps or 1500 J at 10 ps) were tightly focused onto the front surface of the multilayer planar-foil target with approximately 80% of laser energy in a 50- to 60-μm focal spot. The mm-square–sized multilayer target consists of a front-surface Al layer (4 μm) over a thin transport layer (~10 μm) of various Z materials (Au, Mo, and Al), an Al spacer (75 μm), and a Cu tracer layer (12 μm) followed by a 20-μm-thick Al layer. The multilayer target had a 1-mm-thick, 5 × 5-mm^2-wide conductive CH back layer to minimize electron refluxing. Fast electrons were characterized by two primary diagnostics: a spherical crystal imager (SCI) to measure the spatial distribution of fast-electron–induced 8-keV fluorescence radiation in the Cu trace layer and a zinc Von Hamos (ZVH) x-ray spectrometer tuned to measure the absolute Cu K_α yield. The Cu K_α emission is proportional to the fast-electron flux in this single-pass target.

(a)

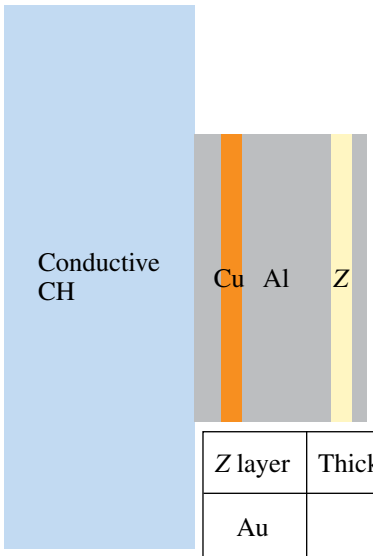

Z layer	Thickness (μm)
Au	10
Mo	14
Al	25

(b)

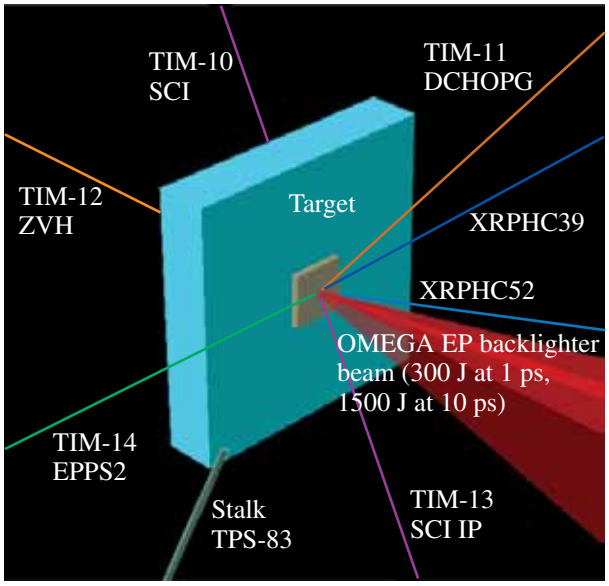

U1355JR

Figure 128.35
Schematic of the (a) multilayer planar-foil target and (b) experimental setup.

In the 1-ps OMEGA EP laser–interaction experiment, we observed a smaller Cu K_α fluorescence spot with the high-Z Au

transport target compared to the Al transport target with good reproducibility. As shown in Fig. 128.36, the measured Cu K_α spot for the Au case is $R_{50} \sim 70$ μm in radius (R_{50} is the radius of the spot counting all the pixels with a signal greater than or equal to the peak value) and 93 μm for the Al target case, which is consistent with the previous Titan results. Collisional particle-in-cell (PIC) modeling, including dynamic ionization and radiation cooling, suggests that strong resistive magnetic fields inside the high-Z transport target collimate fast electrons and reduce the forward-going fast-electron angular spread.[32]

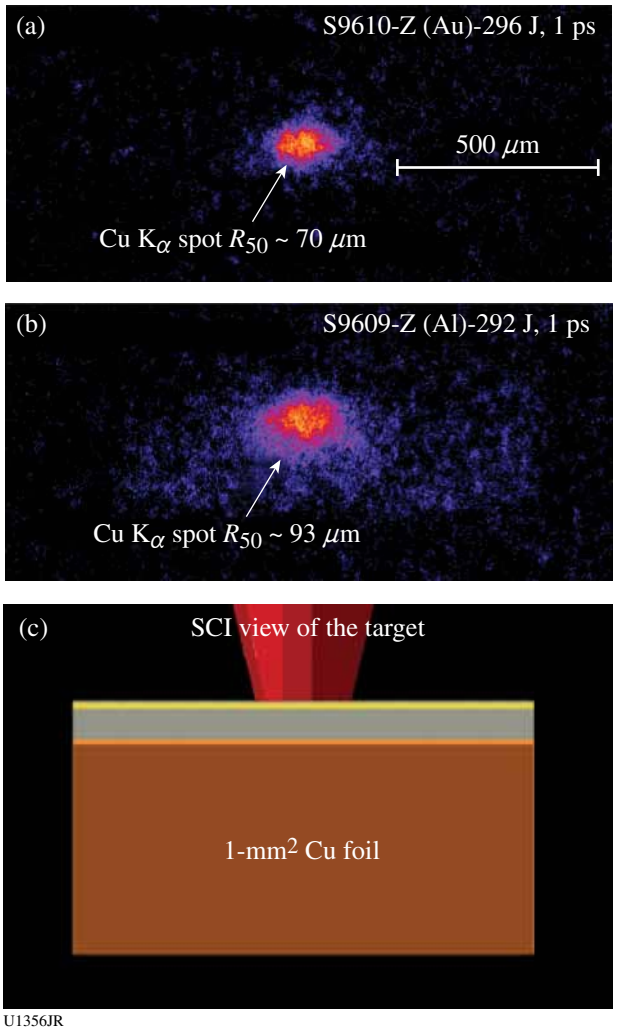

U1356JR

Figure 128.36
SCI recorded Cu K_α radiation spots in a 1-ps interaction experiment: (a) with a Z = Al transport target; (b) with a Z = Au transport target; and (c) SCI diagnostic view of the target. Images (a) and (b) have the same color and spatial scales. A smaller K_α spot is observed in Z = Au transport targets.

Experiments with a 10-ps, 1500-J OMEGA EP pulse showed a large shot-to-shot variation however. The behavior of laser-produced fast electrons and their transport as evidenced in the observed K_α spots was very different compared to the experiments with 1 ps as shown above. Figure 128.37 shows the SCI-recorded Cu K_α images with 9- to 10-ps pulses from three different types of Z-transport targets. It is evident in this case that there are pronounced filamentary structures [Figs. 128.37(a) and 128.37(b)] and irregular shapes [as shown in Fig. 128.37(d)] in the fluorescence spot. With identical Al

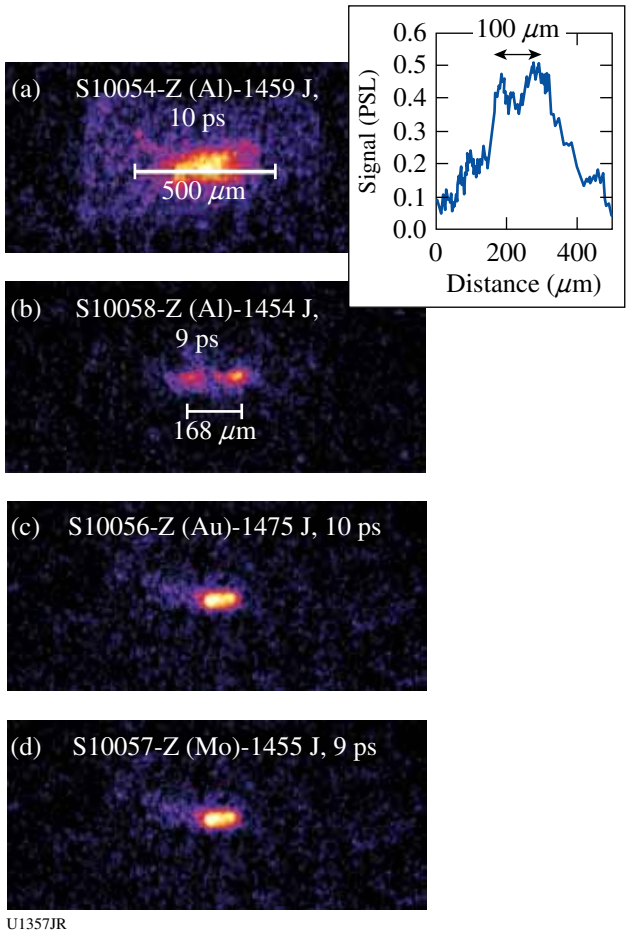

U1357JR

Figure 128.37
SCI-recorded Cu K_α radiation spots in a 10-ps interaction experiment: (a) and (b) with Z = Al transport target [lineout of (a) is shown in the inset]; (c) with Z = Au transport target and (d) with Z = Mo transport target. Images have the same color and spatial scales. Filamentary structures and irregular shapes of fast-electron beams can be clearly seen with a large shot-to-shot variation.

targets, two to three filaments were observed with a separation distance of ~100 μm, which suggests the growth of widely separated stable filaments after a few picoseconds, either in the laser–plasma interaction region or inside the solid target. PIC modeling is underway to study high-intensity laser–plasma interaction (LPI) and fast-electron transport in a 10-ps time scale. Further experimental investigation with similar targets to compare 1-ps versus 10-ps LPI and fast-electron transport will be performed in the coming year with additional hard x-ray spectrometers, together with SCI and ZVH, to fully characterize the fast-electron source and transport phenomena.

Low-Density Plasma Interactions

Principal Investigators: L. Willingale, C. Zulick, A. Maksimchuk, and K. Krushelnick (University of Michigan); P. M. Nilson, R. S. Craxton, C. Stoeckl, and T. C. Sangster (LLE); H. Chen (LLNL); J. Cobble (LANL); and P. A. Norreys and R. Scott (RAL)

The interaction of a high-power, short-duration laser pulse with underdense plasma has been investigated to study laser propagation, channel formation, filamentation, and particle acceleration. To generate an underdense CH target, a long-pulse beam (2.5 ns, ~1200 J in an 800-μm-diam focal spot) is used to create a plasma plume from a foil target. The main interaction beam is then focused into the plasma plume, with the laser propagating parallel to the target surface so that it sees an approximately Gaussian density profile (2-D *SAGE* modeling estimates a width of 650 μm with a peak density of around either 5×10^{19} W/cm^2 or 1.5×10^{20} W/cm^2 depending on the height above the target surface). The channel electromagnetic fields have been imaged simultaneously using a proton probe generated by the second short-pulse beam, which can observe laser filamentation, channel self-correction, and channel-wall instabilities.[33] In addition to the channel imaging, particle spectra are measured with magnetic spectrometers.

The laser pulse length, laser energy, and plasma density are varied to investigate the effect of each parameter. Figure 128.38 shows the electron spectra measured in the direction of laser propagation for different laser pulse lengths, with the labels indicating the laser pulse length, laser power, and peak plasma density. For comparison, the spectra from a 9 ps with 30 TW shot onto a solid 50-μm-thick copper target are shown. Large numbers of electrons are accelerated to high energy during the underdense interaction, many more and to a higher energy than for a solid target. Shot-to-shot variation for similar parameters

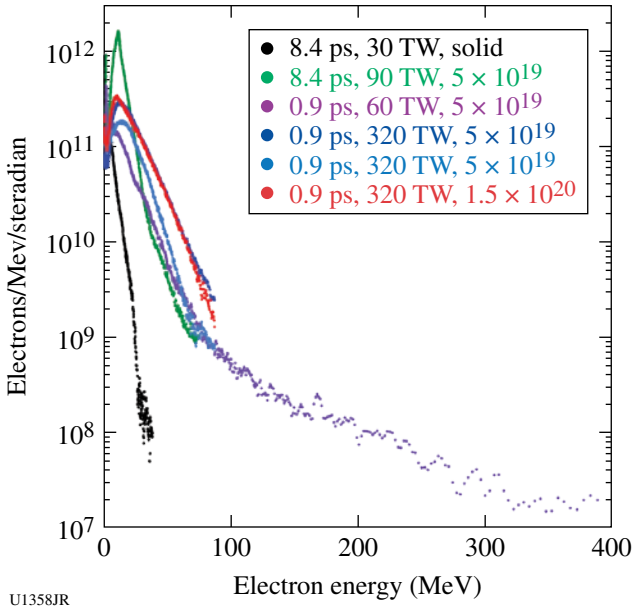

Figure 128.38
Electron spectra for various pulse lengths, powers, and peak plasma densities (labels indicate laser pulse length, laser power, and target density).

may be due to the laser filamentation causing a number of channels within which electrons could be accelerated. The possible acceleration mechanisms are currently under investigation using PIC simulations.

FY11 Laboratory Basic Science Programs

In early 2011, LLE issued a solicitation for LBS proposals to be conducted in FY12. A total of 41 proposals requesting a total of 87.5 shot days of Omega Facility shot time were submitted. An independent review committee comprised of Prof. Farhat Beg (University of California, San Diego), Dr. Robert Heeter (LLNL), Prof. Karl Krushelnick (University of Michigan), Dr. Carolyn Kuranz (University of Michigan), Dr. Paul Keiter (LANL), Prof. Roberto Mancini (University of Nevada, Reno), Dr. Rick Olson (SNL), Prof. Charlie Freeman (State University of New York–Geneseo), Dr. Frederick Marshall (LLE), and Dr. John Soures (Committee Chair, non-voting) reviewed the proposals and recommended that 15 proposals receive 28 shot days at the Omega Laser Facility in FY12. Table 128.VIII lists the successful LBS proposals.

Fifteen LBS projects were allotted Omega Facility shot time and conducted a total of 303 target shots at the facility in FY11. The FY11 LBS research is summarized in this section.

Table 128.VIII: Approved FY12 LBS proposals.

Principal Investigator	Affiliation	Project Title
P. M. Celliers	LLNL	Measurement of the Viscosity of Shock-Compressed Fluids: Studies of Water and Silica
H. Chen	LLNL	Exploring Pair Plasma and Its Applications Using OMEGA EP and OMEGA Lasers
G. Fiksel	LLE	Magnetic Field Compression in Spherical Implosions on OMEGA
G. Fiksel	LLE	Magnetic Reconnection in High Energy Density Plasmas in the Presence of an External Magnetic Field
O. A. Hurricane	LLNL	Measurements of Linear, Nonlinear, and Turbulent-Mixing Regimes in Kelvin–Helmholtz Instability in the Subsonic Regime
A. L. Kritcher	LLNL	Nuclear-Atomic-Plasma Interactions in Laser-Produced Plasmas
B. R. Maddox	LLNL	Dislocations and Twinning at High Pressure and Strain Rate on BCC Metals
D. P. McNabb	LLNL	Thermonuclear Reactions in Stellar Plasmas and High Resolution Measurements of Three-Body Breakup in Isobaric Analogue Reactions
H.-S. Park	LLNL	Astrophysical Collisionless Shock Generation by Laser-Driven Laboratory Experiments on OMEGA and OMEGA EP
P. K. Patel	LLNL	Compton Radiography of Cone-in-Shell Implosions for Fast Ignition
S. P. Regan	LLE	Probing Shocked Liquid H, H/He, CH_4, N_2, and NH_3 with Inelastic X-Ray Scattering and Shock Velocity Measurements: Toward the Equation-of-State of Planetary Interiors
J. R. Rygg	LLNL	Extreme Chemistry: Molecular Fluids at Mbar Pressure
V. A. Smalyuk	LLNL	Measurements of Ablative Richtmeyer–Meshkov Instability in Nonlinear Regime
C. Stoeckl	LLE	Spectroscopy of Neutrons Generated Through Nuclear Reactions with Light Ions in Short-Pulse Laser Interaction Experiments
W. Theobald	LLE	Integrated Fast-Ignition Experiments

Exploring Pair Plasma and Its Applications Using OMEGA EP

Principal Investigator: H. Chen (LLNL)
Co-investigators: L. Willingale (University of Michigan); C. Stoeckl, D. D. Meyerhofer, J. F. Myatt, and P. M. Nilson (LLE); J. Park and R. Tommasini (LLNL); W. Wilks, L. Divol, and P. Michel (LLNL); and J. Seeley (NRL)

In FY11, an LLNL/LLE/NRL team performed a Laboratory Basic Science experiment on the OMEGA EP Laser System to study positron production during high-intensity laser interactions with high-Z targets. This experiment was a follow-up to those of April 2009 and August 2010. In the previous experiments, a record number of positrons was produced using the 1-kJ, 10-ps OMEGA EP backlighter interacting with a 1-mm-thick Au target.[34] It was deduced that a non-neutral pair plasma was made in those shots.[35] In FY11, thanks to the facility improvements, the laser energy was extended to 1400 J for the backlighter beam. The FY11 experiments had two main objectives: to measure the energy scaling of the positron generation and to measure angular divergence of the electron–positron jets. The preliminary results are shown in Figs. 128.39 and 128.40

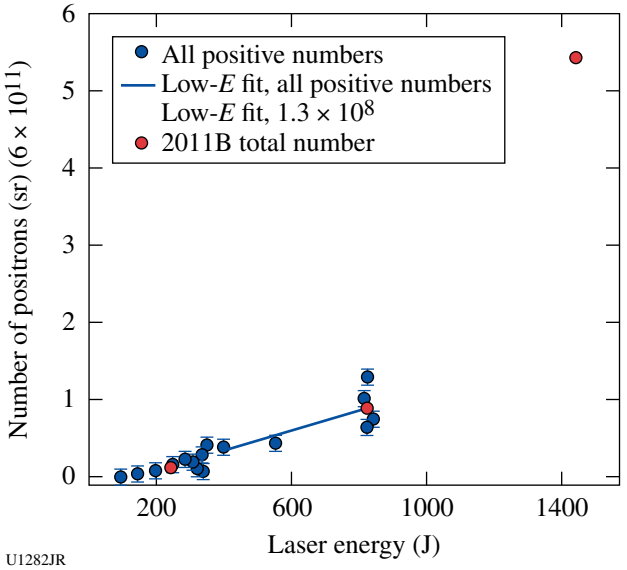

Figure 128.39
Positron number as a function of laser energy. Red dots are from FY11 OMEGA EP experiments. Blue dots are all previous data.

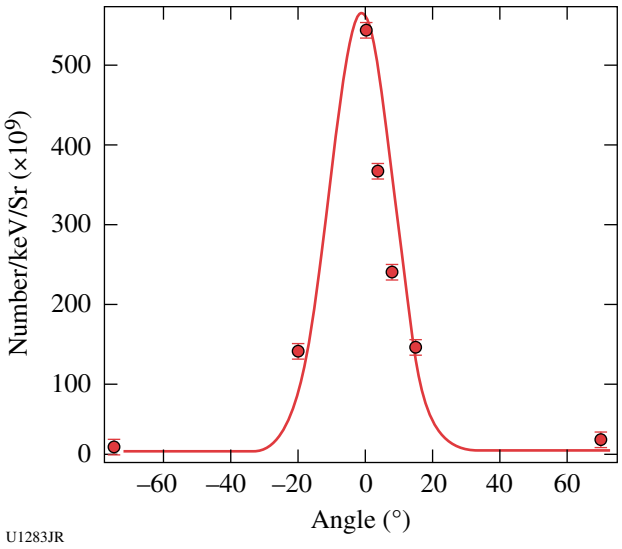

Figure 128.40
Angular divergence of the positron jet measured from FY11 OMEGA EP experiments. (The red dots are measured points and the solid line is a fit to the data.)

for the energy scaling and angular divergence, respectively. A faster increase in positron number was observed once the laser energy exceeded 1 kJ. The electron–positron jet has a very narrow angular divergence of about 6° to 7°. On these shots, the gamma-crystal spectrometer (with an energy coverage between 40 to 700 keV) that was modified to reduce the background radiation was further tested. Annihilation of electron–positron radiation was not observed, perhaps because of low efficiency of the crystal as well as the detector.

Positron research has extended over diverse fields from particle physics and astrophysics to medical applications. This often requires the production of large numbers of positrons on a short time scale, which has been difficult to supply. The new OMEGA EP results could alter the direction of the quest of establishing a laser-produced positron source for research in these fields.

Fusion-Yield Enhancement in Magnetized Laser-Driven Implosions

Principal Investigator: G. Fiksel (LLE)
Co-investigators: M. Hohenberger, J. P. Knauer, and P.-Y. Chang (LLE); K. S. Anderson, R. Betti, and J. R. Davies (FSC/LLE); and F. H. Séguin (MIT/PSFC)

Exploring the magnetization of inertial confinement fusion (ICF) targets is beneficial for both fusion and astrophysical high-energy-density (HED) applications. Magnetization of an ICF hot spot suppresses the electron heat conduction perpendicular to the magnetic field, which increases the plasma temperature, decreases the compression velocity required for ignition, and increases the fusion gain.[36] Because of a high plasma density at the center of a typical ICF target, a magnetic field of the order of tens of megagauss is required to magnetize the electrons. Such large fields can be produced only by compression of an existing seed field.

LLE has been pursuing laser-driven compression as a novel method for reaching super-high magnetic field strengths. Using an LLE-built seed magnetic field generator (MIFEDS),[37] the generation of high magnetic fields (up to 40 MG) and subsequent fusion enhancement in magnetized spherical implosions have been demonstrated. The MIFEDS device is shown in Fig. 128.41. The device's vacuum enclosure contains a high-voltage charging power supply, capacitors, a spark-gap switch, and control circuits. The device stores up to 150 J and delivers a short high-voltage pulse of <10-ns duration to a coil via a transmission line.

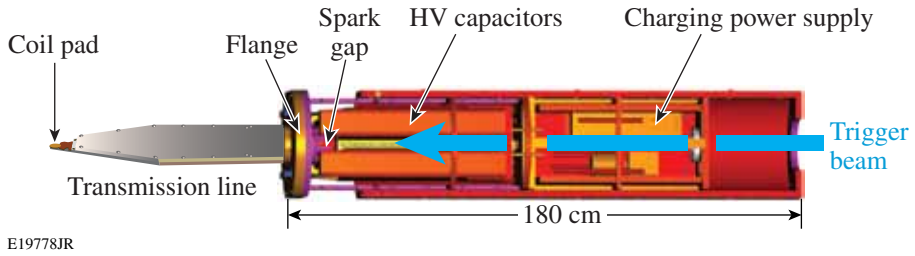

Figure 128.41
A schematic view of MIFEDS. The device's vacuum enclosure contains a high-voltage charging power supply, capacitors, a laser-triggered spark-gap switch, and control circuits. The transmission line is attached via a vacuum feedthrough flange. Tens-of-kilogauss magnetic fields can be generated by discharging MIFEDS through a coil attached to the coil pad at the end of the transmission line.

The applied magnetic field's effect on the fusion yield was studied for implosions in spherical geometry.[38] In these experiments, spherical CH targets with a 430-μm radius were imploded using 40 beams of the OMEGA laser delivering a total of 18 kJ at an average intensity of ~7×10^{14} W/cm^2. The capsules were filled with room-temperature D_2 gas at pressures from 3 to 10 atm. Figure 128.42 demonstrates the fusion enhancement in magnetized targets. For shots where the magnetic seed field was applied, the neutron yield is enhanced by ~30% and the ion temperature by ~15%.

For astrophysical and HEDP applications, MIFEDS has already been used in studies of collisionless shock formation in colliding magnetized plasmas. Future plans include the use of a strong magnetic field to collimate a stream of energetic electrons in a fast-ignition experiment and to apply MIFEDS to astrophysical problems, such as magnetic reconnection in stellar media and momentum transport of incoming matter in accretion disks.

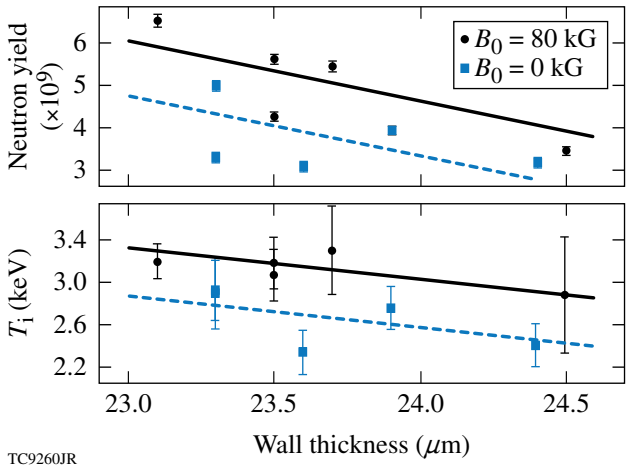

Figure 128.42
Experimental neutron yield and ion temperature plotted against target wall thickness. A clear enhancement of the magnetized implosions at $B_{seed} = 80$ kG (red) compared to the $B_{seed} = 0$ case (blue) is observed. The lines are fits to the data using multiple linear regression.

Short-Pulse Neutron Production on OMEGA EP

Principal Investigators: D. P. Higginson and J. M. McNaney (LLNL); J. Cobble (LANL); and J. A. Frenje (MIT/PSFC)

We have preformed the first-ever measurement of 1-kJ-class, short-pulse-laser–produced neutrons on OMEGA EP. In this experiment, protons and deuterons were accelerated into a LiF slab. These ions produced high-energy neutrons (>10 MeV) through the ^{7}Li(d,xn)^{8}Be reaction (Q = 15 MeV), as well as lower-energy neutrons (~2.5 MeV) through the ^{7}Li(p,n)^{7}Be reaction (Q = −1.6 MeV). Spectrally integrated yields of 3×10^9 n/sr were observed in the forward direction, which is a significant increase over previously observed yields of 8×10^8 n/sr observed on the Titan laser (Fig. 128.43). The yield of neutrons with energies above 10 MeV was 1×10^8 n/sr, which was diagnosed using Cu(n,2n) activation. This experiment also used neutron time-of-flight (nTOF) spectroscopy. The use of nTOF diagnostics is extremely challenging in the short-pulse laser–matter environment because of the high x-ray background created by the laser interaction. We were able to get a relatively clean signal, however, through a careful design of this diagnostic by LLE scientists (Fig. 128.44). In addition to the observation of spectrally and spatially resolved neutron measurements, we have also diagnosed the incident proton and deuteron beams. Knowledge of the incident ion beams means that we will be able to model the entire system in a well-constrained and consistent manner.

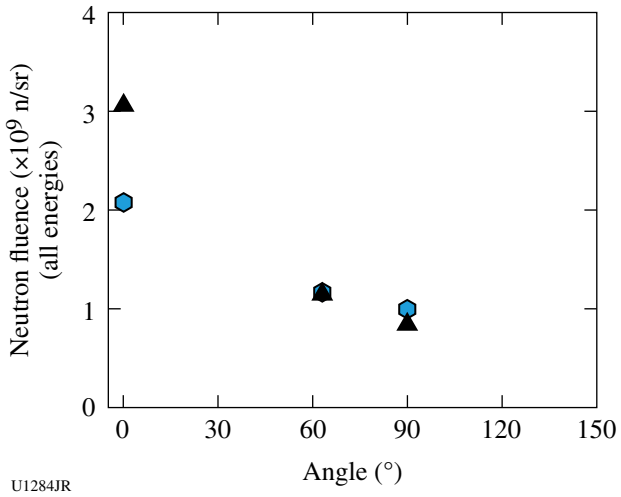

Figure 128.43
Angularly resolved neutron fluence, which is spectrally integrated, as measured with CR-39 detectors, from two different shots with the same nominal laser parameters.

Charged-Particle Stopping Power in Warm, Dense Plasmas

Principal Investigators: S. X. Hu (LLE) and C. K. Li (MIT)

Measuring the stopping power of charged particles in plasmas is of particular interests for ICF. Warm, dense plasmas (of a few-electron-volts temperature and denser than solid), which extensively exist in the universe, make up a new type of matter that can be created in laboratories, for example, by laser-driven shocks and magnetically driven flyer impacts. Such warm, dense matter can readily provide access to strongly coupled

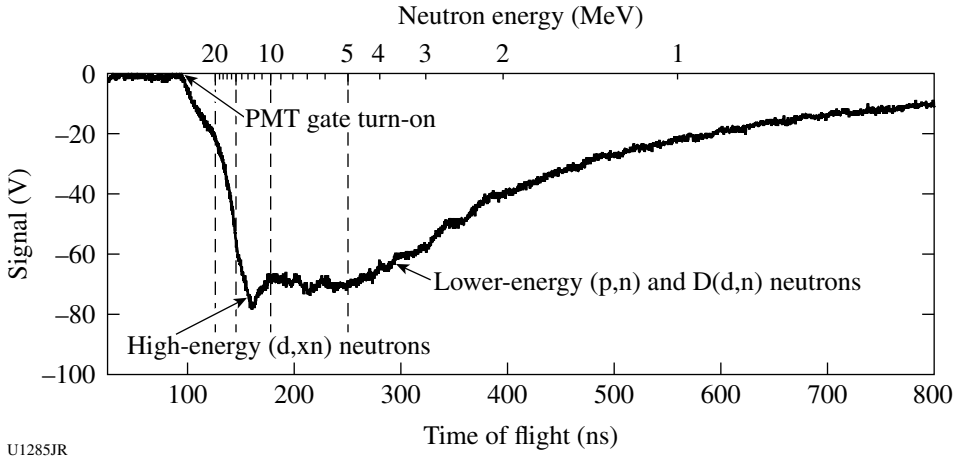

Figure 128.44
Scope traces from neutron time-of-flight spectrometers when shooting a CD_2 foil with ions incident onto a LiF slab. The signal begins with the photomultiplier tube around 100 ns. The first bump is from high-energy neutrons and the following signal is from ^{7}Li(p,n) and D(d,n) neutrons.

and degenerate plasma conditions. The stopping power in such nonideal warm, dense plasmas is still unknown in contrast to the well-studied classical plasma conditions. Investigations of charged-particle stopping power in warm, dense plasmas not only advance the basic understanding of properties of such exotic matter but also find important applications in ICF, e.g., alpha particles stopping in compressed DT shells is critical to initiate the "burn-wave" propagation for ignition. There have been many theoretical predictions in the past decades that have shown an observable reduction in stopping power caused by the coupling and quantum degeneracy effects. There have been no experiments so far, however, that verify such theoretical calculations.

In the LBS experiment carried out in May 2011, we built a platform to measure charged-particle stopping power in laser-shocked plastic (CH) plasmas at the Omega Laser Facility. Using 20 OMEGA beams to drive glass-shell capsules filled with D_2 gas (6 atm) and ^{3}He gas (12 atm), monoenergetic protons with kinetic energies of 14.7 MeV were generated. These protons slowed down passing through the laser-shocked CH plasmas, and their energy spectra were recorded using both a wedged-range-filter spectrometer and track diameter on a CR-39 imaging detector. The CH plasmas were created by eight OMEGA beams staggered in time with a total driving duration of ~4 ns. The plasma conditions were simultaneously characterized by a side-on x-ray radiograph with a V-backlighter, as shown in Fig. 128.45. The laser intensity on target varied from ~10^{14} W/cm^2 to ~5×10^{13} W/cm^2. The CH-foil targets

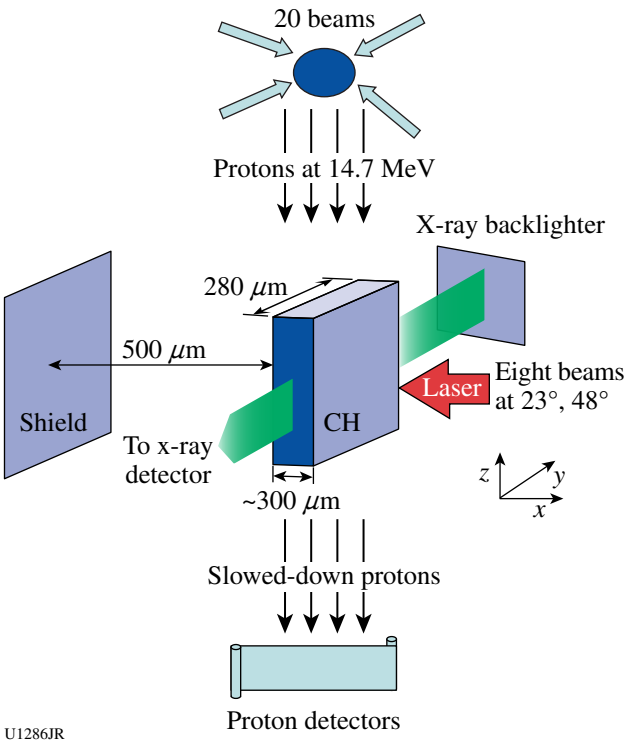

Figure 128.45
The schematic diagram of the experimental setup.

varied in size from 300 μm × 300 μm × 300 μm to 500 μm × 500 μm × 300 μm. A total of eight shots were taken during this one-day campaign.

The typical proton spectra from these experiments are shown in Fig. 128.46. The highest peak represents the initial protons without any slowdown, while the down-shifted peaks correspond to the slowdown protons. In Fig. 128.46(a), the small-sized target [(300 μm)^3] was used and the areal density (ρL) of the undriven CH target sampled by protons is estimated to be ~30 mg/cm^2. This amount of ρL gives ~1-MeV energy loss, which is in agreement with what is observed in Fig. 128.46(a). For the larger targets (500 × 500 × 300 μm^3), Fig. 128.46(b) shows the proton spectrum in which the slowdown proton peak moves further to ~13 MeV as a result of the ρL increase. Although detailed analyses of experiments are under way, these primary results indicate that the platform may be useful for future studies of the charged-particle stopping power in laser-shocked warm, dense plasmas. Some improvements to enhance the proton yield and enlarge the solid angles of acceptance can be optimized for future campaigns.

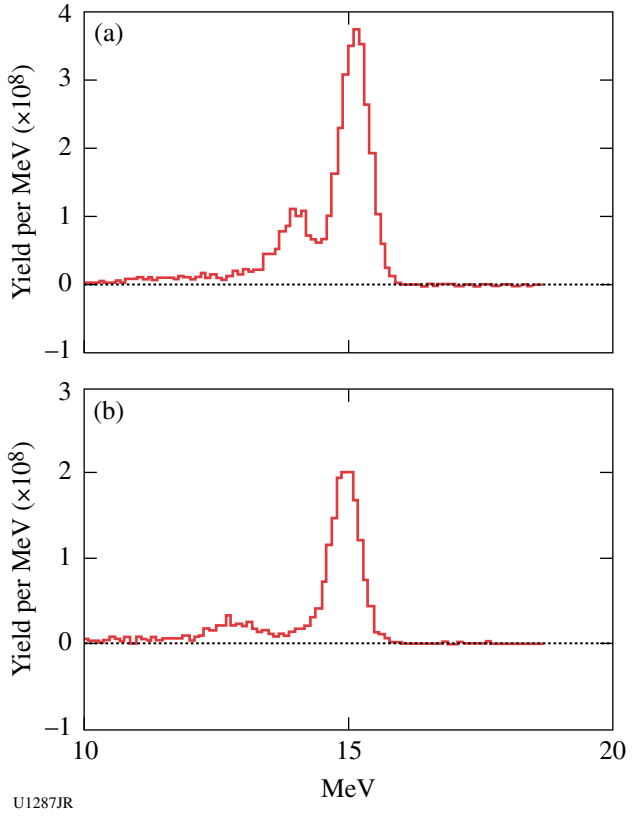

Figure 128.46
The typical proton spectra from the charged-particle stopping experiments.

Measurements of Linear, Nonlinear, and Turbulent-Mixing Regimes in Kelvin–Helmholtz Instability in the Subsonic Flow Regime

Principal Investigators: O. A. Hurricane and V. A. Smalyuk
Co-investigators: H.-S. Park and B. A. Remington (LLNL); and R. P. Drake (University of Michigan)

A Kelvin–Helmholtz (KH) growth experiment was performed on the OMEGA laser using a platform successfully developed in earlier OMEGA experiments.[39–41] Figure 128.47 shows the target schematic, which consists of a plastic ablator and a shock tube. In the shock tube the interface between the low-density foam and the high-density plastic was either flat or had preimposed sinusoidal modulation at a wavelength of 400 μm and an amplitude of 30 μm, as in previous experiments. The central part of the plastic target contained a layer of I-doped CH (CHI) to increase the contrast to 5-keV backlighter x rays. The ablator of the target was directly driven with laser light, producing a strong shock that propagated through the target. The shock produced a velocity gradient at the interface between the foam and plastic. This velocity difference

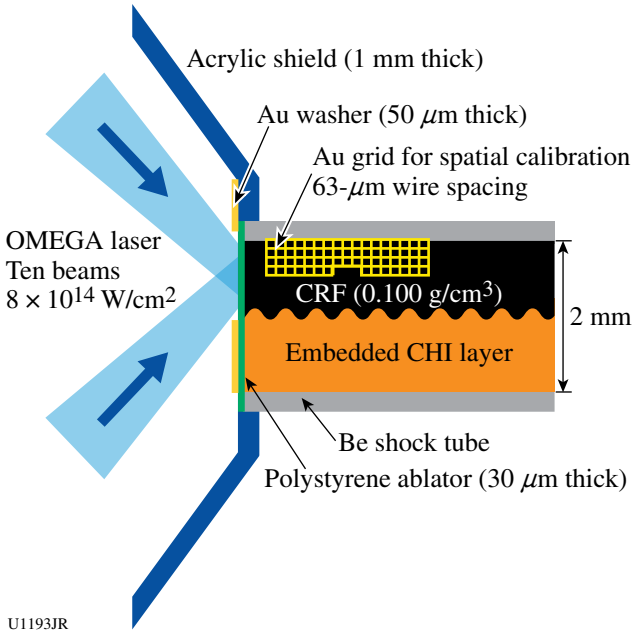

Figure 128.47
Experimental configuration. The interface between lower-density carbon-resorcinol foam (CRF) and higher-density I-doped plastic was either flat or had a preimposed 2-D modulation with wavelength of 400 μm, as in previous experiments. The surface roughness at the interface had rms amplitude of 100 nm. The density of CRF foam was 100 mg/cc.

between two materials resulted in the KH growth of the surface modulations. The density of foam was 100 mg/cc. Previous experiments detected a mixing layer that developed from 3-D, short-scale modulations growing in addition to preimposed 2-D, 400-μm-wavelength modulations. New experiments were performed with flat CH–foam interfaces. These were aimed at measuring 3-D turbulent mixing since in previous experiments the growth of large 400-μm-wavelength modulations could have modified the growth of 3-D, short-scale modulations.

Figure 128.48 shows experimental data. Figures 128.48(a) and 128.48(b) present flat-interface data at 35 ns and 75 ns, respectively. Figure 128.48(c) shows data with 2-D preimposed modulation at 75 ns, taken to confirm the evolution measured in previous experiments. The shock traveled from left to right, so the modulations at the left part of the image had more time to grow than the modulations at the right part. The light color in the image corresponded to foam material, while the dark color corresponded to plastic. A mixing layer developed behind the shock front, as expected, since the Reynolds number was high in this experiment, Re ~ 1×10^6. The mix width was about ~60 μm at ~700 μm behind the shock front, inferred from the measured image at 35 ns, close to mix-model predictions. Growth of 2-D, preimposed modulations [Fig. 128.48(c)] was similar to previous experiments, confirming the repeatability of the drive. In addition, growth of 3-D modulations at the Be tube–foam interfaces was also detected, as shown in both 75-ns images. These experimental data are used to develop and validate mix models that are based on post-processing of hydrodynamic simulations currently in progress.

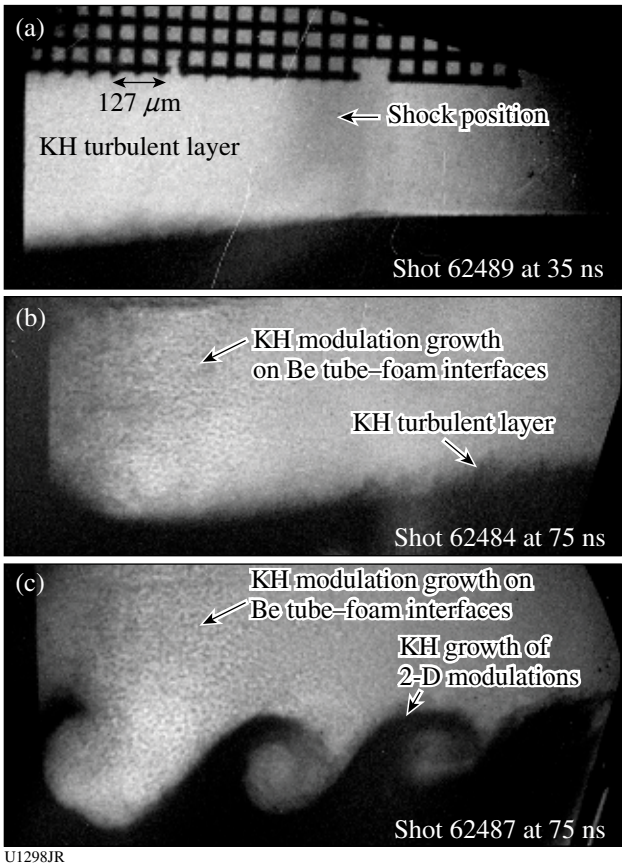

U1298JR

Figure 128.48
X-ray radiographs of KH growth with flat CHI–foam interface were taken at (a) 35 ns, at (b) 75 ns, and with interface having a 2-D modulation at (c) at 75 ns. The areas on the right-hand side of the images experienced less KH growth than those on the left-hand side.

Self-Generated Electromagnetic Fields in Directly Driven ICF Implosions Using Proton Radiography
Principal Investigators: I. V. Igumenshchev (LLE); and C. K. Li and A. Zylstra (PSFC-MIT)

Self-generated electromagnetic fields from surface perturbations and electric fields at ablation surfaces in directly driven implosion targets have been observed and quantified using proton radiography. The surface perturbations were induced by stalk mounts, 10-μm Cu wires, and glue spots. Numerical simulations show good agreement with experimental proton images and predict magnetic fields up to ~5 MG. Proton images allow one to detect the position of the spherical ablation front during the initial stages of implosions.

The experiments were performed with backlighters in the form of foils driven by short-pulse petawatt laser beams from OMEGA EP.[6] This type of backlighter, which has been used on other lasers,[42] should have a smaller source size, a shorter duration, and a potentially higher proton energy than what have been achieved with imploding-pusher backlighters,[9] but with the disadvantages of a much broader spectrum and nonisotropic (strongly forward peaked) emission in both fluence and energy. However, higher spatial resolution obtainable with a smaller source and higher proton energy are useful as well for imaging ICF implosions with higher areal densities than can be studied with 15-MeV protons from exploding pushers and with less proton scattering. The higher proton fluences' broad spectra of these foil backlighters necessitate the use of a different imaging detector; a combination of radiochromic films is used.[42]

The proton source is used to obtain information about imploding ICF capsules that is complementary to the information we are obtaining using exploding-pusher backlighters (see Fig. 128.49). The advantage of this approach over the

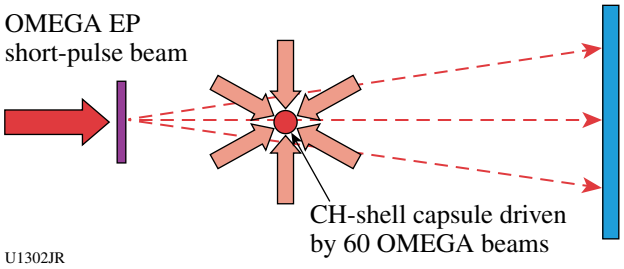

Figure 128.49
Schematic illustration of the experimental setup for imaging an imploding, CH-shell capsule in the OMEGA chamber with protons from a foil backlighter driven by a short-pulse OMEGA EP beam.

exploding-pusher–backlighter approach is that it does not use any beams from OMEGA, meaning that it would be possible to image implosions driven by all 60 OMEGA beams. The experiment employs 860-μm-diam plastic capsules with 20-μm wall thickness. The capsule filling does not play a role in this experiment because the proton radiographs were always taken during the laser pulse, when the compression of the capsule is not significant. The implosions were driven by a 1-ns square pulse with a total laser energy ~30 kJ.

Self-generated electromagnetic fields have been developed from perturbations induced by a stalk-mounted, on-surface, 10-μm-diam Cu wire going around half an implosion capsule and a 50-μm-diam glue spot. Figures 128.50(a)–128.50(d) show proton images taken at ~200, 600, 600, and 300 ps, respectively. The capsule center is projected in the center of each image. The ablation front at the capsule's outer surface is clearly distinguished in Figs. 128.50(a) and 128.50(d) as light circles in proton fluence. These fronts that appear on the images are caused by deflection of the protons by electric fields developed at the ablation and critical surfaces. All figures show features at the bottom that correspond to the stalk mount. One can follow the evolution of electromagnetic fields around the stalk in Figs. 128.50(a), 128.50(d), and 128.50(b) [or Fig. 128.50(c), which shows features very similar to those from the stalk in Fig. 128.50(b)].

Figures 128.50(a)–128.50(c) show targets with the Cu wire. The two images in Figs. 128.50(a) and 128.50(b) show the cases where the wire is located on the side of the target toward the proton source. It is clear that developed magnetic fields deflect protons in such a way that proton trajectories going on both sides of the wire are mostly diverged, forming light strips in the proton fluence. Figure 128.50(c) shows the case where the wire is located on the opposite side of the target with respect to

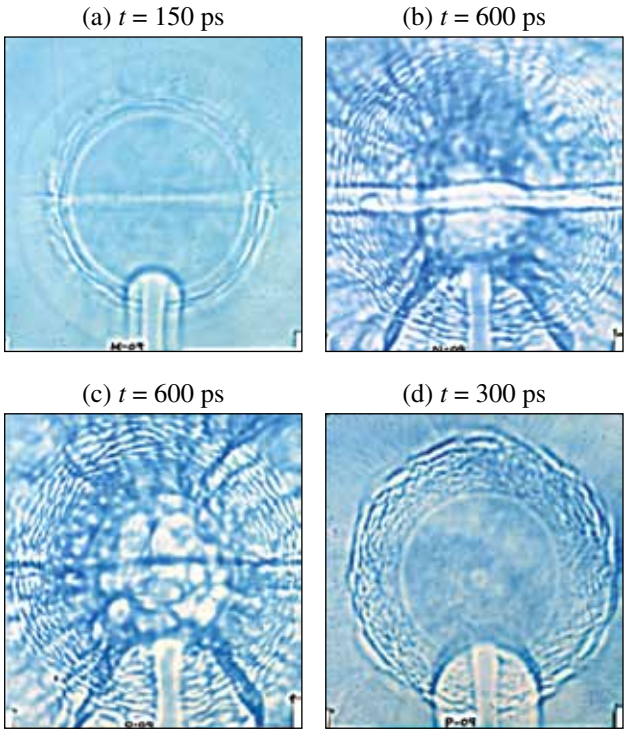

Figure 128.50
Proton images of implosion plastic-shell targets with different surface perturbations. The images show variations of proton fluence that result from the deflection of proton trajectories caused by the interaction with electromagnetic fields. Implosions in (a)–(c) show targets with Cu wire; (a) and (b) correspond to the case where the wire is located on the side of the target toward the proton source and (c), where the wire is on the opposite side of the target. (d) shows the target with a glue spot, which is located on the side of the target toward the proton source.

the proton source. In the latter case the proton rays are mostly converged toward the wire, forming a dark strip in the proton fluence. This is because the protons interact with magnetic fields of similar structure as in the case of Fig. 128.50(b), but the fields here have opposing polarity and opposing signs of the proton deflection angles.

Figure 128.50(d) shows a target at the glue spot, which is located on the target surface toward the proton source. There is a small light circle in the proton fluence located in the center of the image that is clearly associated with the glue spot. Magnetic fields that develop around the glue spot affect proton trajectories in a way that is similar to the fields in the case of the Cu wire in Figs. 128.50(a) and 128.50(b): the trajectories are deflected outward from the glue spot, forming a small light area at the projected location of the glue spot.

Figures 128.51(a)–128.51(c) show preliminary simulation results for the experimental conditions corresponding to Figs. 128.50(a)–128.50(c), respectively, but without modeling the effects of stalk mounts. The horizontal line features are produced by the Cu wires. The simulations show horizontal light strips in the proton fluence in Figs. 128.51(a) and 128.51(b), similar to the experimental results in Figs. 128.50(a) and 128.50(b) where the wire is located on the side of the target facing the proton source. The simulations shown in Fig. 128.51(c) correspond to the case where the wire is located on the opposing side of the target with respect to the proton source. Magnetic fields around the wire cause the proton trajectories to converge toward the wire, resulting in the horizontal dark strip in the proton fluence, which is similar to the dark strip seen in Fig. 128.50(c).

The circular features in Figs. 128.51(a)–128.51(c) are caused by electric fields developed at the ablation and critical surfaces (the light circles in all three images) and at the outer plasma front [the dark outer circle in Fig. 128.51(a)]. All these features can be associated with the corresponding circular features in experimental images [Figs. 128.50(a)–128.50(c)]. Simulations of the magnetohydrodynamic effects and proton images of the stalk mount and glue spot are in progress.

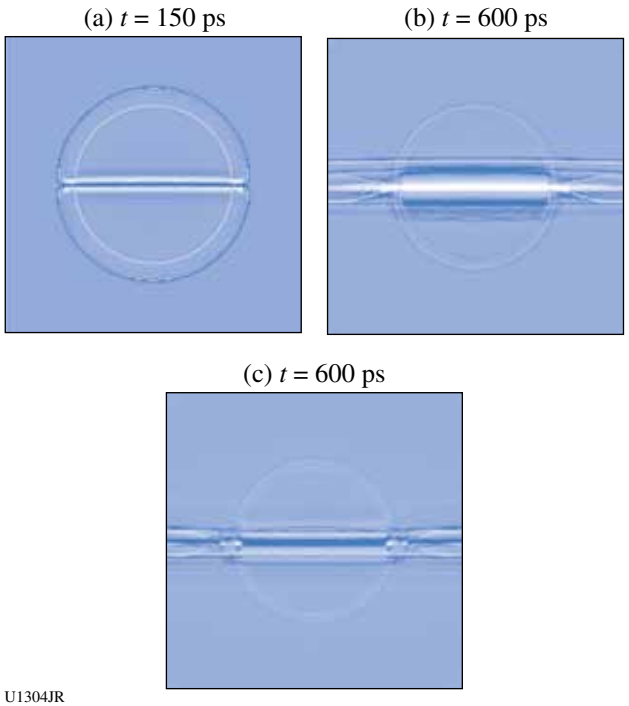

Figure 128.51
Simulated proton fluence for the experimental conditions of implosion targets with a Cu wire shown in Figs. 128.50(a)–128.50(c). The images were simulated employing a proton ray-trace code that initiates proton trajectories from a point source. This code uses distributions of electromagnetic fields obtained using 2-D *DRACO* simulations.[43]

Capsule Adiabat Measurement with X-Ray Thomson Scattering

Principal Investigator: A. Kritcher (LLNL)
Co-investigators: T. Doeppner, O. L. Landen, and S. H. Glenzer (LLNL)

The first simultaneous measurements of electron densities and temperatures of spherically convergent matter via spectrally resolved x-ray Thomson scattering have been performed at the Omega Laser Facility. In these experiments, we infer in-flight adiabats of 1.6 to 2, approaching the desired adiabat of 1.5 for implosions driven by shaped laser pulses (see Fig. 128.52). While Thomson scattering has previously been applied to planar shock systems, here we employed high-energy x rays at ~9 keV to characterize matter densities of $n_e > 10^{24}$ cm^{-3} obtained in spherically convergent geometries. Our signal-to-noise ratios (SNR's) of ~200 obtained at these densities indicate the ability for single-shot characterization of imploding targets to result in a 20% error bar on electron density and temperature if both parameters are simultaneously determined. Measurement of the temperature and density enables us to infer the time-resolved CH and Be capsule adiabats, which can be used to test low-adiabat laser pulse shaping and models that predict shock timing for spherically convergent targets.

Probing microscopic plasma properties results in both elastic and inelastic scattering features. The intensity of the elastic scattering is sensitive to the static structure factor of the material. The Compton feature provides a direct measure of the electron-velocity distribution. For these weakly degenerate plasmas, the velocity distribution is a hybrid of a Thomas–Fermi ($T_e = 0$) and a Boltzmann distribution ($T_e \gg T_F$). The width of the inelastic Compton feature is sensitive to the Fermi temperature T_F, which is only dependent on electron density, and the shape of the red wing is sensitive to electron temperature T_e (Ref. 44). Therefore, the temperature and density are simultaneously determined from first principles by accurately measuring the Compton feature width and shape (see Fig. 128.52).

These experiments complete a series of campaigns to develop a platform that enables us to measure electron temperature and density from imploding Be and CH capsules. These results have been summarized and published in peer-reviewed journals.[44,45]

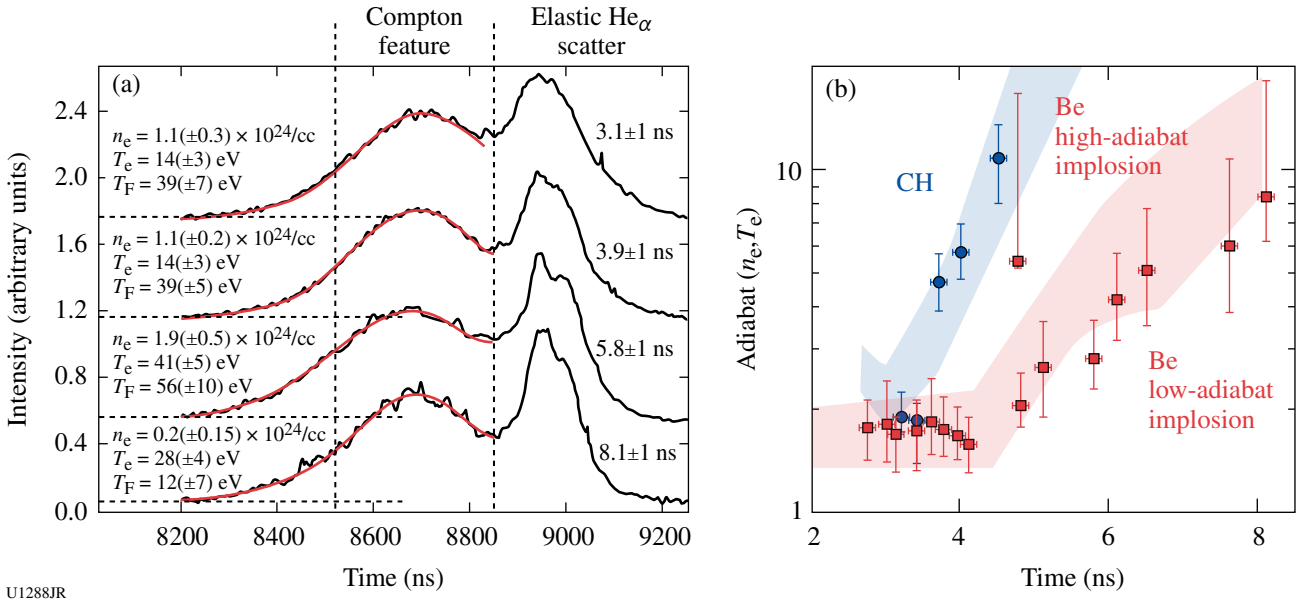

Figure 128.52
(a) Measured (black) and best fits (red) to the Compton feature of the scattered x-ray spectra from Be implosions at various times, yielding n_e and T_e. (b) Adiabat plotted as function of time for compressed Be and CH ablators. Also plotted are 1-D radiation–hydrodynamic calculations.

Astrophysical Collisionless Shock Generation in Laser-Driven Experiments

Principal Investigator: H.-S. Park, S. Ross, and N. Kugland (LLNL)
Co-investigators: A. Spitkovsky (Princeton); Y. Sakawa (Osaka University); G. Gregori (Oxford University); M. Koenig (LULI); D. H. Froula (LLE); R. P. Drake (University of Michigan); and R. Presura (University of Nevada, Reno)

This LBS program studies astrophysical collisionless shocks with counter-streaming plasmas from high-power lasers. Collisions of high-Mach-number flows occur frequently in astrophysics, and the resulting shock waves are responsible for the properties of many astrophysical phenomena, such as supernova remnants, gamma-ray bursts, and jets from active galactic nuclei. Because of the low density of astrophysical plasmas, the mean free path of Coulomb collisions is typically very large. Therefore, most shock waves in astrophysics are "collisionless" since they form as a result of plasma instabilities and self-generated magnetic fields. Laboratory experiments at the laser facilities can achieve the conditions necessary for the formation of collisionless shocks and will provide a unique avenue for studying the nonlinear physics of collisionless shock waves. We are performing a series of experiments on the OMEGA and OMEGA EP lasers, with the goal of generating collisionless shock conditions by the collision of two high-speed plasma flows resulting from laser ablation of solid targets using ~10^{16} W/cm^2 laser irradiation. The experiments will aim to answer several questions of relevance to collisionless shock physics: the importance of the electromagnetic-filamentation (Weibel) instabilities in shock formation, the self-generation of magnetic fields in shocks, the influence of external magnetic fields on shock formation, and the signatures of particle acceleration in shocks. Our first experiments studied the plasma state from a single foil and from double foils whose flows collide "head on," using Thomson-scattering (TS) diagnostics. Our data showed a flow velocity at 10^8 cm/s and an electron density of 10^{19} cm^{-3}, where the Coulomb mean free path was much larger than the interaction system size. Simulations of our experimental conditions show that weak Weibel-mediated current filamentation and magnetic-field generation were likely starting to occur. This report presents the results from these first OMEGA experiments.

Our first OMEGA experiments [AstroPlasmas-11A (10 December 2010) and ColPlasmas-11C (1 June 2011)] concentrated on measuring and understanding the plasma conditions created by the OMEGA lasers on single- and double-foil configurations. Thomson scattering was used to characterize the plasma created by ten heater-drive beams incident on a CH foil. Our two shot days produced high-quality data spanning two different laser intensities, three different probe times, single- versus double-foil geometry, and different flow directions.

The heater-drive beams deliver 5 kJ of energy in a 1-ns square pulse shape. The target geometry is shown in Fig. 128.53. A probe beam of 0.53-μm wavelength (labeled "2ω probe" in the figures) is pointed 4 mm from the foil surface. The TS probe volume was 100 μm × 100 μm × 60 μm. We measured the flow plasma conditions along both the flow direction and the transverse directions. Both shot days produced excellent-quality TS data; an example is shown in Fig. 128.54 for a single foil.

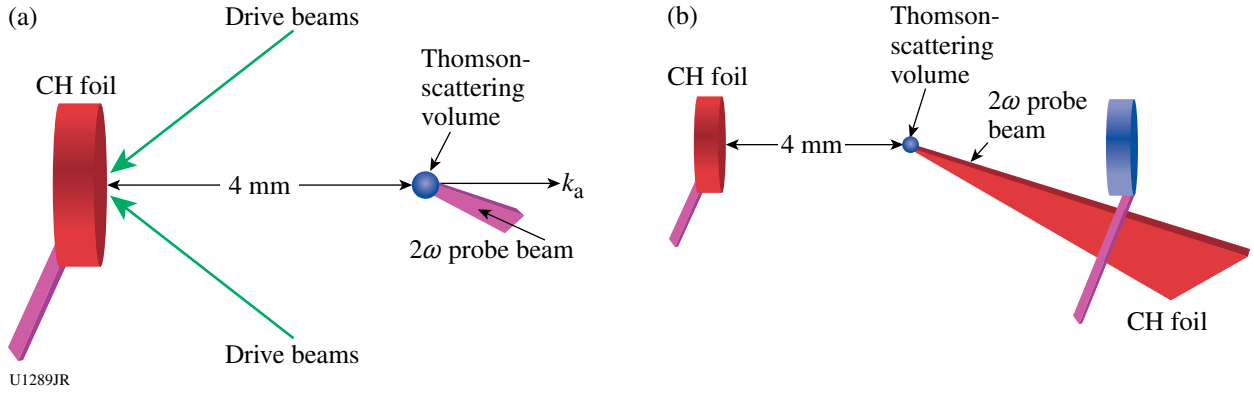

Figure 128.53
Geometry used for astrophysical collisionless shock experiment of June 2011 for the (a) single- and (b) double-foil cases. The laser intensity on the target was 8×10^{15} W/cm^2.

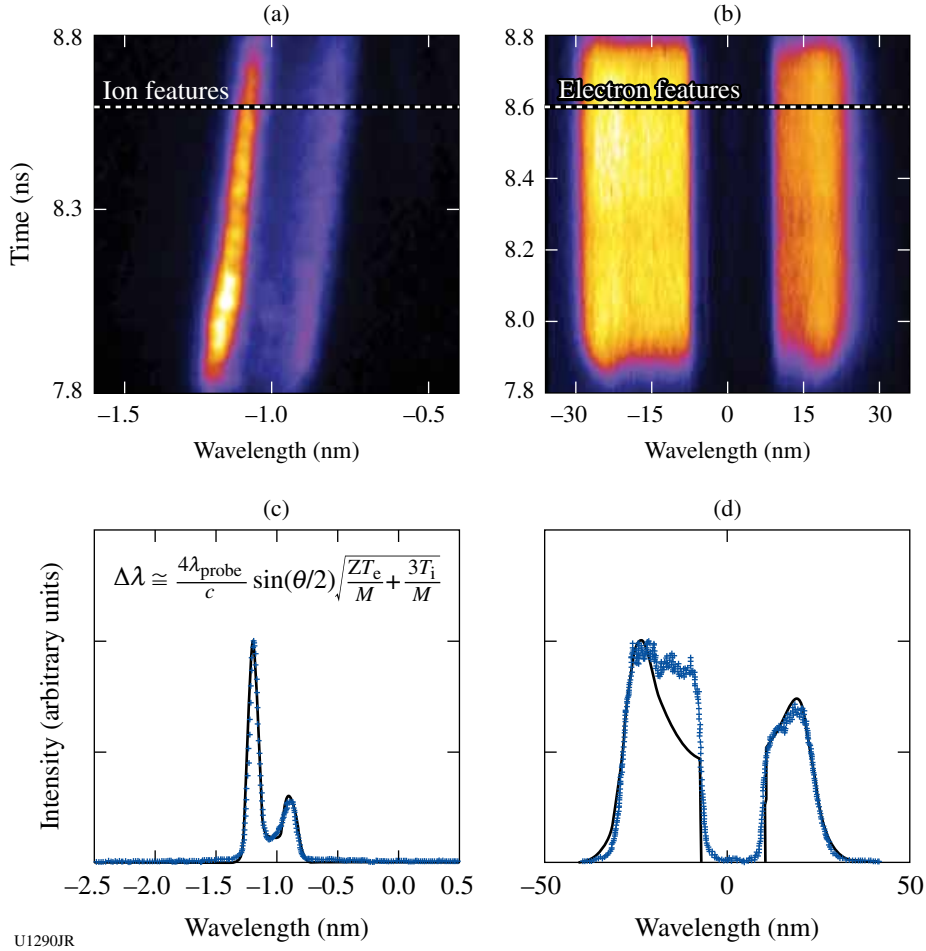

$T_e = 170$ eV
$T_i = 26$ eV
$n_e = 3.1 \times 10^{18}$ cm^{-3}
$v_{flow} = 5.7 \times 10^7$ cm/s
$u_{drift} = 1.2 \times 10^8$ cm/s

Figure 128.54
An example of Thomson-scattering data and fitting for a single-foil shot. (a) Ion features; (b) electron features; (c) ion features' data and fitting; and (d) electron features' data and fitting. A time slice of the ion and electron features is simultaneously fitted to produce T_e, T_i, n_e, v_{flow}, and u_{drift} parameters.

The measured plasma characteristics from different shots covering a 2- to 9-ns time interval and single and double foils are compiled in Fig. 128.55. The flow velocity, electron density, ion temperature, and electron temperature are shown. Different-color data points represent different experimental conditions of single-foil shots (blue), double-foil shots (red), and single foil with 10×-lower drive laser intensity (green). The data are compared to 2-D LASNEX hydrodynamic simulations (for the single-foil case) in solid black curves. There is good agreement between the measured and simulated bulk plasma flow velocity over all three time intervals. The measured electron density shows a sharp increase between 5.0 and 6.0 ns, which is also present in the simulations, indicating that the bulk of plasma arrives at this time. This is consistent with flow arrival at the 4-mm location of the plasma flow with a velocity of ~10^3 km/s. The measured electron temperature is significantly higher than the simulations. We attribute this to reheating the plasma by the TS probe beam. The measured ion temperature is consistent with 2-D simulations. An electron temperature of 170 eV is assumed in this time interval because of a lack of electron feature data.

The double-foil data also showed very interesting results. The difference between the single-foil versus the double-foil data for the ion feature is very striking. Compared to the single-foil flow, the ion temperature and electron density are considerably higher. Another interesting observation is that the flow velocity is reduced systematically for the double-foil flows, indicating interaction between the two flows late in time.

Our first OMEGA EP experiments [EPColPlasmas-11B (26 April 2011) and EPColPlasmas-11D (30 August 2011)] concentrated on developing proton deflectometry and proton radiography diagnostics to understand electric and magnetic fields

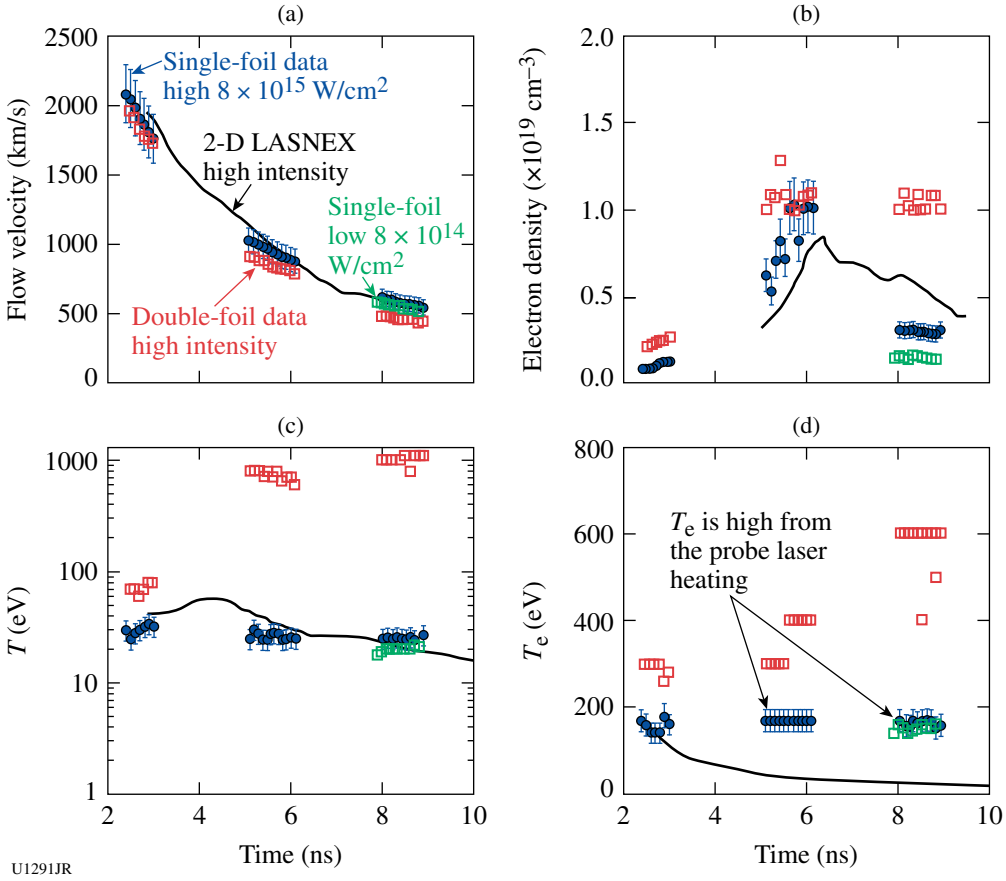

Figure 128.55
Measured plasma parameters from a single-foil flow versus a 2-D hydrodynamics simulation. The high measured electron temperature, compared to that simulated, is likely caused by the probe beam heating. Blue points are single-foil data with laser intensities of 8×10^{15} W/cm^2; green are single-foil data with laser intensities of 8×10^{14} W/cm^2; red are double-foil data with 8×10^{15} W/cm^2 on each foil; the black line is the 2-D LASNEX simulation for the single foil with 8×10^{15} W/cm^2.

generated by the interpenetrating plasmas. The experimental setup is shown in Fig. 128.56. Two long-pulse UV beams drive the CH_2 targets with 2200 J in a 3-ns square pulse. The laser-generated high-velocity plasma flow moves upward and downward, and the entire region between the two targets was probed by two short-pulse-laser-generated proton beams. Since it is known that the long-pulse–driven plasmas can interrupt proton generation, a careful shield design was necessary. Our experiment on 30 August 2011 was successful in generating an interesting time sequence of proton radiography images as shown in Fig. 128.57. There are three different features in these radiographs: (1) large bubble-like features; (2) very fine striation features only at 2 to 5 ns; and (3) two planar disk-like features. We postulate that they may result from laser-ablative Rayleigh–Taylor instabilities, magnetohydrodynamic instabilities, and electrostatic field generation from the hot-plasma expansion and temperature gradient, respectively. We are currently working on the data interpretation and analysis using analytic models, radiation–hydrodynamics simulations, and particle-in-cell simulations.

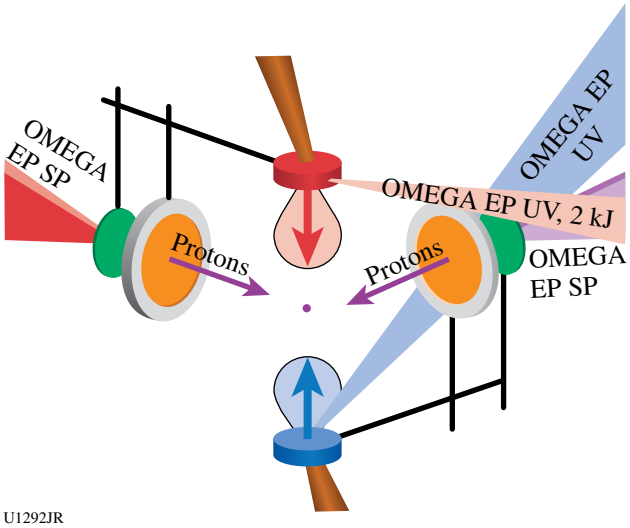

Figure 128.56
OMEGA EP experimental setup. Two UV long-pulse beams illuminates the CH_2 targets creating high-velocity plasma flows. The short-pulse–generated protons are used to radiograph the flowing plasmas.

This LBS project has resulted in the formation of a large international team called the ACSEL (Astrophysical Collisionless Shock Experiments with Lasers) collaboration. ACSEL has key members from LLNL (H.-S. Park); Princeton (A. Spitkovsky); Osaka University (Y. Sakawa); Oxford University (G. Gregori); LULI (M. Koenig); LLE (D. H. Froula); University of Michigan (R. P. Drake); University of Nevada, Reno (R. Presura); and their team members. The results have been presented at many conferences, one paper has been submitted, and many papers are in preparation.[21,25–30,46]

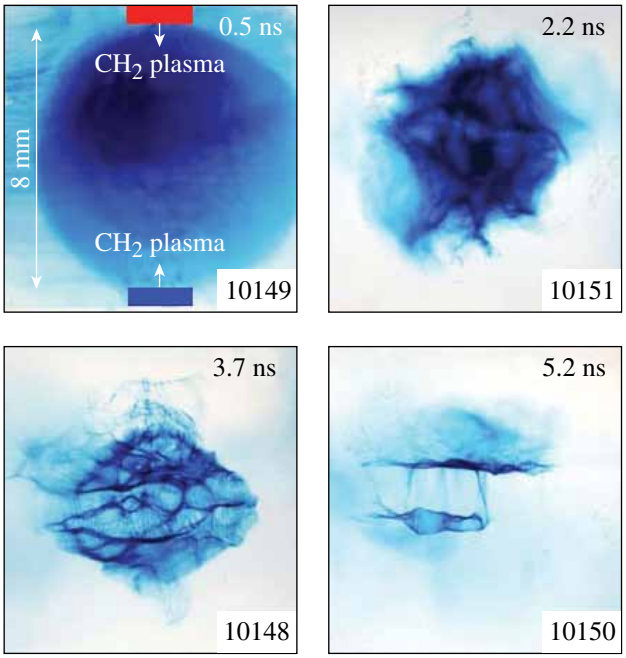

Figure 128.57
Proton-radiography images of the interpenetrating plasmas from the astrophysical collisionless shock experiments of August 2011. The analyses of interpretation of different features using both plasma theories and PIC simulations are in progress.

Electron-Source Characterization for Cone-Guided Fast Ignition

Principal Investigators: P. K. Patel (LLNL) and H. Sawada (University of California, San Diego)
Co-investigators: C. D. Chen, H. S. McLean, and M. H. Key (LLNL); F. N. Beg (University of California, San Diego); R. B. Stephens (General Atomics); and W. Theobald and C. Stoeckl (LLE)

In cone-guided fast ignition (FI), the directionality of laser-generated relativistic electrons escaping from a cone is one of the critical parameters that determine the required ignition laser energy of a FI point design. We have used cone-foil targets to investigate the angular spread of the forward-going electrons by measuring the 2-D profile of Cu K_α x-ray emission with an OMEGA EP spherical crystal imager (SCI). Figure 128.58(a) shows an overview of the experiment. The fast electrons were generated at a cone tip with the OMEGA EP backlighter beam at 300 J in a 1-ps or at 1500 J in a 10-ps pulse duration and transported through a 10-μm-thick Al or Au cone tip. A frac-

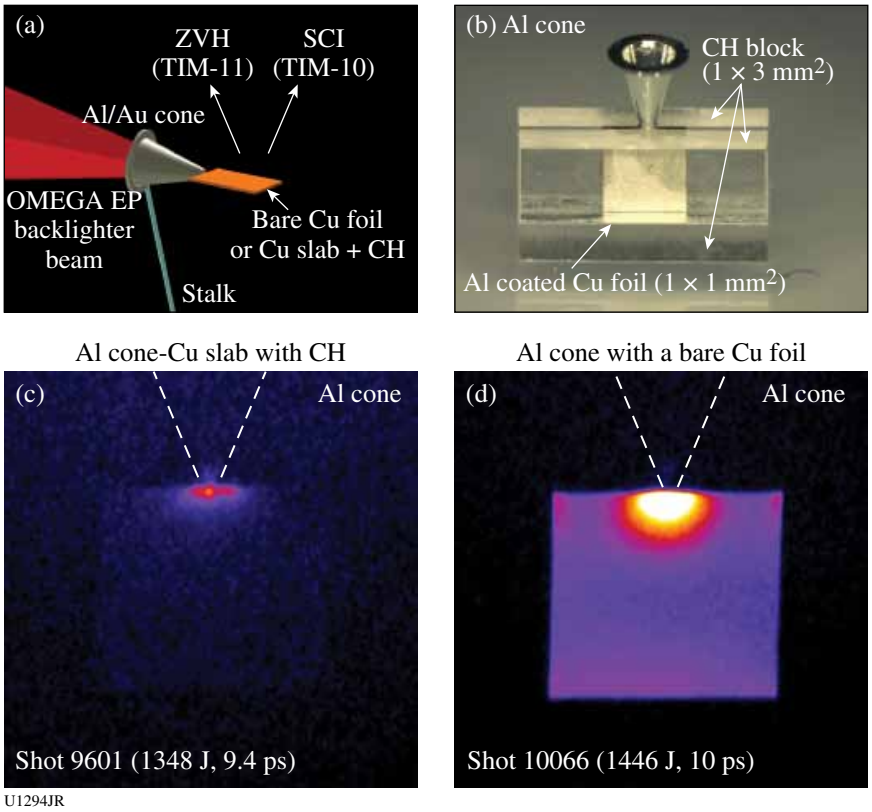

Figure 128.58
(a) Experimental overview and (b) a photograph of an Al cone–Cu slab target. In the bottom row, measured K_α images of (c) Al cone–Cu slab with CH target (shot 9601) and (d) Al cone–bare Cu foil target (shot 10066) at 1500 J in the 10-ps pulse in the same color scale.

tion of the electrons that escaped from the cone were measured in either (1) an aluminum-coated Cu foil surrounded by CH blocks or (2) a bare Cu foil. For both cases, the Cu foil was 1×1 mm^2 and 40 μm thick. As shown in Fig. 128.58(b), the Cu slab consisted of the Cu foil coated with 20-μm-thick aluminum on both sides and 500-μm-thick CH blocks (1×3 mm^2) surrounding it to prevent electron refluxing. The dimensions of the Al and Au cones were identical with a 65-μm wall thickness and 30-μm inner tip diameter. The Cu K_α emission was recorded with the OMEGA EP SCI at 27° and an absolutely calibrated ZVH crystal spectrometer at 41° from the foil normal. Figures 128.58(c) and 128.58(d) show the 2-D monochromatic images of a Cu slab with CH blocks (shot 9601) and a bare Cu foil (shot 10066) attached to the Al cones for 10-ps shots. In the nonrefluxing Cu slab target, the total K_α yield was reduced by a factor of ~7, and the sharper falloff of the emission profile along the laser axis was observed compared to the bare Cu foil. The absolute K_α yield and 2-D K_α emission profile will be modeled with a hybrid PIC code, *LSP*, to infer the electron divergence, electron energy distribution, and laser-to-electron conversion efficiency.

EXAFS Measurements of Iron at Earth's Inner Core Conditions

Principal Investigators: Y. Ping, D. G. Hicks, D. E. Fratanduono, F. Coppari, S. Hammel, J. H. Eggert, J. R. Rygg, R. F. Smith, and G. W. Collins (LLNL); and B. Yaakobi and T. R. Boehly (LLE)

Iron is the most-abundant element at Earth's core. Its properties under extreme conditions are critical for understanding phenomena in geophysics, geochemistry, and seismology. By means of dynamically compressing a thin iron sample sandwiched between diamond anvils with multiple shocks, we achieved off-Hugoniot states of iron at pressures up to 3.5 Mbar and temperatures of ~5000 K, which is the expected condition at Earth's inner solid core. Measurements of extended x-ray absorption fine structure (EXAFS) have been performed with a broadband x-ray backlighter created by a spherical implosion. The results indicate that iron is not at bcc phase under these conditions, which is contradictory to recent simulation results (Fig. 128.59).

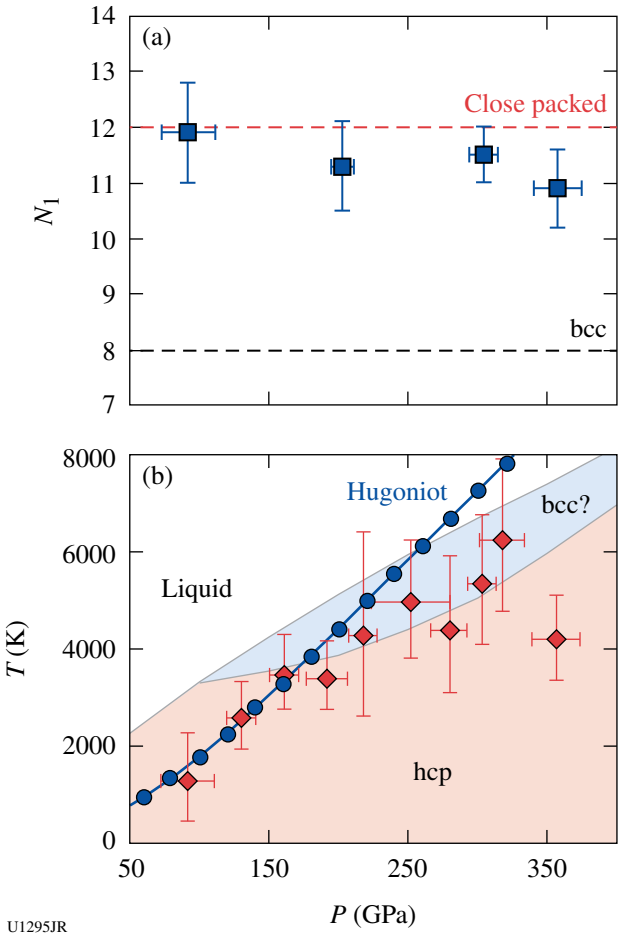

Figure 128.59
(a) The coordination number of the first shell obtained from EXAFS data as a function of pressure, showing that our data are consistent with the close-packed structure but inconsistent with the bcc lattice. (b) The temperature obtained from the Debye–Waller factor in EXAFS data versus pressure. The data are all consistent with the hcp phase, even inside the proposed bcc regime (Ref. 47).

Diagnosing P, ρ, n_e, T_e, and Z of H, H/He, CH_4, and NH_3 Warm, Dense Matter Using Inelastic X-Ray Scattering and Shock-Velocity Measurements: Toward the Equation of State of Planetary Interiors

Principal Investigator: S. P. Regan (LLE)
Co-investigators: T. R. Boehly, S. X. Hu, D. D. Meyerhofer, P. B. Radha, and T. C. Sangster (LLE); K. Falk, G. Gregori, and C. D. Murphy (University of Oxford); B. Crowley (AWE); T. Doeppner, S. H. Glenzer, and O. L. Landen (LLNL); and D. O. Gericke and J. Vorberger (Warwick University)

An experimental platform has been developed on OMEGA to study inelastic x-ray scattering from shocked deuterium and nitrogen. This work was performed in collaboration with Oxford University, Warwick University, and Lawrence Livermore National Laboratory. In the past decade, developments in laser-produced plasma sources and detector efficiencies have resulted in inelastic x-ray scattering becoming a powerful diagnostic providing electron temperature (T_e), electron density (n_e), and ionization (Z) for critical equation-of-state measurements in ICF and planetary science research.[48–52] Laser-ablation–driven shock waves are launched into planar liquid-deuterium targets, creating warm, dense matter with conditions similar to those of an imploding ICF shell during the shock-propagation and acceleration phases. X rays from a backlighter target are scattered off the shocked deuterium. The incident spectrum of the Cl Ly$_\alpha$ emission is shown in Fig. 128.60(a) and the scattered spectrum is shown in Fig. 128.60(b). The incident spectrum is measured by irradiating a parylene D foil target on a separate

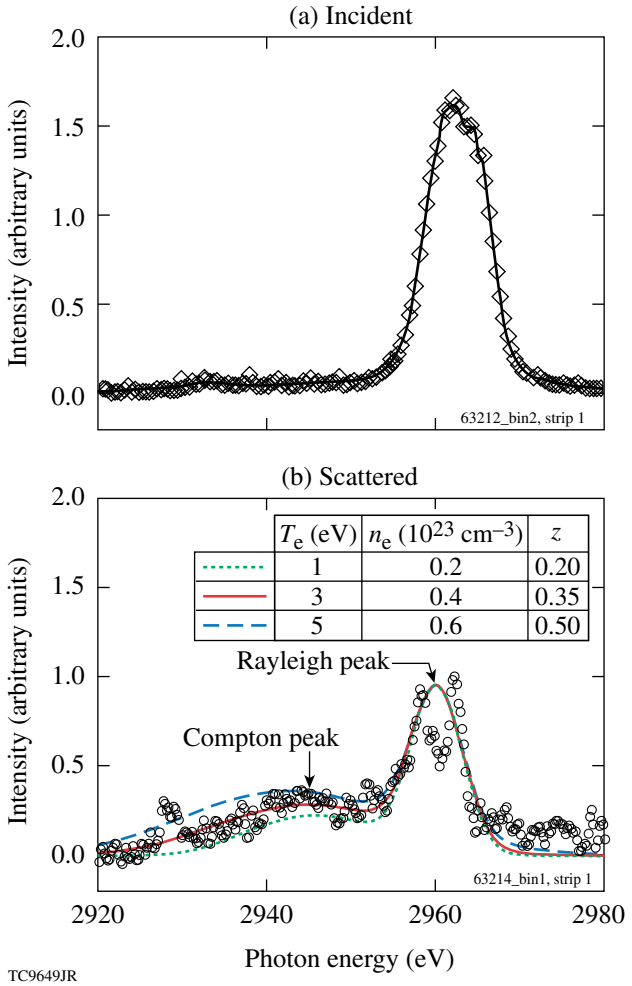

Figure 128.60
Spectra of (a) Cl Ly$_\alpha$ emission incident on shocked liquid deuterium and (b) Cl Ly$_\alpha$ emission scattered from shocked liquid deuterium on a different scale. The colored curves in (b) are predictions of the x-ray scattering (*XRS*) code, indicating that $T_e = 3\pm2$ eV, $Z \sim 0.35\pm0.15$, and $n_e = 0.4\pm0.2\times10^{23}$ cm^{-3}.

laser shot. The scattered spectrum has a strong Rayleigh peak around 2960 eV and a Compton-downshifted feature. Splitting of the Cl Ly$_\alpha$ emission is observed in the scattered spectrum, but not in the incident spectrum, because of differences in the amount of source broadening in each measurement (i.e., the backlighter plasma is bigger than the scattering volume).

Scattered x-ray spectra were calculated using the x-ray scattering *XRS*[53] code for various values of the plasma conditions. Three examples that bracket the experimental data are shown in Fig. 128.60(b). The fit allows one to estimate mean values in the D_2 plasma of $\bar{T}_e = 3 \pm 2$ eV, $\bar{n}_e = 0.4 \pm 0.2 \times 10^{23}$ cm^{-3}, and $\bar{Z} = 0.35 \pm 0.15$. These values are consistent with the 2-D *DRACO*[54] simulations, recognizing that a large part of the Thomson-scattering signal comes from unshocked deuterium. Improvements to the experimental design are planned to provide a smaller, more-homogeneous scattering region with less unshocked deuterium. The elastic (Rayleigh) feature is well fitted by assuming a ion–ion structure factor S_{ii} of unity, indicating weak correlations in the deuterium plasma, which is consistent with predictions from density-functional-theory molecular-dynamics simulations using the VASP package.[55,56] The *XRS* prediction does not include the fine-structure splitting observed in the measured spectrum. These are the first experimental observations of noncollective, inelastic x-ray scattering from shocked liquid deuterium. This work represents an important step toward measuring all the thermodynamic variables needed for equation-of-state research [pressure (P), mass density (ρ), electron density (n_e), electron temperature (T_e), and ionization (Z)]. Future work will combine inelastic x-ray scattering observations with shock-velocity measurements and extend to other materials like nitrogen.

Measurements of Ablative Richtmyer–Meshkov Instability in the Nonlinear Regime

Principal Investigator: V. A. Smalyuk (LLNL)
Co-investigators: B. A. Remington, H.-S. Park, and K. Raman (LLNL); A. Casner and L. Masse (CEA); I. V. Igumenshchev (LLE); and D. Shvarts and Y. Elbaz (NRCN, Beer Sheva, Israel)

Figure 128.61 shows a schematic of an experimental setup for nonlinear Richtmyer–Meshkov (RM) and Rayleigh–Taylor (RT) instability experiments on OMEGA EP. Planar 15-, 30-, and 50-μm-thick CH targets were driven with one UV beam using a 6-ns square pulse shape, a total energy of ~4 kJ, and a laser intensity of $\sim 8 \times 10^{13}$ W/cm^2. Initial target modulations were imposed by laser imprinting of the perturbations in the drive beam during the first ~100 ps of the drive. The growth of the target modulations was measured with x-ray radiography using uranium (~1.3-keV), samarium (~1.8-keV), and tantalum (~2.2-keV) backlighters and a framing camera with 10-μm spatial resolution and 80-ps temporal resolution. The backlighter targets were driven with a 2-ns square pulse shape at an intensity of $\sim 3 \times 10^{14}$ W/cm^2 using three UV beams. Figure 128.62 shows examples of measured images at 1.1 ns (near the end of

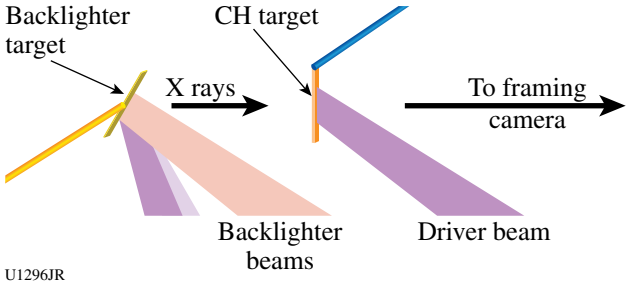

Figure 128.61
Experimental setup.

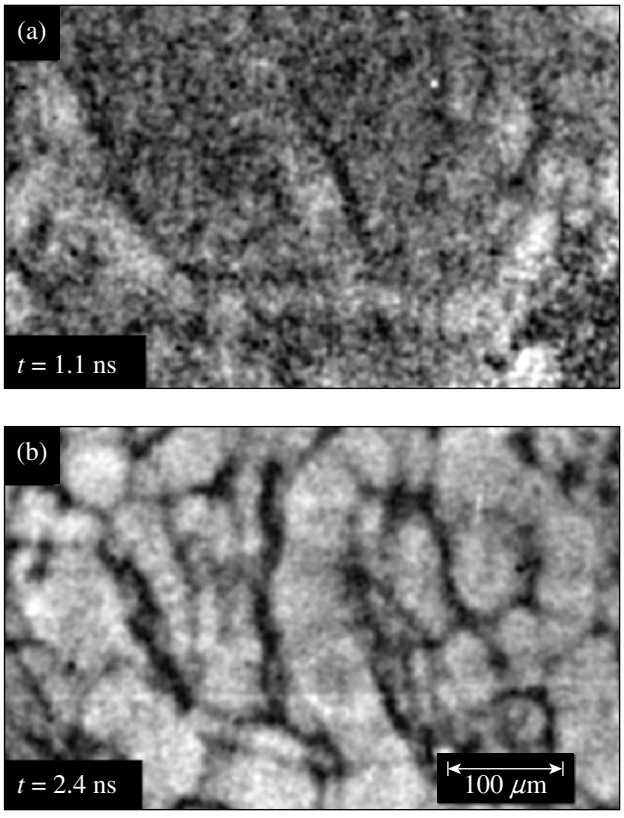

Figure 128.62
X-ray images of 3-D broadband modulations (a) at the end of the Richtmyer–Meshkov instability growth phase and (b) during the Rayleigh–Taylor instability growth phase measured in 30-μm-thick CH targets.

the RM phase) and 2.4 ns (during the RT phase) taken with a 30-μm-thick CH foil and samarium backlighter. Evolution of 3-D broadband modulations was observed in the RM phase for all target types during a shock-transit time before the beginning of acceleration and subsequent RT growth. Thicker targets had larger modulations at the end of the RM phase owing to the longer time for instability development. This provided larger initial modulations in thicker targets for subsequent RT growth. Therefore, this experiment provided data not only on the RM growth of 3-D broadband modulations, but also the dependence of RT growth on initial conditions. Modulation images in the RT phase show developed bubble-spike structures, typical features of nonlinear RT growth. These experiments, therefore, also provided information about nonlinear high-mode generation from known modulations. These experimental data are now being analyzed.

Measurement of Nucleation and Growth of the Fe α → ε Phase Transformation

Principal Investigators: R. Smith, P. M. Celliers, and D. Erskine (LLNL)

The goal of this project is to combine for the first time the recently developed 2-D imaging OMEGA high-resolution velocimeter[57] (OHRV) with the 1-D line VISAR (ASBO) to determine the time dependence and mechanisms associated with nucleation and growth of the $\alpha \rightarrow \varepsilon$ phase transformation in dynamically compressed Fe.

The target design consists of a Au halfraum, a 12% Br/CH reservoir, a vacuum gap, and 50 μm of Fe coated onto a sapphire window (Fig. 128.63). Twenty beams (2-ns square, P6-axis, 300-μm phase plates) from the OMEGA laser were focused onto the inner walls of an Au halfraum generating a near-blackbody source of x rays with a characteristic radiation temperature of ~120 eV. As x rays ablate material from the Br/CH foil, a shock wave is launched into the material.

As the ablatively driven shock reaches the back surface of the reservoir, the 12% Br-CH unloads across the ~0.3-mm vacuum gap, piles up against the front surface of the Fe target, and launches a ramp-compression wave into the sample with a peak longitudinal stress of ~50 GPa. As the Fe sample is dynamically compressed, it undergoes different states of deformation: 1-D elastic, 3-D plastic, and a solid–solid phase transformation from α (bcc) to ε (hcp) phase.

Each stage of compression of the Fe sample results in a change in the sound speed, which modifies the initially smoothly monotonic ramp wave during transit through the sample and is recorded as a structured particle-velocity history, $U_p(t)$, on the line-VISAR diagnostic (ASBO) (Fig. 128.64).

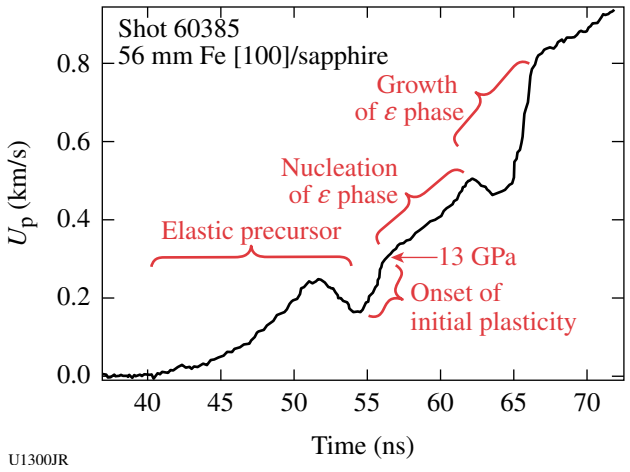

Figure 128.64
Particle velocity versus time for a ramp-compressed Fe/sapphire target as recorded on the 1-D line VISAR (ASBO).

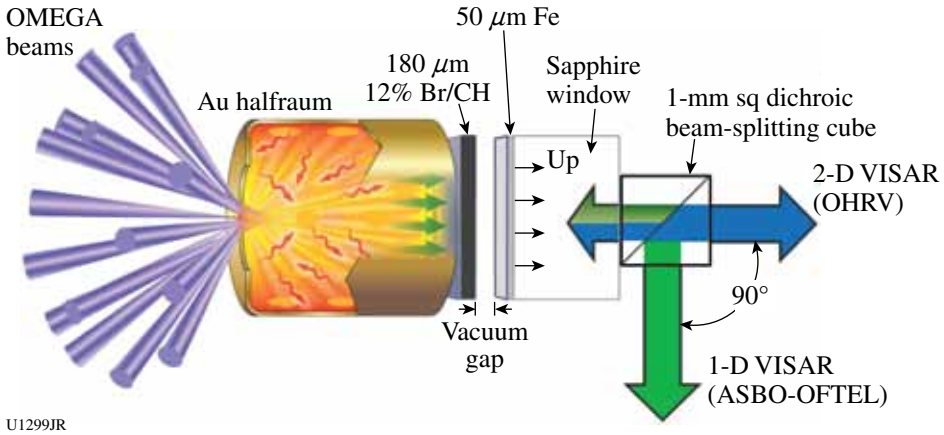

Figure 128.63
Target geometry for a combined 1-D/2-D VISAR diagnosis of a ramp-compressed Fe target.

Snapshots of the 2-D velocity map at the Fe–sapphire interface with the OHRV at velocities close to the velocity pull-back feature on the line VISAR reveal the kinetics associated with the nucleation and growth of the emerging ε phase.

Progress in the Shock-Ignition Inertial Confinement Fusion Concept

Principal Investigators: W. Theobald, R. Nora, K. S. Anderson, R. Betti,* R. S. Craxton, J. A. Delettrez, V. Yu. Glebov, M. Hohenberger, O. V. Gotchev, F. J. Marshall, R. L. McCrory,* D. D. Meyerhofer,* T. C. Sangster, W. Seka, C. Stoeckl, and B. Yaakobi (LLE) (*also Departments of Mechanical Engineering and Physics); A. Casner (CEA); J. A. Frenje (MIT); X. Ribeyre, M. Lafon, and G. Schurtz (Centre Lasers Intenses et Applications, University of Bordeaux, France); and L. J. Perkins and V. A. Smalyuk (LLNL)

Shock ignition is a two-step inertial confinement fusion concept in which a strong shock wave is launched by an intensity spike at the end of the laser pulse to ignite the compressed core.[58] Parametric plasma instabilities[59] such as stimulated Brillouin scattering (SBS), stimulated Raman scattering (SRS), and two-plasmon-decay (TPD) instability are of concern for laser intensities in the range of $\sim 3 \times 10^{15}$ to $\sim 10^{16}$ W/cm^2. The instabilities increase the back-reflection of the laser light from the target, degrading the laser-energy coupling to the capsule. They increase the fraction of the laser energy transferred to suprathermal electrons—a potential source of preheat that could reduce the final core compression. Whether or not these are harmful depends on the hot-electron temperature and the amount of laser energy that is transferred into hot electrons at high laser intensities.[60] The objective of this work is to study the coupling of laser energy from high-intensity beams into a spherically imploding capsule and the laser–plasma instabilities at shock-ignition–relevant laser intensities.

The targets were 34- to 36-μm-thick, 430-μm-outer-radius, deuterated plastic shells coated outside with a 0.1-μm layer of aluminium and filled with D_2 gas with a pressure of ~25 atm. The capsules were imploded using 40 of the 60 OMEGA beams with a low-adiabat pulse shape with ~13.6 kJ of UV laser energy and phase plates. The beams were repointed to achieve improved illumination uniformity. The blue curve in Fig. 128.65(a) shows the drive-pulse shape. A late shock was driven by the remaining 20 beams with an ~600-ps FWHM square-pulse shape (red curve) without phase plates. The intensity was varied by shifting the focus of the 20 beams relative to the shell's center. Figure 128.65(b) shows a schematic for intermediate spike intensity. The foci of the 20 spike beams did not overlap at the critical density for most lens positions. The experimental observables are the neutron yield,[61] the backscattered laser energy,[62] the hard x-ray signal,[63] and the neutron-rate–averaged areal density.[20] The hard x-ray signals were measured with four channels (>20, >40, >60, and >80 keV) (Ref. 63). Areal densities (ρR) were inferred from secondary proton spectra.[20]

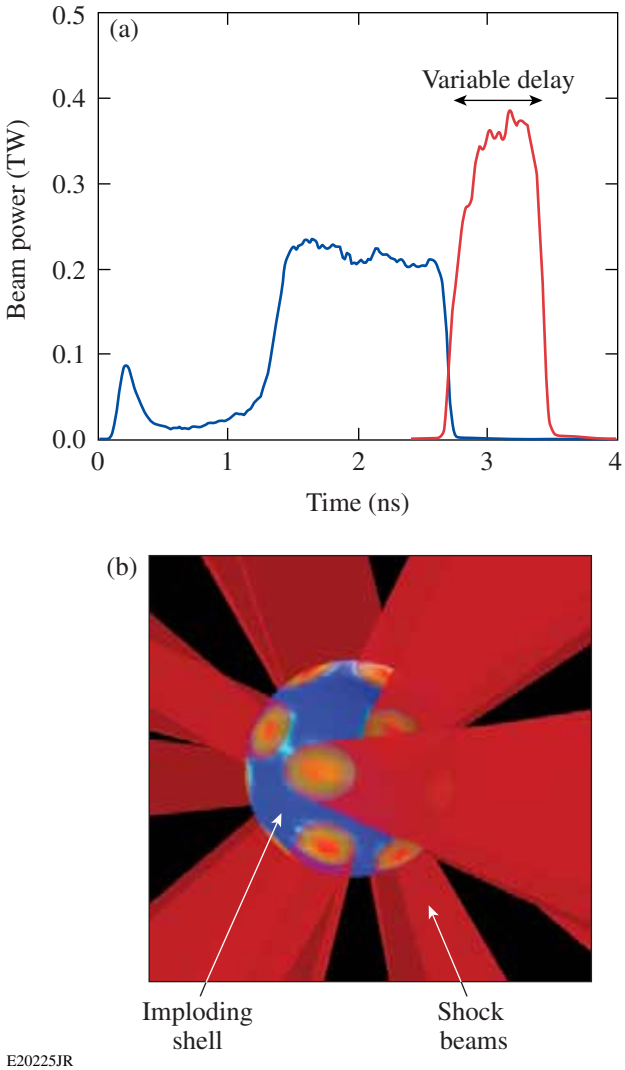

Figure 128.65
(a) The drive-pulse shape (blue) for the 40 beams and the high-intensity pulse (red) for the 20 spike beams. Beam delay and spike intensity were varied. (b) The 20 delayed spike beams were tightly focused onto the critical-density surface, where plasma instabilities led to the generation of energetic electrons and laser backscattering.

Two-dimensional hydrodynamic simulations with the code CHIC[64] are consistent with the measured areal density (see Fig. 128.66). The solid curve is from the 2-D simulation and the dashed line is from a 1-D simulation. The experimental values are noted by solid circles. The simulation values are higher because they represent the areal density at peak neutron production, whereas the experimental values are averaged over the observed neutron-production rate.

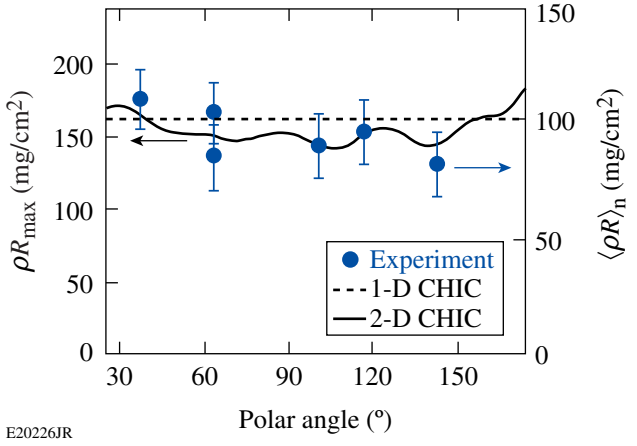

Figure 128.66
Simulated (curves) and measured areal density (circles) as functions of the polar angle. The dashed line is from a 1-D simulation and the solid curve from a 2-D hydrodynamic simulation with the code CHIC.[58]

The effect on the (a) measured and (b) simulated neutron yields is shown in Fig. 128.67 for various spike-onset times. The different symbols represent various focus conditions. Implosions with only 40 drive beams (i.e., no spike beams) produced ~1.5×10^9 neutrons [solid line in Fig. 128.67(a)]. Adding the 20 spike beams enhanced the yield by a factor of up to 2.3, with a trend of lower yields at later times. There is no significant dependence on intensity with the total energy kept constant. A similar trend is observed in the predicted neutron yield [Fig. 128.67(b)]. The enhancement in the simulation is up to a factor of ~3.5 when adding the spike beams because of the extra energy delivered to the target. The yield-over-clean ratio, defined as the measured to predicted neutron number, is about 3% to 5%.

The hard x-ray detector provides information on the hot-electron number and temperature. The hot-electron temperature was determined by fitting estimated values from the convolution of an exponentially decaying hard x-ray spectrum with the sensitivity of the different channels to the measurements in the four channels.[63] The inferred temperature was 45±5 keV for all

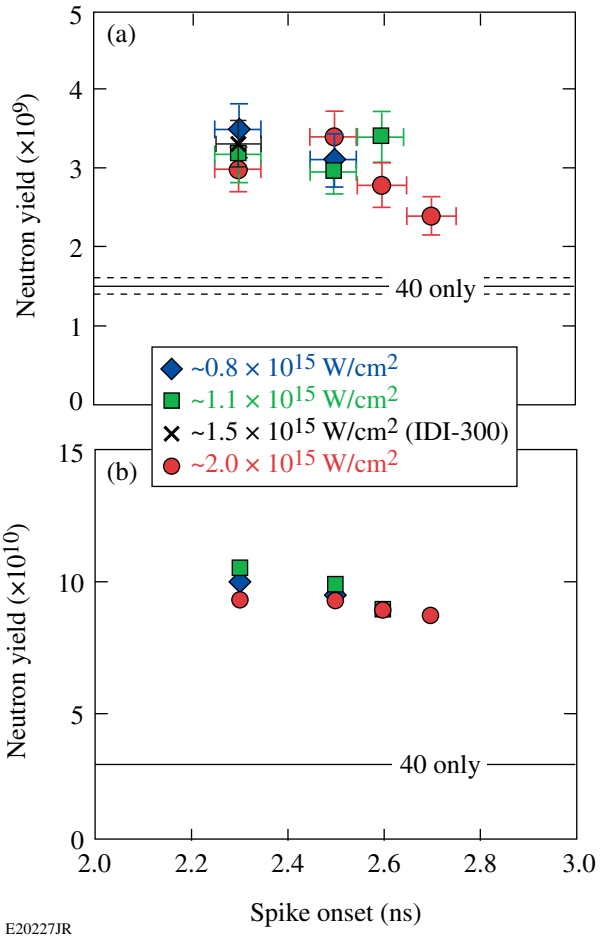

Figure 128.67
(a) Measured and (b) 1-D–simulated neutron yields in 40 + 20-beam implosions for various spike onset times and spike intensities.

shots without phase plates, independent of laser intensity. A low hot-electron temperature is beneficial for shock ignition since these electrons are stopped in a thin outer layer of the imploding target, augmenting the strong hydrodynamic shock. The plasma reflectivity was measured for various laser intensities. Figure 128.68 shows the measured fraction of laser backscatter energy of one shock beam for various laser intensities as a function of the spike onset. No significant variation is observed with spike onset. The reflectivity increases from ~8% at ~0.8×10^{15} W/cm^2 to ~35% at ~8×10^{15} W/cm^2. The simultaneously measured back-reflection through a neighboring drive-beam port remained constant at the level of implosions without the 20 spike beams for all beam delays and lens positions. This shows that the light from the spike beams was scattered back in a narrow cone and that there was no significant spill over into adjacent ports.

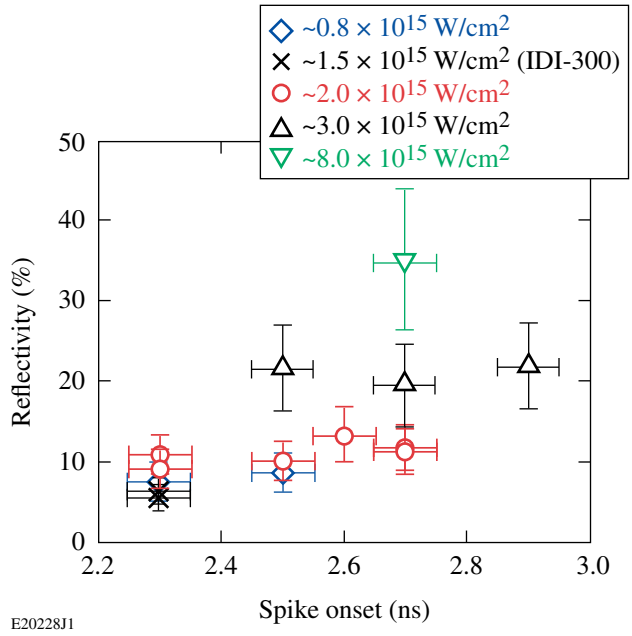

Figure 128.68
Percentage of the laser light reflected back into the solid angle of the focusing lens for various intensities and delay times.

FY11 LLNL OMEGA Experimental Programs

In FY11, LLNL conducted several campaigns on the OMEGA and OMEGA EP Laser Systems, as well as campaigns that used the OMEGA and OMEGA EP beams jointly. Overall, LLNL led 301 target shots involving OMEGA and 81 target shots involving OMEGA EP (not including LLNL-led shots under the LBS program). Approximately 35% of the shots (126 OMEGA shots, 10 OMEGA EP shots) supported the National Ignition Campaign (NIC). The remainder were dedicated to experiments for high-energy-density (HED) physics (168 OMEGA shots, 72 OMEGA EP shots).

Objectives of the LLNL-led NIC campaigns at OMEGA included the following:

- Characterization of long-pulse, high-resolution, laser-produced backlighters
- 4ω Thomson scattering
- Neutron-induced backgrounds for ARIANE
- Thermal-conductivity measurements at a heated CH/Be interface by refraction-enhanced x-ray radiography
- 18-keV x-ray Thomson scattering of shock-compressed beryllium and aluminum
- High-resolution measurements of velocity nonuniformities created by microscopic perturbations in NIF ablator materials
- X-ray Thomson scattering of shock-compressed beryllium on OMEGA EP
- Pb Hohlraums
- Surrogate mix targets with dual backlighting

The LLNL-led HED campaigns covered four main areas of research:

1. Material dynamics and equation of state
   a. Kr Hugoniot measurements to 730 GPa
   b. Ramped compression of different materials
   c. Tin melt
   d. Powder x-ray–diffraction measurements of solid Fe and Ta to 570 GPa
   e. Hohlraum diffraction
   f. Equation of state for foams
   g. Gigabar equation of state
   h. Double pulse
   i. Dynamic and lattice diffraction
   j. Tantalum Rayleigh–Taylor experiments
   k. ICEDrive-11A/ICEHohl-11A
   l. Strength diffraction

2. High-temperature plasma opacity
   a. High-temperature plasma opacity experiments on OMEGA and OMEGA EP

3. Hydrodynamics
   a. Short-pulse, UV backlighting development for the NIF
   b. Backligh ting experiments on OMEGA

4. X-ray source development and application
   a. Iron K-shell x-ray source development
   b. Solar-cell electrostatic discharge

This work was performed under the auspices of the U.S. Department of Energy by Lawrence Livermore National Laboratory under Contract DE-AC52-07NA27344.

National Ignition Campaign Experiments

Characterization of Long-Pulse, High-Resolution-Laser–Produced Backlighters
Principal Investigator: R. Tommasini

In FY10 we characterized short-pulse bremsstrahlung backlighters produced by 10-ps, 1ω laser pulses from the OMEGA EP laser. Using these pulses, we successfully dem-

onstrated Compton radiography of direct-drive implosions of spherical-shell and cone-in shell targets. The cone-in-shell targets are of interest for fast ignition.

In FY11 we characterized long-pulse Bremsstrahlung backlighters produced by 100-ps, 3ω laser pulses from the OMEGA laser. These x-ray sources are of interest for the earliest implementation of Compton radiography on the NIF.[65] The backlighters were produced by overlapping up to 18 100-ps, 3ω OMEGA laser beams with a total power ~8 TW to match or exceed single NIF 3ω quad intensities onto 300-μm-long, 10-μm-diam Au microwires.

The conversion efficiency of the backlighters, into 70- to 200-keV x rays, was measured using an annular step-wedged filter hosted in the custom-built Compton radiography snout (CRS). Figure 128.69 shows a comparison of the conversion from 1ω, 10-ps- (dots) and 3ω, 100-ps- (squares) laser-produced, 10-μm-diam Au backlighters. This target gives conversion efficiencies between 1×10^{-5} and 3×10^{-5}, in the available intensity range 3×10^{16} to 1×10^{17} W/cm^2. As observed, these conversion efficiencies are typically a factor of 7 to 10 less than for planar-foil targets and consistent with the ratio of wire area to laser-spot area. They are also ≈7× less than for 1ω sources at the same intensity, ascribed to the $I\lambda^2$ dependence of hot-electron production. Such efficiencies at 3ω should be sufficient to measure fuel areal densities and radii to 7% accuracy at 20-μm spatial scales on the NIF and to observe 20% fuel areal density and shape nonuniformities up to mode 4.

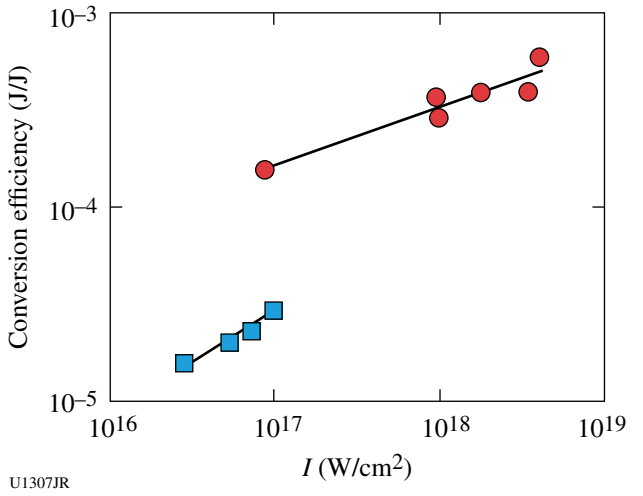

Figure 128.69
Conversion efficiency as a function of laser intensity into 70- to 200-keV x rays from 1ω, 10-ps (dots) and 3ω, 100-ps (squares) laser-produced, 10-μm-diam Au backlighters.

The source size of the 3ω backlighters was measured by fitting experimental radiographic transmission lineouts of tungsten-carbide spheres to simulated radiographs for Gaussian-shaped sources using the spectra measured by the CRS step wedge. This method resulted in typical Gaussian FWHM source sizes of (11±2) μm, in all cases close to the diameter of the Au wires. The pulse durations were inferred from an x-ray streak camera measuring the emission from Au in the spectral region above 3 keV to be 100±5 ps.

4ω Thomson Scattering

Principal Investigator: S. Ross

The 4ω Thomson-scattering measurements were made from foil (shown in Fig. 128.70) and hohlraum targets to determine plasma conditions. Figure 128.71 shows the measurement of Thomson scattering from the ion-acoustic wave (ion feature) and the electron-plasma wave (electron feature) resonances using a 4ω probe beam from a CH-foil target. From the scattered spectra, the electron density, temperature, plasma flow velocity, and ion temperature are measured.

Measurements from foil targets produced excellent data. Hohlraum targets proved more difficult because of the complex target geometry, which produced increased background and

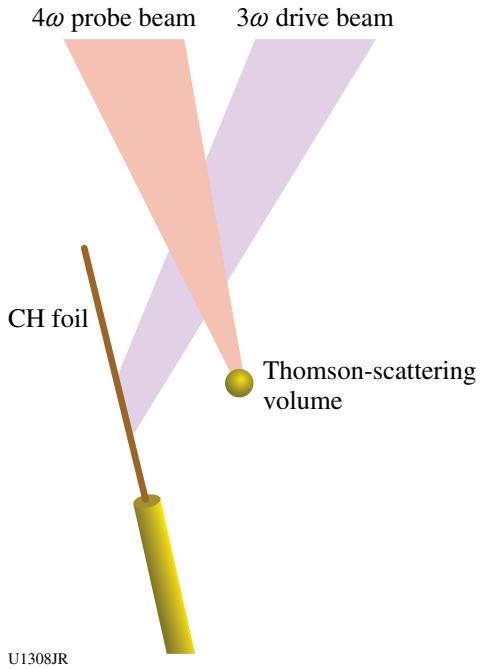

Figure 128.70
The foil-target configuration.

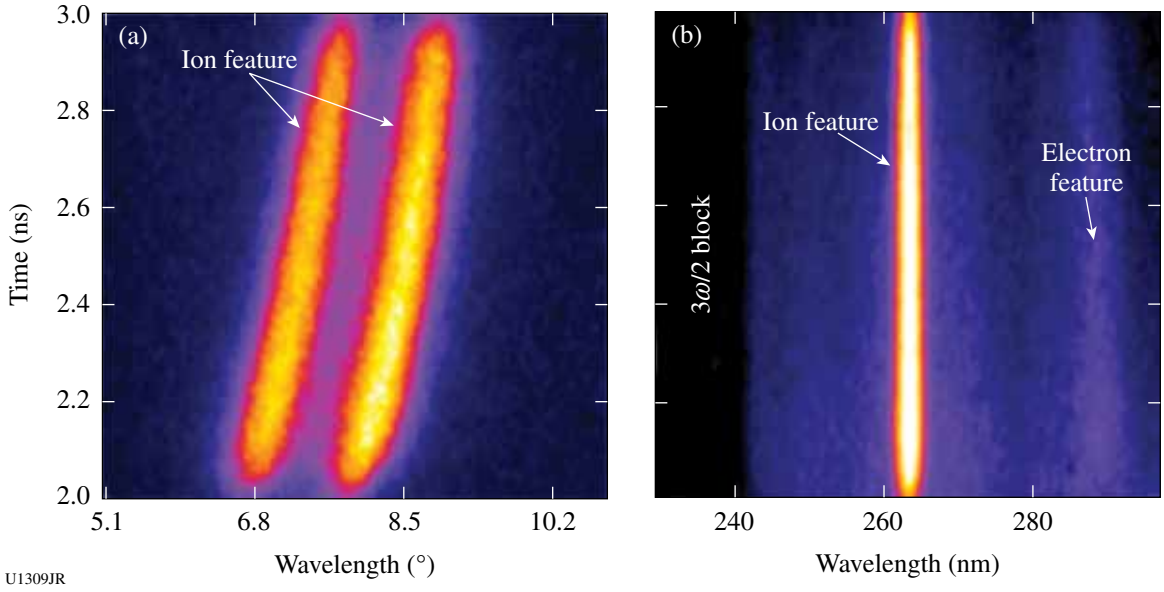

Figure 128.71
Streaked Thomson-scattering data from the resonances of (a) an ion-acoustic wave and (b) an electron-plasma wave.

inhibited probe-beam propagation. The Thomson-scattering diagnostic was activated successfully, and the measurements made from foil and hohlraum targets will be used to improve experimental and diagnostic design for upcoming experiments planned for FY12.

Neutron-Induced Backgrounds for ARIANE

Principal Investigator: V. A. Smalyuk

X-ray imaging instruments will operate in a harsh ionizing radiation background environment on implosion experiments at the NIF. These backgrounds consist of mostly neutrons and gamma rays produced by inelastic scattering of neutrons. The experiment was designed to measure these backgrounds generated in some of the components of x-ray framing cameras used in the ARIANE imaging system: phosphors, fiber-optic plates, and T-MAX 3200 film. The experiment consisted of six implosions with 1.5-mm-outer-diam, 4-μm-thick glass shells filled with 5 atm of DT gas, driven with 60 OMEGA beams with a total UV energy of ~28 kJ. Measured DT neutron yields were in the range from $\sim 3 \times 10^{13}$ to $\sim 4 \times 10^{13}$. Fiber-optic plate samples were coated with five different phosphors (P-11, P-20, P-43, P-46, and P-47) and placed in the OMEGA target chamber at ~21 and ~42 cm from target chamber center. Neutron-induced background signals were detected on T-MAX 3200 film. Figure 128.72 shows an example of the film data, with measured backgrounds in P-43 phosphor, fiber-optic plate, and film (lighter area) and with film only (darker area). Figure 128.73(a)

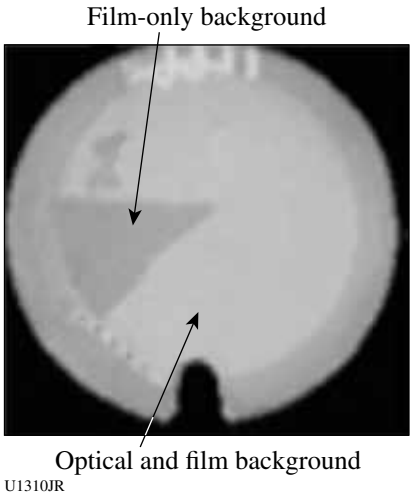

Figure 128.72
Measured optical backgrounds in P-43 phosphor, fiber-optic plate, and film (lighter area); and with film only (darker area).

shows the background intensity as a function of DT neutron exposure measured in P-43 phosphor, fiber-optic plate, and film (diamonds with exponential fitting shown with a solid curve) and in film only (triangles with exponential fitting shown by a dashed curve). Figure 128.73(b) shows background intensity in a fiber-optic plate with a film (diamonds) and in film only (triangles). Measured total backgrounds in samples with P-11, P-46, and P-47 phosphors were similar, with ~50% generated in film, ~20% in fiber-optic plates, and ~30% in phosphors. The

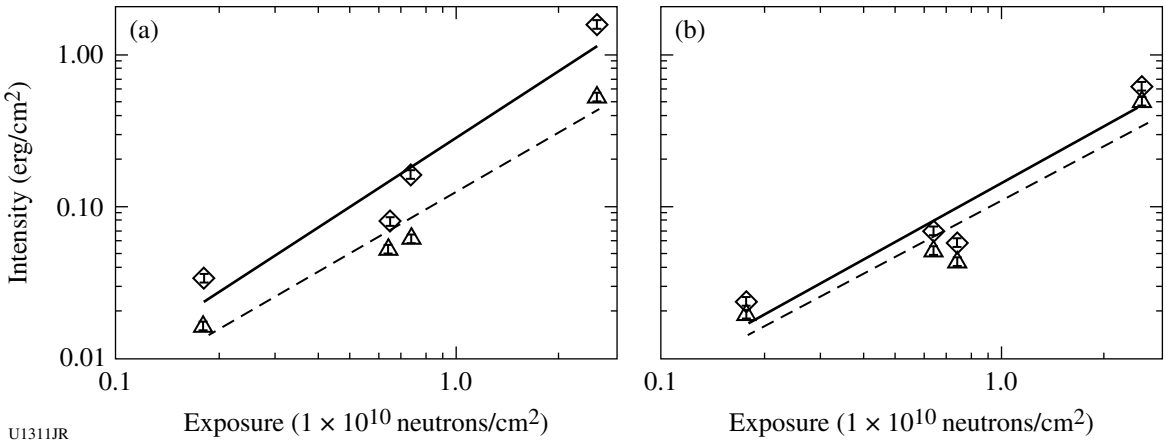

Figure 128.73
(a) Background intensity as a function of DT neutron exposure measured in P-43 phosphor, fiber-optic plate, and film (diamonds with exponential fitting shown with a solid curve); and in film only (triangles with exponential fitting shown with a dashed curve). (b) Backgrounds in fiber-optic plate with a film (diamonds), and in film only (triangles)

total backgrounds generated in both P-20 and P-43 phosphors were about a factor of 1.5 larger than in samples with P-11, P-46, and P-47 phosphors. Based on these measurements, the maximum peak signal is predicted to be about 5× higher than the background for an ARIANE framing camera using P-11 phosphor and film for NIF shots with DT yields of 4×10^{16}. Such a background will be manageable when measuring the shape of the implosion core.

Thermal-Conductivity Measurements at a Heated CH/Be Interface by Refraction-Enhanced X-Ray Radiography
Principal Investigator: Y. Ping

A new series of campaigns are aimed at thermal conductivity measurements at the CH/Be interface under conditions relevant to the NIC target design, where the Be is a surrogate for DT. A novel technique, refraction-enhanced slit projection x-ray radiography, was successfully implemented to measure the evolution of the density profile at a cylindrical CH/Be interface, which was isochorically heated by Ag, L-band, 3-keV radiation. High-quality radiographs enabled us to determine the density gradient near the CH/Be interface from the fringe contrast with 2-μm-level accuracy, from which the thermal conductivity will be inferred (Fig. 128.74). In addition to the expected density evolution caused by thermal conduction, counter-propagating shock and rarefaction waves were also observed and their velocities were measured simultaneously. The multiple observables with the same diagnostic will strongly constrain the equation of state (EOS) of CH/Be and the temperatures after heating. A technical paper based on this

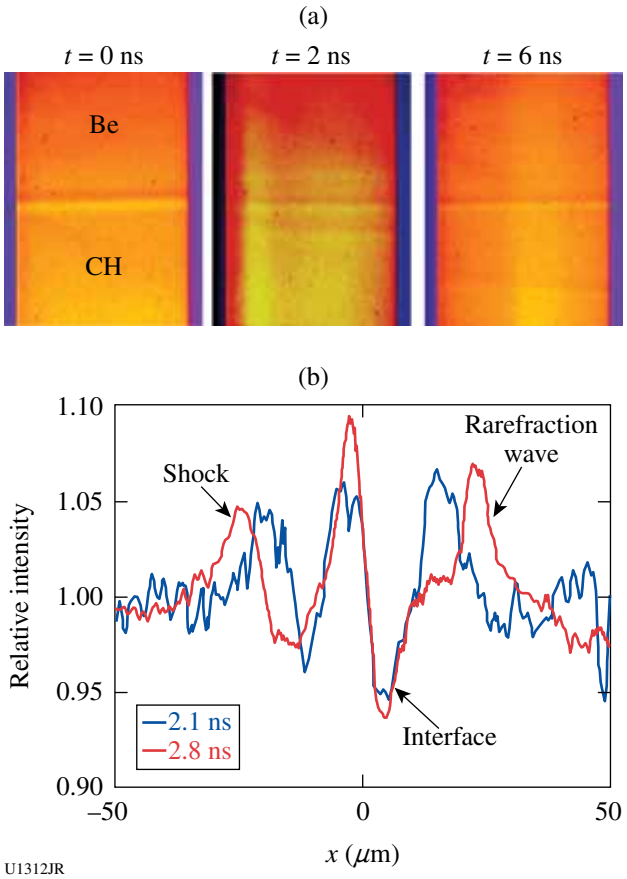

Figure 128.74
(a) 5.4-keV radiographs at $t = 0$, 2, and 6 ns. (b) Lineouts of two frames taken in one shot, showing the shock wave and rarefaction wave counter-propagating from the interface.

campaign has been published,[66] and data are being analyzed to benchmark the transport models in NIC design codes. In FY12 this experimental design will be extended to include cryogenic cells for measuring thermal conductivity of D_2, which is critical for assessing hydro-instability margins during ICF implosions.

18-keV X-Ray Thomson Scattering of Shock-Compressed Beryllium and Aluminum

Principal Investigator: T. Ma

The accurate characterization of material properties under extreme conditions is an important issue for understanding high-energy-density states of matter. We performed two experiments on OMEGA in FY11 in which spectrally resolved x-ray Thomson scattering at 18 keV was used to determine the electron density and temperature of shocked Be and Al. Targets of 125-μm solid beryllium and aluminum were shock compressed to high density (>3× solid density) using nine beams with a total energy of 4.5 kJ in a stacked 1-ns or 3-ns configuration. SG4 distributed phase plates were used to achieve a smooth 800-μm focal spot, yielding a total drive intensity of 3×10^{14} W/cm^2 on the sample.

The materials were probed in the noncollective scattering regime using Mo 2-1 line radiation x rays at ~17.9 keV. In the first portion of the campaign (BeXRTS-11A), the scattering angle was held constant at 90°, while scattering was performed on undriven and driven Be and Al.

In the case of beryllium scattering, both the driven and undriven cases showed, as expected, depressed elastic scattering attributed to the fact that the ionization potential of Be electrons is less than the Compton energy ≈600 eV. Fits to the ratio of elastic to inelastic peaks for the undriven data gave a Z of ~1.5 to 2 [see Fig. 128.75(b)], in agreement with Ref. 67. In the case of Al, the unshifted Rayleigh scattering increased when driving the Al sample, attributed to increased disorder in the heated lattice [see Fig. 128.75(c)]. It was found that the ratio of the elastic to inelastic scattering features in the shocked Al were very sensitive to the ionization potential of the L-shell electrons (when Compton energy > ionization potential of L-shell electrons, these electrons contribute in the same way as free electrons, and only the two K-shell electrons will Rayleigh scatter).

For the last series (BeXRTS-11B), Mo 2-1 line radiation was again employed as an x-ray probe while the scattering angle was varied from 25° to 155° (Compton energy from 60 eV to 1.2 keV). This allowed us to assess the sensitivity to continuum lowering and measure the angularly resolved strength of the static structure factor. Experimental data were found to corroborate the code predictions: at smaller scattering angles, the Compton feature was merged into the Rayleigh, while the relative strength of the inelastic feature grows at a higher scattering angle.

High-Resolution Measurements of Velocity Nonuniformities Created by Microscopic Perturbations in NIF Ablator Materials

Principal Investigator: P. M. Celliers

This campaign focused on three aspects of NIF ablators: (1) continue the survey of NIF Rev5 Ge-doped CH samples (seven shots), (2) continue the survey of diamond samples near the melt curve (two shots), and (3) perform the first test measurements of double-shocked diamond samples (two shots). For the CH samples we also tested a simplified target design in which the shock was transmitted from the ablator directly into the fused-silica window instead of the polymethylmethacrylate (PMMA) layer that was used in previous designs. The results showed that the shock-front reflectivity in the fused-silica window is too low to produce high-quality data, so future designs will continue to use the PMMA layer to capture the shock-front nonuniformities. The two single-shock experiments on diamond samples were designed to probe into the shock-melt region (about 600 GPa), and the results confirmed that partial shock melting produced much smoother shock fronts than lower-amplitude shocks that do not melt the sample. Finally, the two shots on double-shocked diamond were performed to test the drive and measure timing information in preparation for a more-extensive future series. On the first shot, the second-shock overtake was clearly observed (Fig. 128.76); however, the probe was synchronized too early to capture the second-shock overtake event. For the second shot, the probe was adjusted to capture the data just after the second shock overtook the first. On this shot we recorded the first data on shock-front perturbations from double-shocked diamond. This information will be used to design a more-comprehensive future campaign to assess diamond ablators up to the second shock level.

X-Ray Thomson Scattering of Shock-Compressed Beryllium on OMEGA EP

Principal Investigator: A. Pak

This year, two shot days with a total of ten laser shots were used to study laser-shock–compressed beryllium using noncollective x-ray Thomson scattering (XRTS) on OMEGA EP. The primary goal of the first series of this campaign (EPXRTS-11A)

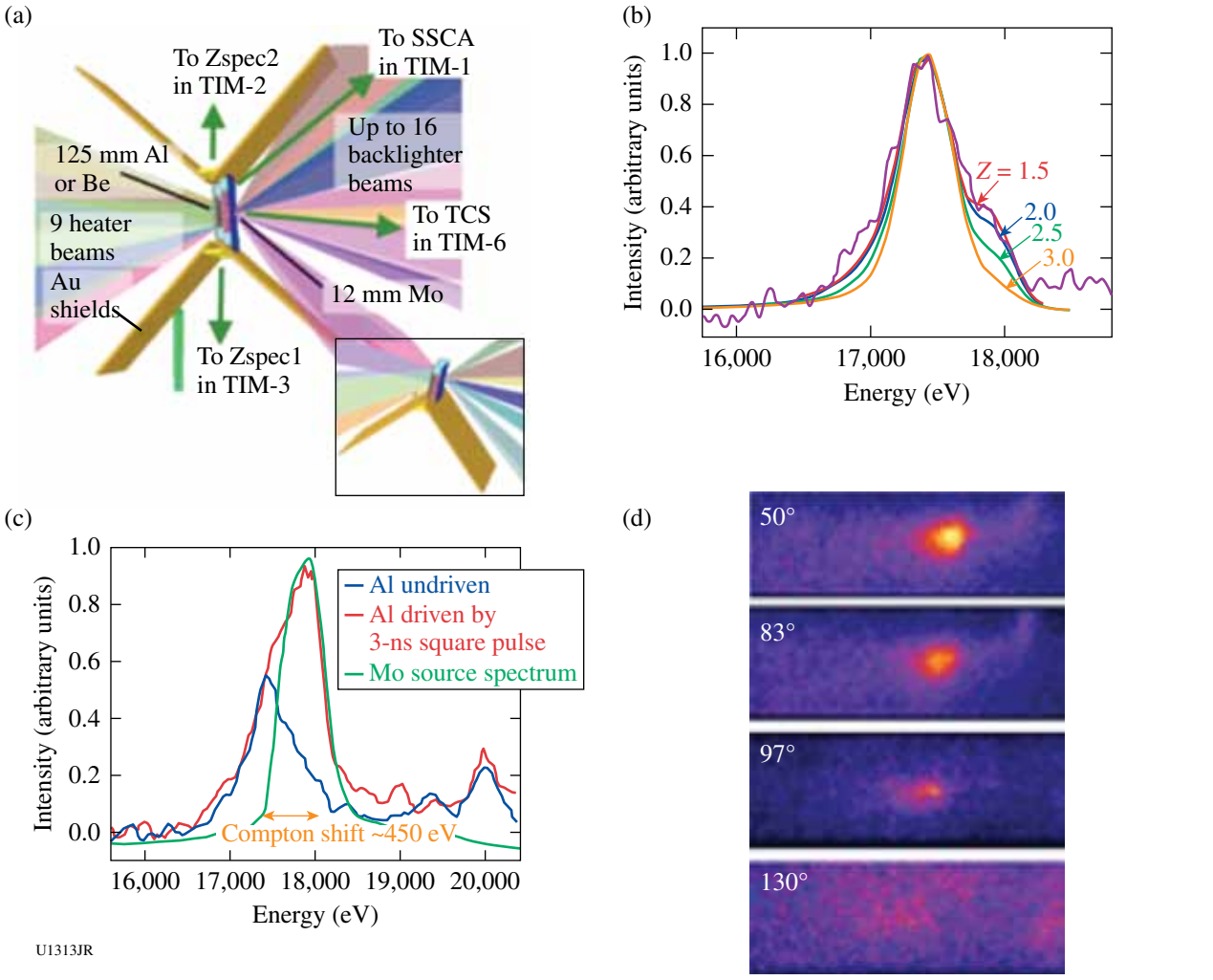

Figure 128.75
(a) The experimental configuration for BeXRTS-11B. Inset shows the single-wing, 90° configuration used in BeXRTS-11A. (b) Fits to the undriven beryllium scattering versus Z. (c) Comparison of source spectrum (green), undriven Al (blue), and driven Al (red) scattered spectra. (d) Al scattering versus increasing scattering angle (scattering k).

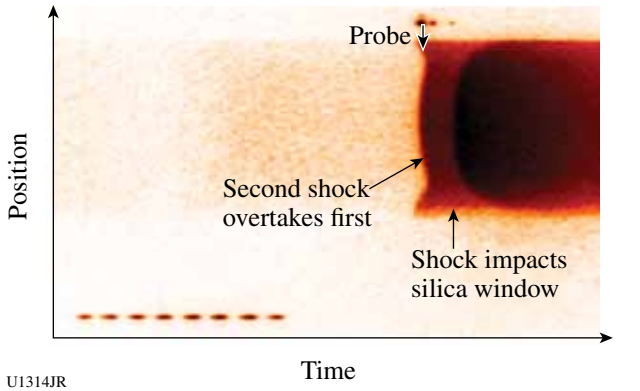

Figure 128.76
Streak record showing the second shock overtake and OHRV (OMEGA high-resolution velocimeter) probe timing for a two-shock drive applied to a noncrystalline diamond ablator sample.

was to develop a suitable experimental platform to study laser-shock–compressed matter with XRTS. Four laser shots were taken to test two scattering targets and two drive conditions. Only one of the scattering targets produced a scattering signal (shown in Fig. 128.77). The goal of the second shot day (EPXRTS-11B) was to use noncollective XRTS at two scattering angles to measure the change in the temperature of the shocked beryllium as the laser's drive-pulse shape was changed from a super-Gaussian shape to a ramped-adiabatic shape. Again four shots with two scattering targets were taken, but a clean scattered spectrum was not measured from this campaign. It is thought that a change in laser-beam configuration prevented the successful scattering target from EPXRTS-11A from producing a scattered signal. The second scattering target, which was modified to reach smaller scattered angles, allowed

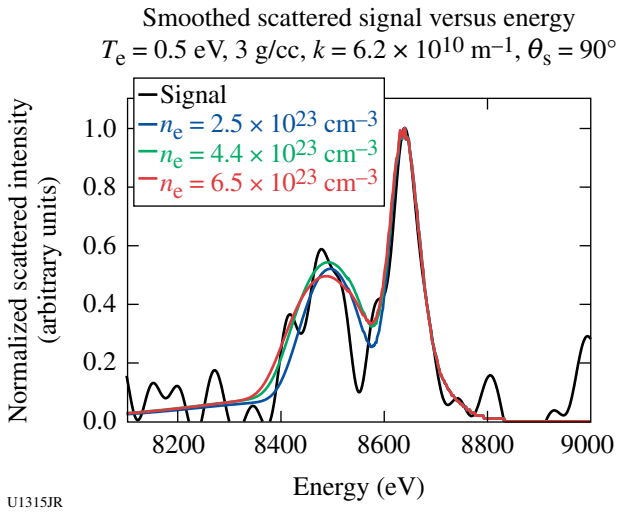

Figure 128.77
Measured scattered signal from EPXRTS-11A (black) versus scattered energy. Here Zn–K_α x rays at 8.64 keV elastically and inelastically scatter through a Be target that has been shocked by a laser with an $I_0 \approx 1 \times 10^{13}$ W/cm^2. Three theoretical scattered spectra are plotted versus energy as a function of density, at a fixed temperature and scattering angle.

for unscattered x rays to reach the detector, preventing a clean scattered signal from being measured.

Pb Hohlraums

Principal Investigator: S. Ross

A comparison of Pb and Au hohlraums shows very similar performance for three shaped laser pulses. The point design for laser inertial fusion energy (LIFE) targets relies on Pb as the primary hohlraum material. Lead and gold hohlraums are predicted to have similar performance and are the first measurements to validate those predictions. The hohlraum performance was measured using Dante to determine the hohlraum radiation temperature (Fig. 128.78) and a full-aperture backscatter station (FABS) to measure the backscattered energy. Both diagnostics show no measurable difference between Pb and Au.

Neutron yield (shown in Fig. 128.79) was also used to assess hohlraum performance, and again Pb and Au hohlraums produced very similar results. These experiments are a successful first step in validating Pb as a viable hohlraum material for a LIFE point-design target.

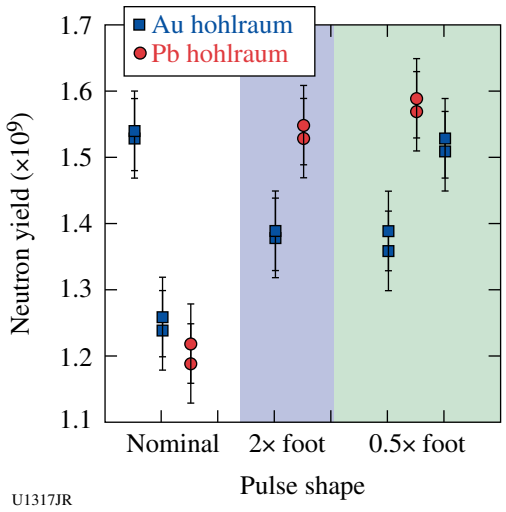

Figure 128.79
The neutron yield is compared for three pulse shapes for the Au and Pb hohlraums.

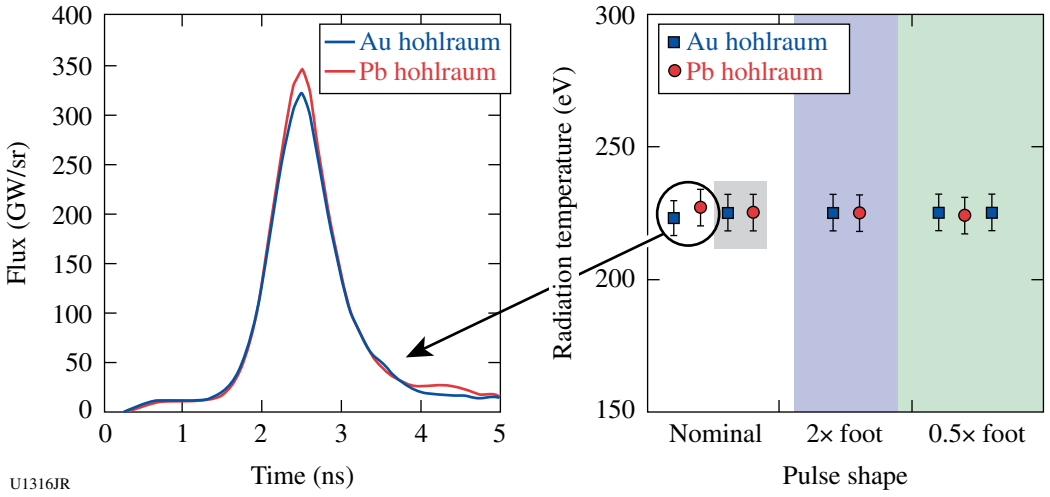

Figure 128.78
Time-resolved Dante flux and peak radiation temperature for Pb versus Au hohlraums.

Surrogate Mix Targets with Dual Backlighting
Principal Investigator: D. Farley

On 13 January 2010 a half day was devoted to OMEGA experiments to test two-color radiography of surrogate mix samples as a means of assessing both density and concentration. The backlighters and surrogate-mix materials were paired so that the backlighter resonance line energies straddled the K edge of one material, while both energies stayed either below or above the K edge of the other material. One type of surrogate mix target used Cu and Ge thin foils mounted on a CH block, which was backlighted separately by Cu (8.4 keV), Ge (9.6 keV), or Zn (9.0 keV) backlighter materials (see Fig. 128.80). This type of surrogate-mix target simulates dopant levels at peak velocity for Ge- and Cu-doped plastic capsules. The other type of surrogate-mix target consisted of Si and Ge foils mounted on the same-sized block of CH to simulate Si and Ge dopants in a CH capsule, paired with Cu and Zr backlighters. Since Zr helium-like emission peaks at ~16.4 keV, it should transmit through Si-doped CH slightly better than Ge-doped CH with no noticeable transmission difference in the overlapped Si/Ge foil region, but there should be an observable change in transmission in the Si/Ge (or Cu/Ge) 100-μm overlapped region for the 8.4-keV Cu backlighter emission. Therefore, comparison of the transmission profiles of the two backlighters would provide an indication of mix width; however, the Zr laser–to–x-ray conversion efficiency will be quite low.

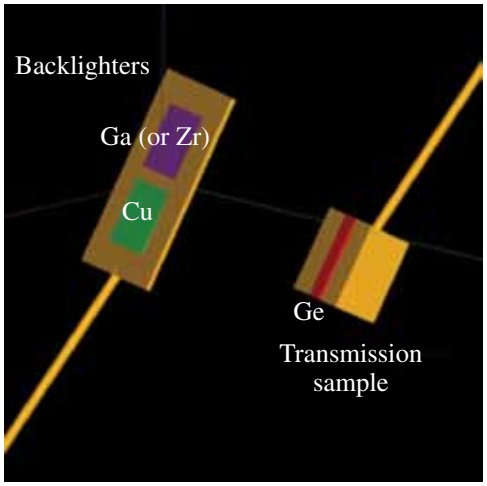

U1318JR

Figure 128.80
Setup of the experiment showing dual backlighters and mix target [Si or Cu on back side of transmission sample (not shown)]. The mix foils overlap ~100 μm when viewed face-on by camera.

C. Reverdin and F. Girard from CEA assisted in these experiments by providing diagnostic support for their CEA x-ray crystal spectrometer (XCCS), which had the spectral range to cover the Zr emission up to ~17 keV. A collection of spectra from the XCCS spectrometer is shown in Fig. 128.81. From this spectral result, the Zr conversion efficiency was estimated at 0.04%, at least 10× lower than for Cu. The transmission profile for the Cu backlighter through the simulated mix sample was as expected. Further work is needed to determine the best dopant–backlighter pairing, but clearly we would have preferred a lower Z such as As or Se, if feasible.

High-Energy-DensityExperiments
1. Material Dynamics and Equation of State

Kr Hugoniot Measurements to 730 GPa
Principal Investigator: J. R. Rygg

Experimental measurement of the Kr Hugoniot was extended up to 730 GPa by launching shocks into Kr samples precompressed in diamond anvil cells to ~0.5 GPa (see Fig. 128.82). VISAR (velocity interferometer system for any reflector) and SOP (streaked optical pyrometer) measurements of the Kr shock front in comparison to concomitant measurements in quartz were used to infer pressure, density, reflectance, and temperature of shocked Kr. In addition, Hugoniot measurements on solid CO_2 precompressed to 1.0 GPa were compared to previous liquid CO_2 measurements to infer Gruneisen Γ of 0.5 and isochoric specific heat of 4.0 k_B/atom for CO_2 ρ, T of 4.5 g/cc, 4 eV.

Ramped Compression of Different Materials
Principal Investigator: R. Smith

The goal of this experiment (RampComp-11A) was to measure the stress–density response of a nanodiamond step target through an indirect-drive ramp-compression technique. As shown in the inset of Fig. 128.83, the target geometry consists of an Au hohlraum with a multistepped diamond sample attached to the back. The target was aligned on the H7–H14 axis on OMEGA. Fifteen beams with 300-μm elliptical phase plates inserted into the beamlines were focused onto the inner walls of the hohlraum. We used a 3.5-ns ramp-laser profile (RM3502) to generate a time-dependent x-ray temperature, which translates into a ramped longitudinal stress wave propagating through the stepped diamond (30/35/40/45-μm) target. The primary diagnostic was the ASBO (active shock breakout) (VISAR), which records the free-surface velocity as a function of time, $u_{fs}(t)$, for each step. Following a Lagrangian sound speed analysis the stress–density response is calculated from the $u_{fs}(t)$ record

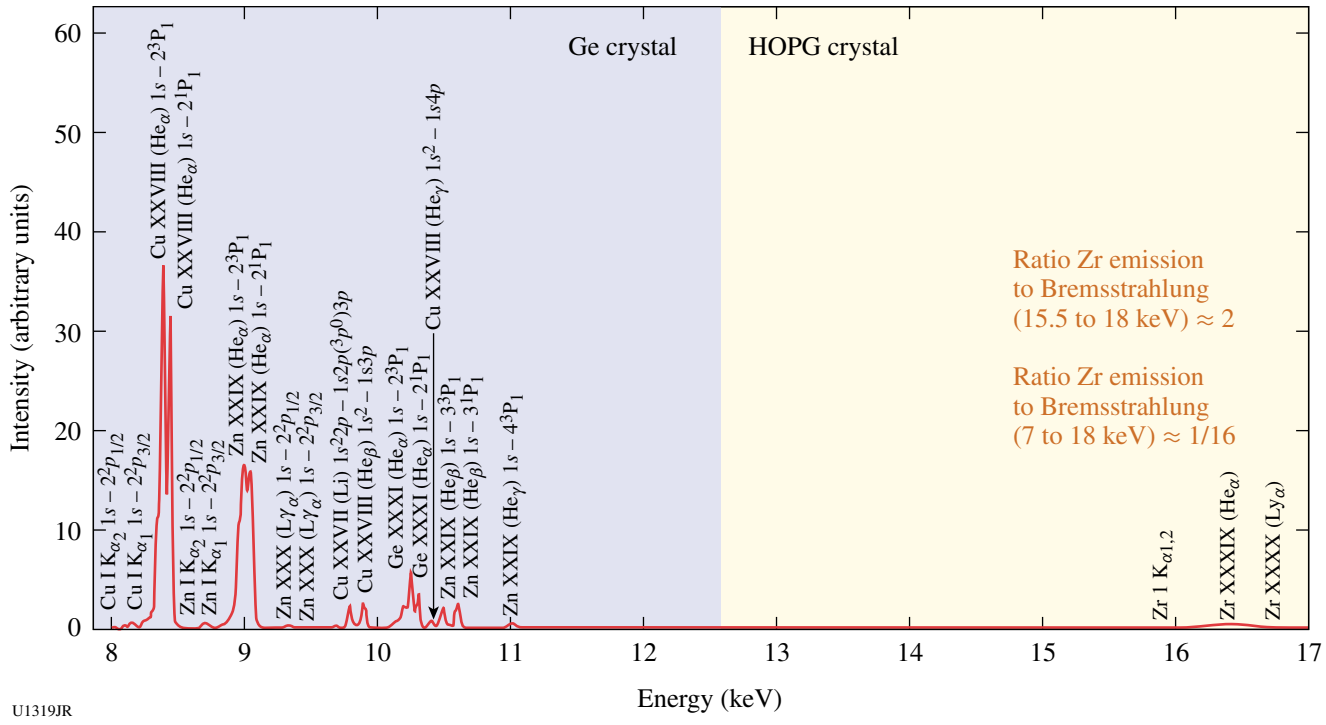

Figure 128.81
Collected spectra from TwoColorBL experiment backlighters, scaled by laser energy that was applied to each foil material. CEA XCCS spectrometer was used.

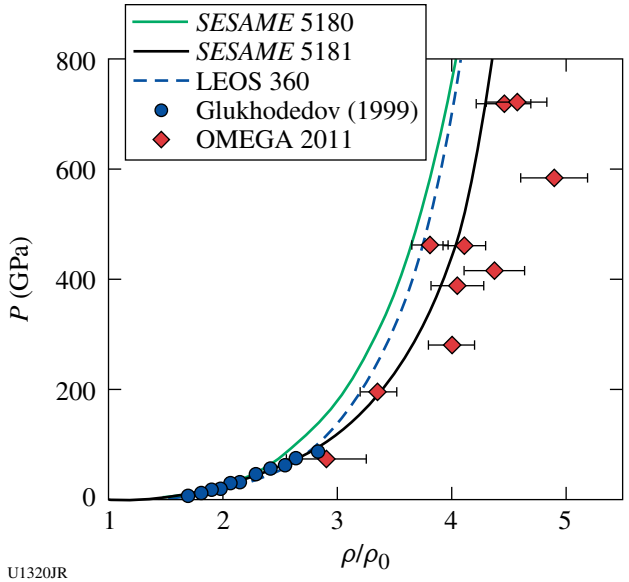

Figure 128.82
Previous experimental measurements of the Kr Hugoniot (blue dots) reached 87 GPa. In FY11, the OMEGA laser was used to extend the range to 730 GPa (red diamonds). The Kr shock pressure and density were inferred by shock-velocity measurements impedance matched to a quartz standard.

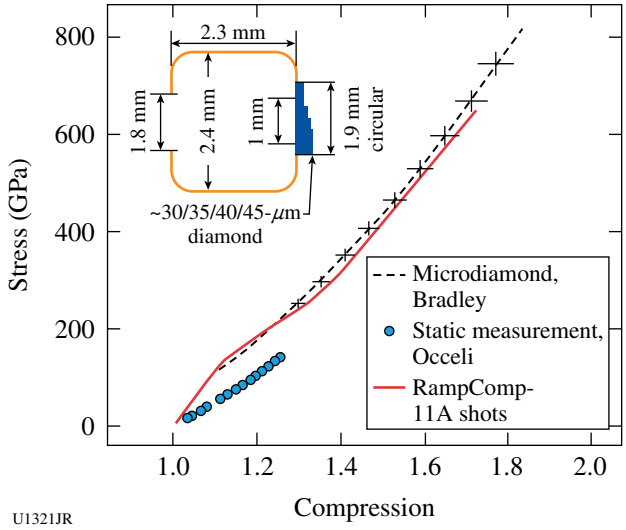

Figure 128.83
Stress–density response of a 200-nm-grain-size nanodiamond sample (red curve). This is an average of seven shots from the RampComp-11A series. Also shown are previous ramp compression data from Bradley[68] on micrograin diamond and static measurements from Occelli.[69] Shown as an insert is the target geometry for the RampComp-11A shot series.

and shown as the red curve in Fig. 128.83. Also shown are previously reported ramp-compression data of Bradley[68] on micrograin data and statically compressed data of Occelli.[69]

The goal of the second day of this experiment (RampComp-11B) shots was to measure the stress–density response of a Ta step target through an indirect-drive ramp-compression technique. As shown in the inset of Fig. 128.84, the target geometry consists of a Au hohlraum with a multistepped Ta sample (with 20-μm diamond ablator) attached to the back. The target was aligned on the H7–H14 axis on OMEGA. Fifteen beams with 300-μm elliptical phase plates inserted into the beamlines were focused onto the inner walls of the hohlraum. We used a 3.5-ns ramp-laser profile (RM3501) to generate a time-dependent x-ray temperature, which translates into a time-dependent ablation of a 20-μm diamond ablator. This results in a ramp longitudinal stress wave propagating through the stepped Ta (6/8/10/12-μm) target. ASBO (VISAR) records the $u_{fs}(t)$ for each step (Fig. 128.84). On the RampComp-11B series, we conducted seven shots in a half day. Using a Lagrangian sound-speed analysis technique,[68] we can extract the stress–density response of Ta to 3 Mbar. These data are currently being prepared for publication.

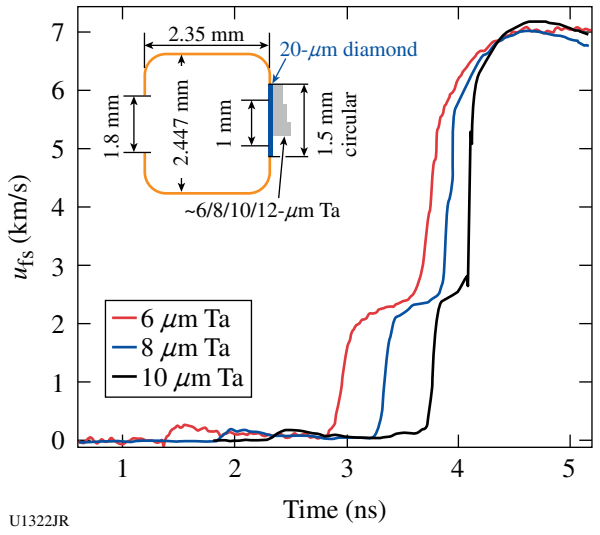

Figure 128.84
Free-surface velocity versus time, $u_{fs}(t)$, for three different thicknesses of Ta. The low-velocity precursors are a result of laser glint of hohlraum walls being absorbed at the diamond/Ta interface. The ramped plateau initiated at ~2 km/s is from the transmitted diamond elastic wave

The goal of the third shot day (RampComp-11C) was to measure the stress–density response of Fe through an indirect-drive ramp compression technique. The target geometry consists of a Au hohlraum with a multistepped diamond sample attached to the back. The target was aligned on the H7–H14 axis on OMEGA. Fifteen beams with 300-μm elliptical phase plates inserted into the beamlines were focused onto the inner walls of the hohlraum. We used a composite laser pulse shape with six beams in the RR1901 pulse shape to launch a 70-GPa shock into the sample followed 2 ns later by nine beams with the RM4002 pulse shape to ramp compress to ~300 GPa. The time-dependent laser power results in a time-dependent longitudinal stress wave propagating through the Fe. Following a Lagrangian sound speed analysis,[68] the stress–density response is calculated from the $u_{fs}(t)$ record and shown as the red curve in Fig. 128.85. Also shown are previously reported shock-compression and static measurements from Dewaele[70] and Dubrovinsky.[71]

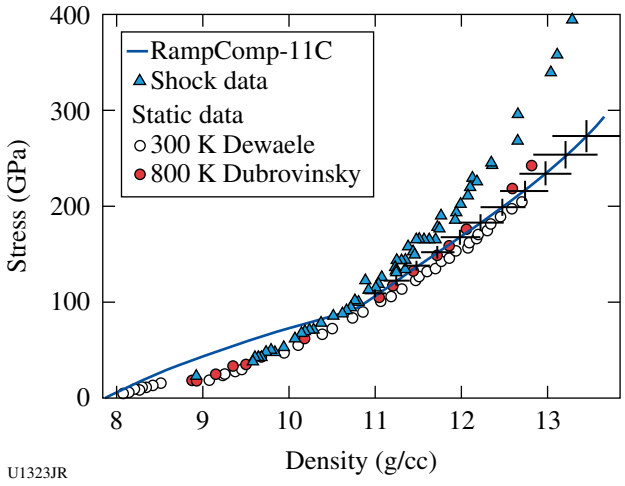

Figure 128.85
Stress–density response of Fe (blue curve). This is an average of six shots from the RampComp-11C series. Also shown are previous shock-compression data and static measurements from Dewaele[70] and Dubrovinsky.[71]

Tin Melt

Principal Investigators: J. M. McNaney and A. Lazicki

During the April 2011 tin-melt campaign, we shocked and/or ramp compressed tin prepared in diamond–tin–diamond or diamond–tin–LiF sandwiched targets, while measuring particle velocities, powder x-ray diffraction, and temperature using the VISAR, powder x-ray diffraction image plate (PXRDIP), and SOP diagnostics. One purpose of the campaign was to probe for high-pressure solid crystalline phases using pure ramp compression in order to extend the solid equation of state to higher pressure, and to look for new phase transitions. We were able to exceed 200 GPa on multiple shots, and we see a shift

in the dominant diffraction peak and the appearance of new features, indicating a phase transition (Fig. 128.86, compared with known diamond anvil cell results[72]). The second purpose of the campaign was to begin exploration of the tin melting curve by creating a pulse shape that would shock-melt tin followed by a ramp compression back across the melting curve, measuring x-ray diffraction at the end of the ramp to confirm recrystallization. We succeeded in generating a shock followed by a ramp to the desired pressures and observed a plateau in the velocity profile consistent with a phase transition such as recrystallization (Fig. 128.87). We also observed x-ray diffraction features that appeared crystalline, indicating that the phase boundary back to the solid had been crossed within the time scale of the experiment. Work is ongoing to verify these observations and to explore the solid to higher pressures and the melting curve to higher temperatures.

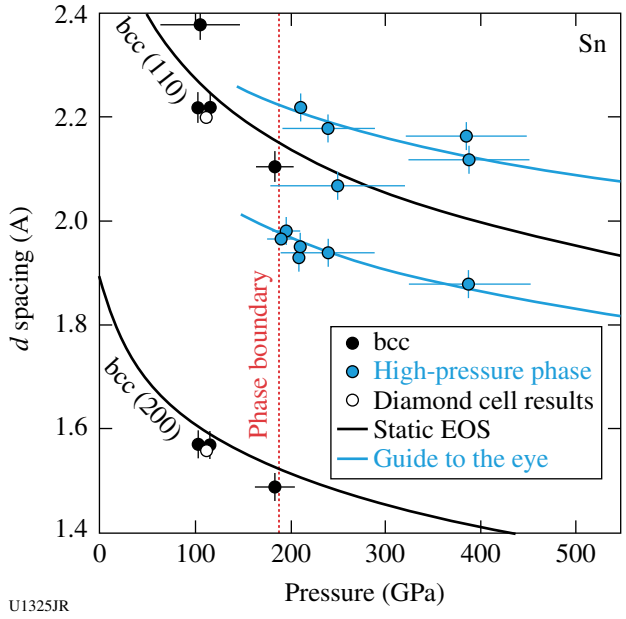

Figure 128.86
Pressure-induced shift in d spacing of different peaks of tin compared to static diamond anvil cell results.

Powder X-Ray–Diffraction Measurements of Solid Fe and Ta to 570 GPa

Principal Investigators: J. R. Rygg and J. Hawreliak

The OMEGA powder x-ray–diffraction platform was further refined in FY11 to obtain diffraction results on solid samples at pressures above Hugoniot melt, including the first detection of the highest solid–solid phase transition to date (to our knowledge) (see Fig. 128.88). Fe and Ta samples were sandwiched between a diamond pusher and window and ramp-compressed

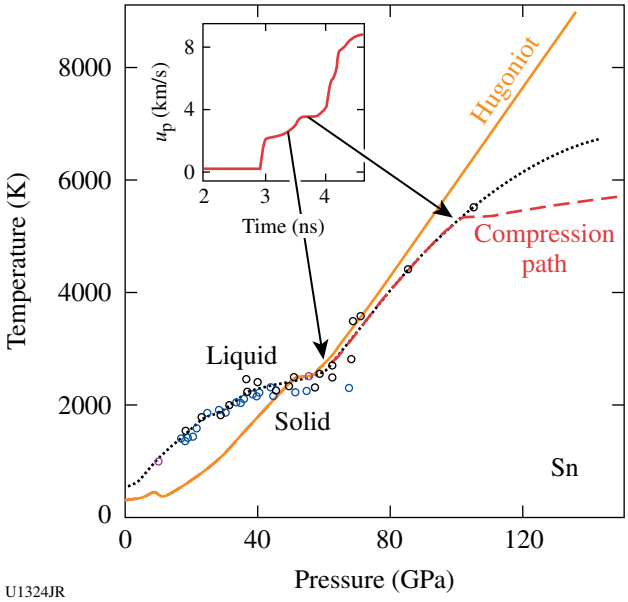

Figure 128.87
Melting curve of Sn with suggested compression path corresponding to observed velocity profile (shown in inset).

to high pressure and density using up to six beams. VISAR velocity measurements were used to infer the pressure history in the sample, and the 8.37-keV Cu–He$_\alpha$ x-ray source, driven by ten beams, was timed to coincide with the peak pressure. The diffraction signal is collimated through a 300-μm-diam aperture and captured on image plate detectors. Density is inferred from the diffraction data by assuming a crystal structure, then verifying self-consistency with a best fit to density. Fe diffraction measurements were consistent with the hexagonal close packing (hcp) phase up to 570 GPa, and an extra peak observed in Ta above 340 GPa is consistent with a phase transition from the body-centered-cubic (bcc)–to–ω phase.

Hohlraum Diffraction

Principal Investigator: J. Hawreliak

In-situ x-ray diffraction (XRD) provides a unique measurement of atomic arrangement that helps us determine the materials' lattice structure and phase, which are key components to understanding a material's equation of state. Many scientific and programmatic objectives will use XRD as a means of understanding the high-pressure state. The current materials platform on the NIF will use a hohlraum drive to load the sample. Our current diffraction techniques may not be compatible with a hohlraum drive or other planned high-pressure materials experiments on the NIF and OMEGA. The objective of this experiment (HohlDiff 11A) is to test an energy-dispersive dif-

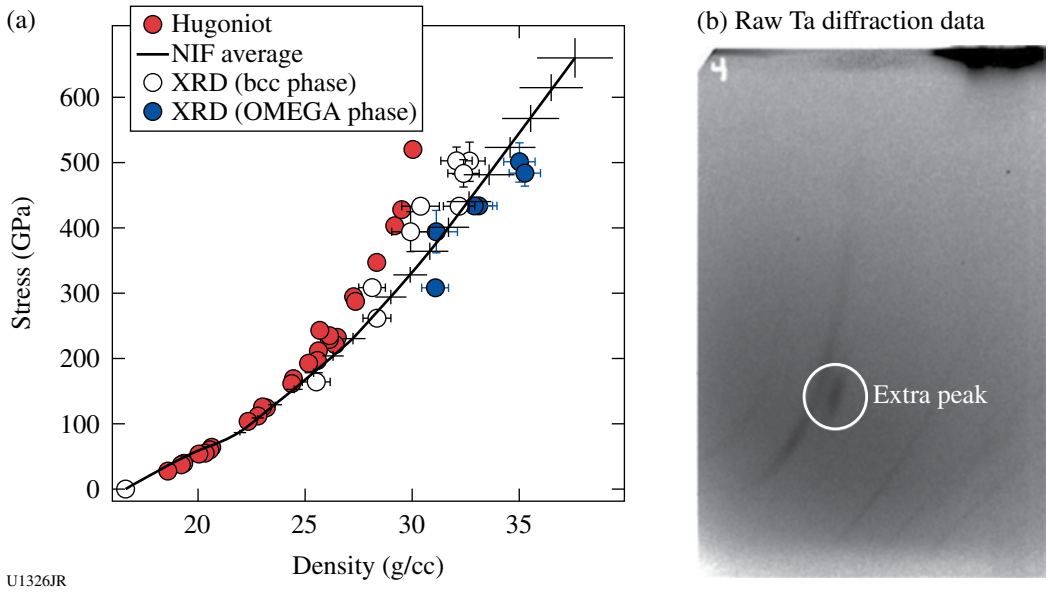

Figure 128.88
(a) Stress density of tantalum, where x-ray–diffraction (XRD) points assume either the ambient bcc phase or ω phase. (b) The appearance of an additional Ta peak for pressures above 340 GPa is consistent with a transition to the ω phase predicted by Burakovski.[73] To the best of our knowledge, this is the highest-pressure solid–solid phase transition observed to date.

fraction technique on the OMEGA EP Laser System, which may be compatible with a hohlraum drive.

The energy-dispersive diffraction technique uses a fixed experimental geometry, with a broadband x-ray source. The relative angle between the x-ray source and detector fixes the angle θ in the Bragg equation $\lambda = 2d \sin\theta$. Then peaks in the scattered energy will correspond to lattice plane spacing d. This technique has the advantage that the detector can be remote from the sample and x-ray source, and because the energy spectrum of the drive can be measured separately, it can be spectrally separated from the diffraction signal. We used the L- and M-shell emission from a cocktail backlighter source to generate a quasi-broadband x-ray spectrum and used the single-photon–counting diagnostic on the OMEGA EP Laser System as our energy dispersive detector.

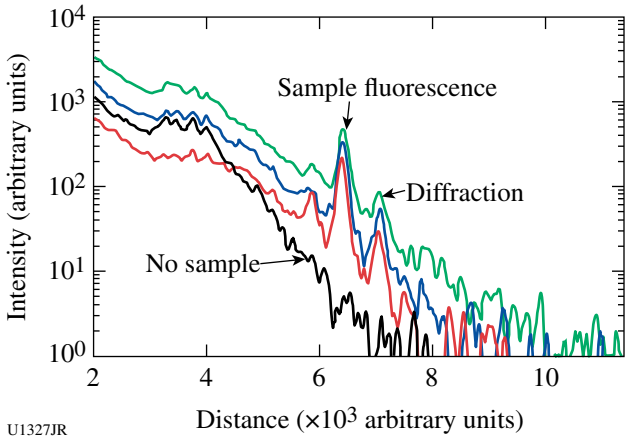

Figure 128.89
The energy-corrected single-photon–counting data from the experiment. The black line is the backlighter when there is no target sample.

Figure 128.89 shows the energy-corrected scattering data from the experiment. The black line is the backlighter when there is no target sample. The low-energy signal suggests we need to better isolate the region viewed by the detector. The remaining three traces are different shots using different backlighter energies and filtering on the detector. There is a very strong peak at ~6.4 keV, which is most likely caused by the fluorescence of the iron target sample. There are weaker peaks that begin to fall into the signal to noise, which are consistent with x-ray diffraction. We can use these results from the current configuration to determine a better experimental configuration that will yield higher diffracted photons on the detector.

Equation of State for Foam

Principal Investigator: J. Hawreliak

Low-density foams are currently being used and will continue to be used as materials in complex integrated experiments to model astrophysical phenomena, particularly for the formation and growth of density-driven hydrodynamic

instabilities. The shock response of the low-density foam is very important to the modeling, developing, and interpretation of these experiments. While velocimetry techniques have been used to measure the shock speed in transparent foams, there is a programmatic and scientific need to get a Hugoniot equation of state in opaque carbon-based foams. To do this, we will use *in-situ* radiography to measure the shock speed and shock density along with the Hugoniot conservation relations to determine the EOS.

The experiment used 16 beams to generate a Ti K-shell backlighter and four stacked beams to generate an ~10-ns drive. When the shock propagated 10 ns into the target, we recorded multiple radiographs over 1 ns using an x-ray framing camera. Figure 128.90(a) is a VISRAD representation of the experiment.

Unfortunately, because of the hot temperatures, we were only able to get two shots, but the data shown in Fig. 128.90(b) are of excellent quality. The data are currently being analyzed but a first calculation of the shock speed is ~20 km/s.

Gigabar Equation of State

Principal Investigator: J. Hawreliak

The HEDP regime is where the energy density of a system is comparable to the binding energy density of a hydrogen molecule, i.e., ~1 Mbar. We can define an atomic unit of pressure in the same fashion as the ground-state energy density of a hydrogen atom, which is ~300 Mbar. As we approach the atomic unit of pressure, we would begin to expect the core and inner shell electrons to be perturbed by the applied pressure. This will lead to novel chemistry and interesting science at high pressures. To achieve these high pressures, we used a convergent spherical geometry. Unlike a planar target, the applied shock pressure increases in strength as it approaches the center.

The experiments performed on the OMEGA laser used 40 beams on the P6–P7 axis in a hohlraum to indirectly drive a converging shock into a spherical capsule of polyacrylamide (PAM). Two backlighters were used to investigate the shock wave in the solid capsule. A gated framing camera on the P6–P7 axis was used to capture images, while an x-ray streak camera recorded a time-resolved radiograph on the axis of the capsule. Figure 128.91(a) shows a VISRAD view of the target configuration. In this configuration we can measure the equation of state by getting two points on the Hugoniot, the shock speed from the time-resolved measurement, and the density from the radiograph.

Figure 128.91(b) shows radiograph images of the shock wave in the capsule at two different times. These images were taken after the drive beams were turned off because of the x-ray signal from the hohlraum overwhelming the radiograph

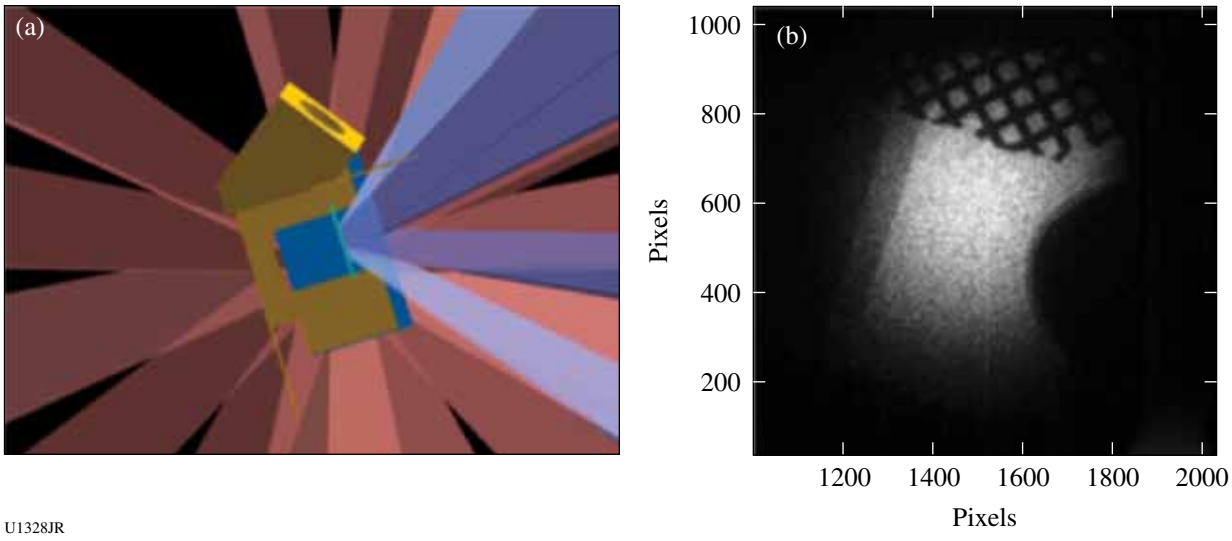

Figure 128.90
(a) A VISRAD model of the experiment from a TIM-4 view; (b) a radiograph taken using an XRFC on TIM-4.

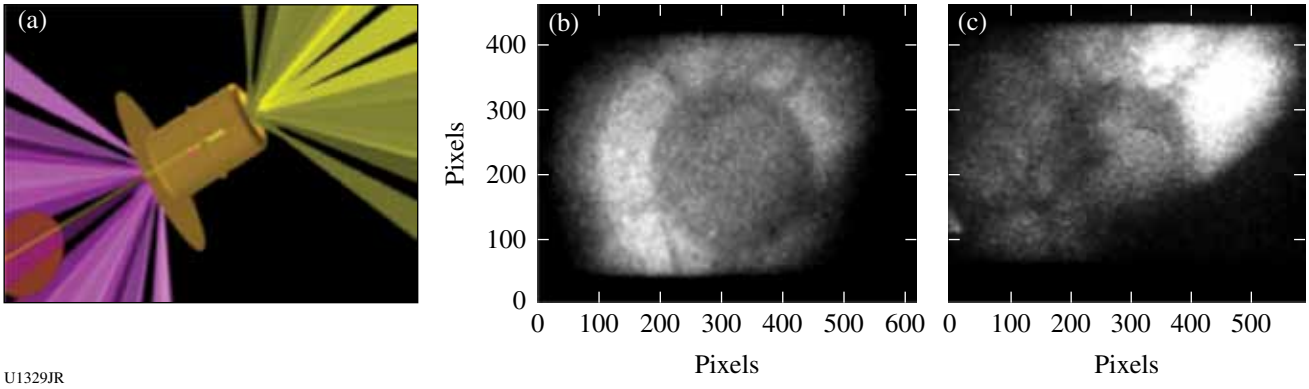

Figure 128.91
(a) A VISRAD model of the experiment, (b) a radiograph of the capsule, and (c) radiograph 1 ns later.

signal. We see clear evidence of the shock wave propagating into the capsule, so while analysis is ongoing, we estimate the shock speed to be 80 km/s.

Double Pulse

Principal Investigators: B. R. Maddox and A. Comley

The goals of this campaign were to measure the sensitivity and the modulation transfer function (MTF) of the x-ray framing camera at 8 keV and 22 keV and to measure the conversion efficiency of a Cu microflag x-ray source using a 100-ps UV pulse. To measure the sensitivity of the x-ray framing camera (XRFC), we used Cu and Ag backlighters and placed filters in front of both the HERIE detector (on TIM-13) and the XRFC (on TIM-10). The filters consisted of a Ta mask and sets of filter steps placed over holes machined into the Ta mask. For the Cu shots, the filters were Cu and Al steps, and for the Ag shots, the filters were Ag and Ta steps with an additional Mo/Pd Ross pair. For the resolution tests, targets consisted of double-ended Au resolution grids aimed at TIM-13 and TIM-10, which were backlit using 5-μm-thick Cu and Ag microflags. After a slow start and an issue with one of the Target Viewing System shutters, we were able to obtain high-quality data on all shots, resulting in data that will be used to calculate the sensitivity and resolution of the XRFC at 8 and 22 keV. Figure 128.92 shows a sample image from shot 10050 of the Au grid projected onto a single-strip XRFC using a 22-keV Ag backlighter. We also obtained very good conversion efficiency data using the single-photon–counting (SPC) camera for the 100-ps UV pulse, finding that the conversion efficiency (CE) at 8 keV was only a factor of 2× lower than that using a 1-ns UV pulse, with CE = 3.5×10^{-3} for the 100-ps UV pulse.

Figure 128.92
Radiograph collected on a single-strip XRFC of a Au grid backlit using a 5-μm-thick Ag microflag.

Lattice Dynamics and Dynamic Diffraction

Principal Investigator: B. R. Maddox

The goal of these campaigns was to develop Bragg diffraction using a petawatt backlighter and to study single-crystal Mo shock compressed along the [111] direction using angle-dispersive Bragg diffraction. These campaigns produced a significant improvement in the quality of Bragg diffraction obtained using a petawatt backlighter, primarily because of the high-quality surface polish conducted at LLNL to remove a thick layer of damage from the rough manufacture polish

and also a new improved beam block design. Bragg diffraction requires one to block the x rays directly from the x-ray source while letting the diffracted x-rays pass. In these experiments the backlighter was a 250-μm-diam, 12-μm-thick Mo foil driven by the OMEGA EP backlighter beam, defocused to 200 μm and using a 100-ps pulse length. The new beam block design is specially shaped to avoid exposed corners, which can produce strong self-emission. The new design is also much closer to the x-ray source, effectively blocking all of the direct x rays while allowing one to use the Target Viewing Systems (xTVS and yTVS) for positioning. A representative diffraction image is shown in Fig. 128.93. Observed in this image are the diffraction lines from the shocked lattice and the unshocked lattice in front of the shock wave. The strong lines are diffraction 17-keV Mo K_α x rays while the faint lines are diffracted K_β x rays. Data spanning all three campaigns resulted in shock-compressed Mo data from 10 GPa to 40 GPa. A transition from elastic compression to plastic flow was observed at ~15 GPa. The diffraction data have been analyzed to extract the yield stress and the von Mises stress. We also observed plastic relaxation times ≪1 ns above 15 GPa. These results are currently being prepared for publication.

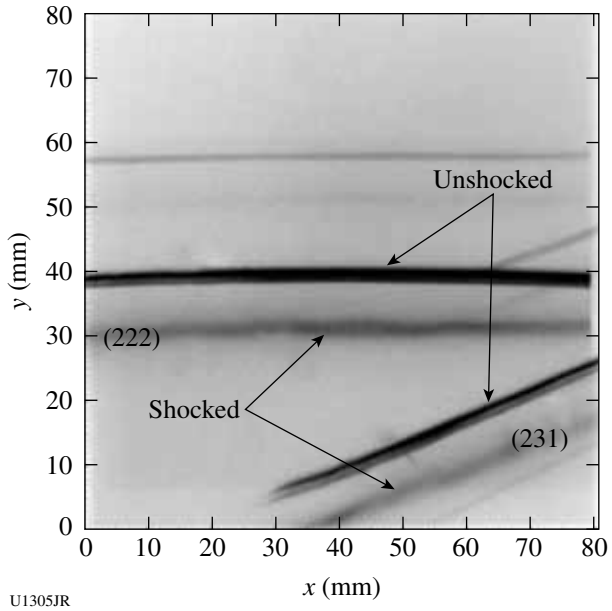

Figure 128.93
Laue diffraction pattern obtained from a single-crystal Ta shock along the [001] direction using a 20.6-J, 1-ns-long UV laser drive.

Tantalum Rayleigh–Taylor Experiments (ICETaRT)
Principal Investigator: H.-S. Park

The goal of the ICETaRT campaigns is to measure dynamic properties of solid-state tantalum (Ta) under high pressures (>1 Mbar) and high strain rates (10^6 to 10^8 s^{-1}). We achieve quasi-isentropic high-pressure conditions by using a unique reservoir–gap–sample configuration, where the sample materials stay well below the melting temperature while they are plastically deforming under high pressure, as shown in Fig. 128.94. This year's campaign studied tantalum material strength properties under these conditions by measuring the growth attributable to the Rayleigh–Taylor (RT) instability in accelerated samples containing a preimposed sinusoidal ripple. We obtained two types of data from each set: drive measurement using the VISAR and face-on radiography using the 20-keV Ag K_α backlighter via the OMEGA EP short-pulse laser. We have obtained a series of successful radiographs over these campaigns. The radiometrics of the Ta stepped data are carefully analyzed to derive the $\rho\Delta Z$ of the ripple growth. The growth factor GF is then defined to be

$$\mathrm{GF} = \frac{(\rho\Delta Z)_{\mathrm{driven}}}{(\rho_0 \Delta Z_0)_{\mathrm{undriven}} \cdot \mathrm{MTF}}, \tag{1}$$

where ρ_0 and ΔZ_0 are initial density and ripple amplitude, respectively, from the pre-shot metrology and MTF is the modulation transfer function measured by the knife edge. Figure 128.95 shows the ripple growth factor as a function of time from the 50-μm-wavelength samples. The simulation results from various material-strength models are also plotted in Fig. 128.95. Note that only the multiscale model fits the data well, which attempts to connect atomistic level behavior to the continuum-level plastic flow using density functional theory, molecular dynamics, dislocation dynamics, and continuum simulations to calculate yield strength. The details of this model are described in Ref. 74.

Flow stress is the stress that is needed for the metal material to flow plastically at a given loading condition and state. The inferred average flow stress using the multiscale model, averaged over the sample with e^{-kz} weighting (where $k = 2\pi/\lambda$ and z is the depth into the foil), is ~60 kbar, which is ~8× higher than the Ta ambient flow stress of 7.7 kbar. We find that the flow

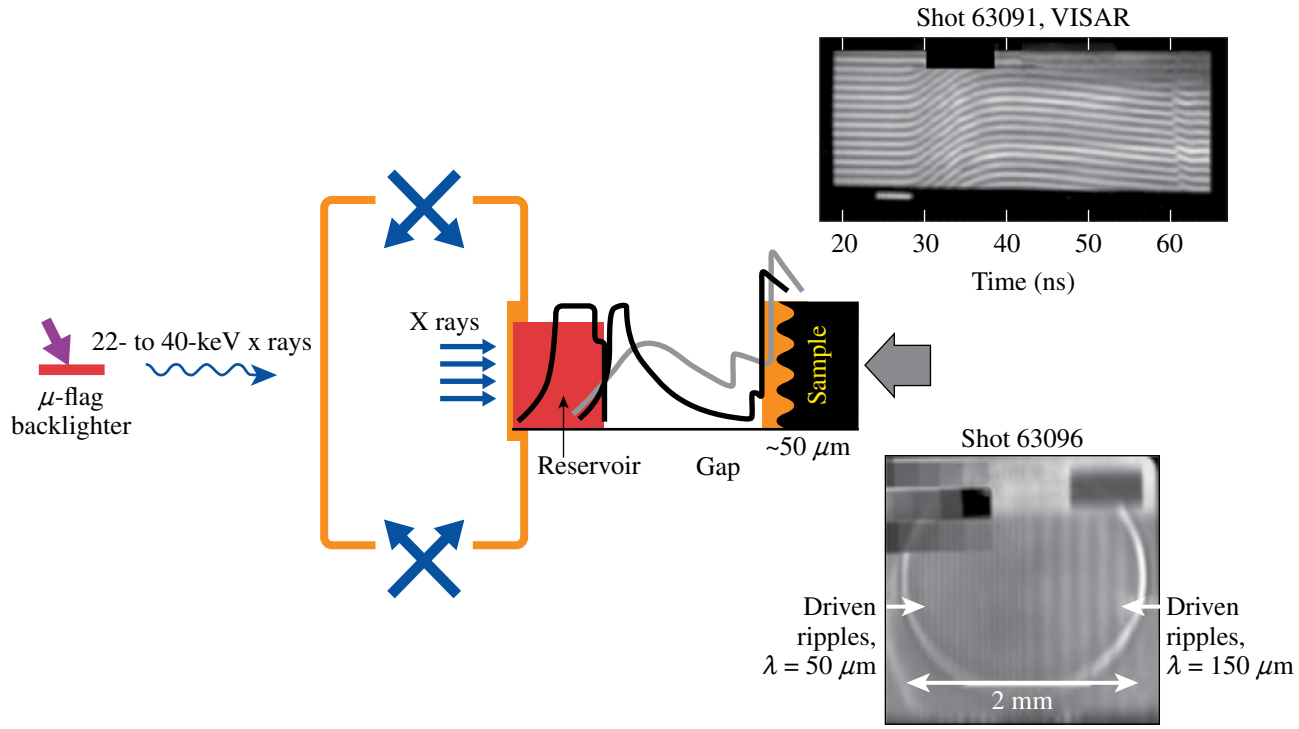

Figure 128.94
ICETaRT experiment configuration for an OMEGA/OMEGA EP joint shot. We take two types of data on each set: drive data using the VISAR and face-on radiography using the OMEGA EP–generated high-energy backlighter.

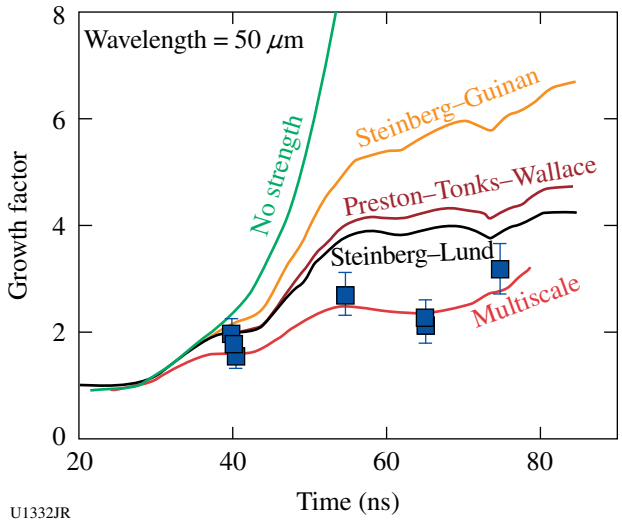

Figure 128.95
Ta Rayleigh–Taylor growth factors as a function of time. The data points are noted as the blue squares. Various material-strength model predictions are plotted.

stress is largest when the strain rate is the largest, indicating that the strain-rate hardening is a dominant factor. From the pressure-dependent shear modulus calculation, the pressure hardening is about a factor of 2, with the remaining factor of 4 because of strain-rate hardening. This result has been submitted and accepted for publication.[75]

The FY11 campaign also completed a study of the Ta grain-size effect on the strength under high-pressure and high-strain-rate conditions. While there are many strength measurements of Hall–Petch grain size scale at ambient conditions,[76] neither previous theory nor experimental measurements under high-pressure dynamic conditions exist. We fabricated three different types of targets that have average grain sizes of 92 μm, 15 μm, and 0.25 μm as shown in Fig. 128.96(a). The face-on radiography data are analyzed in a similar fashion as described above, and the normalized growth factor versus the average grain size is plotted in Fig 128.96(b). The conventional understanding is that the yield strength is stronger with smaller grain sizes known as the Hall–Petch effect and is formulated by $\sigma \sim \sigma_0 + kD^{-1/2}$, where σ is the yield strength, D is the average

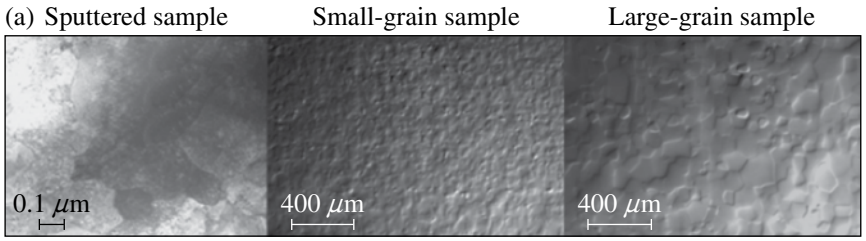

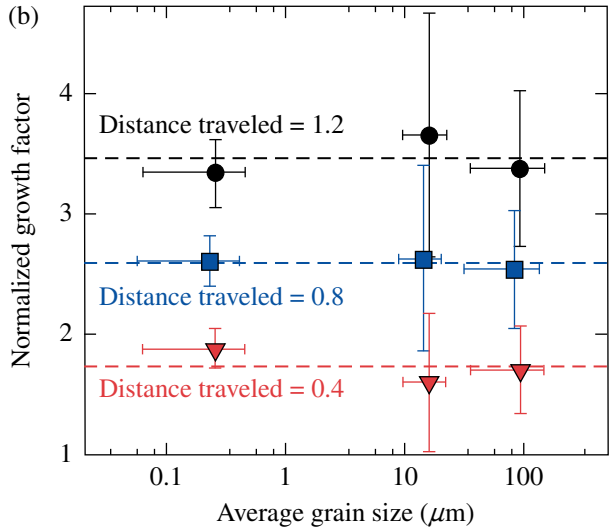

Figure 128.96
(a) SEM and TEM pictures of the different Ta grain-size samples. (b) Growth factor, a measure of material strength, as a function of grain size. No obvious Hall–Petch effect is observed.

grain-size diameter, and σ_0 and k are characteristic coefficients for different materials. This relation is known to hold for many materials. This is because the dislocations, whose mobility quantifies the strength, are pinned against the grain boundary, restricting their mobility. We consider two postulations of why we see no Hall–Petch effect: (1) In our experiment, the dislocations have not moved to the grain boundaries at our times scale of <100 ns; and (2) the work hardening is a dominant factor rather than the grain-size hardening. Our experimental results will be submitted for publication in Nature Materials.

ICEDrive-11A/ICEHohl-11A

Principal Investigators: M. May and A. Comley

The ICEDrive-11A and ICEHohl-11A campaigns were conducted at the Omega Laser Facility as part of the ramped-drive platform development required for the tantalum-strength Rayleigh–Taylor experiment on the NIF. Both half-day campaigns were fielded on the same day and used the 2.5-scale indirect-drive platform developed in the ICETaRT series of experiments, with slight variations in the drive package designed to address various issues as described below.

The ICEDrive-11A target packages are shown in Fig. 128.97. The hohlraum drive is incident on the beryllium ablator shown in the figure. The BrCH (and foam layers if applicable) constitute the reservoir that releases across the gap, thereby generating a ramped pressure wave at the tantalum layer. The ramp drive is characterized using VISAR and SOP. The ICEDrive-11A experiments were designed to test VISAR measurement handoff from thin (100-μm) LiF to thick (1-mm) quartz at pressures of >2 Mbar (a key component of the NIF 5-Mbar drive target designs), test two-layer reservoir foam repeatability, provide further experience with diagnosing the drive through a releasing LiF reservoir, and provide a reference drive shot for the ICEHohl-11A experiments later in the day.

All six target shots returned good data from primary diagnostics VISAR, Dante, and SOP. The peak drive Tr measured from Dante is currently higher than previous campaigns by 3 to 8 eV. The drive (deviating in the opposite direction), as measured by VISAR, is lower by ~15%.

The ICEHohl-11A target packages are shown in Fig. 128.98. The ICEHohl-11A experiments had two objectives. First, in the tantalum strength Rayleigh–Taylor experiment (ICETaRT), a plastic (CH_2) heat shield was placed over the front of the tantalum sample to insulate it from the heating effects of the unloading reservoir. The ability of CH_2 to act as a thermal insulator to the stagnating plasma in a planar geometry was

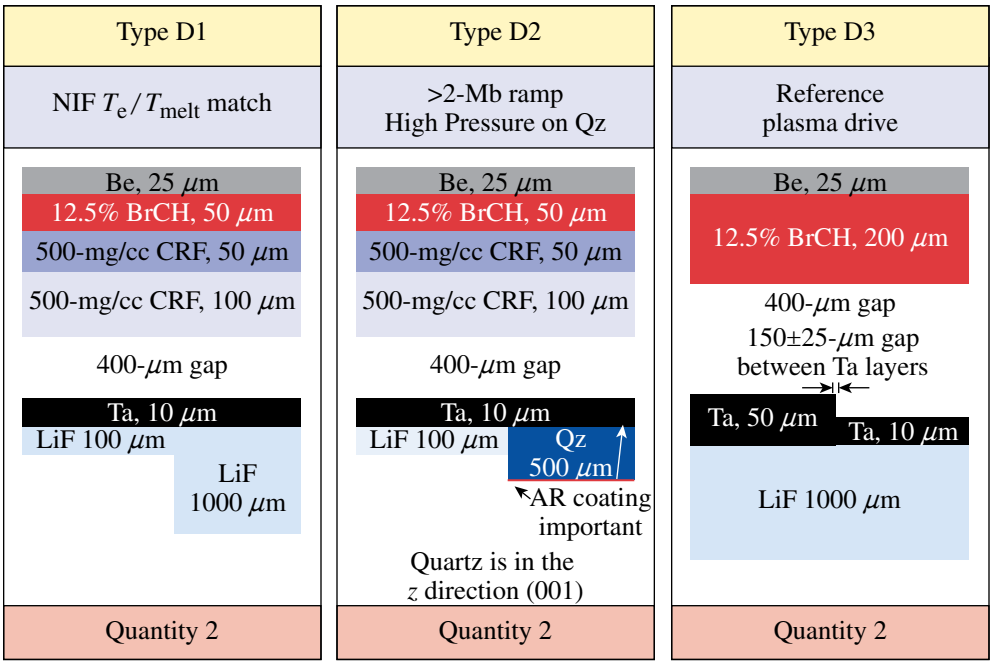

Figure 128.97
ICEDrive-11A target packages.

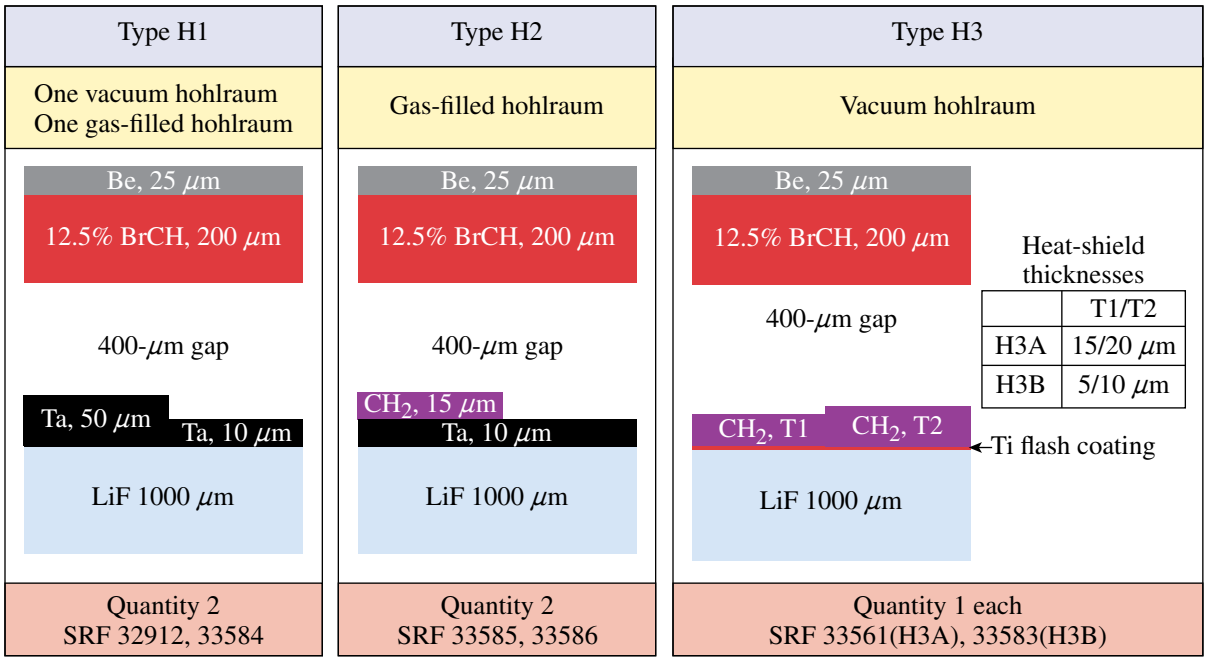

Figure 128.98
ICEHohl-11A target packages.

demonstrated (H3 target in Fig. 128.98) using streaked optical pyrometry. No thermal burnthrough was observed, in agreement with tabular electron-conductivity values.

The second objective was to test the performance of gas-filled hohlraums, particularly with the goal of mitigating late-time shock formation caused by hohlraum stagnation and late-time Tr effects. We tested three neopentane-filled hohlraums, with nominal gas pressures of 26, 129, and 180 Torr. It was found that the timing of the late-time shock could be influenced by the choice of gas fill. With increasing gas-fill pressure, the late-time shock was observed to arrive earlier: the shock time measured relative to the start of the initial ramp for the 180-Torr case was seen to shift ~4 ns earlier compared to the 129-Torr case.

Strength Diffraction

Principal Investigator: B. R. Maddox

The goals of this campaign were to study single-crystal Ta shocked along [001] using Laue diffraction and to measure the broadband x-ray output of a 1-ns UV pulse-driven foil source to that of a 44-beam imploded CH shell source using the dual-crystal spectrometer (DCS). This campaign was also used to test a new Ta crystal target construction scheme to keep the 5-μm-thick Ta single crystals as strain-free as possible. Laue diffraction was obtained using the broadband x-ray diffraction (BBXRD) diagnostic on TIM-4. Dante was used to time the capsule implosion for precise timing between the Ta crystal drive and the x-ray bang time. The results show that the new target construction scheme using a 10-μm n-HDC ablator glued to a Ta crystal with a 40-μm-thick u-HDC tamper effectively kept the Ta crystal from warping and produced high-quality static and shocked-diffraction patterns. Figure 128.99 shows a sample diffraction pattern from one of the image plates of the BBXRD from a Ta sample driven using 20.6 J in 1 ns. Diffraction spots from the shock-compressed lattice and the unshocked lattice ahead of the shock wave are evident in the image. This particular image corresponds to a 9% difference between the longitudinal and lateral strains. High-quality data were also obtained on the broadband spectrum of a Mo-foil backlighter driven by four UV beams at maximum energy with 1-ns pulse lengths, overlapped in space and time onto a 1-mm-diam, 12.5-μm-thick Mo foil. The results showed that the broadband emission of the Mo foil in the 10- to 20-keV range was ~10× lower than that from the imploded CH-shell backlighter. Subsequent campaigns will continue to use the CH shell as the broadband x-ray source for Laue diffraction.

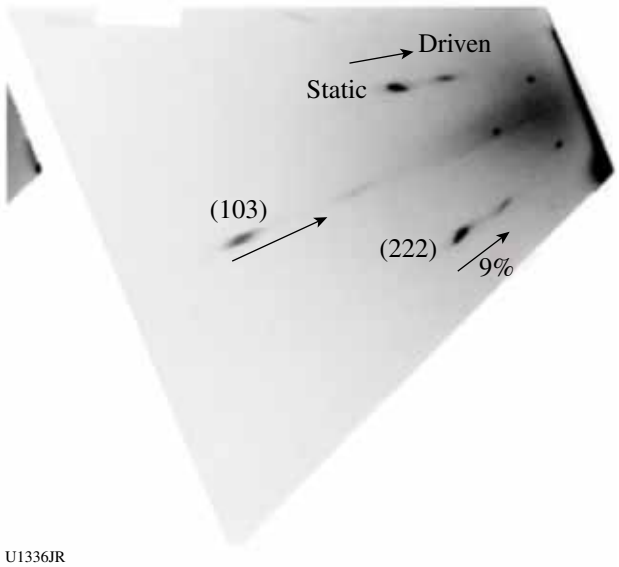

Figure 128.99
Laue diffraction pattern obtained from a single-crystal Ta shock along the [001] direction using 20.6-J, 1-ns-long UV laser drive.

2. High-Temperature Plasma Opacity

High-Temperature Plasma Opacity Experiments on OMEGA and OMEGA EP

Principal Investigators: R. F. Heeter, S. Chen, G. V. Brown, and R. E. Marrs

LLNL opacity research in FY11 had four main directions: First, the MBOP-11 campaign followed up on physics questions from the very successful 2009–2010 Ti opacity shots, where the observed Ti continuum opacity and 1 to 3 line opacity regions did not match code expectations. The new data using thinner samples extended this data by a factor of 4 in sample ρL, pushing the K-shell absorption technique to its optically thin limit. As shown in Fig. 128.100, spectral absorption line positions from charge states consistent with ~120-eV LTE sample temperatures are observed, now with 40% transmission. The new data continue to match the codes quite well, and detailed comparisons are in progress for the continuum and line-gap opacities, where disagreements with older data remain.

The second campaign, NEAHiZ-11, resumed previous work on the non-LTE x-ray emission properties of hot gold plasmas as found in hohlraums at the laser-driven "hot spots." Shots performed in late FY11 extended earlier work to 2× lower intensity (material temperature) and the data are now being compared with simulations.

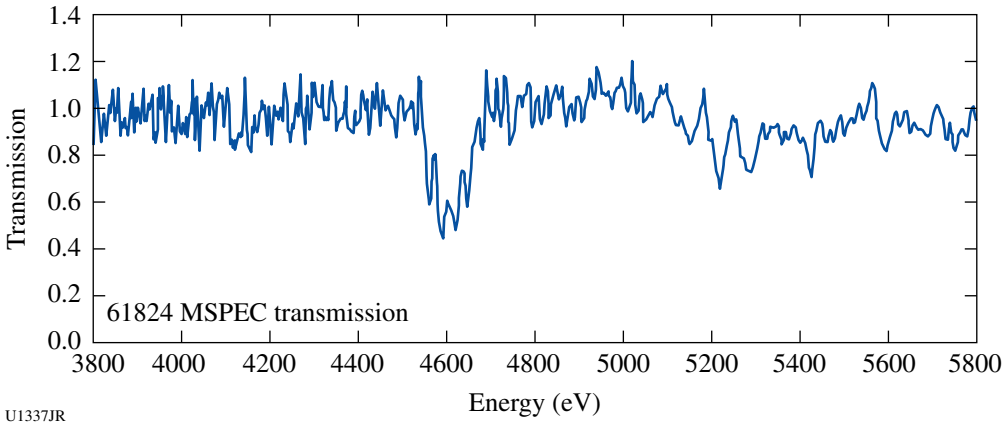

Figure 128.100
A Ti K-shell transmission spectrum with a 0.17-μm Ti sample. Foil expanded to 70 μm from initial 0.17 μm. Sample thickness was reduced 4× from earlier experiments, bringing K-shell features to >40% transmission. Ionization features for F, O, N, and C-like Ti indicate a temperature of 120 eV.

NEAHiZ-11 also supported a third line of inquiry to improve the signal/noise of gated opacity measurements. As part of the non-LTE measurements, the relative sensitivity of XRFC1 [50-ps pulse-forming module (PFM)] was compared with XRFC4 [new microchannel plate (MCP), 400-ps PFM]; the latter showed roughly 300× greater sensitivity for x rays from 250 to 1800 eV, using nearly identical snout setup and target views. The noise in both measurements is similar (therefore, not photon limited) and subsequent investigations established a signal/noise limit of 20:1 for film-based gated x-ray imaging with 60- to 100-μm spatial resolution. This ratio is limited by the film itself and not the scanner or XRFC components. The ratio may be increased by averaging over wider sections of film, or perhaps by modifying the film-developing process.

The fourth research direction was the EPOp-11 series, which successfully developed a novel short-pulse "absorption-emission" opacity platform on OMEGA EP. The initial goal was to cross-check short-pulse heated opacity measurements against similar long-pulse data (Fig. 128.101). Absorption experiments at higher densities and temperatures are possible but maintaining LTE conditions is difficult. In the FY11 experiments, the OMEGA EP sidelighter beam delivered 250 to 900 J in 100 ps with a broad focus to heat Al/Ti/Al_2O_3 opacity samples at 10^{15} to 10^{16} W/cm^2 intensities. The OMEGA EP backlighter beam, delayed by 200 to 300 ps, delivered 800 to 1500 J in 10 ps near best focus, driving a broadband 3- to 6-keV backlighter whose x rays probed the hot, expanded opacity sample. Figure 128.100 shows K-shell x-ray absorption from L-shell Ti ions (F, O, and C-like Ti) at $T > 100$ eV. The inferred temperature is below the ~1000-eV temperatures predicted by the 1-D hydrocodes *HELIOS* and *HYDRA*. Imaging in the transverse direction shows an expansion of ~50 μm (density of ~0.05 g/cc) at the time of this measurement. A separate line of sight enabled us to take space- and energy-resolved sample emission spectra in the 250- to 1600-eV spectral band, which shows similar levels of expansion and ionization.

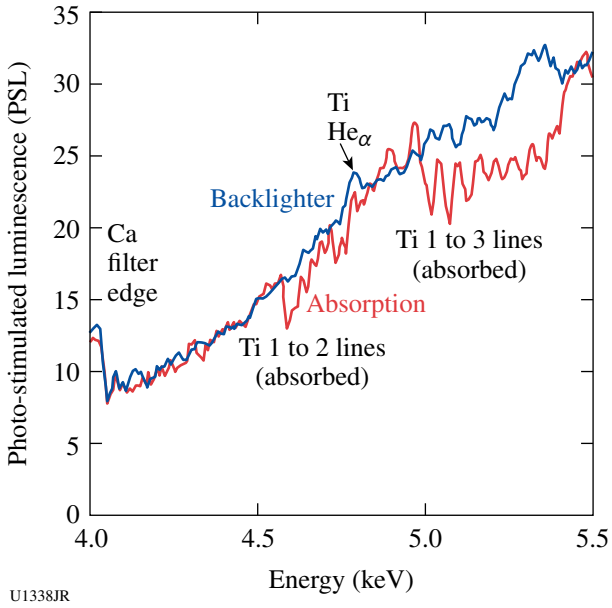

Figure 128.101
First Ti K-shell absorption spectrum from OMEGA EP opacity experiments. Similar charge states are seen in the OMEGA EP experiment as in the OMEGA experiment.

3. Hydrodynamics

Short-Pulse, UV Backlighting Development for the NIF
Principal Investigator: V. A. Smalyuk

High-energy-density complex hydrodynamics experiments on the NIF require short-pulse–backlighting capability. Experiments on the OMEGA EP laser tested the short-pulse, UV beam backlighting concept for the NIF. Four OMEGA EP beams were focused onto 10-μm-thick Ag wires, mounted on 300 × 300-μm-sq, 10-μm-thick polyimide foils to mimic illumination conditions of one quad on the NIF. The total laser energy was ~400 J with an ~100-ps Gaussian pulse shape and a peak laser intensity of $\sim 3 \times 10^{16}$ W/cm^2. Beam mistiming was <50-ps rms and mispointing was <50-μm rms. Results were compared with ~1.2-kJ short-pulse (~100-ps) IR beam backlighting with the same Ag-wire targets, driven at an intensity of $\sim 1 \times 10^{17}$ W/cm^2. Figure 128.102 shows a measured image of the target created with Ag-wire backlighting on an image plate using the high-energy radiographic imager (HERIE) diagnostic located 50 cm from target chamber center on OMEGA EP. It consists of the Au grid used to determine magnification, a 100-μm-thick Au plate used to determine resolution, and seven Cu steps with 18-μm thickness between adjacent steps used to determine contrast and sensitivity. Areas inside and outside of the Au plate were also used to measure noise. Figure 128.103(a) shows an inferred backlighter spectrum, determined by fitting measured intensity at different Cu steps [shown as diamonds in Fig. 128.103(b)].

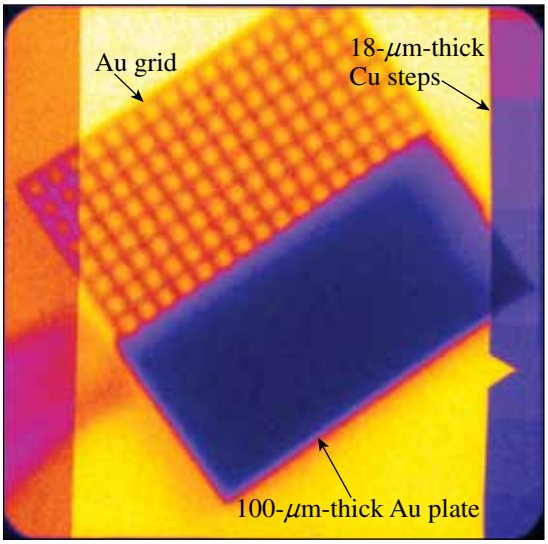

Figure 128.102
X-ray radiograph of the target consisting of an Au grid, a 100-μm-thick Au plate, and seven 17-μm-thick Cu steps.

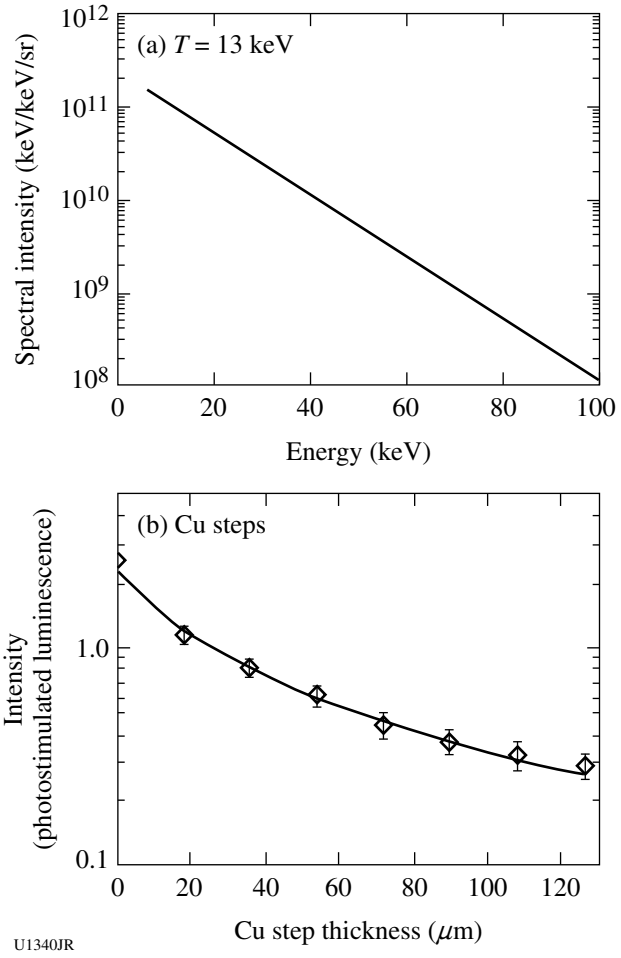

Figure 128.103
(a) Inferred backlighter spectrum, determined by fitting measured intensity in Cu steps, shown in (b) with diamonds. The thick solid line shows a fit to the data assuming an exponential spectrum with temperature of 13±2 keV, presented in (a).

The solid line in Fig. 128.103(a) shows a fit to the data, assuming an exponential backlighter x-ray spectrum with a temperature of 13±2 keV. The inferred temperature was ~100× lower than in experiments with a short-pulse IR beam, while the signal intensity in areas outside the Cu steps (about 2 photo-stimulated luminescence (PSL)] was decreased by ~100×. The ~20-μm spatial resolution was similar to IR-beam experiments, while noise was ~2× higher. The short-pulse UV backlighting might be feasible for complex hydrodynamics experiments on the NIF if hohlraum x-ray backgrounds (generated by mostly hot electrons from Raman laser–plasma instability) do not exceed ~10 PSL on the image plate at 50 cm from the NIF target chamber center. The first complex hydrodynamics experiments on the NIF will measure and mitigate, if necessary, these backgrounds before radiography experiments. The next

campaign on OMEGA EP will be devoted to maximizing the x-ray backlighter signal by scanning a temporal advance of one of the beams with respect to other drive beams.

Backlighting Experiments on OMEGA

Principal Investigator: V. A. Smalyuk

Backlighting experiments were performed on the OMEGA Laser System to study the symmetry of foam balls illuminated with hohlraum x rays. Backlighter targets were driven either with short-pulse IR beams in joint OMEGA EP experiments, or with UV beams in OMEGA-only experiments. In a joint OMEGA EP configuration, 10-μm-thick Ag wires, mounted on 300 × 300-μm-sq, 10-μm-thick polyimide foils were irradiated with an ~1.2-kJ short-pulse (~100-ps) IR beam at a laser intensity of ~1×10^{17} W/cm^2. X-ray radiographs of targets were measured on image plates using the HERIE diagnostic placed ~50 cm from target chamber center with a magnification of ~50. In the OMEGA-only configuration, six OMEGA beams irradiated Ni point-projection backlighter at a laser intensity of ~1×10^{16} W/cm^2. Time-resolved (with ~80-ps temporal resolution) x-ray radiographs of targets were measured on a framing camera with a magnification of ~20. Experiments were very successful, producing high-quality radiographs that set up a baseline for future complex hydrodynamics experiments at the NIF.

4. X-Ray Source Development and Applications

Iron K-Shell X-Ray Source Development

Principal Investigator: K. Fournier

The X-Ray Source Development team, in collaboration with the Defense Threat Reduction Agency and researchers from the French CEA, conducted two campaigns in FY11 that developed and optimized two very different iron K-shell ~6.7-keV x-ray sources. The two sources that were studied were ultralow-density iron-oxide aerogel materials ($FeOOHCl_{0.38}$) and stainless-steel–lined (SS-304) cavities (see Fig. 128.104). The density of the aerogel targets ranged from 3 to 16 mg/cm^3, which resulted in laser-created plasma-radiation sources with densities between 10% to 50% of OMEGA's critical density. The critical measurements included x-ray spectral output from the sources, x-ray images of the volume heating of the target plasma, and streaked images of laser heating in the targets. Side-by-side images of the heated aerogel and foil-lined cavity targets are shown in Fig. 128.104. Results so far show that the aerogel material at 6 mg/cm^3 produced the highest-fluence, 6.7-keV output at 43.1±9.4 J/sr, which is a 2.9% laser-to-x-ray

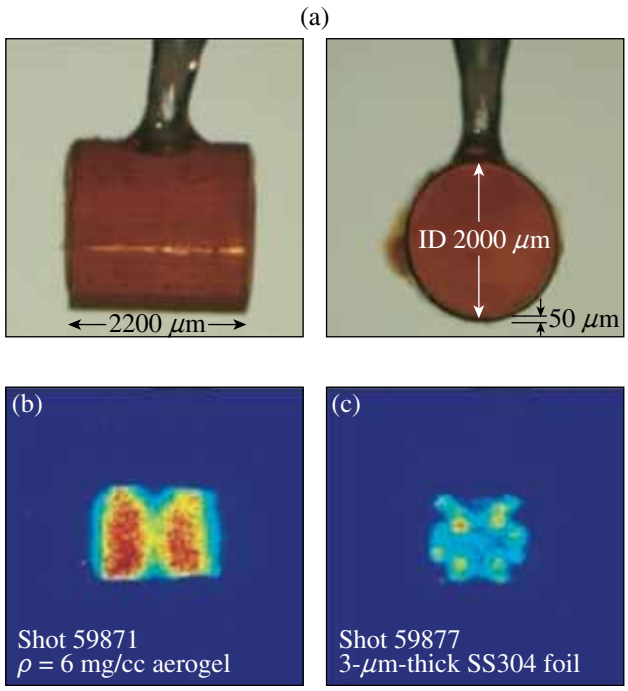

Figure 128.104
(a) Side-on and face-on views of a 12-mg/cm^3 iron-oxide aerogel target for Fe K-shell-11A shots, (b) x-ray framing camera (XRFC) image at 6.7-keV x-ray energy of a 6-mg/cm^3 aerogel target at t = 1.0 ns, and (c) XRFC image at 6.7-keV x-ray energy of a 3-mm-thick steel-lined cavity at 0.8 ns. The Fe K-shell emission from the aerogel target is much brighter than from the foil-cavity target.

conversion. The Fe K-shell yield (6 to 8 keV) of the aerogel targets for three different densities is shown in Fig. 128.105. When measured over all x-ray energies, the targets yielded ≈850 J/sr and ≈1220 J/sr for aerogel and steel-lined cavities, respectively. These targets show promise for reproducible, high-flux, high-fluence x-ray sources to be used in NIF experiments in FY12 and beyond.

Solar Cell Electrostatic Discharge

Principal Investigator: K. Fournier

The X-Ray Source Development team, in collaboration with the Naval Research Laboratory and the Defense Threat Reduction Agency, has begun researching whether we can use the OMEGA target chamber as a test environment for investigating electrostatic discharge phenomena in solar-cell technology. Our initial steps in this process are to characterize the charged-particle flux (both electrons and ions) created by our laser-driven x-ray source before moving on to more-sophisticated tests of biased solar cells and solar-cell arrays. Our first experiments conducted on 14 September 2011 involved the fielding of arrays

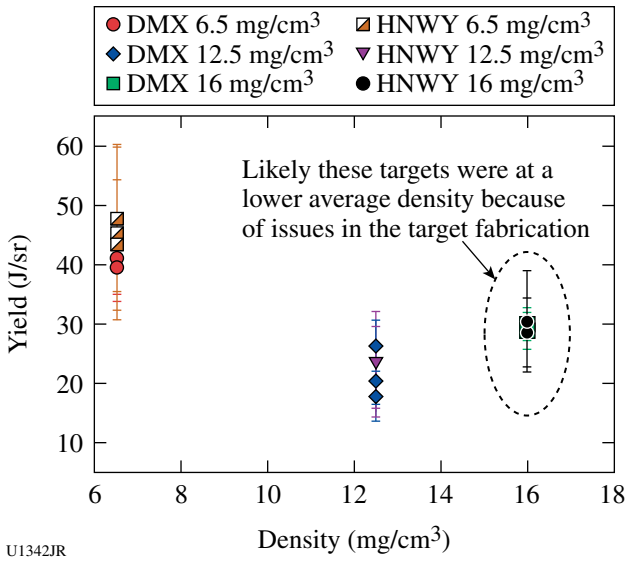

Figure 128.105
Measured Fe K-shell yields in the energy range of 6 to 8 keV for iron-oxide aerogel targets of different densities. The measurements were taken with the CEA diagnostic DMX and the LLNL diagnostic HENWAY; the two diagnostics show excellent agreement.

of Langmuir probes in TIM's that looked at the open face of our x-ray source targets and looked orthogonally to the target's axis. The two lines of sight provided quantitative measurements of x-ray–driven signals on a nanosecond time scale and electron and ion signals on the microsecond time scale. A photograph of one of our probe arrays is shown in Fig. 128.106. The Langmuir probe diagnostic is a new diagnostic created by modifying the x-ray source application (XRSA) cassette that we have used on many previous radiation-effects experiments. We will return to the development of this platform in FY12 with arrays with a greater number of probes on each shot that will allow us to map out the voltage–current curve for the passing ion and electron fluxes and, ultimately, an investigation of the response of a solar-cell array operating under bias to x-ray loading.

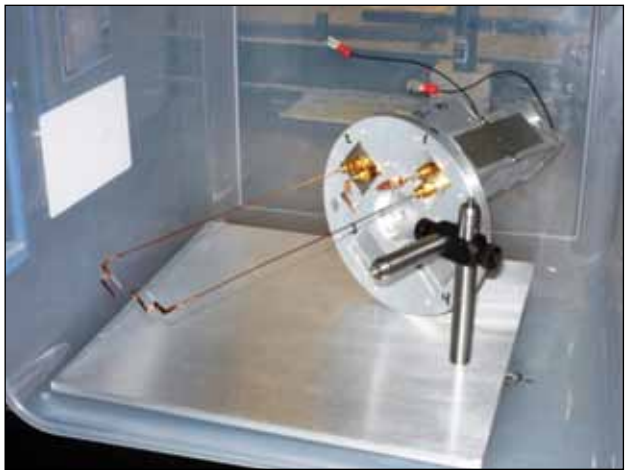

Figure 128.106
An XRSA cassette fitted with two sets of Langmuir probes ready for delivery to the TIM for positioning in the OMEGA laser chamber. The probes measure electron- and ion-particle fluxes passing by their location following laser-irradiation of the x-ray source target at TCC.

FY11 LANL Experimental Programs—Overview

In FY11, Los Alamos National Laboratory (LANL) executed 223 total shots: 195 on the OMEGA Laser System and 28 on the OMEGA EP Laser System. LANL experiments contributed to the National Ignition Campaign in the following ways:

- Measured the x-ray ablative Richtmyer–Meshkov growth of isolated defects on plastic ablators
- Studied branching ratios in DT-fusion plasmas
- Measured the shape of the DT-fusion gamma-ray spectrum
- Continued neutron-imaging development for the NIF

HED campaigns included

- Study of shear and reshock-driven turbulent mixing
- Backlit defect implosion experiments to study the effect of trench defect
- Measuring the effect of capsule asymmetries on neutron yield and ion temperature
- Platform development for dense plasmas and warm, dense matter equation of state
- Measurement of a supersonic radiation wave
- Energetic ion generation for dynamic defect studies

CHaRM: The CHaRM campaign had two outstanding shot days in FY11 where the shock speed and bump's areal-density evolution were measured for multiple bump sizes and target conditions. Existing defects (bumps or divots) on ICF capsules can cause jetting of high-Z material into the hot spot during an implosion, an undesirable consequence of late-stage RT growth. The ablative Richtmyer–Meshkov (aRM) growth sets

the initial conditions for subsequent RT, so the aRM must be understood and controlled to optimize late-time capsule stability. The ablation process of aRM stabilizes the early-stage growth and is even predicted to decrease the amplitude of the initial perturbation. Ignition attempts will consider tailored driving pulse shapes designed to minimize the perturbation amplitude at the onset of RT. Experiments conducted at the Omega Laser Facility are being used to determine the time at which bump amplitudes approach zero for specified target conditions (electron temperature, density).

Nine to fifteen laser beams from OMEGA were used to create a moderate-temperature (70-eV) radiation environment inside a gold halfraum ablating and driving the aRM growth of a 2-D array of Gaussian-shaped bumps (see Fig. 128.107). On-axis, area-backlighting x-ray radiography measured the bump's areal density at different times following the driving laser pulse by recording the transmission of the 2.8-keV Cl He_α line (from saran) through the bumped target with an x-ray framing camera. Summing over all of the identical bumps in the array from the raw radiograph allowed us to construct a composite bump with improved statistics. Averaging lineouts extracted around the azimuth of the composite bump improved statistics even further, resulting in an optical depth radial position bump profile that is converted to areal density using a known calibration on each shot. The areal density at bump center for various times is then compared to simulations of the target geometry.

Before 1-to-1 comparisons can be made, target conditions must be measured independently so that simulations can be tuned to match target conditions in the experiments. This is accomplished by measuring shock speed using the ASBO diagnostic under identical drive conditions as the bump-growth experiments.

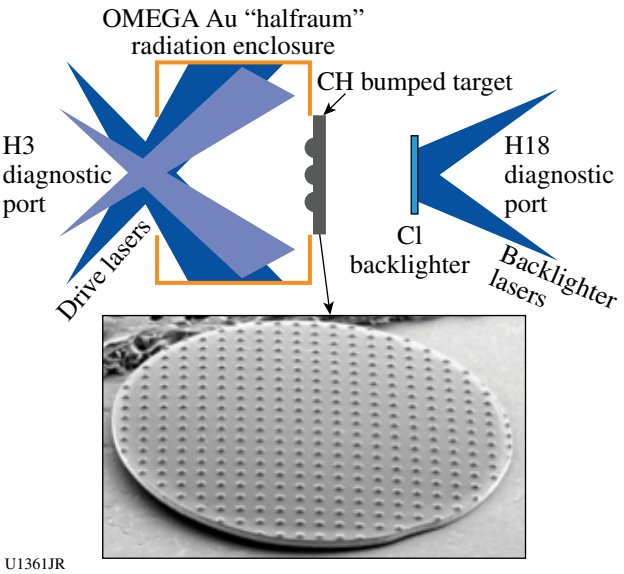

Figure 128.107
Experimental setup for CHaRM.

A shot day in December 2010 focused on the early-time behavior of bump compression and rippled shock formation, which occur just before conventional aRM sets in. These experiments used 2-ns drive pulses in a halfraum, heating it to ~65 eV and driving an ~12.5-μm/ns shock in the plastic ablator as measured by ASBO. The bump's areal density (Fig. 128.108) showed a 2.5× increase along the bump (initially, 12-μm-tall,

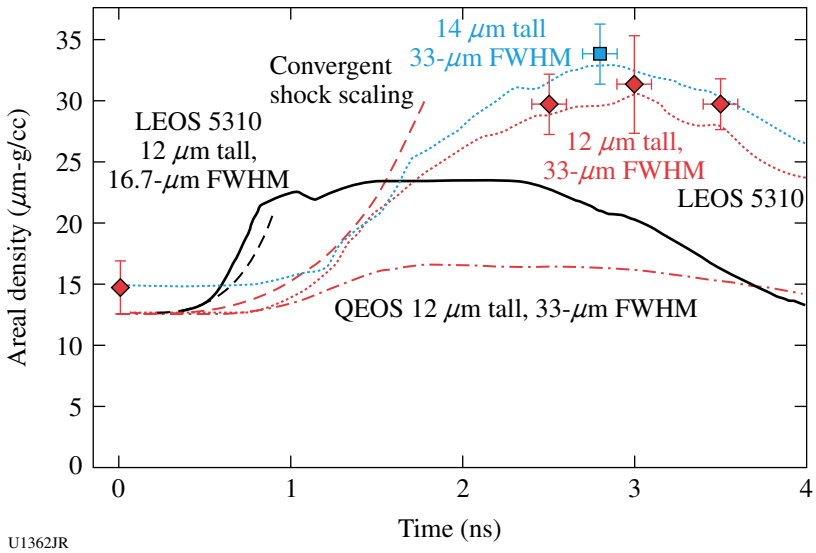

Figure 128.108
Early-time data and simulations using a 2-ns drive.

33-μm FWHM) axis at 3 ns after the start of the drive pulse. This initial increase in areal density is due to lateral compression of the bump as a converging shock propagates through it, raising the density on-axis. Simulations using the LEOS 5310 model showed good agreement with data; however, the QEOS model predicted 6× lower growth than measured owing to its lower compressibility. Results from this shot day were published in Physics of Plasmas.[77]

The goal of the April 2011 shot day was to extend the drive pulse to observe bump behavior well into an established aRM stage. These experiments used 2.5-ns pulse durations stacked end-to-end in clusters 2 and 3 so that the effective pulse width was ~5 ns into the halfraum. Shock speed was measured using a slightly hotter halfraum than in the December experiment (~70 eV), resulting in a 15-μm/ns shock velocity closer to the current NIC foot level, as shown in Fig. 128.109.

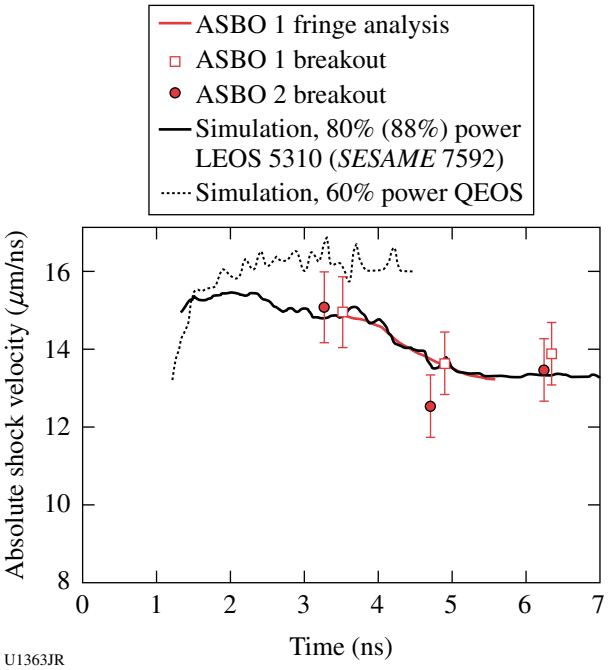

Figure 128.109
Shock-speed data and simulations for an extended 5-ns drive.

The evolution of two sets of bumps, one 6.5 μm tall, 44-μm FWHM, and one 10 μm tall, 34-μm FWHM, was measured out to 6 ns (Fig. 128.110). Similar early-time growth was observed, but evidence of aRM oscillations was not observed in experiments or matched simulations. The cause of this is a lack of sufficiently high spatial-frequency modes that are most effective in changing bump shape in the wide Gaussian bumps that were used. For x-ray–driven aRM, the mode oscillation frequency is much lower than the laser driven (by ~7×), so much more time is needed to witness bump oscillation if bumps are >20-μm FWHM. These results were presented in an oral session at the International Conference on Inertial Fusion Sciences and Applications.[78] Experiments in FY12 will strive to measure oscillations in narrower (~17-μm FWHM) bumps.

ColShock/Shear: The colliding-shock experiments study the evolution of a shocked layer that evolves to a turbulent state and is then shocked a second time. A pre-shot radiograph of a typical target is shown in Fig. 128.111. A shock is launched on

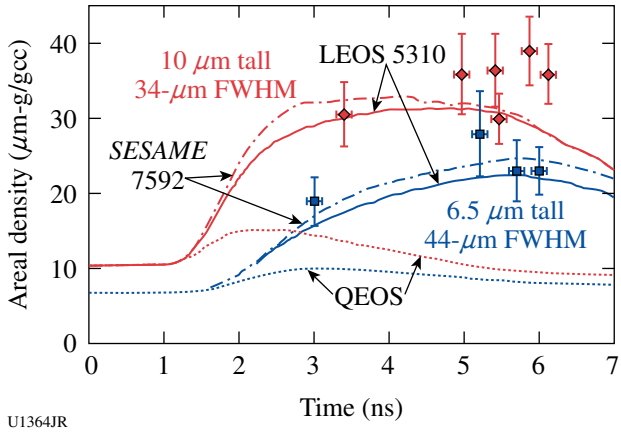

Figure 128.110
Measured and simulated bump evolution using an extended 5-ns drive.

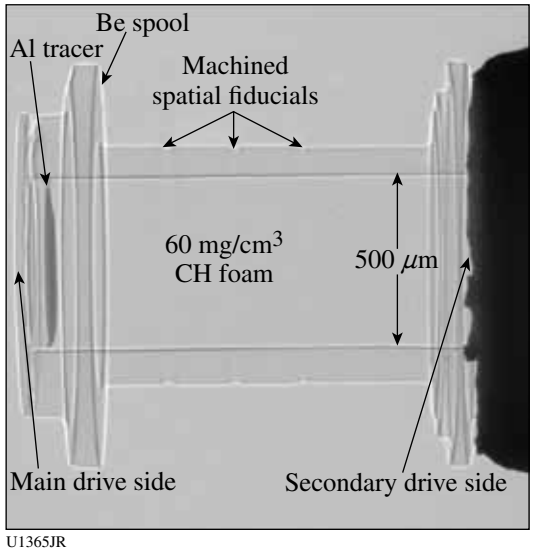

Figure 128.111
A pre-shot radiograph of the colliding-shock target. The main shock is launched from the left-hand side, and 5 ns later the second shock is launched from the right-hand side. Radiographs are obtained from two directions that measure the hydrodynamic evolution of the experiment at different times.

the left-hand side. The shock interacts with an Al tracer layer, which evolves toward a turbulent state over the course of the experiment. A second shock is launched from the right-hand side, which propagates toward the Al layer. The hydrodynamic evolution of the system, including the evolution of the Al layer and the positions of the shocks in both the CH foam and the Be walls, is measured. The x-ray radiograph in Fig. 128.112 taken just after the two counter-propagating shocks interacted.

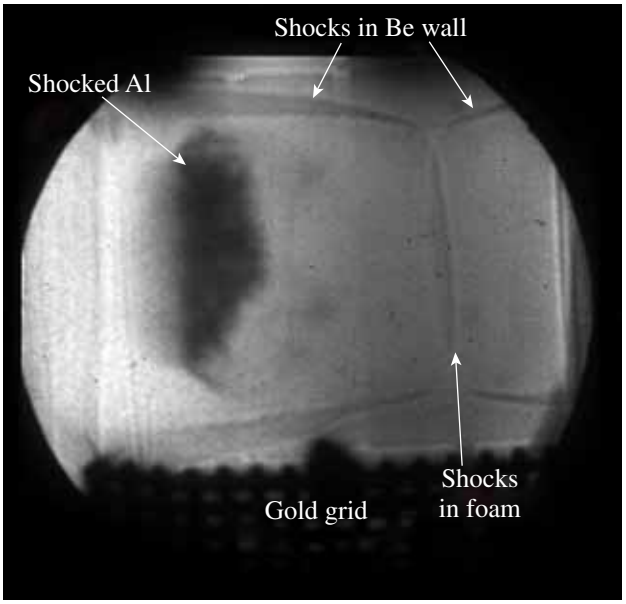

U1366JR

Figure 128.112
Radiograph of a colliding-shock target roughly 8 ns after the initial shock was launched. At this time the counter-propagating shocks have just interacted.

The goal of the Shear experiment is to study mix associated with large deformations or shear. The goal of this experimental campaign is to provide data to further constrain the Besnard–Harlow–Rauenzahn code (BHR),[79] the mix model implemented in the *RAGE* radiation–hydrodynamics code.

A pre-shot radiograph of a typical target is shown in Fig. 128.113. A shock is launched on the left-hand side. The shock propagates through the two different density foams. The shear is caused by the different shock speeds. The hydrodynamic evolution of the system, including the evolution of the Al layer and the positions of the shocks in both the CH foam and the Be walls, is measured with x-ray radiography (see Fig. 128.114).

DTRatio (DTRat): On 25 May 2011, LANL's ICF Gamma-Ray Physics Team led the DT-Ratio Campaign on OMEGA, with external collaborators from AWE, NSTec, LLNL, LLE,

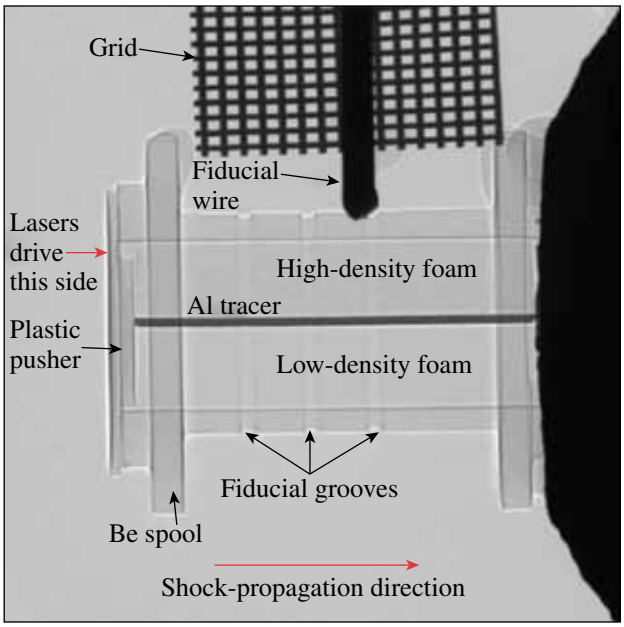

U1367JR

Figure 128.113
A pre-shot radiograph of the Shear target. The shock is launched from the left-hand side. Radiographs are obtained that measure the hydrodynamic evolution of the experiment at different times.

and MIT. The primary experimental objective was to cross-calibrate the fusion branching ratios of DT gamma/neutron against the better-known D^3He gamma/proton. Three types of targets were fielded: six D^3He (D_2 ~ 6 atm, ^3He ~ 12 atm) in glass shells, three DT (50:50) in plastic shells, and two D_2 (15 atm) in glass shells. Three Cherenkov detectors (GCD1, GCD2, and GRH) were successfully operated at the same time. Since the branching ratio study requires accurate diagnosis of multiple fusion products, this study required close collaboration with LLE and MIT. In particular, MIT employed seven proton diagnostics: the proton temporal diagnostics, three wedge range filters, two charged-particle spectrometers; and the magnetic recoil spectrometer, with which they measured spatially averaged proton yield to within 5% accuracy. Figure 128.115 shows preliminary experimental data obtained by GCD-1. The top blue curves show D–^{3}He gamma signals divided by proton yield data (proportional to D–^{3}He gamma/proton branching ratio). The red curve shows D–T gamma signals divided by neutron yield (proportional to D–T gamma/neutron branching ratio). Since the primary D^3He (Eg = 16.66 MeV) and DT (Eg = 16.75 MeV) gamma rays have almost the same energy, it is not necessary to determine the absolute efficiency of the gamma detector. Initial data show that the DT branching ratio is significantly smaller than the D^3He branching ratio (DT/D^3He ~ 0.41), which is in very good agreement with last year's campaign (DT/D^3He ~ 0.42).

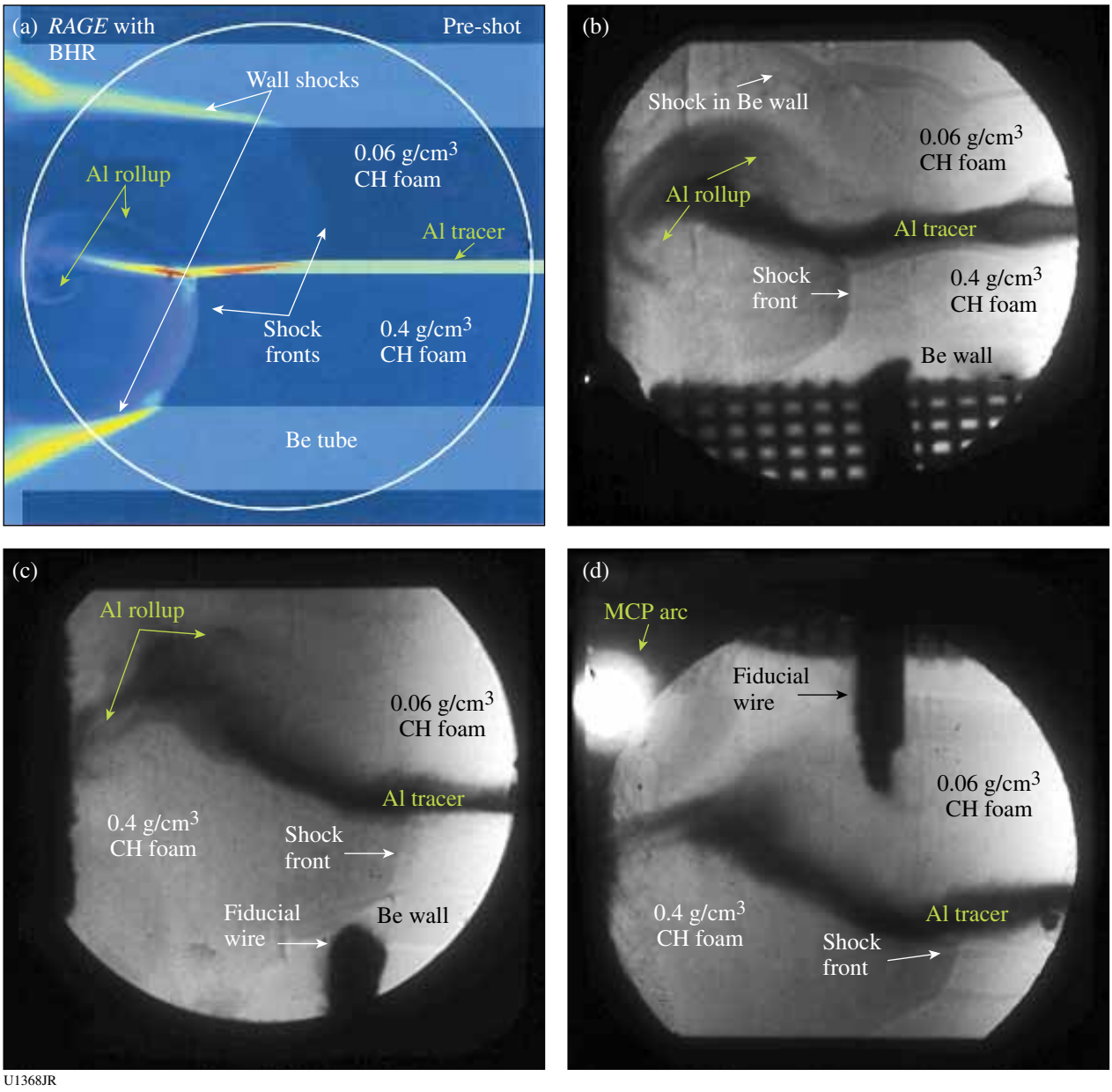

Figure 128.114

(a) Simulation result at 8.25 ns showing the density of the experimental system; (b) x-ray radiograph of the experiment at 8.25 ns. Preliminary comparisons show a number of qualitative similarities; (c) x-ray radiograph of the experiment at 12 ns; and (d) x-ray radiograph of the experiment at 14 ns.

Gamma Reaction History (GRH): In addition to the dedicated DTRat shot day, the ICF Gamma-Ray Physics Team, led by LANL, participated in ten shot days on OMEGA. Through extensive energy thresholding experiments using GCD-1 and GRH across these shot days, the team examined the shape of the DT fusion gamma-ray spectrum. The data in Fig. 128.116 clearly indicate that the DT reaction spectrum consists of more than just a single line at 16.75 MeV, corresponding to de-excitation of the ^{5}He* nucleus to the ground state. DT fusion gamma rays resulting from the transition of ^{5}He* down to the first excited state must also contribute significantly to the spectrum. Figure 128.117 shows the spectrum that is most consistent with the experimental data and modified spectra of the mirror nucleus (^{5}Li*) resulting from D^{3}He fusion extrapolated to the ^{5}He system by quantum-mechanical *R*-matrix calculations. Using this new spectrum, a total t(d,g)^{5}He/t(d,n)^{4}He branching ratio of $(2.7\pm0.7)\times10^{-5}$ has been measured at the Omega Laser Facility. These measurements show that the DT branching ratio at ICF conditions is 2 to 3× less than that of previous measurements at particle accelerator facilities. In a practical sense,

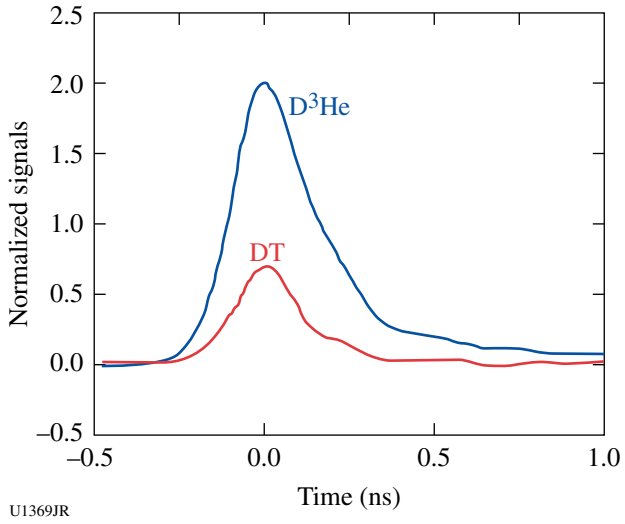

Figure 128.115
2011 DTRat campaign data. The blue curves show D–^{3}He fusion gamma signal normalized by MIT's proton yield. The red curve shows the DT fusion gamma signal normalized by LLE's neutron yield.

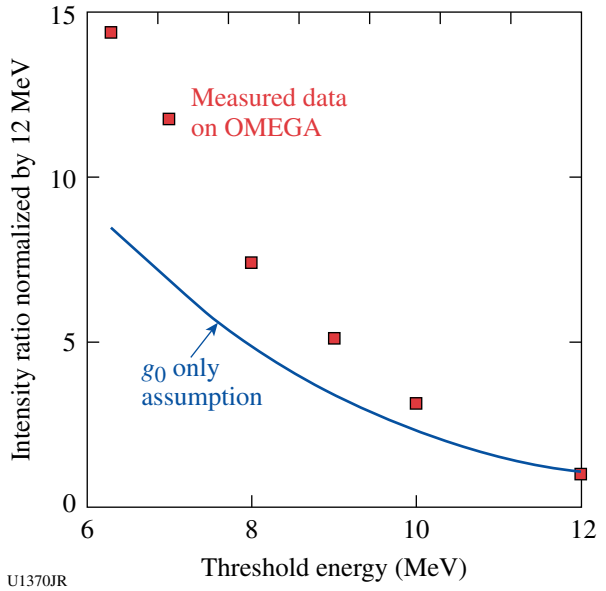

Figure 128.116
Ratio of GCD intensities as a function of threshold energy (MeV), normalized to 12-MeV threshold intensity. The red squares are experimental data. The blue curve was obtained by folding 16.75-MeV single-peak spectra with detector responses of GCD simulated by the *ACCEPT* code.

precise measurement of the branching ratio $t(d,\gamma)^5He$ relative to $t(d,n)^4He$ is important in order to diagnose gamma-ray yields from which to infer parameters such as target areal density and resultant fusion yield of cryogenically layered implosions at the NIF. The experimentally measured DT spectrum and recent DT branching ratio measured on OMEGA have been applied to

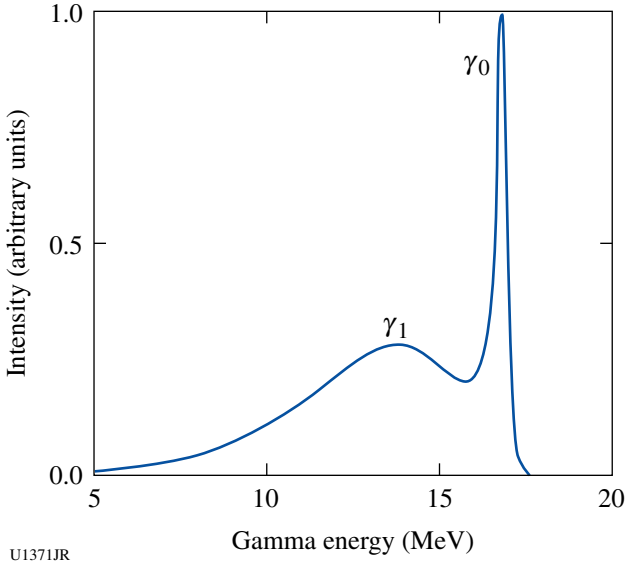

Figure 128.117
Resulting DT fusion gamma-ray spectrum consisting of γ_0 at 16.75 MeV (^{5}He* transition to ground state) and γ_1 at ~14 MeV (^{5}He* transition to first excited state).

improve GRH responses and data analysis for the NIF. In addition, the team continued plastic and glass capsule ρR diagnostic efforts on OMEGA and extended the diagnostic concept to the NIF to provide a capsule implosion ρR parameter.

Defect Implosion Experiments (DIME): Direct-drive experiments on OMEGA have been performed to prototype eventual NIF-ignition applications campaigns. Experimental results are tied to simulations that will lead to better designs for those experiments. Spherical implosion targets with equatorial defects have been irradiated with polar drive—a requirement at the NIF. Collected data reveal implosion symmetry, neutron yield, and temperature and density profiles of the capsules with and without the defect. We have also modeled and measured the zeroth-order hydrodynamics. The testing of hydrodynamic codes provides a guide to accurately plan for polar-drive–ignition studies on the NIF platform. Target-design details are shown in Fig. 128.118. The equator is defined with respect to the polar drive as in Fig. 128.119.

The laser drive for all shots included 40 beams for the nominal LLE polar drive (PD) plus 11 or 12 beams for pumping the saran backlighter. The capsule drive was ~17.5 kJ in a 1-ns, square-topped pulse.

As part of the capsule design, most targets have a 2-μm-thick Ti impurity layer (1% by atom) placed either at the inner wall of the target shell or 3 μm inboard of the inner wall. This

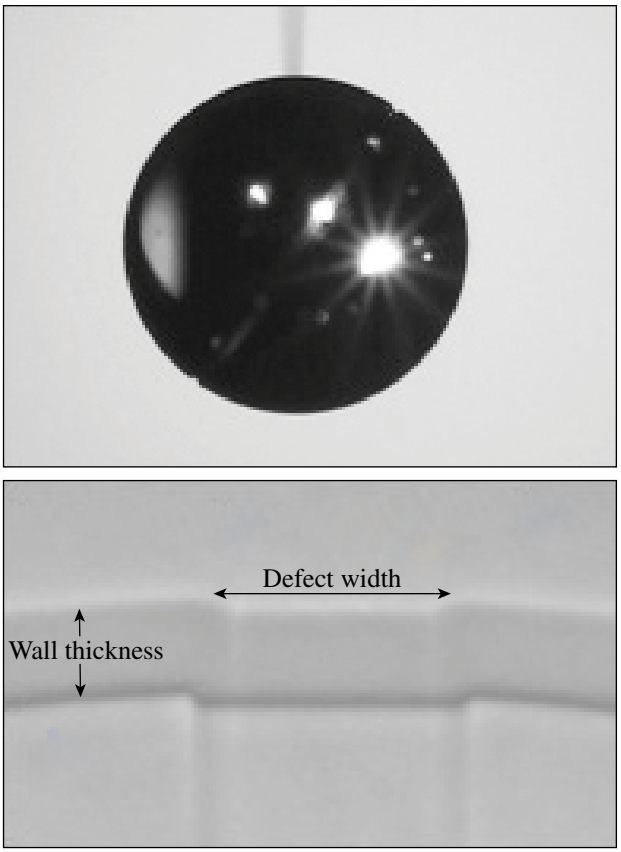

Figure 128.118
(a) Photograph of an 870-μm-diam CH capsule. (b) Detail of the trench defect. Nominal wall thickness is 15 to 17 μm; the trench is ~28 μm wide and 5 to 8 μm deep.

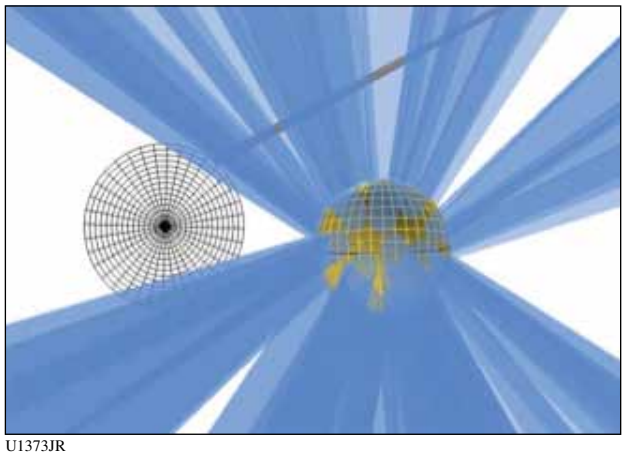

Figure 128.119
A defect target is shown with polar drive. A backlighter foil to the left was used for x-ray radiography. The capsule drive beams are reduced in footprint size to enable one to clearly view the defect target (Visrad model).

is employed as a mix diagnostic for these ablation-driven implosion targets. We also shot thin-walled (8-μm) shells, so-called exploding-pusher targets, and, as a result of these experiments, have moved away from this choice.

Initially scheduled for two shot days this year, DIME benefited from three days, the last two coincident with the forced evacuation of Los Alamos by the state-record Las Conchas wild fire. Targets from another campaign were sequestered in the closed laboratory. Because we had extra DIME targets, we were able to use them during the extra day of shots. In fact, General Atomics (GA) personnel at LLE provided "last-minute" backlighter foils because the DIME backlighters were also locked up in New Mexico for the week prior to the laser shots. As usual, the expertise and professionalism of LLE and GA staff was very efficient and helpful in obtaining laser/target data under trying circumstances. DIME obtained a total of 28 laser shots during these two days plus another 11 shots during a campaign earlier in the year.

For the zeroth-order hydro, we measured bang time and implosion velocity with a gated, x-ray imager. Probing at 2.8 keV, we found that the capsules for the most part were relatively spherical, excepting the final assembly of defect targets. Defining R as the radius of the absorbing material left in the ablator, we plot the time-dependent R in Fig. 128.120. Not shown in Fig. 128.120 is the brightest emission radius of the capsules, for which the absorption feature is no longer visible.

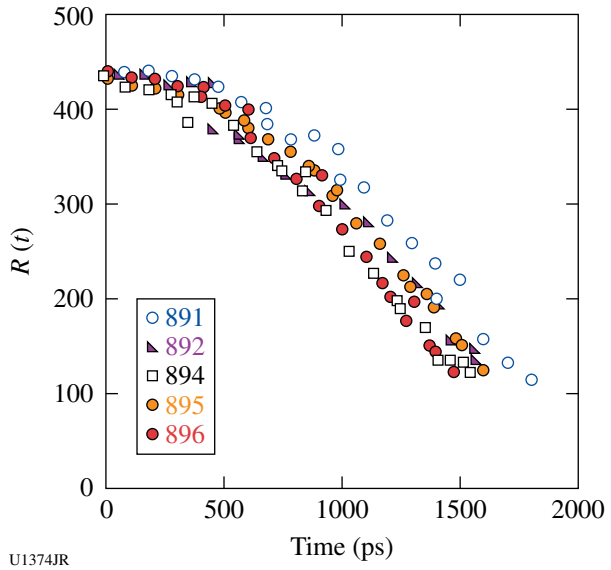

Figure 128.120
Zeroth-order hydrodynamics: capsule radius as a function of time for various shots. The slowest target (891) was a perfect capsule.

In this case, we measure the full width at half maximum as the operational radius. It is uniformly 40±10 μm for the entire period that it is visible (from 1.4 to 1.8 ns), and it is independent of the presence of a defect.

The pathology of the defect capsules is shown in Fig. 128.121. The features suggest a possibility of measuring mix in an ICF capsule under such circumstances, which is why we used the Ti tracer layer in these targets. There are more comments on this later.

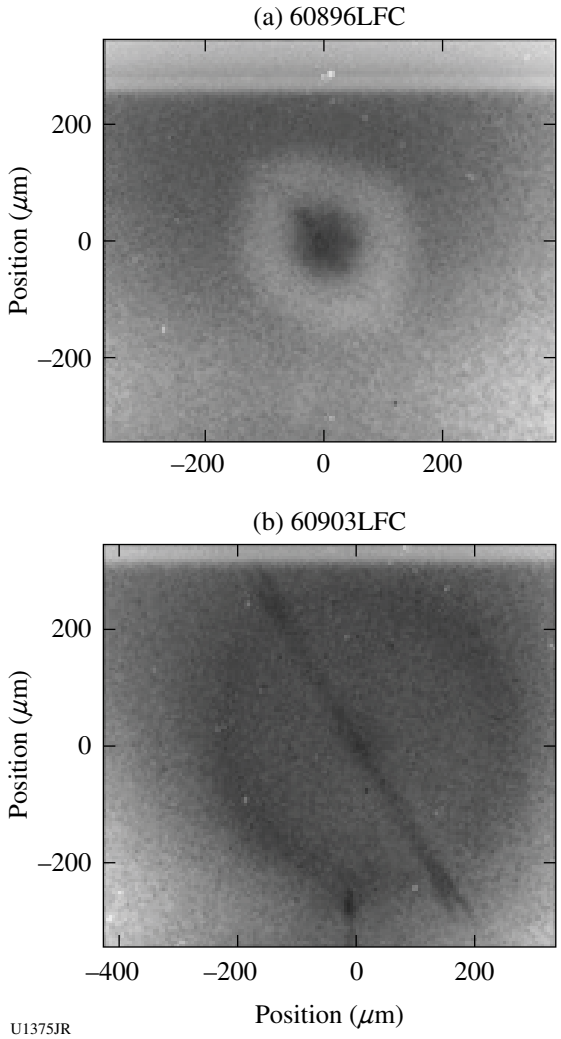

Figure 128.121
(a) The thickening of the thick-walled ablator near peak compression of a defect capsule is very obvious. Note the Lengendre modes associated with the core. (b) A thin-walled capsule earlier in the discharge shows defect detail more dramatically than for the ablative case. The data come from the 80-ps gated x-ray framing camera LFC.

The bang time is measured by two other diagnostics: the SSCA x-ray streak camera and the neutron temporal history diagnostic. These are consistent with, and more accurate than, the x-ray framing camera data. The streak data are especially illuminating. We see in Fig. 128.122 a sample streaked spectrum showing bremsstrahlung from the laser drive and during the final compression (note the consistency of the time with the framing camera). This spectrum shows He-like Ti lighting up before the bang time, indicative of the ablator burning through to the Ti before the laser is turned off at ~1 ns. Figure 128.123

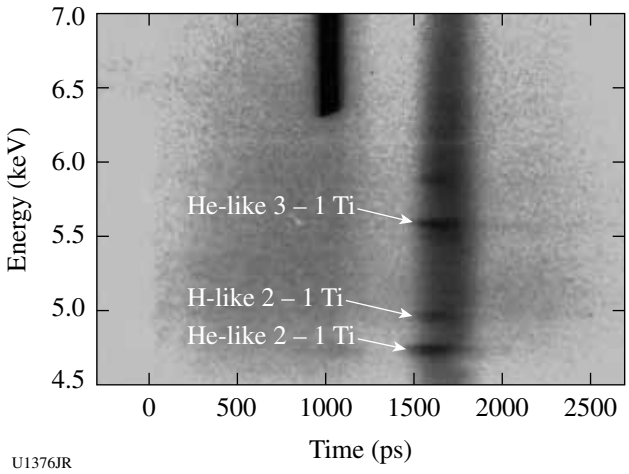

Figure 128.122
X-ray streak record of a defect implosion. The continuum rises up at $t = 0$ with the laser pulse and reaches a maximum at 1 ns. The capsule implosion stagnates from 1.5 to ~1.8 ns. Note the 4.75-keV Ti emission during the laser pulse. The intense dark region at the top ($t \sim 1$ ns) is x-ray shinethrough that lights up the phosphor screen directly and has nothing to do with electrons accelerated from the photocathode in the streak tube.

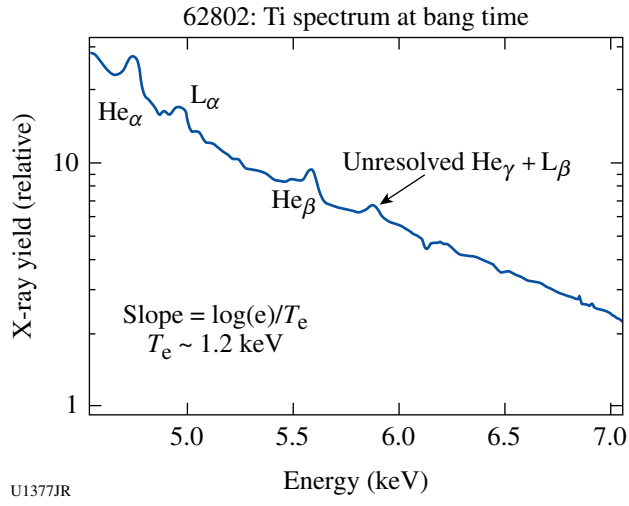

Figure 128.123
Corrected lineout of spectrum at bang time for a defect target.

shows a lineout of the Ti spectrum after corrections are made for filter transmission, crystal reflectivity, and the sensitivity of the CsI photocathode in the streak tube. From this spectrum, we may estimate the electron temperature from the slope of the continuum.

These target shots are instructive in considering the use of these capsules as a mix platform. The idea is that Ti near the inner surface of the ablator shell will light up spectroscopically when the material is heated by the hot gas during stagnation. This is *prima facie* evidence of mix. The appearance of emission before stagnation shows that either the CH wall has burned through prior to stagnation (which would be a bad thing) or that the defect is responsible for the direct laser heating of Ti. This emission is reduced once the laser is extinguished at ~1 ns. Perfect capsules (no defect) show no Ti emission before stagnation. We note that for thinner layers of CH on top of the impurity layer, the Ti will light up and emit; this has already been used to calibrate capsule design codes for experiments on the NIF.

Neutron yield is a measure of the effect of a perturbation on capsule performance. We have accumulated data for a selection of perturbations: perfect capsules versus defect capsules, with/without a Ti impurity layer, with/without a second impurity layer of V, and a perfect Ti target with a NIF-style gas-fill tube. The yield performance is summarized in Fig. 128.124. All deviations from an undoped CH target reduce yield.

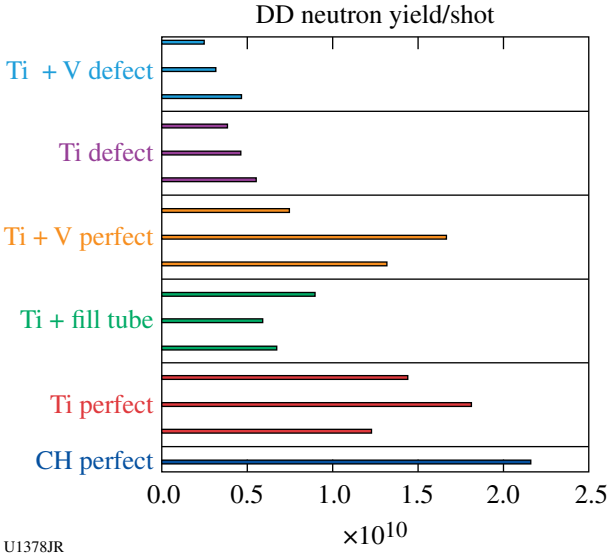

Figure 128.124
Results of neutron-yield measurements for different targets.

Asymmetric Burn Experiments (ABEX): The purpose of the ABEX project is to develop an experimental HED platform to study the impact on the performance of fusion burn caused by hydrodynamic issues related to asymmetrically driven ICF systems. The ABEX capsules were successfully fabricated and 12 successful shots were conducted at the Omega Laser Facility on 5 April 2011. All primary diagnostics obtained data, including neutron yield from both primary D–D and secondary D–T reactions, burn-weighted ion temperature, time-dependent neutron-production rate, time-resolved and time-integrated x-ray pinhole imaging, spatially integrated time-resolved x-ray spectra in the 4- to 7-keV band, and measurements of laser-scattered light.

The initial experiments on OMEGA had two objectives: (1) to successfully manufacture the perturbed targets and determine what manufacturing issues needed to be addressed for future target construction, and (2) to map out the performance versus perturbation-amplitude space for the next experimental series. These goals were met. Specifically, we developed the manufacturing technique to produce capsules that contained a P-8 asymmetry in the radius of the capsule. An image demonstrating this is shown in Fig. 128.125.

In addition to the development of the manufacturing technique, we measured the D–D neutron yield as a function of perturbation amplitude and obtained x-ray images of these capsules at times near the peak compression. In Fig. 128.126, we show a set of images that have an equatorial view of the capsules and demonstrate the asymmetric shape of the capsules at this time. In Fig. 128.127, we show the measured yield as a

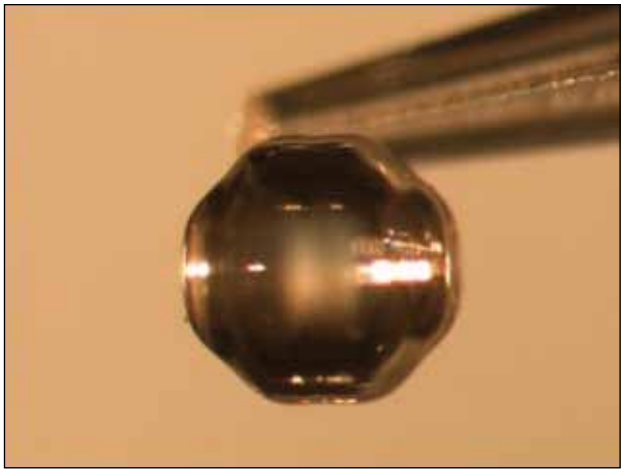

Figure 128.125
Photograph of a machined polyacrylamide (PAMS) mandrel with ±10-mm amplitude perturbation. The axis of symmetry is horizontal in this photograph.

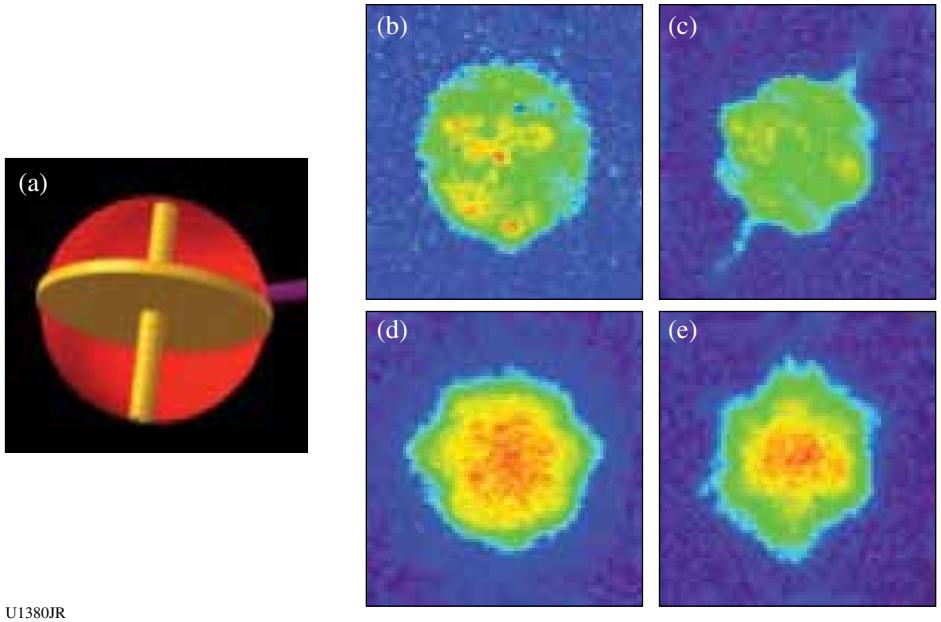

U1380JR

Figure 128.126
Sample images from the time-resolved x-ray pinhole camera in TIM-2 (XRFC1), which had an approximately equatorial view of the target. This camera had a 1-mil copper filter, which primarily passes x rays in the 5- to 9-keV band. Image (a) shows a view of the target from a VisRad model. Images (b) and (d) are from the same shot with a P-8 of ±2.5 mm at (b) 1.35 ns and (d) 1.50 ns, where the bang time was 1.64 ns. Images (c) and (e) are from a different shot with a P-8 of ±10 mm at (c) 1.33 ns and (e) 1.51 ns, where the bang time was 1.63 ns.

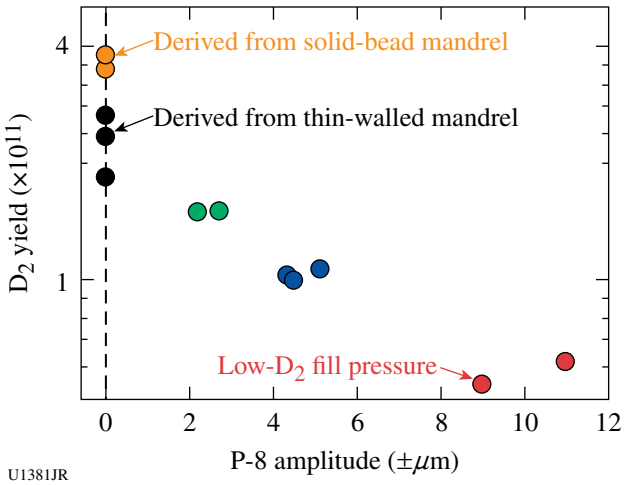

U1381JR

Figure 128.127
Measured primary D–D neutron yield as a function of the P-8 perturbation amplitude for all the targets, including those derived from thin-walled mandrels.

function of perturbation amplitude. These results have helped further develop this experimental platform, and this effort will continue with two shot days in FY12.

Warm, Dense Matter Equation of State (DPEOS): The purpose of the DPEOS project is to measure the equation of state (EOS) of material in the warm, dense matter regime. Currently, we are developing an experimental platform to accomplish this at the Omega Laser Facility. Our experimental platform uses the OMEGA laser to drive a very strong shock into an aluminum sample. The shock is then released into 0.2 g/cm^3 aerogel foam, which is used as a pressure standard. A shock-breakout measurement is used to determine the shock velocity and pressure in the foam. We have also developed an imaging x-ray Thomson spectrometer to measure Compton-scattered x rays from the released aluminum sample. This information can be used to determine the temperature and density of the released aluminum, providing the necessary measurements to determine the EOS.

Our experimental plan for FY11 was to test and measure the shock and release conditions produced in the aluminum sample, finish the design and construction of the imaging x-ray Thomson spectrometer, get it approved for use on OMEGA, and obtain the first EOS measurements on warm, dense matter (WDM) aluminum. We were successful in the first goal, completing a total of 21 shots in two days on OMEGA, and completed our design for the spectrometer, but because of issues with materials used in the spectrometer, we were not able to obtain permission for its use on OMEGA. We expect this problem to be remedied for our shots in FY12. The accomplishments included verification of the shock conditions in the experimental design and the resolution of many issues related to the x-ray scattering measurements to be carried out in the future. An example of the data we obtained is shown in Fig. 128.128. This figure contains the VISAR signal and the shock-breakout measurement that demonstrates a release pressure near 5 Mbar. Other measurements demonstrate that we have an effective x-ray backlighter for the scattering measure-

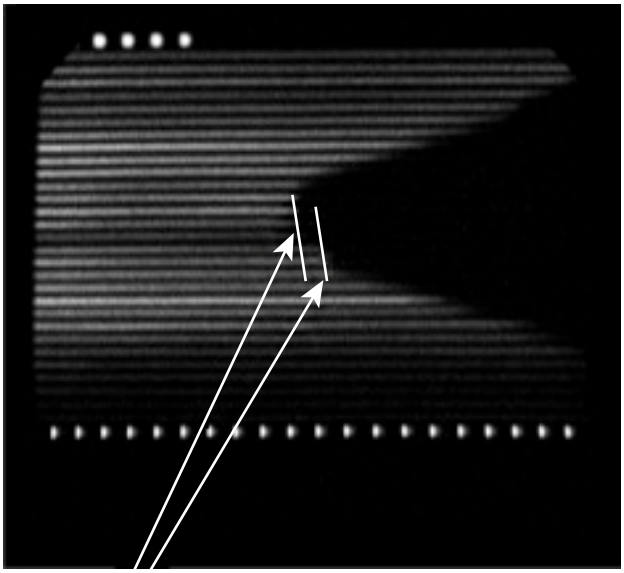
U1382JR

Figure 128.128
Shock-breakout measurement from the ASBO diagnostic. The arrows point to shock-breakout occurrence at two different positions from a stepped target. The measurements indicate a shock velocity of 5.7×10^6 cm/s, corresponding to a pressure of ~540 GPa.

ments and that our x-ray background signal is relatively low. One shot day is planned for FY12 and we expect to obtain our first measurements with the spectrometer on that day.

NIF-5: The NIF-5 campaign had three shot days during FY11: 10 February, 7 July, and 29 September 2011. The 7 July date was cancelled because of the Las Conchas fire. The remaining two shot days were used to study the effect of wall albedo on supersonic radiation flow. We obtained very good data return on both days, with a much-improved signal level and timing calibration on our second shot day.

The purpose of the 10 February shots on OMEGA was to study the effect of wall albedo on supersonic radiation flow down a gold tube filled with low-density SiO_2 foam. We modified the wall albedo of the gold tube by varying its inner profile. While our original intent was to maintain a constant inner surface area to isolate the effect of the profile, this was not possible without other modifications that would also modify the problem [such as the rear entrance hole (REH) diameter, foam volume, etc.).

An experimental campaign on OMEGA EP explored the conversion efficiency of CsI backlighters as a function of the backlighter material size using a 40-ps laser pulse. The results from this campaign provided valuable data now being used to evaluate possibilities for future NIF campaigns. The 29 September OMEGA shot day was a continuation of the campaign begun on 10 February. With this series of shots, we hoped to obtain enough data to wrap up our investigation. We modified the wall albedo of the gold tube by varying its inner profile, although in this case we limited ourselves to only two different profiles. We also maintained a constant inner surface area and foam mass to isolate the effect of the inner profile. We achieved this by varying the length of the cylinder of one type to match the surface area of the other, while lowering the foam density so that the total foam mass of both types of cylinders also matched. We did this for two foam densities. We maintained an identical radiation source for both: the halfraum, laser entrance hole (LEH), and REH were the same for all cases. The data obtained on both shot days are used to validate our codes.

An overview of the target is shown in Fig. 128.129. The halfraum and cylinder were mounted along the P6–P7 axis ($\theta = 63.44°$, $\varphi = 342°$), with the LEH facing P7. The radiation coming from the halfraum heats the foam; we then observe the self-emission of the heated foam from two orthogonal diagnostic axes. Imaging of the holes on the side of the cylinder was conducted from H14, while imaging of the radiation breakout from the end of the cylinder from P6.

The side view was measured using the SSCA streak camera with the SXI 6.6× snout. The camera was rotated 60° cw, so that the row of diagnostic holes was perpendicular to the streak direction. The view, after rotation, is shown in Fig. 128.130(a). Two fiducial beams were aimed at points along the row of

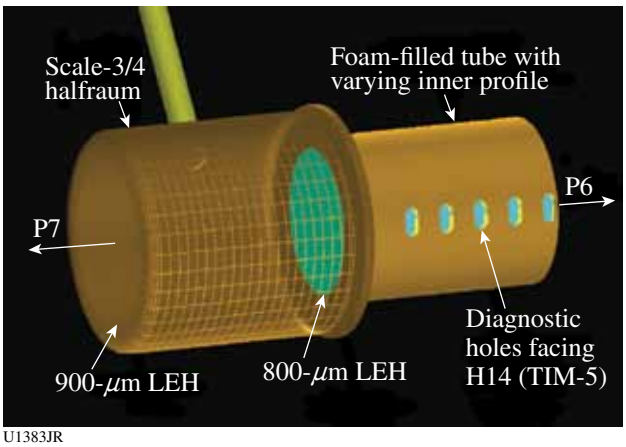

U1383JR

Figure 128.129
Halfraum target with cylinder is mounted along the P6–P7 axis, with LEH facing P7. Diagnostic holes face H14 and the back end faces P6. (Short-cylinder target type is shown.)

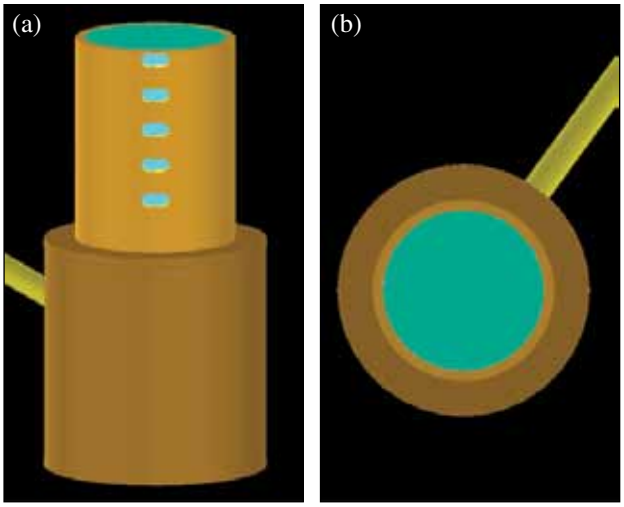

U1384JR

Figure 128.130
Diagnostic views for SSCA/SXI6.6x from (a) H14/TIM-5 and (b) XRFC3/SXR4x from P6/TIM-4. (Short-cylinder target type is shown.)

holes (within view of our vertical imaging slit) to provide a time fiducial on the streak record. One was aimed at a point below the bottom-most (first) hole and fired late (~1.5 ns) to mitigate its effect on the data. The second beam was fired later to provide an accurate calibration of the streak time/distance on film. Since the fall time of the x-ray emission from the fiducial beam spots do not accurately reflect the laser beam's fall time, we use the time between the two fiducial rise times for our calibration. Unfortunately, this means the second fiducial is aimed at a point in between the third and fourth holes of the long cylinder targets. The second fiducial was timed late to minimize any effect it may have on the data. The end-on view was recorded using XRFC3 with the SXR-4X diagnostic snout. This diagnostic consists of three independently filtered channels, two of which include a mirror and filter combination, measured at four different times. The third one is a direct view with a 25-mm-thick Be filter. We fielded practically identical setups on the mirror and filter combination channels, resulting in eight images, each at a different time. The view from this diagnostic is shown in Fig. 128.130(b).

In addition to our primary goal, we also used four shots of our second shot day to obtain the x-ray spectrum of SbI_3—a different backlighter material being considered as a replacement for CsI for our NIF-5 spectroscopy absorption diagnostic. We obtained enough data to allow us to make this determination and analysis is underway.

We met all of our campaign goals for both shot days. On 10 February we obtained 13 shots with good data on all of the primary diagnostics. Even though SXI had not been used in years, it produced data on every shot and also recorded an accurate timing fiducial along with the data. On 29 September, 14 shots were taken with returned data on all the primary diagnostics.

Neutron Imaging: During April 2011, successful neutron source images were obtained at the Omega Laser Facility, using the NIF Version 2 neutron-imaging pinhole. These images represent a significant milestone for the project. This pinhole was designed to provide higher-resolution images and to cover a larger effective field of view at the target plane than previous versions of this diagnostic by addressing pointing uncertainties in the NIF alignment system. The pointing tolerance at the NIF for individual pinholes is ~100 μrad, so by constructing an array of "mispointed" pinholes, the effective field of view may be increased. The pointing locations for the NIF Version 2 pinhole are illustrated in Fig. 128.131. Each pinhole points about 35 μm away from its nearest neighbor.

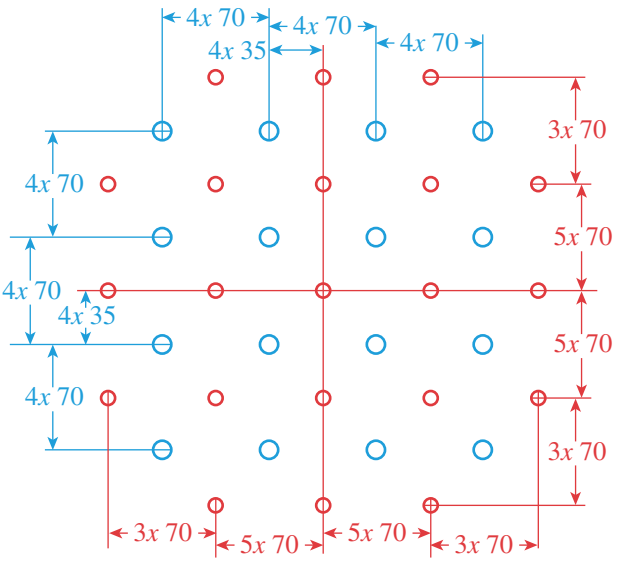

U1385JR

Figure 128.131
Pointing of the 37 NIF Version 2 pinholes at the target plane.

Figure 128.132 shows the front face of the NIF Version 2 pinhole, engineered by V. Fatherley of P-24 and fabricated by D. Schmidt and F. Garcia of MST-7. The dark squares on the gold background are the openings for each individual pinhole.

Figure 128.133 shows a sample of the data collected on the OMEGA laser on 14 April 2011. The image in Fig. 128.133(a) is from a direct-drive implosion of a CH capsule producing 2×10^{13} neutrons using the OMEGA laser. Clearly present


U1386JR

Figure 128.132
Image of the NIF Version 2 pinholes at the end of the 20-cm-long aperture body.

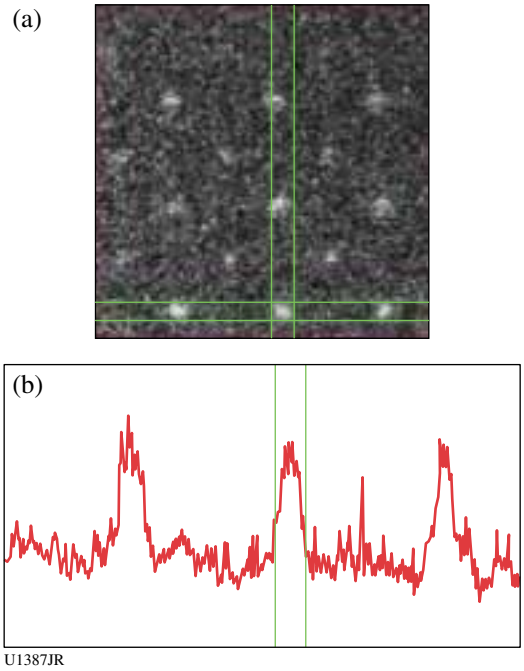

U1387JR

Figure 128.133
Shot 61898 on the OMEGA laser. (a) Clear images of the individual pinholes are present, and (b) the column-averaged lineout shows their relative signal to noise.

are images from both the small and large pinholes within the aperture array. Because of the size of the imaging fluor on OMEGA, not all the pinhole images would fit within the camera. Figure 128.133(b) shows the column-averaged lineout within the green box drawn on the image. From this data it is clear that the Version 2 pinhole works as an imaging array and can be brought to the NIF for further testing and use in imaging experiments.

In addition to this success, the team successfully fielded a new camera system that collected images from the start of the campaign. Furthermore late-time modifications to the pinhole mounting hardware that significantly reduced uncertainties in the pinhole pointing were also implemented.

OMEGA EP Ions: Los Alamos experimental team members have completed a new round of experiments on the OMEGA EP Laser System to test laser-generated ion beams at 10× higher energy than similar lasers such as LANL's own Trident Laser System (which operates at around 100 J).

The objective of this work is to develop laser-driven carbon ion beams for ICF studies. To do this, new tools were developed to study the focusing characteristics of these ion beams. Consistent production of multi-MeV ion beams was demonstrated, using a kilojoule of short-pulse laser energy with a conversion efficiency of several percent, and proton beams of nearly 70 MeV, the highest energies seen on the OMEGA EP laser, and near the world record in energy were achieved (see Fig. 128.134).

Ion beams are produced when an energetic and ultra-intense laser interacts with a thin solid target at relativistic intensities. The interaction produces large currents (MA) of electrons coursing through the target. The currents produce extreme electric fields on the rear surface of the order of teravolts per meter (TV/m), which in turn accelerate the ions into an MeV beam of roughly 10^{14} to 10^{15} ions in a picosecond (10^{-12} s). When focused, this beam has the potential of delivering tens of joules of energy into a spot of the order of tens of microns.

Using a combination of experiments on the LANL Trident Laser Facility and OMEGA EP, the team demonstrated the non-ballistic focusing nature of the ions from hemi-shelled targets. This was the topic of a recent invited talk and article given at the American Physical Society Division of Plasma Physics's annual meeting in Chicago in November 2010.[80]

This work has led to a new design for a focusing target, the "cusped hemi," which is a modified hemi-shell target with multiple radii of curvature to optimize the ion focusing and conversion efficiency (Figs. 128.135 and 128.136). These cusped hemis are made from 10-μm-thick diamond using

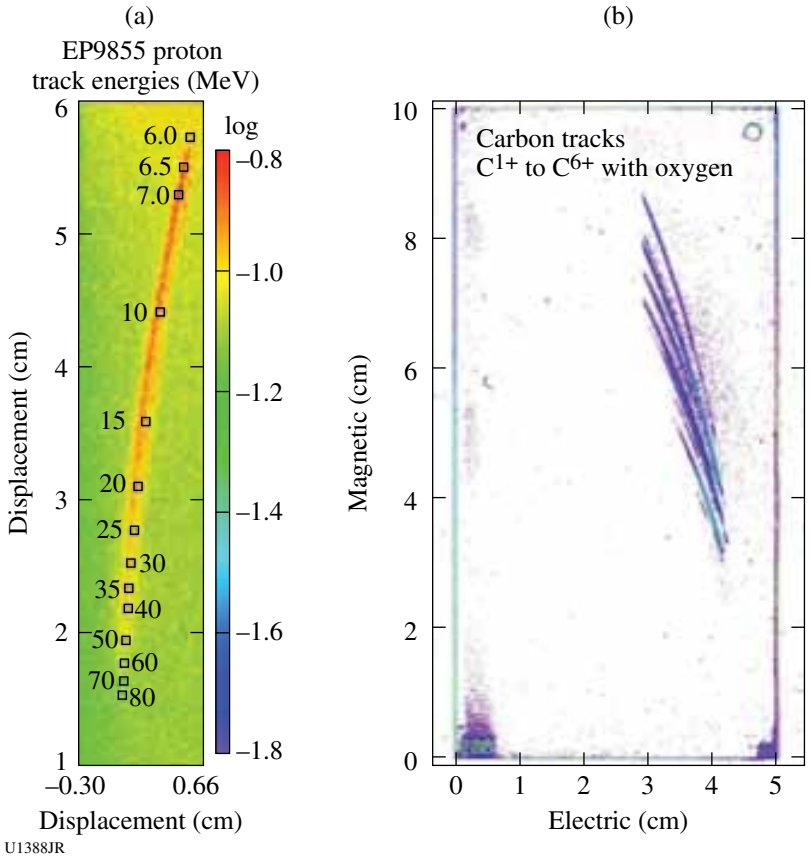

Figure 128.134
Thomson parabola (TPIE) data showing (a) high-energy protons up to nearly 70 MeV from OMEGA EP using 1 ps and ~400 J of laser energy and (b) carbon species up to 30 MeV in energy using 10 ps and 1000 J of laser energy.

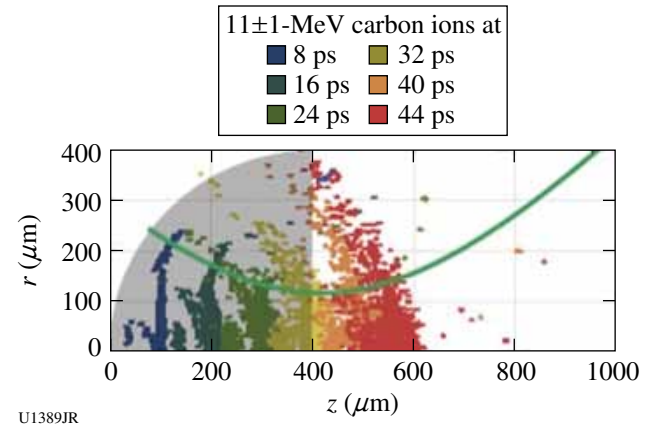

Figure 128.135
Simulated spatiotemporal data from the *LSP* code showing 11-MeV ions in a 1-MeV band for different time steps (colors) born on the hemi-shell's inner surface (gray) accelerated to the right and the ensemble trajectory as the green curve overlay.

chemical vapor deposition. The latest campaign on OMEGA EP (July 2011) tested these novel targets, the preliminary results of which indicate that they have outperformed their progenitors.

FY11 AWE OMEGA EP and OMEGA Experimental Programs

In FY11, AWE led six shot days on the OMEGA and OMEGA EP lasers. This work encompassed the development of MeV x-ray sources (one day in jointly funded collaboration with CEA) and 22- to 52-keV x-ray backlighters (three days in collaboration with LLNL, of which one was LLNL funded), a Laue x-ray diffraction study of the dynamics of shocked tantalum crystals (one day), and capsule implosions in asymmetrically driven hohlraums (one day).

MeV X-Ray Sources on OMEGA EP

Prinicpal Investigators: R. Edwards and C. Aedy (AWE); C. Courtois, J. Gazave, O. Landoas, and O. Peyssonneaux (CEA); and C. Stoeckl (LLE)

High-intensity ($I\lambda^2 > 10^{19}$ W/cm^2 μm^2) laser–plasma experiments have been used for several years to study the generation of energetic particles such as electrons, positrons, and protons. When energetic electrons propagate in a high-Z solid target located behind the interaction area, they produce a high-energy (>MeV) Bremsstrahlung emission source of potential interest

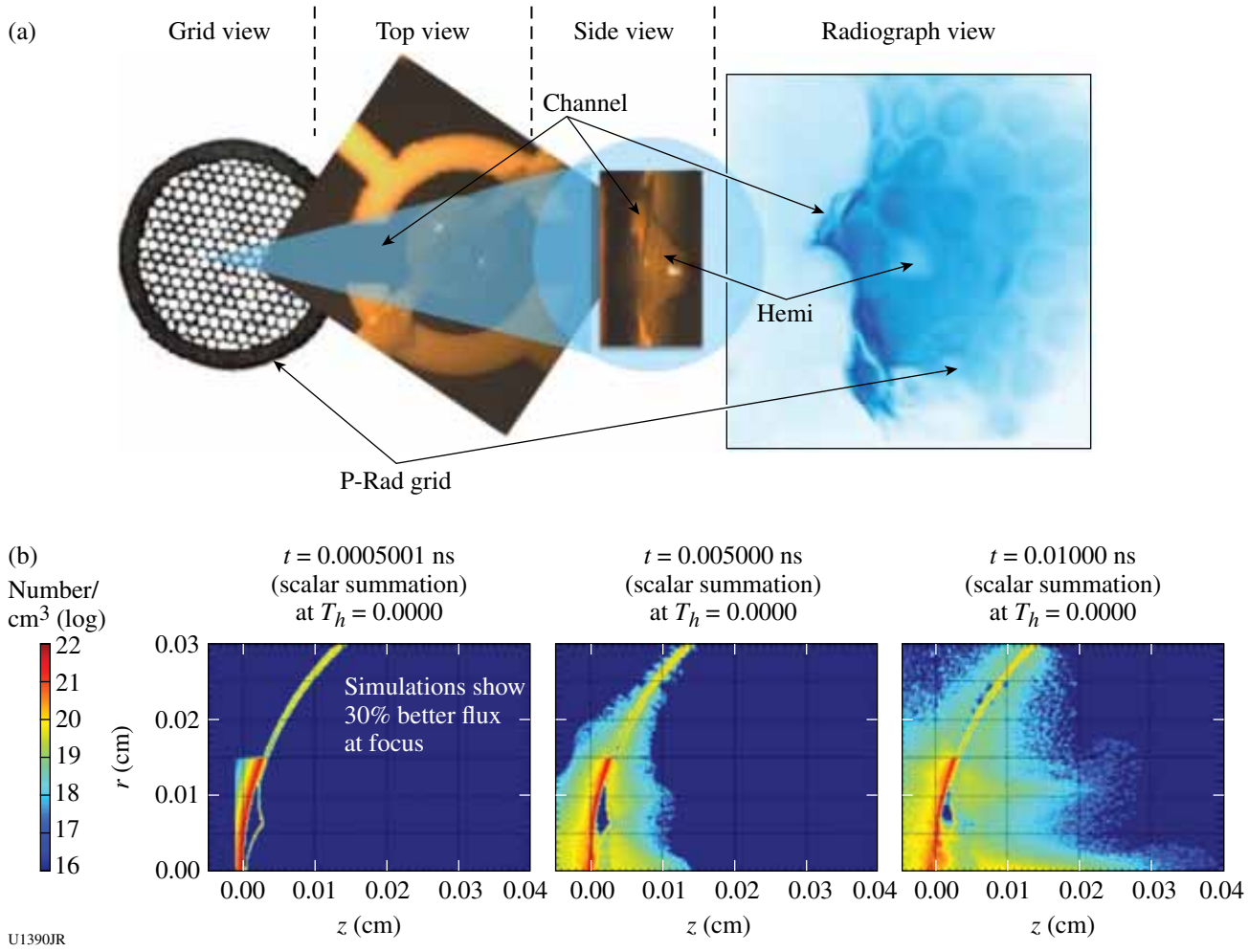

Figure 128.136

(a) Proton radiograph (P-Rad) of a cusped hemi (far right) starts with the radiography beam passing through a hexagonal grid (far left), and then the cusped-hemi target assembly (center, top, and side views) to create an image of the hemi target on a radiochromic film (RCF) stack with the grid superimposed (far right). The image in the RCF is formed from the cross-linking of a polymer dye in the active layer of the film caused by the energy deposited by the proton beam. The resulting image can then be deconvolved to measure the electric field strengths of the accelerating and preplasma fields formed by a second laser interacting with the hemi-apex, and used to refine the focusing design. (b) Simulations show a 30% increase in the flux of carbon ions at the focus of the cusped-hemi design compared to a traditional hemi-shell target. Left axis on the plots are r (cm), the radial dimension of the simulation in cm, and bottom axes are z, the length in cm; color scale indicates the carbon-ion density number/cm^3 (log) from blue (10^{15}) to red (10^{22}) for three separate time steps, just as the laser interacts, then 4.5 ps later, and 5 ps after that, using a 10-ps pulse duration.

in nuclear-activation, radiation-effects, and radiation-safety studies. Laser-produced, multi-MeV x-ray sources are also of significant interest for radiography applications since intense, short-duration (picosecond) lasers can be focused to a micron-scale focal spot, which potentially gives access to high temporal and spatial resolution x-ray sources.

The present experiment is the third of this type performed on OMEGA EP by AWE in collaboration with CEA. The MeV x-ray source is produced by focusing a short-duration laser pulse (the "backlighter") onto a 2-mm-thick, 2-mm-diam tantalum cylinder target coated at its front surface with a 10-μm-thick layer of plastic. In the present experiment, with the use of new gratings in the compressor, the backlighter energy on target increased to 1.5 kJ in 10 ps, which is significantly higher than was delivered (~1 kJ) during previous AWE/CEA campaigns on OMEGA EP. For one of the shots, a nanosecond-duration heating beam (250 J, 1 ns with phase-plate smoothing) was used to produce a preformed plasma that was intended to increase the short-pulse energy absorption.

The x-ray source size is estimated from radiography of a resolution grid [Fig. 128.137(a)] and an "image-quality indicator" (IQI) test object. The lower-energy part of the x-ray spectrum is inferred from the radiography of a "Tower of Hanoi" [Fig. 128.137(b)] filter stack and filtered dosimeters. The high-energy (>10-MeV) component of the x-ray spectrum is studied from ^{63}Cu (λ,n) ^{62}Cu and ^{12}C (γ,n) ^{11}C photonuclear reaction measurements.

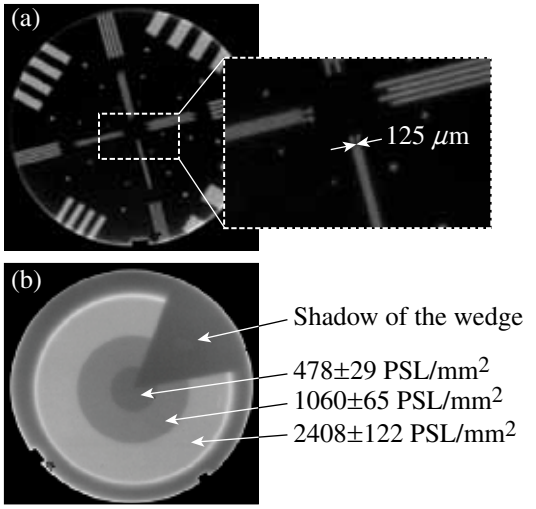

Figure 128.137
(a) Radiographic images of the resolution grid, with detail shown and (b) the Tower of Hanoi test object.

Figures 128.137(a) and 128.137(b) show, respectively, the radiography image of a 15-mm-thick tungsten resolution grid and the tungsten Tower of Hanoi object. Figure 128.137(a) demonstrates that a 125-μm-wide slot can be easily solved by the radiography source, implying that the x-ray source is relatively small (of the order of a few hundred microns). This is in agreement with previous data where the x-ray source size was inferred using a penumbral imaging technique. Figure 128.138 shows data from the IQI test object (ρR = 90 g/cm^2).

When the backlighter beam is used without the heating beam, the estimated x-ray temperature is around 3 MeV and an x-ray dose of up to 5 rad in air is measured at 1 m from the source. When both beams are used, the x-ray dose is a factor of 2 lower. This confirms previous data obtained on OMEGA EP, where x-ray emission is consistently lower when the long pulse is used (to create a preformed plasma) in combination with the short pulse. The future 4ω laser probe could be used to investigate this point by establishing the density profile of the preformed plasma with which the short pulse later interacts.

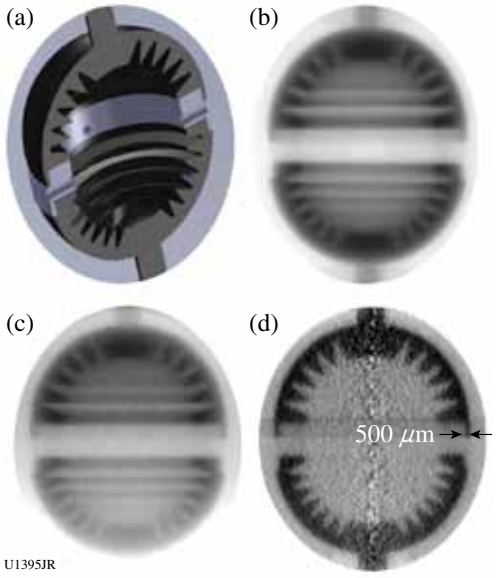

Figure 128.138
(a) CAD section view of the image-quality indicator (IQI) test object. Radiography images of the IQI through (b) 28-g/cm^2 and (c) 61-g/cm^2 tungsten equivalent. (d) Density map obtained from (c) after tomography.

High-Resolution 22- to 52-keV Backlighter Sources with Applications for X-Ray Radiography

Principal Investigators: K. Vaughan, A. Moore, K. Wallace, D. Gate, S. McAlpin and R. M. Stevenson (AWE); and V. A. Smalyuk, S. G. Glendinning, B. R. Maddox, H.-S. Park, and C. Sorce (LLNL)

AWE successfully led three shot days (TinMan-11A, HEERD-11A, and TinMan-11B) to investigate x-ray–backlighter microwire targets in the 22- to 52-keV region, in collaboration with LLNL.

Many HED experiments, in particular those investigating ICF applications, require x-ray diagnostic capabilities providing enough photons in a single event to probe HED targets with sufficient contrast and resolution. In light of this, much work has been undertaken to address the development of x-ray probes in the 20- to 100-keV energy range and spatial resolution of less than 20 μm (Refs. 81–84).

The OMEGA EP short-pulse beam was used to irradiate silver, samarium, and ytterbium microwire targets, delivering 22-, 40-, and 52-keV K_α x rays, respectively. The microwire targets, produced by the AWE Target Fabrication group, consisted of 10-μm × 10-μm × 300-μm wire of the K_α-generating material, supported by a 300-μm × 300-μm × 6-μm CH sub-

strate and held by a 6-μm-diam carbon fiber. To characterize the source size and demonstrate 2-D resolution, a secondary grid target was positioned 10 mm from target chamber center in the direction of the primary radiography diagnostic. Details of the microwire and grid targets are shown in Fig. 128.139.

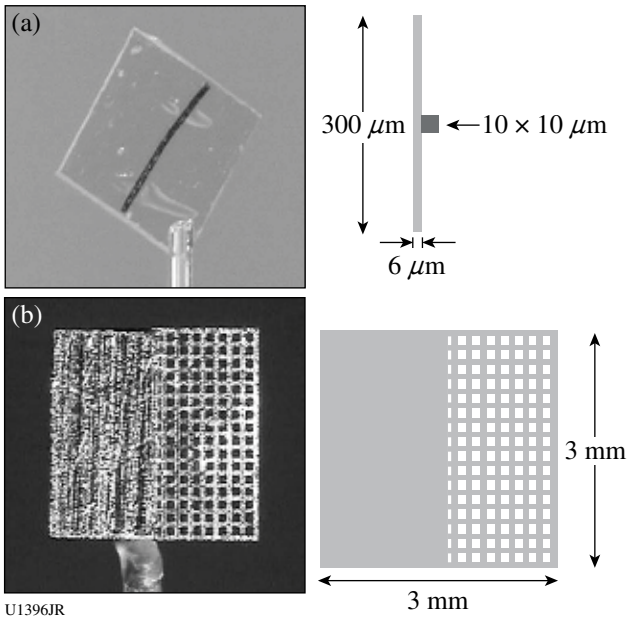

Figure 128.139
Microwire and grid targets. (a) The microwire target shown is a silver microwire supported by a thin CH flag. Other microwire targets fabricated from samarium and ytterbium were also supported by thin CH flags. (b) The grid target shown consists of a solid gold foil and a gold grid. The striations apparent on the foil part of the target are a result of the manufacturing process and are not a feature of the material.

Data were recorded using the transmission crystal spectrometer (TCS) and the high-energy radiography imager for OMEGA EP (HERIE) mounted on diametrically opposed ports of the target chamber (TIM-10 and TIM-13), each with an end-on view of the microwire target. The microwire targets were irradiated at a range of irradiances, incorporating changes in the laser parameters including focal spot size (85 μm to 200 μm), pulse duration (10 ps and 100 ps), and beam energy (100 J to 850 J), to investigate the K_α yield over a large parameter space.

Excellent experimental data were obtained for all microwire targets. Figure 128.140 shows a radiograph of the grid target backlit by a samarium microwire. A simple analytical line-spread function analysis of the images indicates that high resolution (<20 μm) was achieved in two dimensions.

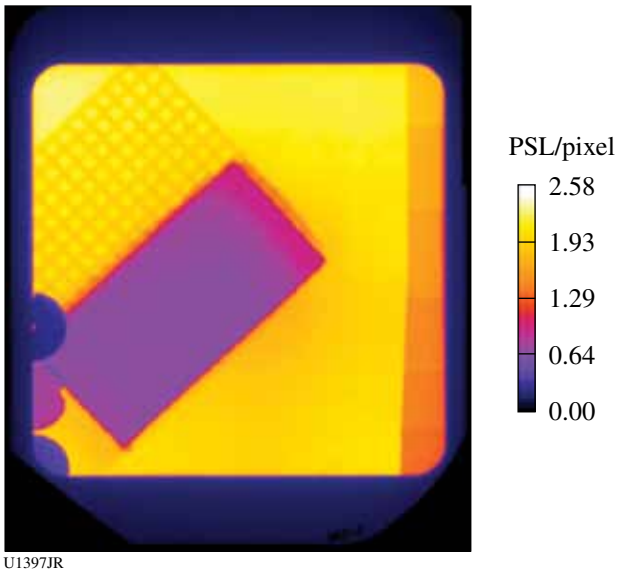

Figure 128.140
A typical radiograph collected by the HERIE diagnostic using a samarium microwire irradiated at 6×10^{17} W/cm^2. Signal strength is shown in units of PSL/pixel. A copper step wedge ranging in thickness from 36 μm to 126 μm (top to bottom) is shown along the right-hand side of the radiograph. In the lower left-hand corner are three tantalum disks of thicknesses 750 μm, 75 μm, and 250 μm (top to bottom), respectively.

Future work on backlighter development continues with strong collaboration between AWE and LLNL.

Laue X-Ray Diffraction Studies of Crystal-Lattice Dynamics

Principal Investigators: A. Comley, J. M. Foster, S. Rothman, N. Park, P. A. Rosen, N. Bazin, and D. Gate (AWE); M. Suggit, A. Higginbotham, and J. Wark (Oxford); and B. R. Maddox, B. A. Remington, H.-S. Park, S. Prisbrey, and A. Elsholz (LLNL)

In the ShkLaue-11A campaign, we further developed our broadband x-ray ("white-light") Laue diffraction platform designed to probe the lattice dynamics of single-crystal [100] tantalum under shock-loaded conditions, building on our initial study in StrDiff-11A (see LLNL programs section).

In the experiment, an implosion capsule backlighter (980-μm outer diameter with a 10-μm-thick CH wall) driven by 44 OMEGA beams (each beam delivered 500 J of energy in a 1-ns square pulse and SG4 phase plates were used) was employed to generate a smooth, broadband spectrum of x rays to produce the white-light diffraction pattern, recorded using

the LLNL broadband x-ray diffraction diagnostic (BBXRD). A single beam (10 to 40 J in a 1-ns square pulse, with an SG8 phase plate) was used to drive a shock in the tantalum crystal via a 10-μm-thick diamond ablator. The 5-μm-thick tantalum crystal was of [100] orientation.

We obtained an excellent data set that revealed a clear trend of increasing lattice strain anisotropy with a drive pressure in the 1- to 2-Mbar range, controlled in the experiment by varying the laser energy on the crystal target package (Fig. 128.141). VISAR was used to infer the pressure in the sample.

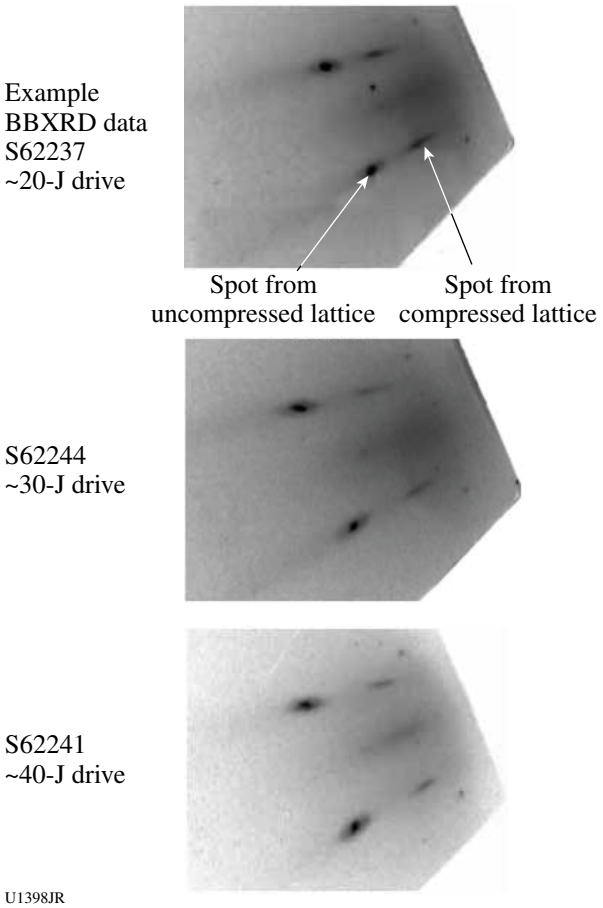

Figure 128.141
Raw BBXRD data showing how diffraction pattern varies with laser-drive energy on the tantalum crystal target package. Each pattern contains characteristic spots, each of which can be attributed to either the shocked or unshocked regions in the crystal, and to specific crystallographic lattice planes. Increasing laser drive energy (and pressure) results in increased spatial separation between the shocked and unshocked spots, indicative of increasing strain anisotropy in the lattice.

Asymmetrically Driven Hohlraums
Principal Investigators: J. M. Foster and S. McAlpin (AWE)

AWE carried out one day of OMEGA experiments (Hohl-Dyn-11A) to conclude a study of capsule implosions in asymmetrically driven hohlraums.

In previous work,[85,86] a tailored angular and temporal asymmetry of radiation drive was achieved by several means: asymmetry of laser-beam energy and timing, asymmetry of capsule position and hohlraum wall material (albedo), and by introducing an annular restriction of diameter (baffle) within one part of the hohlraum. In these experiments, a 1.6-mm-diam, 2.7-mm-long hohlraum was heated by up to 30 beams of the OMEGA laser. X-ray backlighting of a thin-wall glass capsule (600-μm-diam, 3.5-μm-thick wall, 30-μm CH ablator) or silica aerogel sphere (600-μm-diam, 300-mg cm^{-3} density) provided the primary diagnostic of the angular distribution of radiation drive near the center of the hohlraum. The hydrodynamics was diagnosed using an area x-ray backlighting source together with a 16-image pinhole camera and four-strip–gated MCP detector.

In the most recent experiments, the same experimental platform of the hohlraum and thin-shell capsule was used, but x-ray point-projection backlighting was employed to obtain a single image of greater spatial resolution than had been formerly obtained. The point-projection backlighting technique has the additional advantage of highlighting (by virtue of x-ray refraction, the so-called "phase-contrast" enhancement effect) steep density gradients in the imploding capsule. Thin-shell capsules with walls of uniform thickness and walls that incorporate a shallow equatorial-groove defect were used, and a subset of the asymmetric hohlraum geometries used in the earlier (area-backlit experiments) provided the radiation drive. Excellent experimental data (Fig. 128.142) were obtained, demonstrating the sensitivity of the point-projection–imaging technique for this type of experiment. The data are being used to constrain 2-D hydrocode simulations.

FY11 CEA Experiments at the Omega Laser Facility

CEA Vulnerability Diagnostics on OMEGA: Vulnerability is a key point for the design of plasma diagnostics. Some diagnostics operating on megajoule class lasers require the integration of optical components with electronic devices. The Omega Laser Facility is a fundamental tool for studying the behavior of these elements under irradiation as the DT shot campaigns reproduce the perturbing source expected at early times on the NIF and LMJ. The aim is to maintain in opera-

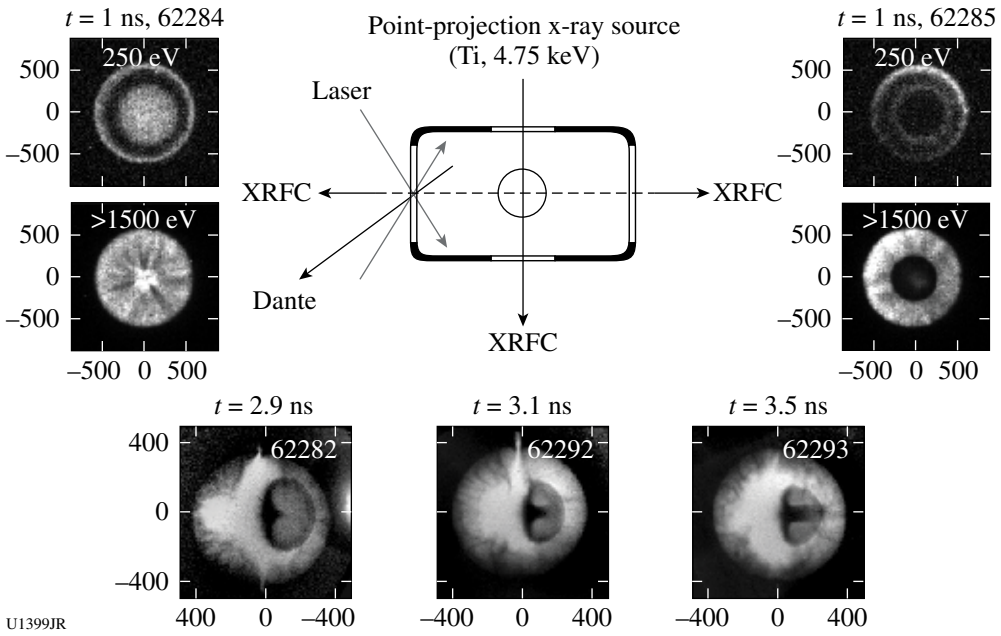

Figure 128.142
The asymmetrically imploded capsule is diagnosed using x-ray framing cameras (XRFC's) viewing along the hohlraum axis and by point-projection imaging viewing orthogonal to the hohlraum axis. The axial views record self-emission from the capsule and hohlraum (which serves as a backlighter for the capsule in one direction) at early time. The orthogonal, point-projection imaging view records details of the asymmetric implosion, with phase-contrast enhancement of the steep density gradient at the glass/ablator interface. Structure around the perimeter of the closing diagnostic hole is also revealed with high spatial resolution (10 μm).

tion the diagnostic and preserve its nominal performance for neutron yields of ~10^{17}.

During the 8 March 2011 shot campaign, the amount of parasitic light generated by standard optical glasses and fiber bundles was quantified using a set of photomultipliers installed inside the Target Bay at 5 m from TCC (Fig. 128.143). Glasses presented different behavior in terms of the amount of emitted light and decay time (Fig. 128.144). As a result of such studies, glasses that are prone to scintillators have been identified and their use must be minimized on the NIF/LMF diagnostic systems.

In addition to these characterizations, the vulnerability of an active pixel sensor (APS) based on a complementary metal oxyde semiconductor (CMOS) has been studied. The objectives consisted of the evaluation of the durability of the APS in such a radiative environment, measurement of the APS recovery [Fig. 128.145(b)], and the radiation-induced charge generation

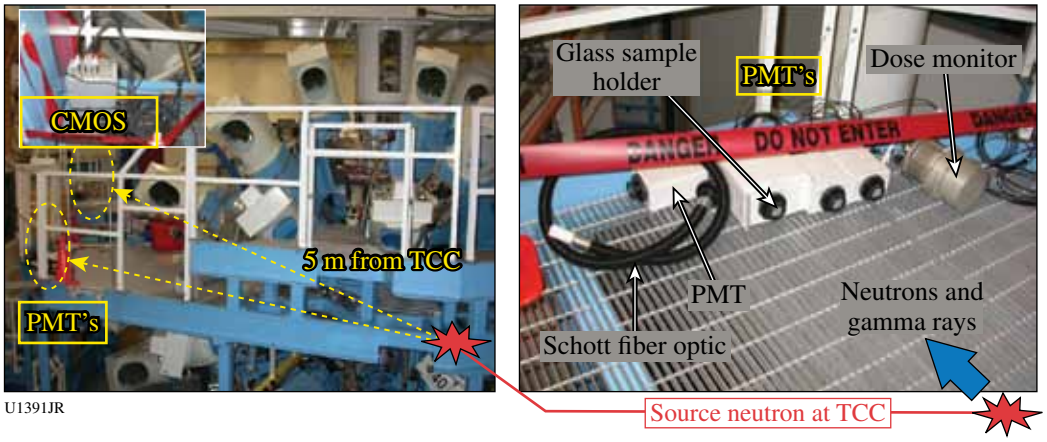

Figure 128.143
Experimental setup.

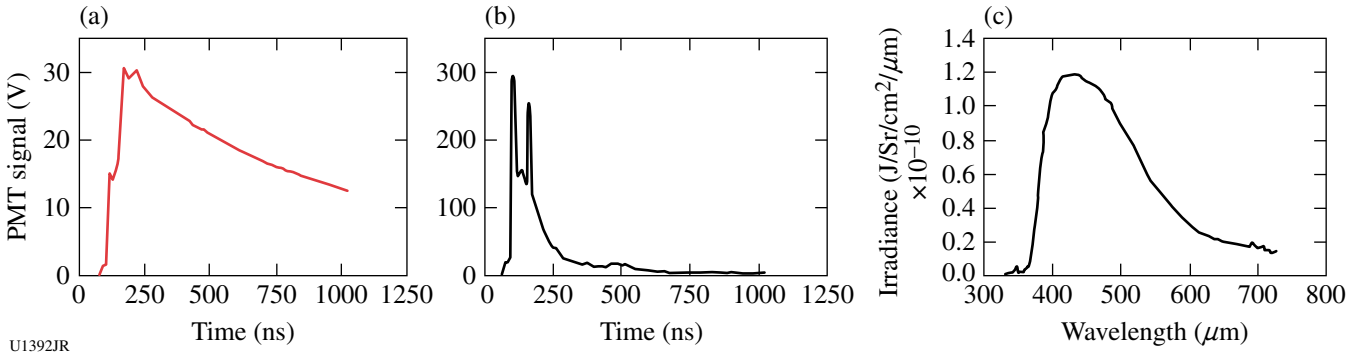

Figure 128.144
Typical behavior observed on OMEGA for (a) CaF2 and [(b) and (c)] Schott optical fibers bundle.

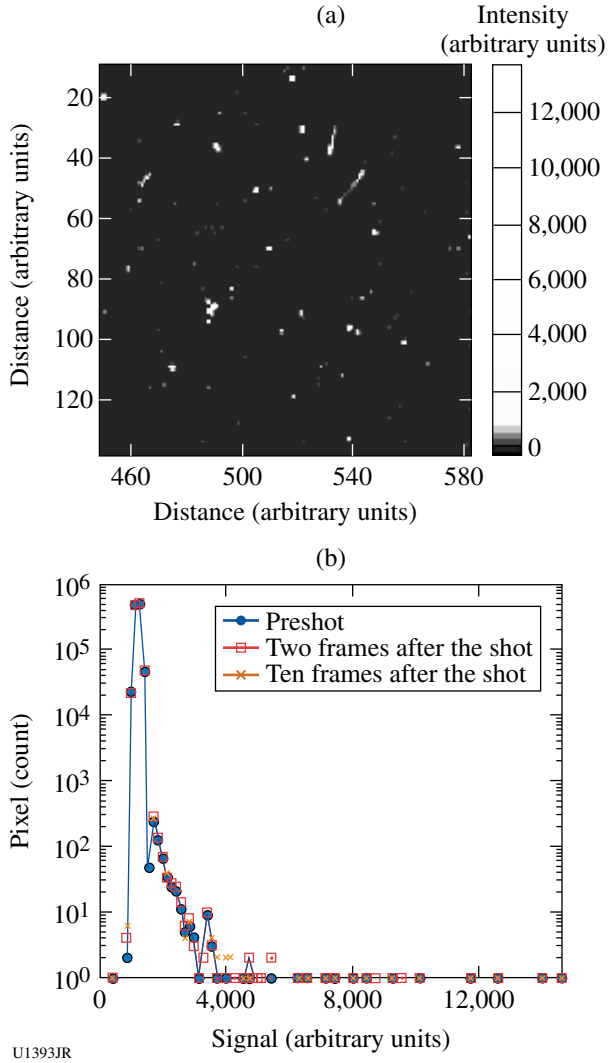

Figure 128.145
Typical image recording obtained with (a) APS and (b) kinetic of APS recovery.

by the mixed neutrons/gamma rays pulse [Fig. 128.145(a)]. The collected charge distribution inside the image sensor has been successfully measured: the APS remains functional after a DT shot and induced charges inside the pixel are removed. No permanent change in the dark-current distribution has been observed after irradiation.

CEA Neutron Imaging on OMEGA: Over the past ten years, CEA developed the LMJ neutron-imaging diagnostic (NIS) on OMEGA using penumbral or annular coded aperture techniques.[87–90] The previous optimized NIS system provided a 20-μm spatial resolution in the source plane and a very good signal-to-noise ratio (SNR). Both the penumbral and the annular imaging techniques were developed successfully, and the annular (ring) technique seems the most promising way to achieve higher-resolution images with a good SNR. Nevertheless, the annular imaging technique is very sensitive to misalignment (<50 μm in a 200-μm field of view) compared to the penumbral aperture.[91,92] The use of the annular aperture required the retraction/insertion of the TIM. The alignment technique was not accurate enough, so a new aperture manipulator was designed to increase rigidity and to allow one to change apertures online without retracting the TIM (cf., Fig. 128.146). A new lighting system, embedded in the aperture manipulator tritium protection, now allows one to align the diagnostic even if the opposite port is not available to use a backlighting technique. Penumbral and annular apertures are positioned on the same axis in a pre-alignment phase. The final alignment accuracy was also improved by using a cross-hair target at the target chamber center (TCC).

Apertures were placed at 26 cm and the large neutron camera (scaled for LMJ) at 13 m from TCC (magnification = 50). As in the previous campaigns, alignment was performed

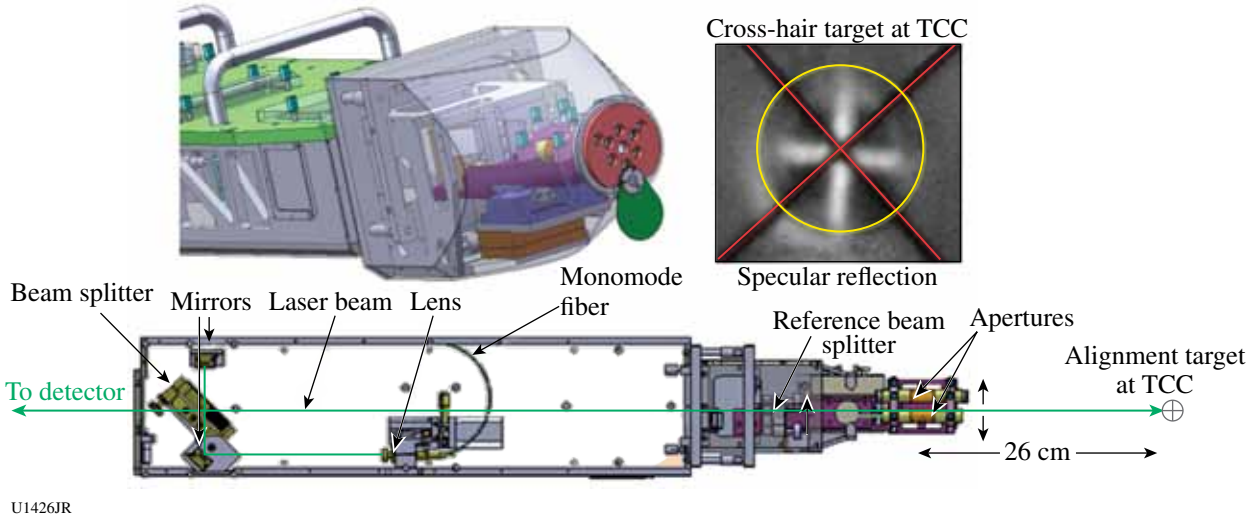

Figure 128.146
New aperture manipulator design allowing for the placement online of either a penumbral or annular aperture at 26 cm from TCC. The image shows the cross-hair target placed at TCC aligned on the axis defined by the telescope reticule placed at 8 m from TCC.

using the penumbral aperture. First images were obtained with the penumbral aperture and the diagnostic was aligned on the first shot. The aperture change was made between shot 61416 and shot 61419. The penumbral and annular images analysis shows a position difference in the image plane of only 144 μm (2 pixels). This corresponds to an aperture relative misalignment of only 3 μm in the source plane. During the entire shot day, alignment settings were not modified. Spherical, prolate, and oblate 14-MeV neutron core images were obtained by varying the laser-energy balance and compared to x-ray images from the LLE GMXI diagnostic in the 4- to 7-keV range (cf., Fig. 128.147). The neutron image SNR is in the 30 to 50 range and the system resolution is ~16 μm.

First shot alignment is a crucial issue for megajoule-class lasers with a long line of sight (40 m for LMJ), and it was demonstrated again this year. The new alignment system and method now allow us to use both penumbral and annular apertures.

FY11 Center for Radiative Shock Hydrodynamics—Experiments

The Center for Radiative Shock Hydrodynamics (CRASH) is a scientific computing center where part of the Center's effort is to predict experimental data and quantify uncertainty in experimental data. CRASH is part of the Predictive Science Academic Alliance Program (PSAAP). The main experiment that CRASH models is a radiative-shock experiment. In this system the radiative flux is so large that radiative effects must be considered when modeling the system since they affect the shock dynamics. The CRASH code is a 3-D Eulerian radiation–hydrodynamics code based on an adaptive, massively parallel magnetohydrodynamics code. Experiments for this year focused on obtaining early-time data of a radiative-shock system.

Figure 128.148(a) shows a radiograph of a radiative shock at 4.5 ns after the start of the laser drive. This image was taken with a four-strip x-ray framing camera using the area radiography technique. In this experiment, ten OMEGA laser beams are used with a 380-J/beam in a 1-ns square pulse to irradiate a 20-μm Be disk. SG8 distributed phase plates (DPP's) and the smoothing by spectral dispersion (SSD) technique at maximum modulation smooth the laser beams, which launch a shock into the Be disk. The shock breaks out of the disk and into nominally 1.1 atm of Xe gas. The shock moves rapidly (over ~150 μm/ns initially) and becomes so hot that radiative effects become important in the system. As the shock moves down the tube, it sweeps up more Xe and becomes a dense Xe layer with an entrained Xe flow behind the shock. This is evident in late-time data that we previously obtained and are shown in Figs. 128.148(b) and 128.148(c), which show a radiative shock observed at 13 and 26 ns, respectively.

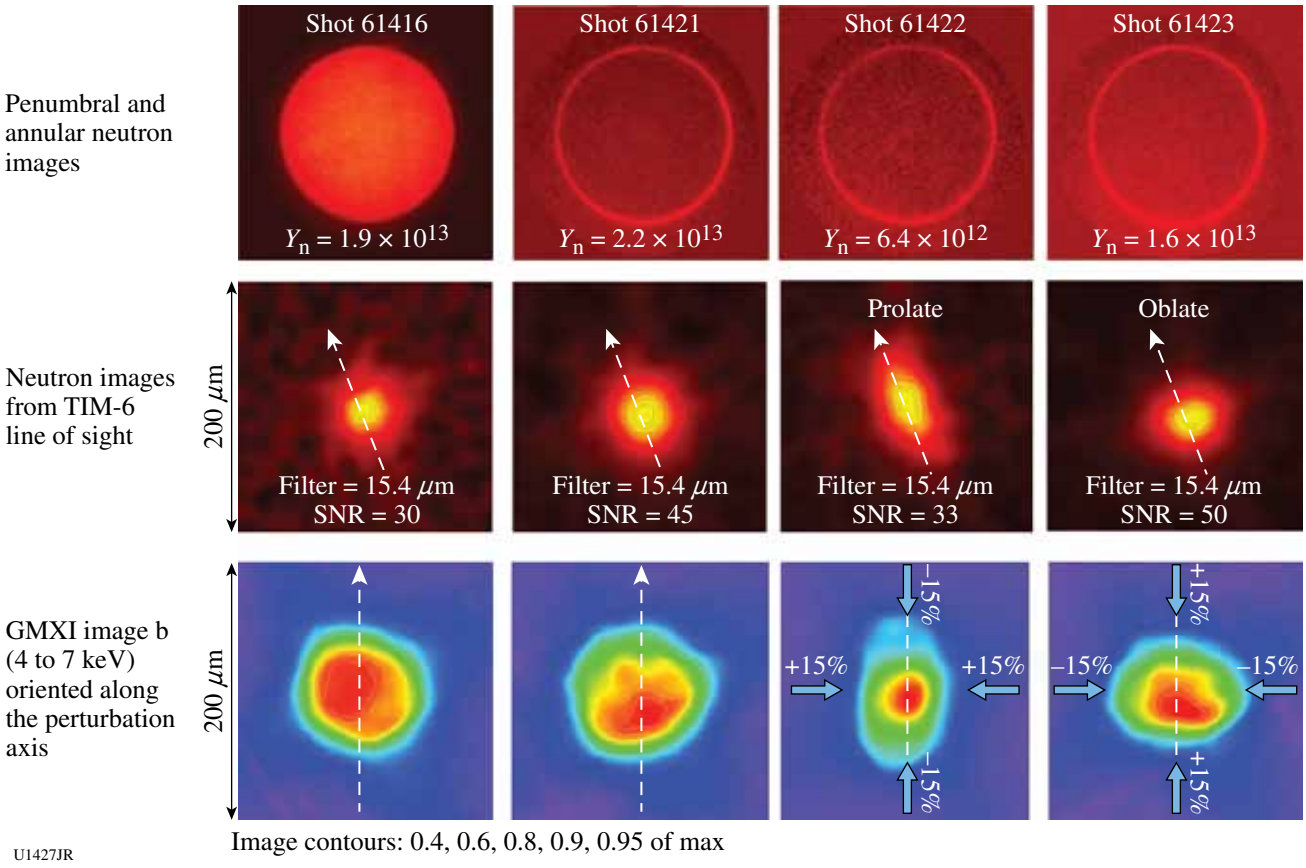

Figure 128.147
Neutron and LLE x-ray images obtained during spherical, oblate, and prolate implosions. The dashed white arrows show the perturbation axis on neutron and x-ray images.

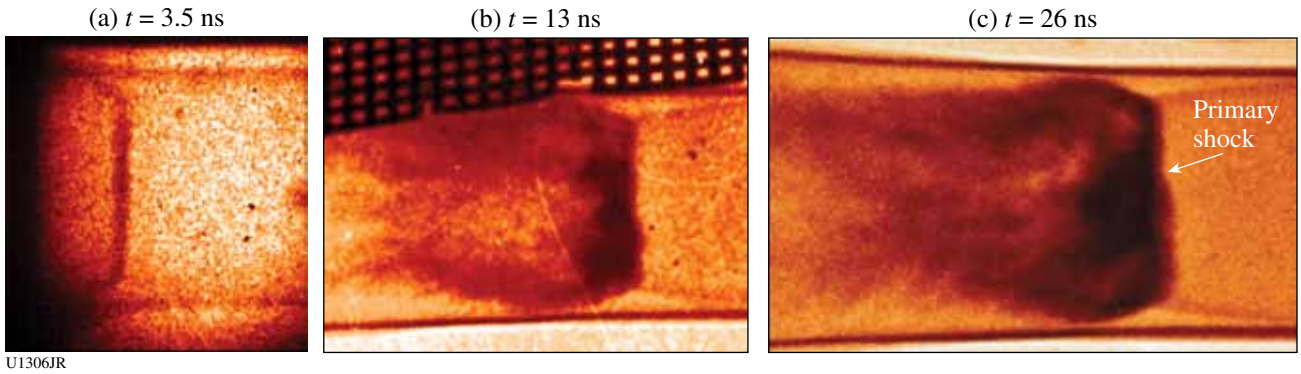

Figure 128.148
X-ray radiographs of a radiative shock experiment at (a) 3.5 ns, (b) 13 ns, and (c) 26 ns. As the shock moves down the Xe-filled tube, it accumulates more Xe.

REFERENCES

1. M. A. Morales *et al.*, Proc. Natl. Acad. Sci. **106**, 1324 (2009).
2. W. Lorenzen, B. Holst, and R. Redmer, Phys. Rev. Lett. **102**, 115701 (2009).
3. T. Nagayama, R. C. Mancini, R. Florido, R. Tommasini, J. A. Koch, J. A. Delettrez, S. P. Regan, and V. A. Smalyuk, J. Appl. Phys. **109**, 093303 (2011).
4. C. K. Li, F. H. Séguin, J. A. Frenje, J. R. Rygg, R. D. Petrasso, R. P. J. Town, P. A. Amendt, S. P. Hatchett, O. L. Landen, A. J. Mackinnon, P. K. Patel, V. Smalyuk, J. P. Knauer, T. C. Sangster, and C. Stoeckl, Rev. Sci. Instrum. **77**, 10E725 (2006).
5. T. R. Boehly, D. L. Brown, R. S. Craxton, R. L. Keck, J. P. Knauer, J. H. Kelly, T. J. Kessler, S. A. Kumpan, S. J. Loucks, S. A. Letzring, F. J. Marshall, R. L. McCrory, S. F. B. Morse, W. Seka, J. M. Soures, and C. P. Verdon, Opt. Commun. **133**, 495 (1997).
6. L. J. Waxer, D. N. Maywar, J. H. Kelly, T. J. Kessler, B. E. Kruschwitz, S. J. Loucks, R. L. McCrory, D. D. Meyerhofer, S. F. B. Morse, C. Stoeckl, and J. D. Zuegel, Opt. Photonics News **16**, 30 (2005).
7. J. R. Rygg, F. H. Séguin, C. K. Li, J. A. Frenje, M. J.-E. Manuel, R. D. Petrasso, R. Betti, J. A. Delettrez, O. V. Gotchev, J. P. Knauer, D. D. Meyerhofer, F. J. Marshall, C. Stoeckl, and W. Theobald, Science **319**, 1223 (2008).
8. C. K. Li, F. H. Séguin, J. A. Frenje, M. Rosenberg, R. D. Petrasso, P. A. Amendt, J. A. Koch, O. L. Landen, H. S. Park, H. F. Robey, R. P. J. Town, A. Casner, F. Philippe, R. Betti, J. P. Knauer, D. D. Meyerhofer, C. A. Back, J. D. Kilkenny, and A. Nikroo, Science **327**, 1231 (2010).
9. C. K. Li, F. H. Séguin, J. A. Frenje, J. R. Rygg, R. D. Petrasso, R. P. J. Town, P. A. Amendt, S. P. Hatchett, O. L. Landen, A. J. Mackinnon, P. K. Patel, V. A. Smalyuk, T. C. Sangster, and J. P. Knauer, Phys. Rev. Lett. **97**, 135003 (2006).
10. C. K. Li, F. H. Séguin, J. A. Frenje, J. R. Rygg, R. D. Petrasso, R. P. J. Town, P. A. Amendt, S. P. Hatchett, O. L. Landen, A. J. Mackinnon, P. K. Patel, M. Tabak, J. P. Knauer, T. C. Sangster, and V. A. Smalyuk, Phys. Rev. Lett. **99**, 015001 (2007).
11. C. K. Li, F. H. Séguin, J. A. Frenje, J. R. Rygg, R. D. Petrasso, R. P. J. Town, O. L. Landen, J. P. Knauer, and V. A. Smalyuk, Phys. Rev. Lett. **99**, 055001 (2007).
12. C. K. Li, F. H. Séguin, J. R. Rygg, J. A. Frenje, M. Manuel, R. D. Petrasso, R. Betti, J. Delettrez, J. P. Knauer, F. Marshall, D. D. Meyerhofer, D. Shvarts, V. A. Smalyuk, C. Stoeckl, O. L. Landen, R. P. J. Town, C. A. Back, and J. D. Kilkenny, Phys. Rev. Lett. **100**, 225001 (2008).
13. C. K. Li, F. H. Séguin, J. A. Frenje, R. D. Petrasso, P. A. Amendt, R. P. J. Town, O. L. Landen, J. R. Rygg, R. Betti, J. P. Knauer, D. D. Meyerhofer, J. M. Soures, C. A. Back, J. D. Kilkenny, and A. Nikroo, Phys. Rev. Lett. **102**, 205001 (2009).
14. R. D. Petrasso, C. K. Li, F. H. Séguin, J. R. Rygg, J. A. Frenje, R. Betti, J. P. Knauer, D. D. Meyerhofer, P. A. Amendt, D. H. Froula, O. L. Landen, P. K. Patel, J. S. Ross, and R. P. J. Town, Phys. Rev. Lett. **103**, 085001 (2009).
15. O. V. Gotchev, P. Y. Chang, J. P. Knauer, D. D. Meyerhofer, O. Polomarov, J. Frenje, C. K. Li, M. J.-E. Manuel, R. D. Petrasso, J. R. Rygg, F. H. Séguin, and R. Betti, Phys. Rev. Lett. **103**, 215004 (2009).
16. C. K. Li, F. H. Séguin, J. H. Frenje, M. J. Rosenberg, H. G. Rinderknecht, A. B. Zylstra, R. D. Petrasso, P. A. Amendt, O. L. Landen, A. J. Mackinnon, R. P. J. Town, S. C. Wilks, R. Betti, D. D. Meyerhofer, J. M. Soures, J. Hund, J. D. Kilkenny, and A. Nikroo, "Impeding Hohlraum Plasma Stagnation in Inertial Confinement Fusion," to be published in Physical Review Letters.
17. F. H. Séguin, C. K. Li, M. J.-E. Manuel, H. G. Rinderknecht, N. Sinenian, J. A. Frenje, J. R. Rygg, D. G. Hicks, R. D. Petrasso, J. Delettrez, R. Betti, F. J. Marshall, and V. A. Smalyuk, "Time Evolution of Filamentation and Self-Generated Fields in the Coronae of Directly Driven ICF Capsules," to be published in Physics of Plasmas.
18. A. B. Zylstra *et al.*, "Measurements of Hohlraum-Produced Fast Ions," submitted to Physics of Plasmas.
19. J. A. Frenje, C. K. Li, F. H. Séguin, D. T. Casey, R. D. Petrasso, D. P. McNabb, P. Navratil, S. Quaglioni, T. C. Sangster, V. Yu. Glebov, and D. D. Meyerhofer, Phys. Rev. Lett. **107**, 122502 (2011).
20. F. H. Séguin, J. A. Frenje, C. K. Li, D. G. Hicks, S. Kurebayashi, J. R. Rygg, B.-E. Schwartz, R. D. Petrasso, S. Roberts, J. M. Soures, D. D. Meyerhofer, T. C. Sangster, J. P. Knauer, C. Sorce, V. Yu. Glebov, C. Stoeckl, T. W. Phillips, R. J. Leeper, K. Fletcher, and S. Padalino, Rev. Sci. Instrum. **74**, 975 (2003).
21. H.-S. Park, D. D. Ryutov, J. S. Ross, N. L. Kugland, S. H. Glenzer, C. Plechaty, S. M. Pollaine, B. A. Remington, A. Spitkovsky, L. Gargaté, G. Gregori, A. Bell, C. Murphy, Y. Sakawa, Y. Kuramitsu, T. Morita, H. Takabe, D. H. Froula, G. Fiksel, F. Miniati, M. Koenig, A. Ravasio, A. Pelka, E. Liang, N. Woolsey, C. C. Kuranz, R. P. Drake, and M. J. Grosskopf, "Studying Astrophysical Collisionless Shocks with Counterstreaming Plasmas from High Power Lasers," to be published in High Energy Density Physics.
22. A. Spitkovsky, Bull. Am. Phys. Soc. **56**, Paper B6.00001 (2011).
23. A. Spitkovsky, presented at the Twenty-Second International Conference on Numerical Simulation of Plasmas, Long Branch, NJ, 7–9 September 2011.
24. A. Spitkovsky, presented at the Center for Magnetic Self-Organization (CMSO) General Meeting, Durham, NH, 17–20 October 2011.
25. H.-S. Park, presented at ICHED (International Conference on High Energy Density Physics), Lisbon, Portugal, 17–20 May 2011.
26. H.-S. Park, presented at the 7th International Conference on Inertial Fusion Sciences and Applications, Bordeaux, France, 12–16 September 2011.
27. Y. Sakawa, presented at The Seventh International Conference on Inertial Fusion Sciences and Applications, Bordeaux-Lac, France, 12–16 September 2011.
28. J. Ross, Bull. Am. Phys. Soc. **56**, 282 (2011).
29. L. Gargaté, A. Spitkovsky, H.-S. Park, N. L. Kugland, J. S. Ross, B. A. Remington, S. M. Pollaine, D. D. Ryutov, G. Gregori, Y. Sakawa,

Y. Kuramitsu, H. Takabe, D. H. Froula, G. Fiksel, F. Miniati, M. Koenig, A. Ravasio, N. Woolsey, and M. Grosskopf, presented at the Interrelationship Between Plasma Experiments in Laboratory and Space, Whistler, Canada, 10–15 July 2011.

30. M. Grosskopf, presented at the 11th International Workshop on the Interrelationship Between Plasma Experiments in the Laboratory and in Space (IPELS), Whistler, Canada, 10–15 July 2011.

31. M. Wei, presented at the 38th European Physical Society Conference on Plasma Physics, Strasbourg, France, 27 June–1 July 2011.

32. R. Mishra, presented at the 7th International Conference on Inertial Fusion Sciences and Applications, Bordeaux, France, 12–16 September 2011.

33. L. Willingale, P. M. Nilson, A. G. R. Thomas, J. Cobble, R. S. Craxton, A. Maksimchuk, P. A. Norreys, T. C. Sangster, R. H. H. Scott, C. Stoeckl, C. Zulick, and K. Krushelnick, Phys. Rev. Lett. **106**, 105002 (2011).

34. H. Chen, S. C. Wilks, D. D. Meyerhofer, J. Bonlie, C. D. Chen, S. N. Chen, C. Courtois, L. Elberson, G. Gregori, W. Kruer, O. Landoas, J. Mithen, J. Myatt, C. D. Murphy, P. Nilson, D. Price, M. Schneider, R. Shepherd, C. Stoeckl, M. Tabak, R. Tommasini, and P. Beiersdorfer, Phys. Rev. Lett. **105**, 015003 (2010).

35. H. Chen, D. D. Meyerhofer, S. C. Wilks, R. Cauble, F. Dollar, K. Falk, G. Gregori, A. Hazi, E. I. Moses, C. D. Murphy, J. Myatt, J. Park, J. Seely, R. Shepherd, A. Spitkovsky, C. Stoeckl, C. I. Szabo, R. Tommasini, C. Zulick, and P. Beirsdorfer, High Energy Density Phys. **7**, 225 (2011).

36. R. Betti, K. Anderson, T. R. Boehly, T. J. B. Collins, R. S. Craxton, J. A. Delettrez, D. H. Edgell, R. Epstein, V. Yu. Glebov, V. N. Goncharov, D. R. Harding, R. L. Keck, J. H. Kelly, J. P. Knauer, S. J. Loucks, J. A. Marozas, F. J. Marshall, A. V. Maximov, D. N. Maywar, R. L. McCrory, P. W. McKenty, D. D. Meyerhofer, J. Myatt, P. B. Radha, S. P. Regan, C. Ren, T. C. Sangster, W. Seka, S. Skupsky, A. A. Solodov, V. A. Smalyuk, J. M. Soures, C. Stoeck, W. Theobald, B. Yaakobi, C. Zhou, J. D. Zuegel, J. A. Frenje, C. K. Li, R. D. Petrasso, and F. H. Séguin, Plasma Phys. Control. Fusion **48**, B153 (2006).

37. O. V. Gotchev, J. P. Knauer, P. Y. Chang, N. W. Jang, M. J. Shoup III, D. D. Meyerhofer, and R. Betti, Rev. Sci. Instrum. **80**, 043504 (2009).

38. P. Y. Chang, G. Fiksel, M. Hohenberger, J. P. Knauer, R. Betti, F. J. Marshall, D. D. Meyerhofer, F. H. Séguin, and R. D. Petrasso, Phys. Rev. Lett. **107**, 035006 (2011).

39. O. A. Hurricane, High Energy Density Phys. **4**, 97 (2008).

40. E. C. Harding *et al.*, Phys. Rev. Lett. **103**, 045005 (2009).

41. O. A. Hurricane *et al.*, Phys. Plasmas **16**, 056305 (2009).

42. M. Borghesi *et al.*, Rev. Sci. Instrum. **74**, 1688 (2003).

43. I. V. Igumenshchev, F. J. Marshall, J. A. Marozas, V. A. Smalyuk, R. Epstein, V. N. Goncharov, T. J. B. Collins, T. C. Sangster, and S. Skupsky, Phys. Plasmas **16**, 082701 (2009).

44. A. L. Kritcher *et al.*, Phys. Rev. Lett. **107**, 015002 (2011).

45. A. L. Kritcher *et al.*, High Energy Density P hys. **7**, 271 (2011).

46. D. D. Ryutov *et al.*, Phys. Plasmas **18**, 104504 (2011).

47. A. B. Belonoshko, R. Ahuja, and B. Johansson, Nature **424**, 1032 (2003).

48. S. H. Glenzer, Rev. Mod. Phys. **81**, 1625 (2009).

49. S. H. Glenzer *et al.*, Phys. Rev. Lett. **90**, 175002 (2003).

50. G. Gregori *et al.*, Phys. Rev. E **67**, 026412 (2003).

51. H. Sawada, S. P. Regan, D. D. Meyerhofer, I. V. Igumenshchev, V. N. Goncharov, T. R. Boehly, R. Epstein, T. C. Sangster, V. A. Smalyuk, B. Yaakobi, G. Gregori, S. H. Glenzer, and O. L. Landen, Phys. Plasmas **14**, 122703 (2007).

52. S. H. Glenzer *et al.*, Phys. Rev. Lett. **98**, 065002 (2007).

53. G. Gregori *et al.*, High Energy Density Phys. **3**, 99 (2007).

54. P. B. Radha, V. N. Goncharov, T. J. B. Collins, J. A. Delettrez, Y. Elbaz, V. Yu. Glebov, R. L. Keck, D. E. Keller, J. P. Knauer, J. A. Marozas, F. J. Marshall, P. W. McKenty, D. D. Meyerhofer, S. P. Regan, T. C. Sangster, D. Shvarts, S. Skupsky, Y. Srebro, R. P. J. Town, and C. Stoeckl, Phys. Plasmas **12**, 032702 (2005).

55. G. Kresse and J. Furthmüller, Phys. Rev. B **54**, 11169 (1996).

56. J. Vorberger *et al.*, Phys. Rev. B **75**, 024206 (2007).

57. P. M. Celliers, D. J. Erskine, C. M. Sorce, D. G. Braun, O. L. Landen, and G. W. Collins, Rev. Sci. Instrum. **81**, 035101 (2010).

58. R. Betti, C. D. Zhou, K. S. Anderson, L. J. Perkins, W. Theobald, and A. A. Solodov, Phys. Rev. Lett. **98**, 155001 (2007).

59. W. L. Kruer, *The Physics of Laser–Plasma Interactions*, Frontiers in Physics, Vol. 73, edited by D. Pines (Addison-Wesley, Redwood City, CA, 1988).

60. R. Betti, W. Theobald, C. D. Zhou, K. S. Anderson, P. W. McKenty, S. Skupsky, D. Shvarts, V. N. Goncharov, J. A. Delettrez, P. B. Radha, T. C. Sangster, C. Stoeckl, and D. D. Meyerhofer, J. Phys., Conf. Ser. **112**, 022024 (2008).

61. V. Yu. Glebov, D. D. Meyerhofer, C. Stoeckl, and J. D. Zuegel, Rev. Sci. Instrum. **72**, 824 (2001).

62. W. Seka, D. H. Edgell, J. P. Knauer, J. F. Myatt, A. V. Maximov, R. W. Short, T. C. Sangster, C. Stoeckl, R. E. Bahr, R. S. Craxton, J. A. Delettrez, V. N. Goncharov, I. V. Igumenshchev, and D. Shvarts, Phys. Plasmas **15**, 056312 (2008).

63. C. Stoeckl, V. Yu. Glebov, D. D. Meyerhofer, W. Seka, B. Yaakobi, R. P. J. Town, and J. D. Zuegel, Rev. Sci. Instrum. **72**, 1197 (2001).

64. X. Ribeyre *et al.*, Plasma Phys. Control. Fusion **50**, 025007 (2008).

65. R. Tommasini, S. P. Hatchett, D. S. Hey, C. Iglesias, N. Izumi, J. A. Koch, O. L. Landen, A. J. MacKinnon, C. Sorce, J. A. Delettrez, V. Yu. Glebov, T. C. Sangster, and C. Stoeckl, Phys. Plasmas **18**, 056309 (2011).

66. Y. Ping *et al.*, J. Instrum. **6**, P09004 (2011).

67. H. J. Lee, P. Neumayer, J. Castor, T. Döppner, R. W. Falcone, C. Fortmann, B. A. Hammel, A. L. Kritcher, O. L. Landen, R. W. Lee, D. D. Meyerhofer, D. H. Munro, R. Redmer, S. P. Regan, S. Weber, and S. H. Glenzer, Phys. Rev. Lett. **102**, 115001 (2009).

68. D. K. Bradley *et al.*, Phys. Rev. Lett. **102**, 075503 (2009).

69. F. Occelli, P. Loubeyre, and R. LeToullec, Nat. Mater. **2**, 151 (2003).

70. A. Dewaele *et al.*, Phys. Rev. Lett. **97**, 215504 (2006).

71. L. S. Dubrovinsky *et al.*, Phys. Rev. Lett. **84**, 1720 (2000).

72. S. Desgreniers, Y. K. Vohra, and A. L. Ruoff, Phys. Rev. B **39**, 10,359 (1989).

73. L. Burakovsky, D. L. Preston, and R. R. Silbar, Phys. Rev. B **61**, 15,011 (2000).

74. N. R. Barton *et al.*, J. Appl. Phys. **109**, 073501 (2011).

75. H.-S. Park *et al.*, "Experimental Results of Ta Material Strength at High Pressure and High Strain Rate," to be published in AIP for the SCCM proceedings.

76. H.-S. Park *et al.*, "Tantalum Material Strength Dependence on Grain Sizes at 100 GPa Pressure and 107 s^{-1} Strain Rates," in preparation.

77. E. N. Loomis, D. Braun, S. H. Batha, C. Sorce, and O. L. Landen, Phys. Plasmas **18**, 092702 (2011).

78. E. N. Loomis, presented at the 7th International Conference on Inertial Fusion Sciences and Applications, Bordeaux, France, 12–16 September 2011.

79. A. Banerjee, R. A. Gore, and M. J. Andrews, Phys. Rev. E **82**, 046309 (2010).

80. D. T. Offermann et al., Phys. Plasmas **18**, 056713 (2011).

81. H.-S. Park, D. M. Chambers, H.-K. Chung, R. J. Clarke, R. Eagleton, E. Giraldez, T. Goldsack, R. Heathcote, N. Izumi, M. H. Key, J. A. King, J. A. Koch, O. L. Landen, A. Nikroo, P. K. Patel, D. F. Price, B. A. Remington, H. F. Robey, R. A. Snavely, D. A. Steinman, R. B. Stephens, C. Stoeckl, M. Storm, M. Tabak, W. Theobald, R. P. J. Town, J. E. Wickersham, and B. B. Zhang, Phys. Plasmas **13**, 056309 (2006).

82. H.-S. Park *et al.*, Phys. Plasmas **15**, 072705 (2008).

83. E. Brambrink, H. G. Wei, B. Barbrel, P. Audebert, A. Benuzzi-Mounaix, T. Boehly, T. Endo, C. Gregory, T. Kimura, R. Kodama, N. Ozaki, H. S. Park, M. Rabec le Gloahec, and M. Koenig, Phys. Plasmas **16**, 033101 (2009).

84. B. R. Maddox *et al.*, Phys. Plasmas **18**, 056709 (2011).

85. K. Vaughn, S. McAlpin, J. M. Foster, R. M. Stevenson, S. G. Glendinning, and C. Sorce, Phys. Plasmas **17**, 056316 (2010).

86. *LLE 2009 Annual Report, October 2008–September 2009*, Laboratory for Laser Energetics, University of Rochester, Rochester, NY, LLE Document No. DOE/NA/28302-923 (January 2010); *LLE 2010 Annual Report, October 2009–September 2010*, Laboratory for Laser Energetics, University of Rochester, Rochester, NY, LLE Document No. DOE/NA/28302-985 (January 2011).

87. L. Disdier, A. Rouyer, D. C. Wilson, A. Fedotoff, C. Stoeckl, J. L. Bourgade, V. Yu. Glebov, J.-P. Garçonnet, and W. Seka, Nucl. Instrum. Methods Phys. Res. A **489**, 496 (2002).

88. L. Disdier, A. Rouyer, A. Fedotoff, J.-L. Bourgade, F. J. Marshall, V. Yu. Glebov, and C. Stoeckl, Rev. Sci. Instrum. **74**, 1832 (2003).

89. L. Disdier, R. A. Lerche, J. L. Bourgade, and V. Yu. Glebov, Rev. Sci. Instrum. **75**, 2134 (2004).

90. A. Rouyer, Rev. Sci. Instrum. **74**, 1234 (2003).

91. L. Disdier, A. Rouyer, I. Lantuéjoul, O. Landoas, J. L. Bourgade, T. C. Sangster, V. Yu. Glebov, and R. A. Lerche, Phys. Plasmas **13**, 056317 (2006).

92. I. Thfoin, O. Landoas, T. Caillaud, L. Disdier, M. Vincent, J.-L. Bourgade, B. Rossé, T. C. Sangster, V. Yu. Glebov, G. Pien, and W. Armstrong, Rev. Sci. Instrum. **81**, 033503 (2010).

The Third Omega Laser Facility Users' Group Workshop

Introduction

A capacity gathering of 115 researchers from 25 universities and laboratories and 9 countries met at the Laboratory for Laser Energetics (LLE) for the third Omega Laser Facility Users' Group (OLUG) workshop. The purpose of the three-day workshop was to facilitate communication and exchanges among individual Omega Laser Facility users and between users and the LLE management; to present ongoing and proposed research; to encourage research opportunities and collaborations that could be undertaken at the Omega Laser Facility and in a complementary fashion at other facilities (such as the NIF or LULI); to provide an opportunity for students, postdoctoral fellows, and young researchers to present their research in an informal setting; and to provide LLE management with feedback from the users about ways to improve the Facility and future experimental campaigns. The interactions were wide-ranging and lively, as can be seen in photographs shown in this article.

The Omega Laser Facility Users consist of 266 members from 32 universities and 23 centers and national laboratories; their names and affiliations can be found at **www.lle.rochester.edu/media/about/documents/OLUGMEMBERS.pdf**. OLUG is by far the largest users' group in the world in the field of high-energy-density (HED) physics, and it is certainly one of the most active.

U1400JR

Figure 128.149

A capacity gathering of 115 researchers from 25 universities and laboratories around the world participated in this year's workshop. The users' group itself has 266 members from 32 universities and 23 laboratories, making it by far the largest such high-energy-density-physics group in the world. The Omega Facility is now a member of the National Users' Facility Organization, which in turn promotes science education and outreach throughout the nation. The next annual Omega Laser Facility Users' Workshop will occur on 25–27 April 2012.

The first two mornings of the workshop comprised 13 science and Facility presentations. The Facility talks proved especially useful for those unfamiliar with the art and complexities of performing experiments on OMEGA. But since the Facility is constantly changing and improving, even experienced users significantly benefited from these updates. The overview science talks, given by leading world authorities, described the breadth and excitement of HED science undertaken at the Omega Laser Facility. The next section of this article contains a summary of the range of presentations and activities.

About 50 students and postdoctoral fellows, 44 of whom were supported by travel grants from NNSA, attended the workshop and presented 37 of the 57 contributed poster and oral presentations. The content of their presentations ranged from target fabrication to simulating aspects of supernovae; the presentations generated spirited discussions, probing questions, and friendly suggestions. In addition, 20 contributed presentations were made by professional scientists and academics.

An important function of the workshop was to develop a set of **Findings and Recommendations** (p. 253) to help set future priorities for the Omega Laser Facility.

These findings were grouped into four areas: 60-beam OMEGA, OMEGA EP, general Facility improvements, and the accessibility of OMEGA operational information. These categories comprise a report given to Omega Facility management (highlights to follow). LLE management is currently using these recommendations as a guide for making decisions about Omega Laser Facility operations, priorities, and future changes.

One highlight of the workshop was the panel of students and postdoctoral fellows who discussed their experiences at the Omega Laser Facility and presented their thoughts and recommendations on Facility improvements. Wide-ranging and engaging discussions were sparked by this forum, which resulted in the student/postdoctoral report.

Another important event was a job fair designed to bring students together with potential future employers and to discuss career opportunities that exist at national laboratories, in private industry, and at universities.

Finally, one of the important decisions made at the workshop was the scheduling of the next one. It will be held at LLE on 25–27 April 2012. Meetings of the Users' Group and interested

U1401JR

Figure 128.150
About 50 students and postdoctoral fellows, 44 of whom received travel assistance from an NNSA grant, attended and made 37 presentations. Travel assistance has already been arranged for the next annual workshop. The workshop places tremendous emphasis on the participation of young researchers.

members of the HED community are formulating plans for this fourth workshop. In addition, an annual meeting, in which the status of the **Findings and Recommendations** (p. 253) will be updated, will occur during the fall APS/DPP Conference.

The Presentations

A diverse set of 70 talks and posters were presented over a three-day period. In morning sessions, invited talks on the Facility and science were given. The invited science talks focused on several important topics, including HED plasmas in general, laboratory astrophysics, ignition in inertial confinement fusion (ICF), the physics of shock and fast ignition, and future experiments on OMEGA and the NIF.

The Omega Facility talks presented important details and developments on the status and performance of OMEGA/OMEGA EP from pulse shaping and duration to beam smoothing; the qualification process for interfacing new experiments; the present, and soon-to-be operating, set of diagnostics; and the critical role of targets, from design, to procurement, to full characterization, to fielding, and finally shooting.

In addition to the 13 invited presentations, 57 contributed posters and talks covered a wide spectrum of work on OMEGA from target fabrication to fast-ignition experiments to basic and novel nuclear physics experiments. Work was also presented on opportunities for taking physics platforms developed on OMEGA to other facilities that are both larger (the NIF) and smaller (Jupiter, Trident, and LULI, as examples). The invited and contributed presentations formed much of the basis for the discussions that resulted in the **Findings and Recommendations** (p. 253) for the Omega Facilities; topics and chairpersons for each are presented herein.

The photographs provide a representative sampling of the workshop's talks, interactions, and ambience.

U1403JR

Figure 128.151

In the plenary sessions, 13 authorities spoke about the science and opportunities of HED physics and described the evolving capabilities of the Omega Laser Facility needed to reach new science frontiers. Here LLE Director Dr. Robert L. McCrory, a strong supporter of OLUG since its inception, welcomes the users and talks about the evolving capabilities of the Facility that keep it at the cutting edge of research.

The 13 Findings and Recommendations of the OMEGA 2011 Users' Workshop (reports and presentations can be found on-line at www.lle.rochester.edu/about/OLUG11_workshop/index.php):

1. Tammy Ma, Chair, LLNL. *Findings and Recommendations of the Student/Postdoc Panel*.

2. Louise Willingale, Chair, University of Michigan. *Bringing OMEGA EP Performance up to Full Specification, and 4ω Probe Utilization*.

U1404JR

Figure 128.152
University of Rochester astrophysicist Adam Frank gave a stellar talk on instabilities and clumping processes in jets and in astrophysical and laboratory settings.

U1405JR

Figure 128.153
University of New Hampshire (UNH) theorist Will Fox talked about theoretical aspects of 3-D reconnection in laboratory and astrophysical settings. UNH is one of 32 universities who are members of the OMEGA Users' group. University researchers, 107 in number, comprise the largest component of OLUG's 266 members.

3. Mingsheng Wei, Chair, GA. *Long-Pulse Operations of OMEGA EP.*

4. Carolyn Kuranz, Chair, University of Michigan. *Independent Operations of the Three Legs of OMEGA 60.*

U1406JR

Figure 128.154
Nuclear physicist Dennis McNabb of LLNL described new and exciting opportunities in plasma nuclear science that are emerging on OMEGA and the NIF. Several contributed workshop talks, as well as Facility recommendations, focused on this nascent frontier field, whose origins directly derive from recent OMEGA Users' experiments. Subsequent to the workshop, a joint MIT, LLNL, and LLE press conference (**www.web.mit.edu/press/2011/omega-laser.html**) announced the results of the first basic nuclear physics experiments obtained in ICF. Many more such experiments are either already underway or are being actively planned on OMEGA.

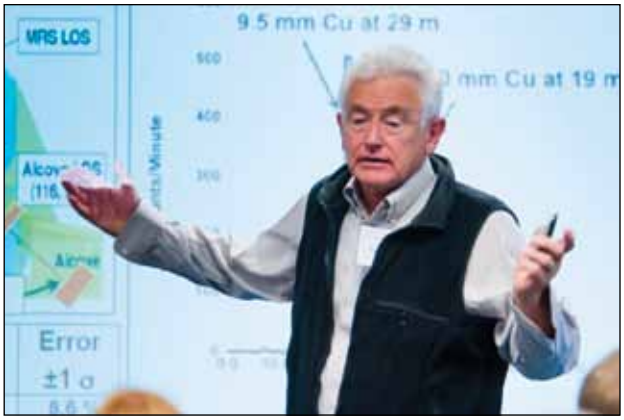

U1407JR

Figure 128.155
Joe Kilkenny of General Atomics talked about the importance and pervasiveness of moving diagnostics and experimental platforms from OMEGA to the NIF. Many critical diagnostics at the NIF, such as the magnetic recoil (neutron) spectrometer, were first developed and used on OMEGA before being duplicated and deployed on the NIF.

5. Dustin Froula, Chair, LLE. *Work to Develop a Simulation Capability for the OMEGA External Users.*

6. Peter Norreys, Chair, Rutherford Appleton Laboratory. *Dual Foci for the Omega 60 Facility.*

7. Dennis McNabb (LLNL) and Johan Frenje (MIT), Chairs. *Developing Implosion Capabilities on OMEGA with Arbitrary Fuel Mixtures of Tritium for Advancing Plasma Nuclear Science.*

8. Alex Zylstra, Chair, MIT. *An Ultra-Low-Charged-Particle Spectrometer for Studying Nucleo-Synthesis Reactions in OMEGA Implosions.*

9. Nareg Sinenian (MIT) and Jim Cobble (LANL), Chairs. *Utilization of Thomson Parabola on OMEGA for Characterizing Implosion Ion-Loss Channels and for Studying Nucleo-Synthesis Reactions in OMEGA Implosions.*

U1408JR

Figure 128.156
Sam Morse, the Omega Facility Director, talked about changes in the Facility and LLE's implementation of OLUG'S Findings and Recommendations. Sam leads the Facility's cognizant, approachable engineers and managers who are constantly working to facilitate and improve users' experiments. A very strong and cordial relationship exists between the users and the LLE management team, and extensive discussions occur throughout the year between OLUG and the management regarding OLUG's Findings and Recommendations.

U1410JR

Figure 128.158
Two poster sessions presented an opportunity for informal discussions about OMEGA experiments and their connections to important work at other HED facilities, especially the NIF.

U1409JR

Figure 128.157
Don Cook, NNSA's Deputy Administrator for Defense Programs, talked to the OMEGA Users about NNSA's perspective on HED science on OMEGA and on the value they place on the users' work and research.

U1412JR

Figure 128.159
The workshop provided many opportunities for informal interactions and discussions and for sowing the seeds of new experimental and theoretical efforts.

U1411JR

Figure 128.160
Thirty-seven posters and contributed talks were given by students and postdoctoral fellows.

U1413JR

Figure 128.161
The student–postdoc panel, chaired by LLNL's Tammy Ma, led an engaging discussion about issues that young researchers face in performing experiments on OMEGA. This panel formulated their own Findings and Recommendations that became part of the workshop proceedings.

U1415JR

Figure 128.162
Thirteen different Findings and Recommendations for the Facility were extensively discussed by User leads and Chairs (shown here from top to bottom are Maria Gatu-Johnson from MIT; Hye-Sook Park from LLNL; and Carolyn Kuranz from University of Michigan). Women physicists have an extremely strong presence at every level of OLUG, from the Executive Committee to the chairs of the major OLUG committees on Findings and Recommendations.

10. Hans Herrmann, Chair, LANL. *Gamma-Ray Spectrometry for Plasma Nuclear Science and Implosion Physics.*

11. Maria Gatu-Johnson, Chair, MIT. *A Low-Energy Neutron Spectrometer for Plasma Nuclear Science and Implosion Physics.*

12. Gennady Fiksel, Chair, LLE. *Developing Magnetic Inertial Fusion Platforms for Basic Science and Implosion Physics.*

13. Hye-Sook Park, Chair, LLNL. *Cu-K_α Crystal Imaging on OMEGA EP for HED Physics.*

U1416JR

Figure 128.163
Tours of OMEGA and OMEGA EP were a critical component of the workshop and greatly appreciated by users new and old. Here LLE engineer Steve Stagnitto is shown in the OMEGA viewing gallery talking with workshop attendees about the intricacies and challenges of organizing a successful experimental program.

U1418JR

Figure 128.165
The workshop banquet was enjoyed by all and offered a wonderful opportunity for good cheer and good food. The making of lifelong colleagues and friends is one of the lasting results of the Users' worksho Good friends make for good science!

U1417JR

Figure 128.164
Physicist Ray Leeper discussed career opportunities in research at Sandia National Laboratory. Lawrence Livermore National Laboratory and Los Alamos National Laboratory also presented overviews of laboratory research opportunities. These talks presented a unique opportunity for young researchers to learn about research not only on OMEGA, but at the other major facilities, at Universities, and in the private sector.

Questions Addressed in the General Workshop Sessions:

What new avenues of research should we be pursuing on the Omega/Omega EP Laser Facilities?

What Facility improvements, large or small, can improve current research and help us pursue science at the cutting edge?

How can the administrative organization and the infrastructure at LLE better support ongoing and groundbreaking research?

What additional platforms/experiments/diagnostics might advantageously be built and coordinated, e.g., between OMEGA and the NIF, and/or between OMEGA and Trident or Jupiter?

The OMEGA Laser Users' Meeting was held at the APS/DPP conference in Utah on 15 November 2011. The next OMEGA Laser Users' Workshop will be held at LLE on 25–27 April 2012.

ACKNOWLEDGMENT

This OMEGA Users' Workshop is made possible in part by the generous support of the National Nuclear Security Administration for travel expenses of students and postdocs; by the Office of Fusion Energy Sciences for support of general workshop costs; by General Atomics; by the Fusion Science Center; by the MIT/Plasma Science and Fusion Center; and by the Laboratory for Laser Energetics for the use and availability of critical resources and support. In addition, OLUG thanks the LLE management for their responsiveness to our Findings and Recommendations. For capturing through his lens the workshop ambiance, OLUG thanks Eugene Kowaluk. R. D. Petrasso is the editor for this Proceeding.

Publications and Conference Presentations

Publications

S.-W. Bahk, "Highly Accurate Wavefront Reconstruction Algorithms over Broad Spatial-Frequency Bandwidth," Opt. Express **19**, 18,997 (2011).

T. R. Boehly, V. N. Goncharov, W. Seka, S. X. Hu, J. A. Marozas, D. D. Meyerhofer, P. M. Celliers, D. G. Hicks, M. A. Barrios, D. Fratanduono, and G. W. Collins, "Multiple Spherically Converging Shock Waves in Liquid Deuterium," Phys. Plasmas **18**, 092706 (2011).

J. Bromage, J. Rothhardt, S. Hädrich, C. Dorrer, C. Jocher, S. Demmler, J. Limpert, A. Tünnermann, and J. D. Zuegel, "Analysis and Suppression of Parasitic Processes in Noncollinear Optical Parametric Amplifiers," Opt. Express **19**, 16,797 (2011).

P. Y. Chang, G. Fiksel, M. Hohenberger, J. P. Knauer, R. Betti, F. J. Marshall, D. D. Meyerhofer, F. H. Séguin, and R. D. Petrasso, "Fusion Yield Enhancement in Magnetized Laser-Driven Implosions," Phys. Rev. Lett. **107**, 035006 (2011).

C. G. Freeman, G. Fiksel, C. Stoeckl, N. Sinenian, M. J. Canfield, G. B. Graeper, A. T. Lombardo, C. R. Stillman, S. J. Padalino, C. Mileham, T. C. Sangster, and J. A. Frenje, "Calibration of a Thomson Parabola Ion Spectrometer and Fujifilm Imaging Plate Detectors for Protons, Deuterons, and Alpha Particles," Rev. Sci. Instrum. **82**, 073301 (2011).

E. Głowacki, K. L. Marshall, C. W. Tang, and N. S. Sariciftci, "Doping of Organic Semiconductors Induced by Lithium Fluoride/Aluminum Electrodes Studied by Electron Spin Resonance and Infrared Reflection-Absorption Spectroscopy," Appl. Phys. Lett. **99**, 043305 (2011).

S. D. Jacobs, "MRF with Adjustable pH," in *Optical Fabrication, Testing, and Metrology IV*, edited by A. Duparré (SPIE, Bellingham, WA, 2011), Vol. 8169, Paper 816902.

K. L. Marshall, S. K.-H. Wei, M. Vargas, K. Wegman, C. Dorrer, P. Leung, J. Boule III, Z. Zhao, and S. H. Chen, "Liquid Crystal Beam–Shaping Devices Employing Patterned Photoalignment Layers for High-Peak-Power Laser Applications," in *Liquid Crystals XV*, edited by I. C. Khoo (SPIE, Bellingham, WA, 2011), Vol. 8114, Paper 81140P.

C. Miao, R. Shen, M. Wang, S. N. Shafrir, H. Yang, and S. D. Jacobs, "Rheology of Aqueous Magnetorheological Fluid Using Dual Oxide-Coated Carbonyl Iron Particles," J. Am. Ceram. Soc. **94**, 2386 (2011).

M. Mikulics, P. Kordoš, D. Gregušová, R. Adam, M. Kočan, S. Wu, J. Zhang, R. Sobolewski, D. Grützmacher, and M. Marso, "Monolithic Integration of Ultrafast Photodetector and MESFET in the GaN Material System," IEEE Photonics Technol. Lett. **23**, 1189 (2011).

R. Nora and R. Betti, "One-Dimensional Planar Hydrodynamic Theory of Shock Ignition," Phys. Plasmas **18**, 082710 (2011).

B. B. Pollock, C. E. Clayton, J. E. Ralph, F. Albert, A. Davidson, L. Divol, C. Filip, S. H. Glenzer, K. Herpoldt, W. Lu, K. A. Marsh, J. Meinecke, W. B. Mori, A. Pak, T. C. Rensink, J. S. Ross, J. Shaw, G. R. Tynan, C. Joshi, and D. H. Froula, "Demonstration of a Narrow Energy Spread, ~0.5 GeV Electron Beam from a Two-Stage Laser Wakefield Accelerator," Phys. Rev. Lett. **107**, 045001 (2011).

J. E. Schoenly, W. D. Seka, and P. Rechmann, "Near-Ultraviolet Removal Rates for Subgingival Dental Calculus at Different Irradiation Angles," J. Biomed. Opt. **16**, 071404 (2011).

R. Xin and J. D. Zuegel, "Amplifying Nanosecond Optical Pulses at 1053 nm with an All-Fiber Regenerative Amplifier," Opt. Lett. **36**, 2605 (2011).

B. Xu and S. X. Hu, "Effects of Electron-Ion Temperature Equilibration on Inertial Confinement Fusion Implosions," Phys. Rev. E **84**, 016408 (2011).

J.-H. Yang and R. S. Craxton, "An Empirical Model of Collective Electrostatic Effects for Laser-Beam Channeling in Long-Scale-Length Relativistic Plasmas," Phys. Plasmas **18**, 082703 (2011).

Forthcoming Publications

S. H. Chen and S. K.-H. Wei, "Modification of the Stokes–Einstein Equation with a Semi-Empirical Microfriction Factor for Correlation of Tracer Diffusivities in Organic Solvents," to be published in Industrial and Engineering Chemistry Research.

C. Dorrer, S. K.-H. Wei, P. Leung, M. Vargas, K. Wegman, J. Boulé, Z. Zhao, K. L. Marshall, and S. H. Chen, "High-Damage-Threshold Static Laser Beam Shaping Using Optically Patterned Liquid-Crystal Devices," to be published in Optics Letters.

I. Íñiguez-de-la-Torre, S. Purohit, V. Kaushal, M. Margala, M. Gong, R. Sobolewski, D. Wolpert, P. Ampadu, T. González, and J. Mateos, "Exploring Digital Logic Design Using Nanometer-Scale Devices Through Monte Carlo Simulations," to be published in IEEE Transactions on Nanotechnology.

S. K.-H. Wei, S. H. Chen, K. L. Marshall, C. Dorrer, and S. D. Jacobs, "Azimuthal Anchoring Energy and Pixel Resolution in a Photopatterned Liquid Crystal Cell Using Coumarin-Based Photoalignment Layers," to be published in the Japanese Journal of Applied Physics.

J.-H. Yang, R. S. Craxton, and M. G. Haines, "Explicit General Solutions to Relativistic Electron Dynamics in Plane-Wave Electromagnetic Fields and Simulations of Ponderomotive Acceleration," to be published in Plasma Physics and Controlled Fusion.

Conference Presentations

The following presentations were made at the NAS/NAE ICF Targets Panel, Rochester, NY, 6–8 July 2011:

D. H. Froula, "Laser–Plasma Interaction in Direct-Drive Implosions."

R. L. McCrory, "Overview of LLE's ICF Program."

D. D. Meyerhofer, "Facilitating NIF Polar Drive."

D. D. Meyerhofer, "Shock and Fast Ignition."

P. B. Radha, "Polar-Drive Target Design."

T. C. Sangster, "Direct-Drive Progress on OMEGA."

M. J. Grosskopf, R. P. Drake, C. C. Kuranz, E. M. Rutter, H. S. Park, N. Kugland, S. Pollaine, S. Ross, B. A. Remington, D. Ryutov, A. Spikovsky, L. Gargate, G. Gregori, A. Bell, C. Murphy, Y. Sakawa, Y. Kuramitsu, H. Takabe, D. Froula, G. Fiksel, F. Miniati, M. Koenig, A. Ravasio, E. Liang, and N. Woolsey, "Hydrodynamic Simulation of Laboratory Astrophysics Experiments Generating Collisionless Shocks with Intense Lasers," Interrelationship Between Plasma Experiments in Laboratory and Space, Whistler, Canada, 10–15 July 2011.

D. D. Meyerhofer, "Diagnostics for High-Energy-Density Physics," HEDP Summer School, San Diego, CA, 10–16 July 2011.

P. W. McKenty, "ICF Research at the Laboratory for Laser Energetics: The Path to Polar-Drive Ignition," JOWOG 37, Aldermaston, United Kingdom, 11–15 July 2011.

S. P. Regan, R. Epstein, B. A. Hammel, L. J. Suter, J. Ralph, H. Scott, M. A. Barrios, D. K. Bradley, D. A. Callahan, G. W. Collins, S. Dixit, M. J. Edwards, D. R. Farley, S. H. Glenzer,

I. E. Golovkin, S. W. Haan, A. Hamza, D. G. Hicks, N. Izumi, J. D. Kilkenny, J. L. Kline, G. A. Kyrala, O. L. Landen, T. Ma, J. J. MacFarlane, A. J. MacKinnon, R. C. Mancini, F. J. Marshall, R. L. McCrory, N. B. Meezan, D. D. Meyerhofer, A. Nikroo, K. J. Peterson, T. C. Sangster, P. Springer, and R. P. J. Town, "Diagnosing Implosions at the National Ignition Facility with X-Ray Spectroscopy," 17th International Conference on Atomic Processes and Plasmas, Belfast, Ireland, 19–22 July 2011.

K. L. Marshall, S. K.-H. Wei, M. Vargas, K. Wegman, C. Dorrer, P. Leung, J. Boule III, Z. Zhao, and S. H. Chen, "Liquid Crystal Beam-Shaping Devices Employing Patterned Photoalignment Layers for High-Peak-Power Laser Applications," SPIE Optics and Photonics, Liquid Crystals XV, San Diego, CA, 21–25 August 2011.

S. D. Jacobs, "MRF with Adjustable pH," Optical Fabrication, Testing and Metrology IV, Marseille, France, 5–8 September 2011.

The following presentations were made at the 7th International Conference on Inertial Fusion Sciences and Applications, Bordeaux, France, 12–16 September 2011:

R. L. McCrory, D. D. Meyerhofer, R. Betti, T. R. Boehly, T. J. B. Collins, R. S. Craxton, J. A. Delettrez, D. H. Edgell, R. Epstein, D. H. Froula, V. Yu. Glebov, V. N. Goncharov, D. R. Harding, S. X. Hu, I. V. Igumenshchev, J. P. Knauer, S. J. Loucks, J. A. Marozas, F. J. Marshall, P. W. McKenty, T. Michel, P. M. Nilson, P. B. Radha, S. P. Regan, T. C. Sangster, W. Seka, R. W. Short, D. Shvarts, S. Skupsky, V. A. Smalyuk, J. M. Soures, C. Stoeckl, W. Theobald, B. Yaakobi, J. A. Frenje, D. T. Casey, C. K. Li, R. D. Petrasso, F. H. Séguin, S. P. Padalino, K. A. Fletcher, P. M. Celliers, G. W. Collins, and H. F. Robey, "Progress in Direct-Drive Inertial Confinement Fusion."

P. W. McKenty, T. J. B. Collins, J. A. Marozas, T. J. Kessler, J. D. Zuegel, M. J. Shoup III, R. S. Craxton, F. J. Marshall, A. Shvydky, S. Skupsky, V. N. Goncharov, P. B. Radha, R. Epstein, T. C. Sangster, D. D. Meyerhofer, R. L. McCrory, J. D. Kilkenny, A. Nikroo, M. L. Hoppe, M. M. Marinak, A. J. MacKinnon, M. J. Schmitt, P. A. Bradley, G. R. Magelssen, and T. J. Murphy, "Preparing for Polar-Drive Ignition on the NIF."

H.-S. Park, N. Kugland, S. Ross, B. Remington, S. Pollaine, D. Ryutov, A. Spitkovsky, L. Gargate, G. Gregori, A. Bell, C. Murphy, Y. Sakawa, Y. Kuramitsu, H. Takabe, D. Froula, G. Fiksel, F. Miniati, M. Koenig, A. Ravasio, E. Liang, N. Woolsey, and M. Grosskopf, "Collisionless Shocks in Laser Driven Laboratory High Energy Density Plasmas."

P. B. Radha, F. J. Marshall, T. R. Boehly, T. J. B. Collins, R. S. Craxton, D. H. Edgell, R. Epstein, J. A. Frenje, V. N. Goncharov, J. A. Marozas, R. L. McCrory, P. W. McKenty, D. D. Meyerhofer, R. D. Petrasso, T. C. Sangster, A. Shvydky, and S. Skupsky, "Polar Drive on OMEGA."

S. P. Regan, R. Epstein, B. A. Hammel, L. J. Suter, J. Ralph, H. Scott, M. A. Barrios, D. K. Bradley, D. Callahan, C. Cerjan, G. W. Collins, S. N. Dixit, J. Edwards, D. R. Farley, S. Glenn, S. H. Glenzer, I. E. Golovkin, S. W. Haan, A. Hamza, D. G. Hicks, N. Izumi, J. D. Kilkenny, J. L. Kline, G. A. Kyrala, O. L. Landen, T. Ma, J. J. MacFarlane, R. C. Mancini, R. L. McCrory, N. B. Meezan, D. D. Meyerhofer, A. Nikroo, K. J. Peterson, T. C. Sangster, P. Springer, and R. P. J. Town, "Diagnosing Implosions at the National Ignition Facility with X-Ray Spectroscopy."

A. Richard, V. Allouche, E. Alozy, F. Aubard, S. Bazzoli, T. Beck, J. Baggio, J. L. Bourgade, J. Y. Boutin, M. Briat, S. Brygoo, T. Caillaud, C. Cherfils, C. Chollet, P. Combis, S. Darbon, D. Dennettière, J. L. Desmeuzes, A. Duval, J. Fariat, J. Favier, S. Gary, J. Gazave, S. Girard, V. Glebov, J. C. Gomme, D. Gontier, O. Henry, S. Huevlan, H. P. Jacquet, J. P. Jadaud, O. Landoas, P. Llavador, B. Marchet, R. Marmoret, R. Maroni, I. Masclet-Gobin, D. D. Meyerhofer, J. P. Le Breton, G. Oudot, S. Perez, G. Pien, J. Raimbourg, C. Reverdin, P. Romary, R. Rosch, B. Rosse, A. Rousseau, D. Rubin de Cervens, T. C. Sangster, C. Schoech, P. Semécurbe, G. Souillé, P. Stemmler, C. Stoeckl, I. Thfoin, C. Trosseille, P. Troussel, J. L. Ulmer, L. Videau, B. Villette, R. Wrobel, and C. Zuber, "Diagnosis Development for Plasma Experiments on LMJ."

T. C. Sangster, E. J. Bond, J. A. Caggiano, D. T. Casey, M. J. Eckart, J. A. Frenje, S. Friedrich, M. Gatu-Johnson, V. Yu. Glebov, E. P. Hartouni, R. Hatarik, S. P. Hatchett, H. W. Herrmann, C. J. Horsfield, M. Hutton, J. D. Kilkenny, J. P. Knauer, R. A. Lerche, J. McNaney, M. J. Moran, D. H. Munro, S. J. Padalino, P. K. Patel, D. Schneider, and C. Stoeckl, "High-Accuracy Ion-Temperature and Areal-Density Measurements with the NIF nTOF Suite."

W. Theobald, A. Casner, R. Nora, X. Ribeyre, K. S. Anderson, R. Betti, R. S. Craxton, J. A. Delettrez, J. A. Frenje, V. Yu. Glebov, O. V. Gotchev, M. Hohenberger, M. Lafon, F. J. Marshall, R. L. McCrory, D. D. Meyerhofer, L. J. Perkins, T. C. Sangster, G. Schurtz, W. Seka, V. A. Smalyuk, C. Stoeckl, and B. Yaakobi, "Progress in the Shock-Ignition Inertial Confinement Fusion Concept."

J. D. Zuegel, C. Dorrer, I. A. Begishev, R. Cuffney, T. J. B. Collins, E. Hill, J. H. Kelly, B. E. Kruschwitz, J. A. Marozas, P. W. McKenty, A. V. Okishev, R. G. Roides, D. F. Browning, G. V. Erbert, and M. W. Bowers, "Polar-Drive Beam Smoothing for Direct-Drive Ignition on the National Ignition Facility."

D. H. Froula, "Laser–Plasma Interactions in Direct-Drive Implosions," Assessment of Inertial Confinement Fusion Targets, Washington, DC, 20–21 September 2011.

The following presentations were made at Ultrafast Optics 2011, Monterey, CA, 26–30 September 2011:

J. Bromage, C. Dorrer, and R. K. Jungquist, "Temporal Contrast Degradation at the Focus of Ultrafast Pulses from High-Frequency Spectral Phase Modulation."

J. Bromage, M. Millecchia, J. Bunkenburg, R. K. Jungquist, C. Dorrer, and J. D. Zuegel, "A Cylindrical Öffner Stretcher Design for Reduced Chromatic Aberrations and Improved Temporal Contrast in Ultrafast Laser Systems."

C. Dorrer, "Interferometric Techniques for Optical-Pulse Characterization."

J. Qiao, P. A. Jaanimagi, R. Boni, J. Bromage, and E. Hill, "Measuring Short Pulse Using a High-Speed Streak Camera on Kilojoule, Petawatt-Class Laser Systems."

R. Xin and J. D. Zuegel, "All-Fiber Directly Chirped Laser Source (DCLS) for Chirped-Pulse Amplification."


1850
MELIORA
UNIVERSITY of
ROCHESTER